UNIVERSITY OF BIRMINGHAM

ADVANCED MODELLING FOR THE ORTHOGONAL CUTTING OF UNIDIRECTIONAL CARBON FIBRE REINFORCED PLASTIC COMPOSITES

by

ALESSANDRO ABENA

Department of Mechanical Engineering

University of Birmingham

A thesis submitted to:
University of Birmingham
for the degree of:

DOCTOR OF PHILOSOPHY

Department of Mechanical Engineering
University of Birmingham
June 2017

Abstract

The rapid increase in the industrial utilisation of carbon fibre reinforced plastic composites in recent years has led to growing interest in numerical modelling of these materials during machining. Lately, the micro-mechanical approach has been implemented via the finite element method (FEM) using zero thickness cohesive elements. Usually, these elements experience excessive distortion; while poor thrust force prediction is generally associated with the deletion of failed elements in FEM. In this thesis, a novel cohesive model was developed. A smoothed particle hydrodynamics (SPH) method was implemented to avoid element deletion during the analysis. However, the absence of a cohesive layer did not permit the collection of information on the interface behaviour. Therefore, a hybrid model, based on the FEM to SPH conversion, was deployed to introduce a cohesive layer, while avoiding element deletion. In-house experiments were conducted to support and validate the hybrid model. The design of experiments method was utilised to identify the significant process parameters. The results showed that the novel cohesive model prevented the excessive distortion shown by the zero thickness cohesive elements. The SPH enabled more accurate prediction of the thrust force, more realistic chip formation mechanisms and the

capability to simulate the bouncing back. For instance, for fibre orientation of θ=0° the thrust force improves from 0.11 N/mm to 1.99 N/mm; and the bouncing back amount has been found equal to the cutting edge radius of the tool ($\sim$5μm). The hybrid approach enables implementation of the novel cohesive model showing an improvement of the thrust force prediction when compared with the FEM. In particular, for fibre orientation of θ=0° the thrust force predicted acts in same direction as the experimental force; while the FEM shows the opposite direction. The hybrid approach was able to capture the effect of a round cutting edge, as was highlighted in the experimental results at fibre orientation θ=0° and θ=90°. The experiments highlighted the strong influence of the rake angle and fibre orientation on the bouncing back. For θ=135°, while negative or slightly positive (α=10°) rake angles lead to a high amount of bouncing back, a high positive rake angle (α=30°) leads to an actual depth of cut higher than the set nominal depth of cut.

Acknowledgements

I would like to express my great gratitude to my supervisor **Dr. Khamis Essa** for the patient guidance, encouragement and advice he has provided, helping me to achieve the set goals.

I would like to express my sincere gratitude to **Dr. Sein Leung Soo** for his support and availability all over the PhD project.

My sincere thank also goes to **Mr. Peter Thornton** for his help and guidance during the experiments.

I would like to thank **Dr. Ali Mohamed Abdelhafeez** for his help in planning the experimental work.

I would like to thank **Dr. Pavel Penchev** for carrying out the laser machining on the composite material.

I would also like to thank **Mr. Amir Hajiyavand** and **Mr. Tawfik Badawy** for their availability.

I gratefully acknowledge the Department of Mechanical Engineering for providing a studentship which financially supported this work.

I would like to thank **Miss Irene Abena** and **Mr. Hallam Hartley Henry** for their support and help.

Last but not the least, I would like to thank **My Family** for their support and encouragement during my studies, and **Miss Vanessa Indrizzi** for always being at my side with her love and patience.

This thesis was copy-edited for the conventions of language, grammar and spelling by Janet's Proofreading Service.

List of publications

- A. Abena, S.L. Soo, and K. Essa. A finite element simulation for orthogonal cutting of UD-CFRP incorporating a novel fibre-matrix interface model. *Procedia CIRP*, 31:539-544, 2015.

- A. Abena, S.L. Soo, and K. Essa. Modelling the orthogonal cutting of UD-CFRP composites: Development of a novel cohesive zone model. *Compos Struct*, 168:65-83, 2017.

Contents

List of Figures

List of Tables

Nomenclature

Abbreviations

2FI 2-factorial interaction

ANOVA Analysis of variance

CFRP Carbon fibre reinforced plastic

CSDMG Damage variable for cohesive surfaces in general contact

DOC Depth of cut

DOE Design of experiment

EHM Equivalent homogeneous material

FEM Finite element method

FRP Fibre reinforced plastic

FV Field variable

PEEQ Equivalent plastic strain

QUADSCRT Quadratic nominal stress damage initiation criterion

RSM Response surface method

SDEG Scalar stiffness degradation variable

SDV Solution dependent state variable

SPH Smoothed particle hydrodynamics

UD-CFRP Unidirectional carbon fibre reinforced plastic

Vel Cutting speed

VUMAT User subroutine to define material behaviour

VUSDFLD User subroutine to redefine field variables at a material point

Symbols

α Rake angle of the tool

β Tilt angle of the sample

δ Displacement

δ^0 Displacement at damage initiation

δ^f Displacement at failure

δ^{max} Maximum displacement

ϵ Strain

γ Clearance angle of the tool

ν Poisson's ratio

$\bar{\epsilon}$ Strain vector

$\bar{\epsilon}_0^{pl}$ Equivalent plastic strain at the onset of damage

$\bar{\epsilon}_f^{pl}$ Equivalent plastic strain at failure

$\overline{\overline{CF}}$ Connectivity matrix for fibre and cohesive elements

$\overline{\overline{CM}}$ Connectivity matrix for matrix and cohesive elements

$\overline{\overline{El}}_{phase-name}$ Matrix of elements

$\overline{\overline{Nd}}_{phase-name}$ Matrix of nodes

$\overline{\overline{P}}$ Stiffness matrix

$\bar{t}$ Stress vector

σ Normal stress

σ_u Failure strength

σ_y Yield strength

σ_{y0} Yield stress at the onset of damage

τ Shear stress

θ Fibre orientation

C_{ij} Coefficients of the stiffness matrix for fibre

d, D Damage variable

E Young's modulus

F_c Cutting force

F_t Thrust force

G Shear modulus

G^C Fracture energy

P^d Stiffness of the damaged material

R Machining force

r Cutting edge radius of the tool

t_n^0, σ_{max} Normal strength

t_s^0, t_t^0, τ_{max} Shear strength

T_0 Constitutive thickness

X Longitudinal strength

x_1 Fibre orientation

x_2 Rake angle of the tool

x_3 Cutting speed

x_4 Depth of cut

Chapter 1

Introduction

1.1 Background and motivation

Fibre reinforced plastic (FRP) composite materials are increasingly being used in high performance applications within various industrial sectors. Reasons for their employment can be traced to their superior properties in terms of specific strength/stiffness, corrosion resistance, damage tolerance and resistance to fatigue; as well as thermal and acoustic insulation power, when compared with conventional material/alloys. This can be seen in Figure 1.1 for carbon fibre reinforced plastic (CFRP) composites [1]; the material of interest in this thesis.

In recent years, the use of CFRP composites for applications where high performances are required has increased significantly, particularly in the aerospace sector.

Since the 1980s, composite materials' employment has grown considerably. Today, it represents more then 50% of the entire structure of the last generation of aeroplanes (Figure

1.2) [2, 3], and involves growing investments. In fact, the amount of carbon fibre composites increased from about 3 ton/unit in the A300-600, up to about 32 ton/unit in the A350. It has been predicted that carbon fibre demand will grow to 183,000 tons in 2020, leading to an increase in investments from USD $15.4 billion in 2013 to $35 billion in 2020 [4].

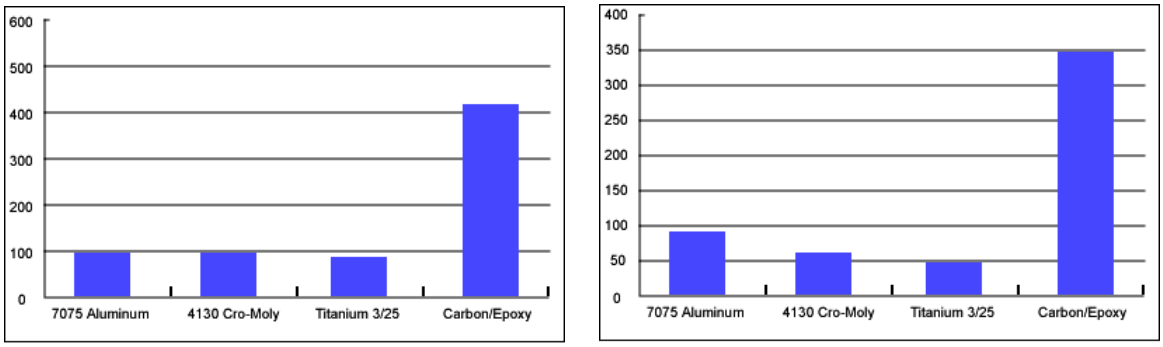

(a) *(b)*

Figure 1.1: Comparison between carbon/epoxy and conventional materials in terms of (a) stiffness to weight ratio; and (b) strength to weight ratio [1].

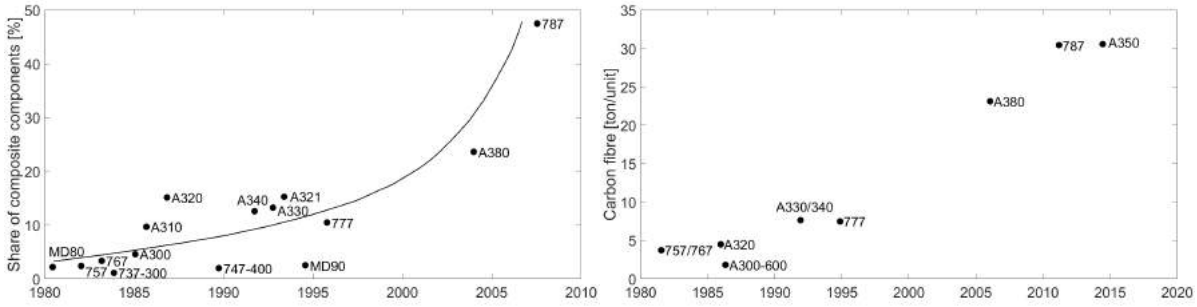

(a) *(b)*

Figure 1.2: Amount of (a) composite materials; and (b) carbon fibre composites, employed on aeroplanes' structures over the past years [2, 3].

Great efforts have been made during the past few years to increase the amount of composite percentage employed, leading to the well-known Boeing 787 Dreamliner and Airbus A350 XWB shown in Figure 1.3. In only seven years, carbon fibre composite employment increased by almost 50% in the Boeing plane, to 53% in the Airbus one [5–8].

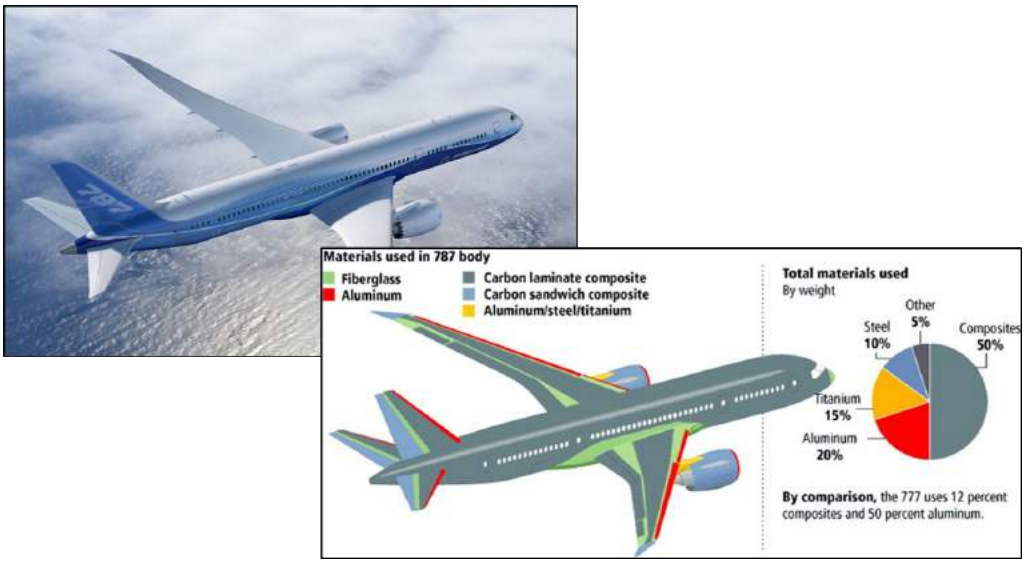

(a)

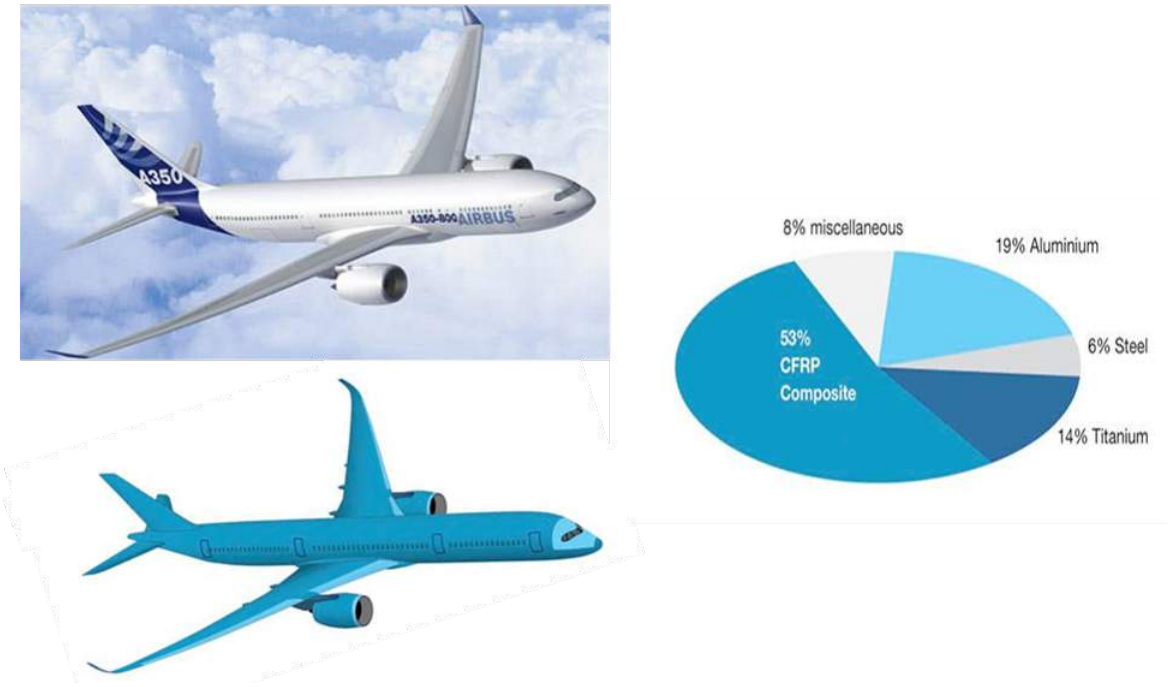

(b)

Figure 1.3: Material used in (a) Boeing 787 Dreamliner structure [5, 6]; and (b) Airbus A350 XWB structure [7, 8].

Consequently, conventional material usage reduced, with steel in particular dropping from 10% to 6%.

Depending on the task, each component is realized using a different composite material. In particular, it is possible to notice from the overall amount of composite materials used, the carbon fibre laminate composite represents the largest part; it is mainly present on the fuselage and wings.

During production, machining operations are required for the removal of excess material to meet dimensional tolerances or for producing holes for assembly. While conventional materials are well known, composite materials are relatively new and the tool-workpiece interaction and its effect on the machined component are not yet fully understood.

The inhomogeneous and anisotropic nature of composite materials still represents a challenge in terms of machinability. Defects can arise during machining in each phase of the material, hence involving the fibre, matrix, and fibre-matrix interface. The presence of such flaws can compromise surface integrity and lead to poor component in-service performance. The importance of minimizing/eliminating workpiece damage following machining, has led industries and researchers to investigate these processes.

During complex machining operations, such as drilling and milling, the tool encounters fibres at different orientations ($0° \leq \theta < 180°$), making the process difficult to investigate. Indeed, it has been observed that the chip formation mechanisms during machining change depending on the fibre orientation and so affecting the final quality of the component. In order to simplify the problem, and better understand the effect of fibre orientation, orthogonal cutting is usually studied.

Until now experimental investigations have generally focused on observing the chip formation mechanism, and on measuring the machining force and the surface roughness. Conversely, studies providing information on damage and on the amount of elastic recovery experienced by the component after machining (bouncing back) are limited. In addition, it is still very challenging to obtain in-situ observations of the tool-workpiece interaction during cutting at the micro-scale level, and to measure local deformation and stresses in each phase of the material.

While the experimental approach represents a foundational step for the understanding of the machining process, alternatives, including analytical, empirical and numerical approaches, have also been employed. The analytical approach has proved to be incapable of taking into account the complexity of the process. The empirical approach needs experimental calibration, and its results are reliable only in the range used for that calibration. Moreover, it can only provide limited information, such as cutting force and thrust force.

The numerical models seem to be the most flexible tool for studying the machining of CFRP. In fact, they can provide detailed information at different scale levels (from the macro-scale to the micro-scale), that could be difficult to obtain using different approaches (experimental, analytical, and empirical). However, the numerical approach still needs to be validated against experimental results.

Over the years, orthogonal cutting simulation has been continuously improved in an attempt to make it as accurate as possible. In particular, models implementing the composite as an equivalent homogeneous material have been widely used. Recently, a micro-mechanical approach, where each phase (fibre, matrix, fibre-matrix interface) is simulated separately, has

been employed. This allows analysis of the material removal, observing the damage formation and propagation in each phase of the material. The accuracy and reliability of the simulation are strongly dependent on the assumptions made, and on material data availability. To date, information on material properties for each phase of CFRP composite is still limited.

In conclusion, the necessity to improve the quality of CFRP components requires a better understanding of the tool-workpiece interaction and of its effect on the machined material. The limited knowledge at the micro-scale level represents the main motivation for the present thesis. In fact, the understanding of the chip formation mechanisms and the damage formation and propagation during cutting in each phase of the composite material (matrix, fibre, fibre-matrix interface) can help in improving the quality of the final component, minimising the presence of flaws that can compromise surface integrity and lead to poor in-service component performance. As numerical models represent a powerful tool to investigate the process, they are employed for the investigation. Up-to-date, numerical studies implementing the micro-mechanical approach are still few, and two-dimensional models are usually used, leaving a large amount of room for improvement.

1.2 Aim and objectives

The aim of this project is to develop a comprehensive numerical model for the orthogonal cutting of unidirectional carbon fibre reinforced plastic (UD-CFRP) composite, to improve prediction of machining force and material deformation and failure at the micro-scale level. Particular attention will be given to cohesive models, and to mesh-free methods to develop

models which are able to provide a more accurate prediction of the fibre-matrix interface behaviour and thrust force, respectively.

The aim of the work is achieved by means of the following objectives:

- developing a novel cohesive model for the fibre-matrix interface simulation able to avoid excessive distortion experienced by cohesive elements in existing models;
- developing a finite element model for the orthogonal cutting of UD-CFRP implementing fibres with cylindrical geometry;
- implementing a new modelling approach based on the mesh-free smoothed particle hydrodynamics method (SPH) to improve the thrust force prediction;
- developing a hybrid model based on the FEM to SPH conversion to combine the advantages of both methods;
- carrying out in-house experiments for model validation, and to investigate the effect of the machining parameters on the quality of the final component.

1.3 Thesis structure

In Chapter 2 there is a review of different approaches (experimental, analytical, empirical, and numerical) used in the literature to investigate the orthogonal cutting of FRPs. For each approach, findings are presented, and both advantages and drawbacks are also highlighted.

In Chapter 3, particular attention is given to cohesive models used to simulate the fibre-matrix interface. A review and a comparison are provided, highlighting the drawbacks and

advantages of each model. Based on the comparison, a new cohesive zone model, implemented in a two-dimensional extruded geometry, is developed to overcome the limitations of existing models. Validation of the numerical models is realised using experimental results from the literature.

In Chapter 4 a cylindrical geometry for fibres is considered. The difference against the 2D-extruded model is highlighted. In particular, the discrepancy in terms of predicted damage extension, chip formation mechanisms, cutting force and thrust force is provided. Validation of numerical models using experimental results from the literature is presented.

In Chapter 5, the smoothed particle hydrodynamic (SPH) method considering cylindrical fibres is employed to improve the thrust force prediction, avoiding element deletion during analysis. The validation for the SPH method is done using experimental results from the literature. A comparison with the 3D-FEM model is also presented.

In Chapter 6, in order to provide more detailed information to support the numerical models' development and validation, in-house experiments carried out for the orthogonal cutting of UD-CFRP are presented and the results are described. Types of chips obtained and chip formation mechanisms observed are analysed. The influence of the machining parameters on the cutting force, thrust force, damage extension, surface quality and bouncing back is also investigated, by means of the response surface method (RSM) and the analysis of variance (ANOVA) technique. Finally, an optimization for minimizing the surface roughness and the damage extension in the final component is realised for different fibre orientations.

In Chapter 7, due to the absence of cohesive elements when using the SPH method, a novel hybrid model with cylindrical fibres is developed. It implements FEM to SPH element

conversion after failure, trying to combine advantages of both methods. The results obtained from experiments carried out in Chapter 6 are used for the model validation.

Finally, conclusions of the work carried out are summarised in Chapter 8, where also suggestions for future works are reported.

Chapter 2

Literature review

2.1 Introduction

In this chapter an introduction to composite materials, and an overview of the orthogonal cutting of these materials are presented. Different approaches used to study this process are reported; which include experimental, analytical, empirical, and numerical approaches. For each of them the advantages and drawbacks are highlighted.

2.2 Overview of composite materials

A composite material is made up of two or more constituents or phases with significantly different physical and chemical properties that, when combined, produce a material with characteristics diverse from the individual components [9]. The constituent present as a continuous phase is called *matrix*, to which a *reinforcement* phase is added to improve its

properties, as represented in Figure 2.1. The matrix's purpose is to protect the reinforcement from the external environment, and redistribute the loads applied on the composite material to the reinforcement.

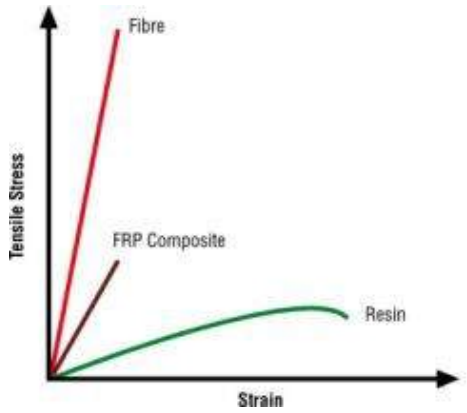

Figure 2.1: Tensile stress-strain curve for matrix, fibre and FRP composite material [10].

The matrix and reinforcement phases can be realized using various materials. The former can be made of metals, ceramics or polymers, to which additives can be added in order to enhance the properties. The latter presents in different shapes, e.g. continuous fibres, discontinuous fibres or particulates, and can be orientated according to a preferred direction or randomly. Furthermore, continuous fibres are usually used in the form of textile fabrics having different configurations (e.g. plain weave, three-harness satin weave, five-harness satin weave [11]).

In composite material, the shape and arrangement of the reinforcement determine the level of anisotropy of the lamina. In particular, since the fibres are characterised by high properties (strength and stiffness) along the axis direction, reinforcement in the shape of perfectly aligned long fibres presents a high level of anisotropy. Composite materials are composed by laminae stacked one on top of each other in a certain sequence forming multi-

plies. Depending on the loads that the component needs to withstand during service, it is possible to design the stacking sequence to optimize the in-service performance.

Materials for the matrix and the reinforcement, and the reinforcement shape and arrangement can be chosen depending on the area of application. Metal matrices are generally reinforced by means of metals or ceramic materials; they are more expensive than the conventional materials they replace. Hence they are used where the performance improvement justifies the cost [12], such as for structural components for aerospace application or in automotive engines.

Ceramic matrices are used together with ceramic reinforcement to ensure high strength and stiffness at high temperature, e.g. SiC/RBSN composite shows a Young's modulus of 138 GPa, a yield stress of 154 MPa and a tensile strength of 251 MPa at temperature of 1400 °C [13]. Ceramic matrices with ceramic reinforcement are used for example in heat shield systems for space vehicles during the re-entry phase, components for high temperature gas turbines, and brake disks [13].

Polymer matrices present a reinforcement made of glass, carbon or aramid fibres and are employed in many applications, such as aerospace, sport, and transportation industries. A comparison between fibre types, when used in a typical high-performance unidirectional epoxy prepreg, is provided in Figure 2.2. Polymeric matrices can be divided into two main groups: thermoplastics and thermosets. They differ in molecular structure. While the former can be melted easily when heated, the latter are always in a solid state [11, 14]. Stiffness reduction and abrupt variation of the heat capacity are detected when polymers are heated over a characteristic transition temperature, called the glass transition temperature T_g. It

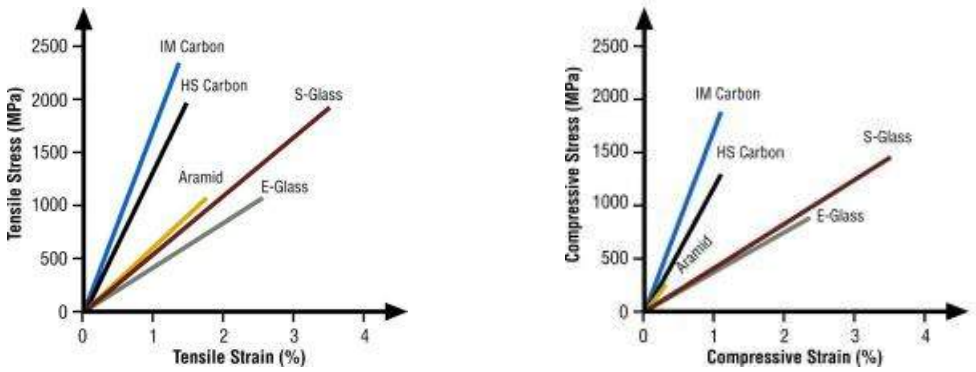

Figure 2.2: Comparison between fibre types used in a typical high-performance unidirectional epoxy prepreg in terms of (a) tensile; and (b) compressive behaviour [10].

represents the maximum temperature the polymeric material can undergo during service. This limit is higher in thermosets (e.g. T_g=65-175 °C for epoxy) than in thermoplastics (e.g. T_g=55-80 °C for polyammide) [11]. Instead, thermoplastic polymers present a strain to failure higher than metals and thermosets materials. For example the polyammide thermoplastic matrix has a strain to failure in the range 150%-300%, while aluminum alloys (7075 T6) and epoxy thermoset matrix have a strain to failure of 11% and 1.5%-8%, respectively. In general, polymeric matrices show stiffness and strength lower than that of metals and ceramics; for example, the Young's modulus is 2.6-3.8 GPa for epoxy, 71 GPa for aluminum alloys (7075 T6), 380 GPa for alumina (99.9% pure), and the tensile strength is 60-85 MPa for epoxy, 572 MPa for aluminum alloys (7075 T6), 282-551 MPa for alumina (99.9% pure).

Glass fibres employed in polymeric matrices are widely used because of their low cost and high corrosion resistance, making them suitable for marine applications and the chemical industry. However, their use in fields where high performance is required is limited [11].

Carbon fibres present high stiffness and strength (Young's modulus and tensile strength

for HM carbon fibre up to about 400 GPa and 4.5 GPa, respectively) together with low density (1.8 g/cm^3) and a moderate cost. Their properties make them greatly required for aerospace applications, and in all sectors where high stiffness to weight and strength to weight ratios are desired. While glass fibres are isotropic, carbon fibres are transversely isotropic, and both fibre types are highly abrasive.

Aramid fibres (trade name Kevlar) are used as substitutes for carbon fibres in sport applications and protective clothes. In fact, they show ductile behaviour under impact, while carbon fibres tend to fail in a brittle manner.

2.3 Machining of composites

Even if composite materials are realised near net-shape, machining operations are required for the removal of excess material to meet dimensional tolerances and for producing holes for subsequent assembly. Methods for material removal can be divided into two groups [11]: conventional and nonconventional. The former includes edge trimming, milling, drilling, countersinking, turning, sawing, and grinding; while the latter employs waterjet and laser beam cutting.

In particular, turning is a process used to finish machining of axisymmetric FRP composite parts. The workpiece rotates around its axis of symmetry, while the cutting tool is fed parallel to the axis, removing a layer of material whose thickness is equal to the set depth of cut. In contrast, in milling the tool rotates around its axis and can have more than one active cutting edge. It engages the workpiece in the radial direction, with the machined surface parallel to

the tool axis. It is mainly limited to deburring and trimming, as well as to achieving contour shape accuracy. Finally, drilling represents one of the most important machining operations that is carried out on composites for making holes required for assembly.

Composite materials are relatively new, and their inhomogeneous and anisotropic nature leads to very complex chip formation mechanisms. Machining of composites using the above material removal methods can produce defects both at the macro-scale and at the micro-scale level: involving matrix cracking, matrix burning, fibre fracture, fibre pullout, fibre-matrix debonding and delamination [11, 15]. In particular, matrix burning takes place when the temperature during machining exceeds the glass transition temperature of the matrix; the debonding represents the detachment between fibre and matrix within a single ply; the delamination represents the detachment between two consecutive plies; and the fibre pullout takes place when the fibre is removed from the matrix leaving a void in it. Hence, defects' reduction and surface integrity improvement during machining operations represent a challenge in order to reduce the possibility of the component integrity and performance compromised whilst in-service.

2.4 Orthogonal cutting

In the case of conventional methods, machining operations such as drilling or milling on composite materials represent complex processes to be analysed. A simplification can be considered in order to facilitate its comprehension, where it regards the orthogonal cutting machining for different fibre orientations; hence downgrading a complex three-dimensional

problem to multiple and simpler two-dimensional problems. For instance, when milling the local angle between the tool velocity vector and the fibre direction changes continuously during machining due to the tool revolution, as represented in Figure 2.3. It varies by increasing from 0° at point (a) to 90° at point (c), up to 180° at point (e); which corresponds again to the initial condition relative to point (a).

During machining, if an infinitesimal time interval is considered, the variation in direction of the tool velocity vector could be neglected, and the cutting condition could be schematized

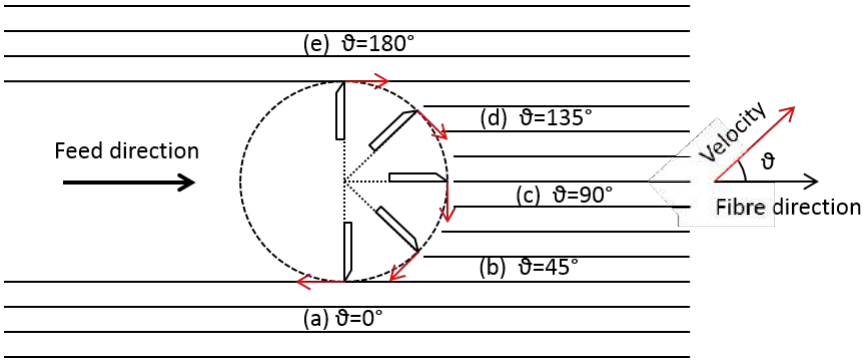

Figure 2.3: Schematic of milling on FRP materials.

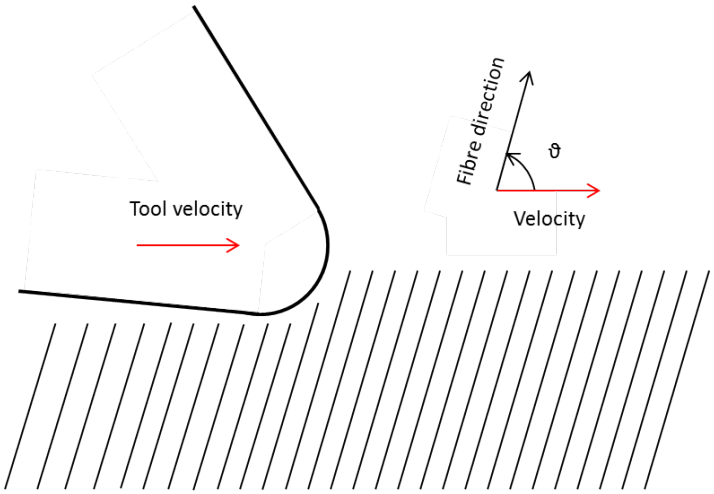

Figure 2.4: Schematic of cutting condition for an infinitesimal time interval considered during milling on FRPs.

as reported in Figure 2.4, which represents the orthogonal cutting on FRPs for a fixed fibre orientation. Hence, the understanding and the capacity to predict the material deformation and failure during the orthogonal cutting considering several fibre orientations could help in defect reduction and surface integrity improvement, even for more complex machining operations. This simplification has been widely used over the past years and still represents a fundamental step in investigating the complex nature of composite machining.

The orthogonal cutting on composites has been studied using different approaches: experimental, analytical, empirical, and numerical. They are described in the following sections.

2.5 Experimental investigation of the orthogonal cutting of UD-FRPs

In machining operations it is important to optimize the output parameters, which generally include machining force, surface roughness and the amount of damage after machining. In fact, the machining force is linked to tool wear and so connected to the tool change frequency and to the surface quality reduction. A high tool change rate is responsible for the higher cost of the final component; affecting also the material volume produced per hour, which decreases due to the time necessary for the tool change. Instead, the surface roughness is representative of the final surface quality, where a low value is desirable to obtain a smooth surface. Finally, it is important to minimize the damage in the final component in order to reduce the probability of failure during service.

The parameters that can be modified in order to optimize the outputs are represented by fibre orientation, tool geometry, cutting speed and depth of cut. The tool geometry features comprise rake angle α, clearance angle γ, and cutting edge radius r (Figure 2.5). The optimization phase requires knowing the effect of the machining parameters on the output variables, and consequently the ability to control the former to obtain the desired characteristics in the final component.

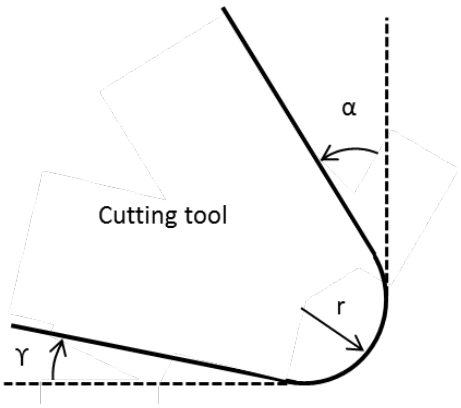

Figure 2.5: Schematic of tool geometry where symbols r, α, γ represent the cutting edge radius, the rake angle and the clearance angle respectively.

For this purpose, the experimental equipment is very important in order to obtain the desired information and for its subsequent analysis. Different methods and equipment have been used over the past years. One of the first attempts to investigate the orthogonal cutting of carbon fibre reinforced plastic was carried out by Koplev *et al.* [16] in 1983. A quick stop device was used to examine the material deformation near the tool, and the macrochip method was used for collecting the chip during cutting. The latter method is set up by covering the sample surface with a thin layer of rubber-based glue. The chip remains stuck to the glue while machining, allowing it to be collected for observation and analysis. Even if this method

has been widely employed providing useful information on the chip morphology [16–19], the free surface of the chip is not totally free, as the glue layer constraints its deformation.

Scanning electron microscopes (SEM) have been widely used for observing and measuring damage in machined samples, such as fibre-matrix debonding depth and fibre pullout [15], and for studying the chip morphology [18, 20–22]. Indeed, the SEM allows observation of the machined sample at very high magnification. The Alicona infinite focus G4 optical scanner has also been used for 3D surface topography analysis and surface roughness measurement [23]; while chip morphology has also been assessed by means of an optical microscope [23, 24].

Nowadays, a high-speed camera is usually part of the experimental set-up [23, 25, 26]. Similarly, high-speed photography was also used by Pwu and Hocheng [27]. These techniques facilitate observation of the dynamic tool-workpiece interaction during machining. However, observation at micro-scale level is still challenging, making it difficult to observe the material deformation in the vicinity of the cutting edge.

Cutting force and thrust force measurement is generally carried out using a dynamometer, which can be mounted on the tool [18, 20, 21, 25, 28], or on the workpiece [23, 24, 26, 29, 30]. Usually a piezoelectric dynamometer is used [23–26, 29–31] and connected to an acquisition system through a charge amplifier.

2.5.1 Chip formation mechanisms

Chip formation mechanisms have been investigated in several studies leading to a general understanding of material removal mechanisms during machining. They have been found to be deeply affected by the fibre orientation θ and the tool rake angle α, as schematically shown

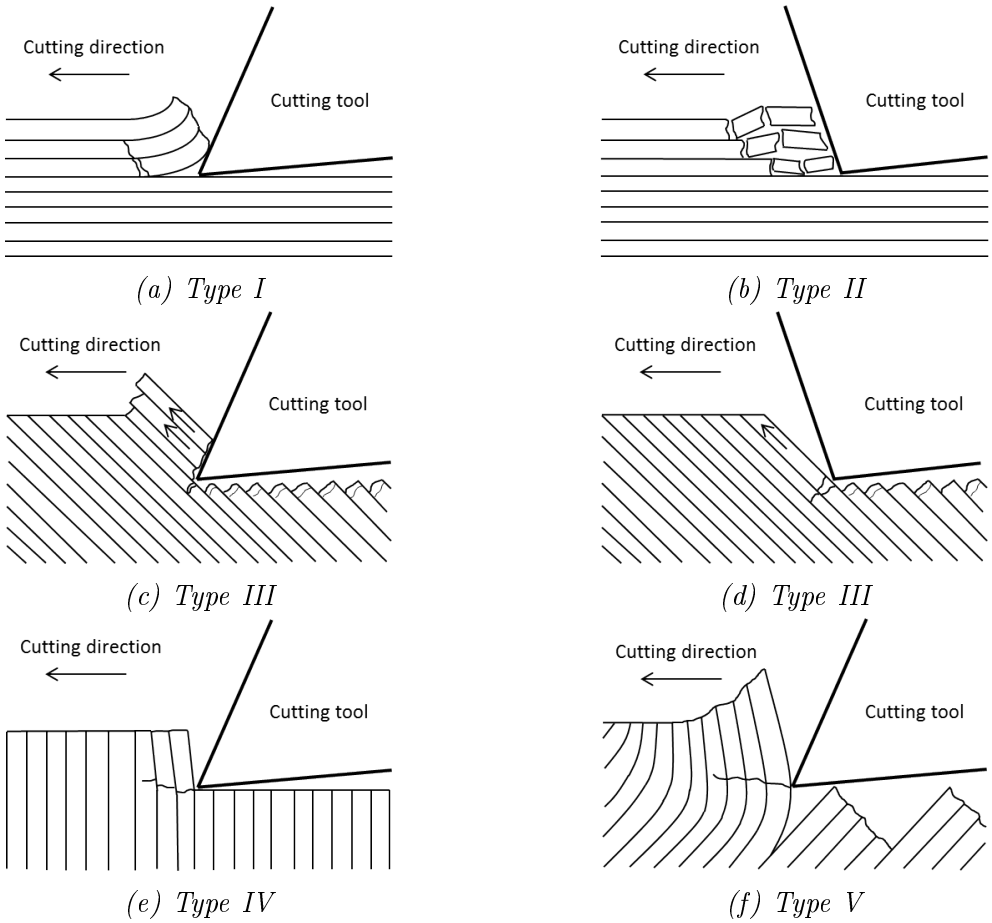

Figure 2.6: Influence of fibre orientation and tool rake angle on the chip formation mechanisms [18]: (a) θ=0°- α>0°; (b) θ=0°- α<0°; (c) θ=45°- α>0°; (d) θ=45°- α<0°; (e) θ=90°- α>0°; (f) θ=135°- α>0°.

in Figure 2.6 [18]. It is possible to identify five different types of chip formation mechanisms depending on fibre orientation and tool rake angle.

In the following, the angle θ between the cutting speed vector and the fibre direction will be measured counterclockwise from the velocity direction, as reported in Figure 2.4.

For fibre orientation θ=0° and positive rake angle, the tool progression causes an opening load (Mode I), leading to fibre-matrix interface failure with consequent fibre bending. The chip slides along the rake face until the crack, induced by bending, takes place ahead of

the cutting edge, and propagates perpendicular to the fibre axis [17, 18, 25, 32]. This is illustrated by Type I in Figure 2.6(a). The propagation of the opening ahead of the tool due to fibre bending has been found to be dependent on the depth of cut. An increase in the depth of cut causes an increase in the opening dimension [21]. For negative rake angles, fibres undergo compressive stress in the axial direction. Tool progression causes sliding loads (Mode II) with fractures at the fibre-matrix interface. Since fibres cannot leave the cutting region because of the negative rake angle, compressive stress increases, leading to fibre failure due to buckling with crack propagation perpendicular to the fibre axis [17, 18, 24]. This is defined as Type II, and shown in Figure 2.6(b).

For $0°<\theta<75°$ and independently from the rake angle, the chip formation mechanism is caused by compression induced shear across the fibre axis, and shear fracture of fibre-matrix interface along the fibre direction [17, 18, 32]. This is presented as Type III in Figure 2.6(c-d). When cutting all fibre angles up to $\theta=90°$, chip flow takes place on a plane parallel to the fibre orientation [29, 32]. The chip formation mechanism for $75°<\theta<90°$ is characterized by compression induced fracture perpendicular to the fibre axis, and interface fracture due to shear along the fibre-matrix interface [18, 32]. This is representative of Type IV, and shown in Figure 2.6(e).

For $\theta>90°$ the chip formation mechanism becomes more complicated, involving considerable out-of-plane displacement, intra-laminar shear at the fibre-matrix interface, and bending deformations due to compression exerted by the tool; which leads to fibre and matrix failure usually below the cutting plane [25, 26]. This is observable as Type V in Figure 2.6(f).

The chip formation mechanisms described above are characteristic of machining realised using a tool with a sharp cutting edge (nose radius of a few micrometer). A different chip formation mechanism has been observed for fibre angle θ=90° by Pwu and Hocheng [27] when machining with a round cutting edge. They used a cutting edge radius 10-20 μm to cut UD-FRP with fibre diameter of 7-10 μm. In this case, the tool is not able to cut the fibre at the contact point, but it exerts compression loading on the sample causing fibre bending. Fibre deflection increases with tool progression until bending failure takes place, usually below the cutting plane. In addition, since matrix material is weaker than fibres, matrix fracture between two consecutive fibres takes place during tool advancement.

Studies considering the effect of a round cutting edge at the micro-scale level are few in the literature. For this reason, an investigation on the tool-workpiece interaction will be carried out by means of experimental and numerical approaches in this thesis.

In addition, the tool-workpiece interaction changes if a round cutting edge is considered [11, 24] as represented in Figure 2.7.

When a sharp cutting edge is used only a chipping zone is present ahead of the tool but when a round cutting edge is used the material ahead of the tool is divided in two

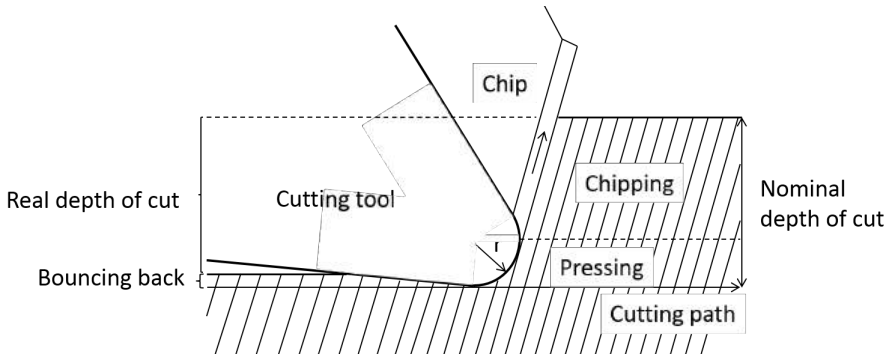

Figure 2.7: Tool-workpiece interaction when machining with a round cutting edge [11, 24].

parts: pressing and chipping. During tool progression the material in the pressing region is compressed under the tool, exhibiting an elastic recovery after the tool has passed. The amount of spring back the material undergoes is called *bouncing back*. Instead, the material in the chipping zone becomes chip during cutting. Due to bouncing back the real depth of cut obtained after machining differs from the nominal depth of cut.

Wang and Zhang [24] investigated the bouncing back for different fibre orientations using a tool with a cutting edge radius of 50 μm. For θ<90° the bouncing back amount was found to be about, or slightly more than, the cutting edge radius. Hence, if the nominal depth of cut is set to a value equal or lower than the tool radius, no cut is displayed, and the workpiece undergoes only large deformation. For θ>90° the material elastic recovery can reach more than double the tool radius.

The bouncing back variation with the nominal depth of cut for fibre orientation θ=30° is

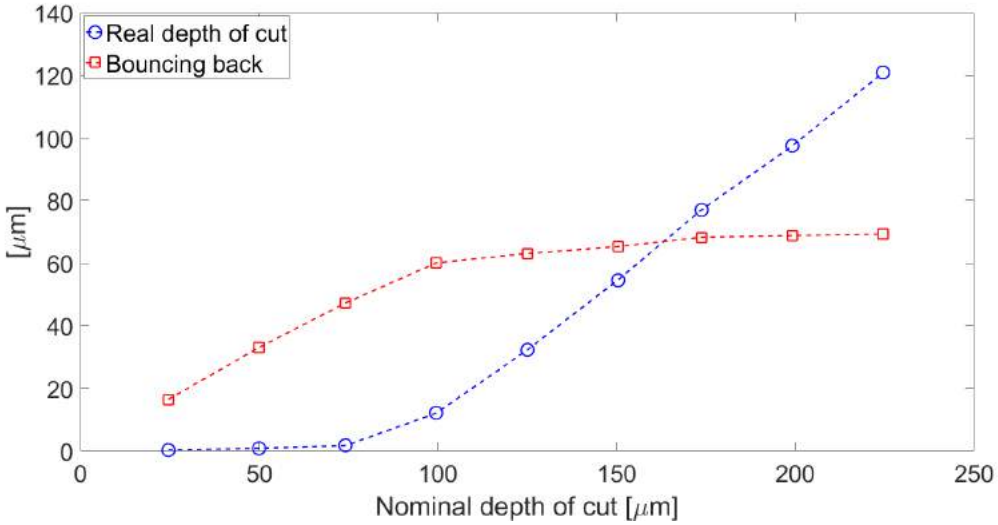

Figure 2.8: Influence of the nominal depth of cut on the bouncing back for fibre orientation θ=30° [24].

reported in Figure 2.8. Increasing the nominal depth of cut, the amount of bouncing back increases, being equal to the set depth of cut. This behaviour is observed for depth of cut values up to almost the tool's radius dimension. When this value is exceeded, the amount of elastic recovery continues to increase, but its value becomes less than the nominal depth of cut, leading to the actual depth of cut greater than zero. A further increase in the depth of cut causes an increase both of the actual depth of cut and of the bouncing back. A value for the nominal depth of cut, after which the bouncing back amount remains constant, can be observed ($\sim$100 μm), leading to an increase of the real depth of cut equal to the increase of the nominal depth of cut. In addition, material experiencing spring back comes in contact with the clearance face exerting a pressure on it, and so contributing to the thrust force.

Despite the fact that the bouncing back represents an important parameter affecting the actual depth of cut, and thrust force, information in the literature is still limited. This is due to the difficulty in measuring it because it takes place at a micro-scale level. For this reason, the effect of the machining parameters on the bouncing back amount will be investigated in this thesis.

2.5.2 Type and morphology of the chip

Chip size and shape have been found dependent mainly on the fibre orientation and the depth of cut. Indeed, the influence of these parameters was studied by Li *et al.* [26] for UD-CFRP (T700 carbon fibres and E765 epoxy resin). For θ=0° a powder like chip was observed for a depth of cut equal to 0.1 mm. Increasing its value to 0.5 mm a crack formed along the fibre-matrix interface ahead of the tool, causing fibre bending. In addition, a second

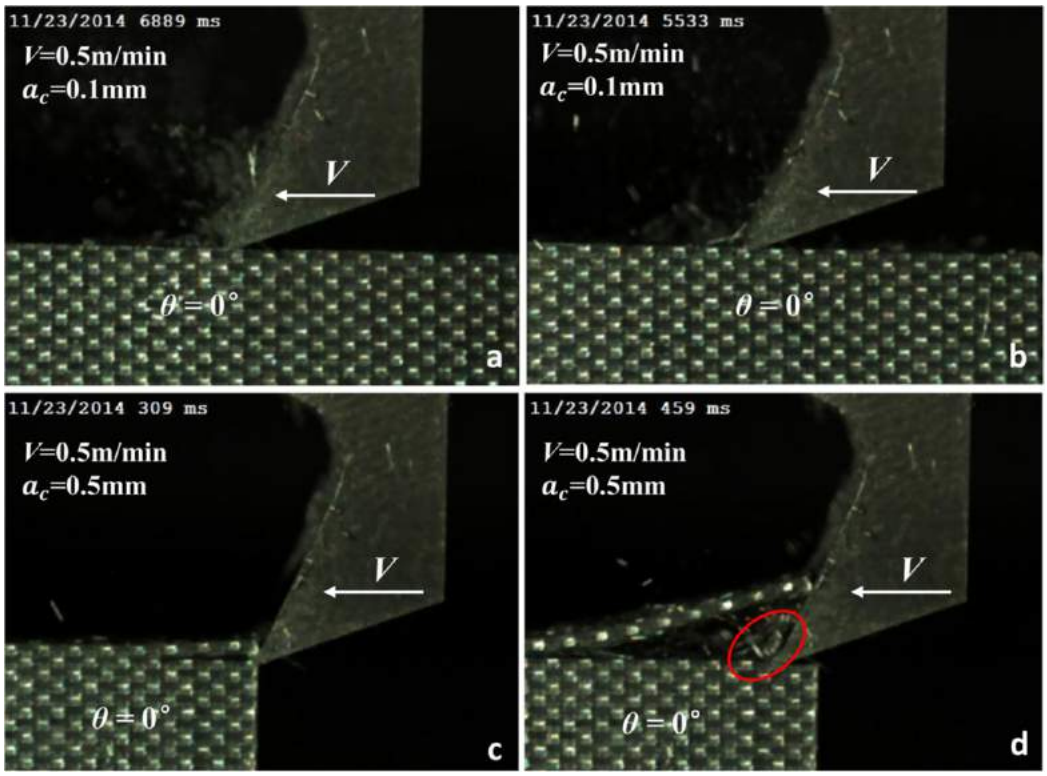

Figure 2.9: Chip formation evolution during orthogonal cutting of UD-CFRP for fibre orientation θ=0° at depth of cut (a-b) 0.1 mm and (c-d) 0.5 mm [26].

cutting zone near the tool tip was detected below the plane containing the interface failure that previously occurred. In this case, two different types of chips, forming at the same time, were observed (Figure 2.9): a blocky chip, due to fibre fracture under bending after the interface failure, and a powder like chip, originating from the second cutting zone. For $15° \leq \theta < 75°$ the continuous and ribbon like chip, observed at low depth of cut (0.1 mm), was replaced by a blocky chip when cutting with 0.5 mm depth of cut. The continuous chip was formed by weakly connected tiny chips that might easily break with tool advancement. This is in agreement with what has been observed by Zitoune *et al.* [21] when machining UD-CFRP material made of T2H carbon fibres and EH25 epoxy resin. In particular, a continuous chip was observed for $\theta=45°$ for all the machining length when using a low depth of cut (0.07

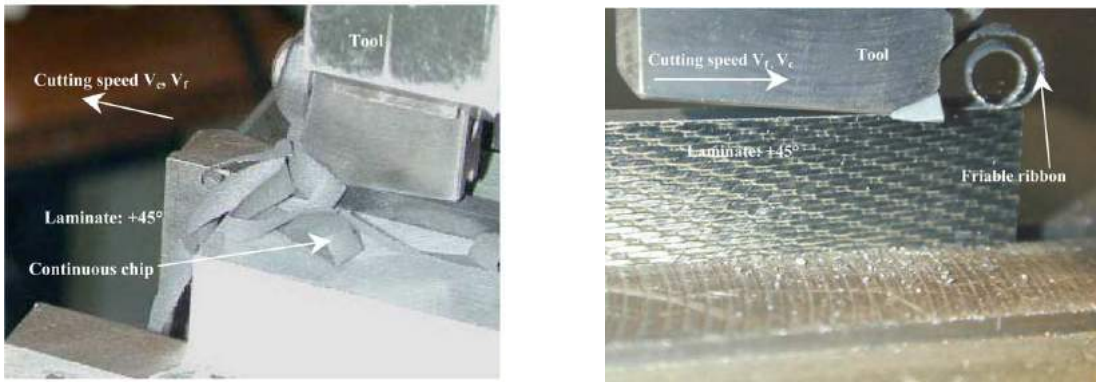

(a) *(b)*

Figure 2.10: Chip formation during orthogonal cutting of UD-CFRP for 45° fibre orientation at depth of cut (a) 0.07 mm and (b) 0.125 mm [21].

mm), as shown in Figure 2.10(a). A friable ribbon like chip was obtained increasing the depth of cut (0.07 mm<DOC≤0.2 mm), as observable in Figure 2.10(b). At a higher depth of cut (DOC>0.2 mm) a blocky chip was observed, but differently by Li *et al.* [26], after the shear deformation takes place, the chip is split into small parallelepiped flying particles.

In the case of 75°<θ≤180°, Li *et al.* [26] observed a continuous ribbon like chip at a depth of cut 0.1 mm, and a blocky chip for the depth of cut of 0.2 mm, as shown in Figure 2.11. This was in disagreement with what was observed by Zitoune *et al.* [21] when machining at a fibre angle of θ=90°. In fact, they observed a non-continuous chip formed by very fine particles for 0.05 mm<DOC<0.3 mm, which was replaced by a chip composed of small needles for DOC>0.3 mm.

Furthermore, the rake angle seems to affect the chip type, continuous or discontinuous, favouring one over the other. In particular, a large positive rake angle tends to cause a continuous chip, while a small positive value leads to a discontinuous chip. Conversely, the clearance angle does not affect the type of chip [11].

Since studies generally include positive rake angles, a lack of information on the type of chip when machining with a negative rake angle has been observed. For this reason, the effect of machining with a negative rake angle will be investigated in this thesis.

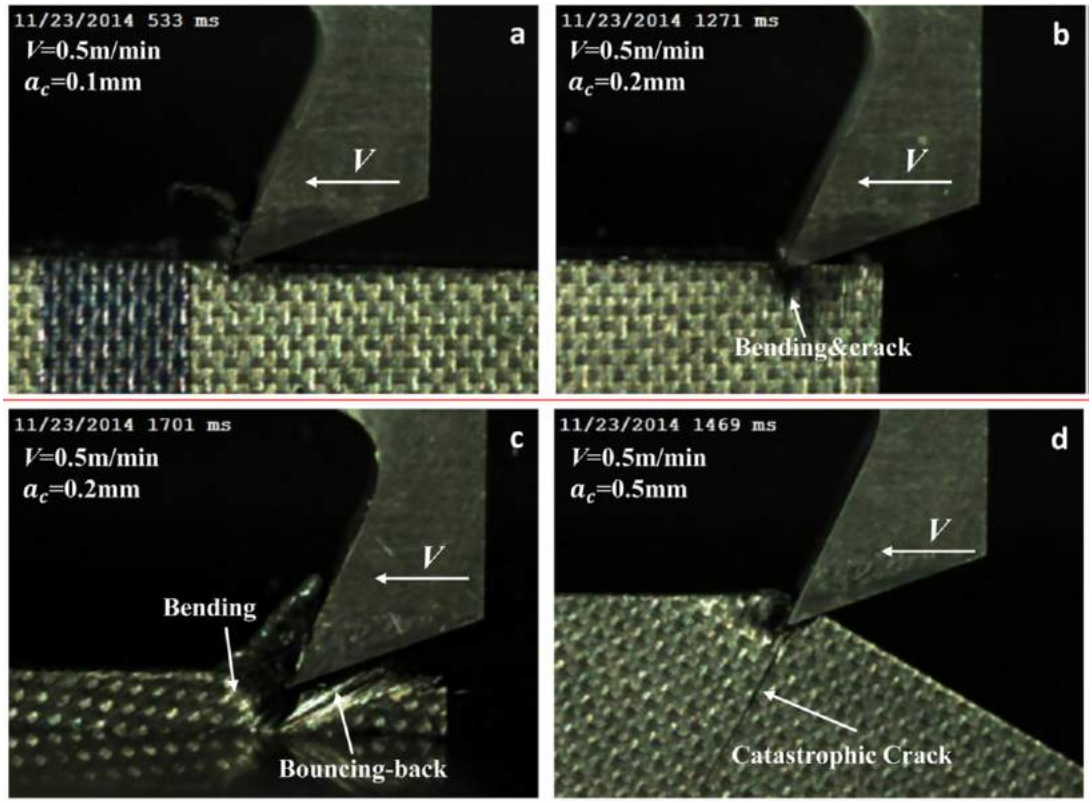

Figure 2.11: Chip formation evolution during orthogonal cutting of UD-CFRP for fibre orientation (a) θ=90° at depth of cut 0.1 mm; (b) θ=90° at depth of cut 0.2 mm; (c) θ=150° at depth of cut 0.2 mm; and (d) θ=120° at depth of cut 0.5 mm [26].

2.5.3 Surface quality

Surface roughness (Ra) is generally chosen as a parameter to represent the quality of the machined surface. The influence of the rake angle, depth of cut and fibre orientation on surface quality was studied by Wang and Zhang [24] and shown in Figure 2.12.

Independent from the depth of cut, it was found out that a critical fibre angle exists

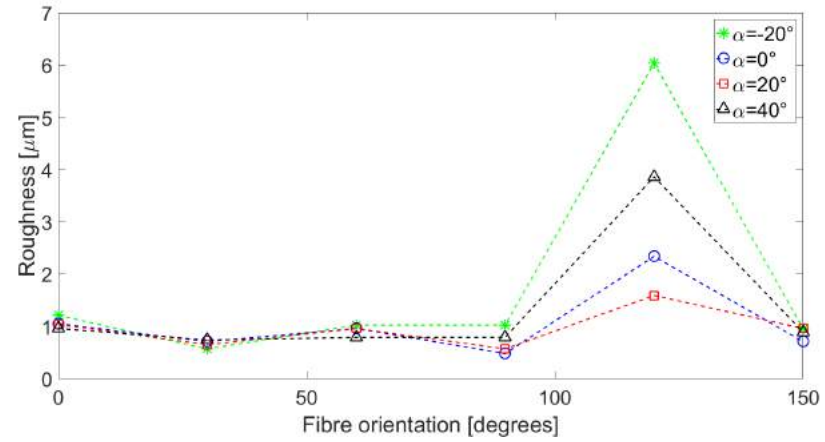

(a)

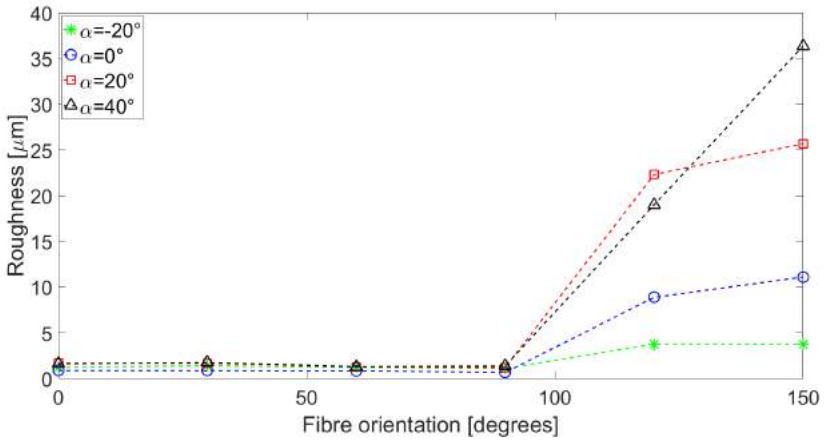

(b)

Figure 2.12: Surface roughness (Ra) trend with fibre orientation, rake angle at depth of cut (a) 1 μm; and (b) 50 μm [24].

(θ=90°), after which a large increase of the surface roughness takes place. Before this angle, a very slight fluctuation can be observed with values within 0.6 μm and 1.2 μm for depth of cut less than the fibre diameter (Figure 2.12(a)). Similarly, for depth of cut bigger than the fibre diameter (Figure 2.12(b)) the variation is between 1 μm and 1.5 μm, independent from the rake angle. This trend was also confirmed by Ramulu [32] and Arola *et al.* [17]. Hence, Wang and Zhang [24] pointed out that the influence of the depth of cut, rake angle and fibre

orientation on the surface roughness can be neglected for $0°\leq\theta\leq90°$. For fibre angles $\theta>90°$ and a depth of cut less than the fibre diameter, an increase of the surface roughness was observed for fibre orientation up to $\theta=120°$, followed by a decrease. The effect of the rake angle on the surface roughness was observed for $90°<\theta<150°$, showing a maximum influence at $\theta=120°$. For fibre orientation $\theta=150°$ the effect of the rake angle again becomes negligible. In contrast, for a depth of cut bigger than the fibre diameter no decrease of the surface roughness was observed for high values of fibre orientation, but it increases with a slope depending on the rake angle. A larger rake angle causes a higher rising rate of the surface roughness.

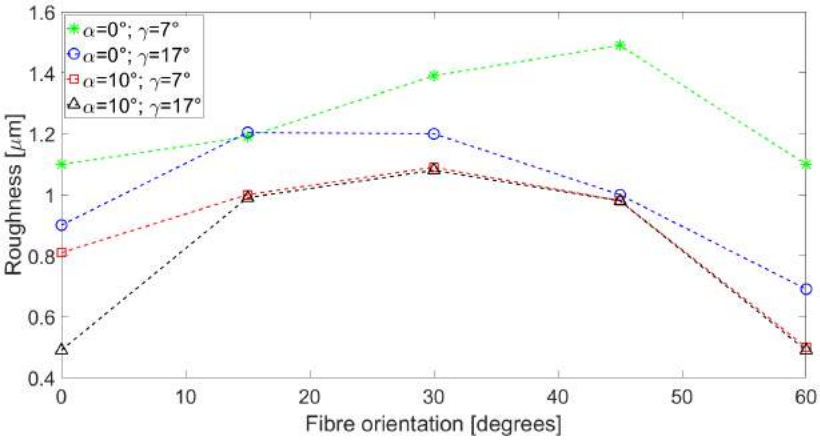

Figure 2.13: Influence of the clearance angle on the surface roughness (Ra) considering two different rake angles [17].

The effect of the clearance angle can be observed considering the experimental results obtained by Wang *et al.* [18] for fibre orientations $0°\leq\theta\leq60°$ and different rake angles (Figure 2.13). Indeed they found out that a higher rake angle leads to a better surface quality. For rake angle $\alpha=0°$ the clearance angle increase (from $\gamma=7°$ to $\gamma=17°$) always causes a slight improvement in the surface quality except for $\theta=15°$. Increasing the rake angle, the benefit

due to a higher clearance angle reduces, except for θ=0°.

2.5.4 Induced damage and surface integrity

The extent of the damage in the machined component was found by Wang and Zhang [24] to be dependent on the depth of cut and fibre orientation. They observed that a decrease in the depth of cut results in a reduced amount of subsurface damages; this was also confirmed by Koplev *et al.* [16]. The fibre angle represents the most important parameter affecting the amount of damage arising during machining. For fibre orientation θ=0°, fibre failure due to bending or buckling takes place ahead of the tool, slightly affecting the material below the cutting plane. In fact, no cracks beneath the top layer [16, 20] or a maximum depth of damage of two fibre diameters can be observed in Figure 2.14.

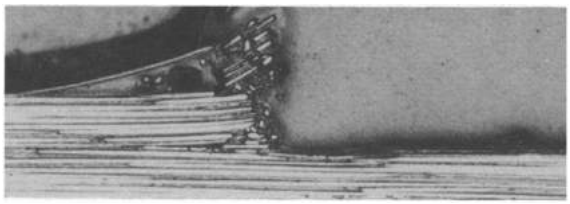

Figure 2.14: Machining induced damage for fibre orientation θ=0° [16].

For fibre orientation θ=30°, even if the surface obtained is relatively smooth with no visible cracks, single broken and pulled out fibres were observed by Voß *et al.* [20].

For fibre orientation θ=45°, small deflection and significant compression of the fibres have been observed during cutting by Iliescu *et al.* [33]. Macro-crack propagates in a plane parallel to the fibre direction with fibre failure perpendicular to the fibre axis. A blocky chip originates and subsurface damages take place below the cutting plane, as visible in Figure

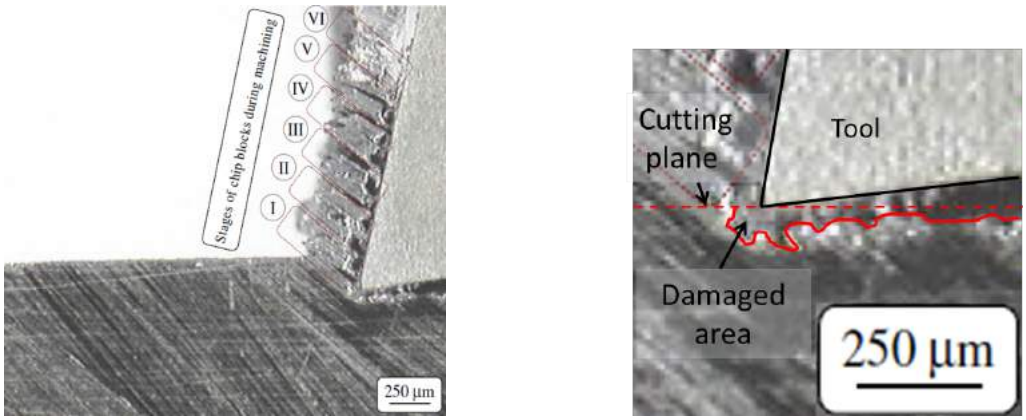

(a) (b)

Figure 2.15: (a)Machining induced damage for fibre orientation θ=45° [34]; and (b) magnification of the tool-workpiece interaction area.

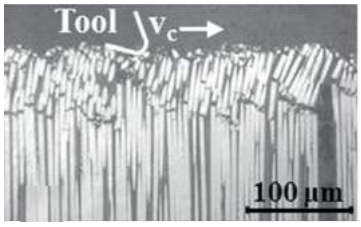

Figure 2.16: Machining induced damage for fibre orientation θ=90° [20].

2.15. However, a good surface quality is obtained.

Damages arising when machining with fibre orientation θ=90° are larger than those observed for lower fibre orientations, and are shown in Figure 2.16. In fact, cracks reaching approximately a depth of 0.1-0.3 mm below the cutting plane were observed by Koplev *et al.* [16]. This is due to bending failure of the fibres below the cutting plane accompanied by considerable matrix fracture, and to the compression exerted by the tool on the material below [16, 27]. The fibre bending with the following spring back was captured by Zitoune *et al.* [21] and Iliescu *et al.* [33] during machining, and is shown in Figure 2.17.

Higher fibre orientations θ>90° result in a very large amount of fibre bending, which remain compact (in bundles) until failure with a massive amount of damage [33] as shown

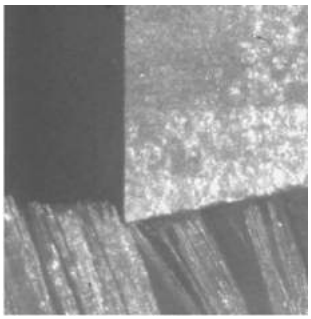

Figure 2.17: Fibre bending when machining at fibre orientation θ=90° [33].

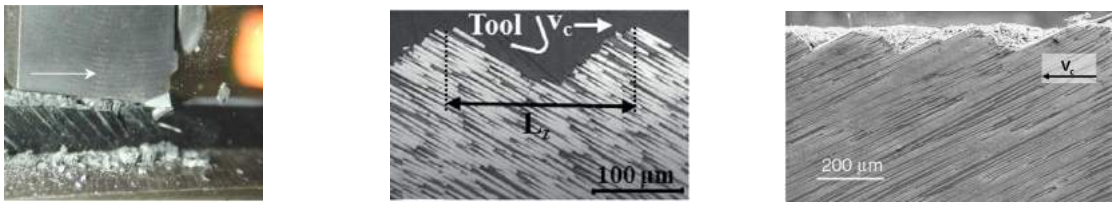

(a) *(b)* *(c)*

Figure 2.18: Machining induced damage for fibre orientation (a-b) θ=135° [20, 21]; and (c) θ=150° [24].

in Figure 2.18(a). It was related to the high surface roughness value by Wang and Zhang [24] who found a surface roughness (Ra) of 36 μm for rake angle α=40° and fibre orientation θ=150°. In addition, usually a saw-tooth profile can be observed [20] as shown in Figure 2.18(b-c).

Measurements of damage extension in the machined workpiece were carried out by Bhatnagar *et al.* [35] for fibre orientation 0°≤θ≤90°, and three different depths of cut (0.1 mm, 0.2 mm, 0.3 mm), as shown in Figure 2.19. For all depths of cut the damage extension was found to be minimum in the range 15°≤θ≤30°, increasing slowly up to θ=60°. After that angle a large increase can be observed, reaching the maximum value at θ=90°. Furthermore, damage depth increases with depth of cut increase, as previously mentioned.

Debonding, which represents the amount of elastic recovery that the workpiece experiences

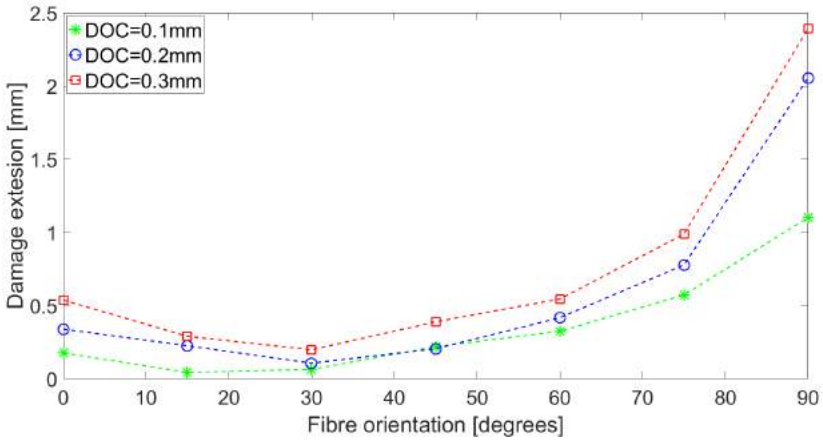

Figure 2.19: Damage extension for different fibre orientations and depth of cut (DOC) [35].

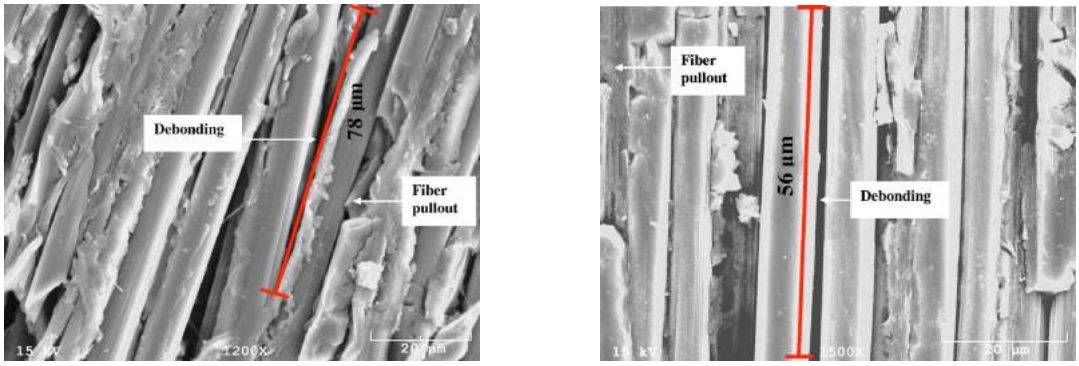

(a) *(b)*

Figure 2.20: Machining induced damage for fibre orientation (a) θ=60°; and (b) θ=90° [15].

after machining, and fibre pull-out were measured by Dandekar and Shin [15] using a scanning electron microscope (SEM), as shown in Figure 2.20. The orthogonal cutting of UD-CFRP, using a depth of cut of 0.1 mm and a cutting edge radius of 10 μm, was performed. Both examples of damage were found to grow with the fibre orientation increase. In particular, a debonding length of 47 μm, 56 μm, 78 μm and a fibre pullout of 30 μm, 40 μm and 58 μm were detected for fibre orientations θ=60°, θ=90°, and θ=120°, respectively.

Finally, the effect of the cutting speed during machining was studied by Wei *et al.* [30], showing that its increase causes a reduction of the maximum damage depth. It was explained

with the consideration that the time for the damage to propagate in the material reduces with the increase of the cutting speed.

When machining at fibre orientation θ=0°, the machined surface is characterised by visible fibres fractured perpendicularly to their direction [16, 24] (Figure 2.21). A few fibres are also smashed, and the matrix is visible between two consecutive fibres.

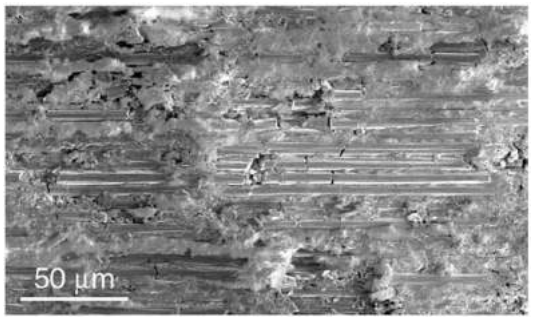

Figure 2.21: Machined surface for fibre orientation θ=0° [24].

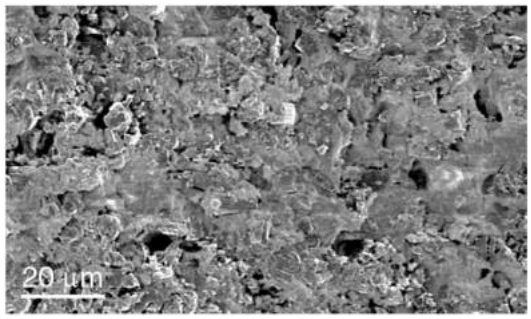

Figure 2.22: Machined surface for fibre orientation θ=90° [24].

In contrast from θ=0°, at θ=30° and θ=90° fibres are not visible and they are covered by a layer of matrix material [16, 18, 24] (Figure 2.22).

It is important to notice that even if for fibre angles θ=0° and θ=90° the surface roughness value was found to be equal to 1 μm by Wang and Zhang [24], they show a different surface integrity due to the different chip formation mechanisms.

2.5.5 Cutting force and thrust force

The tool-workpiece interaction during orthogonal cutting, for a sharp tool cutting edge, can generally be represented as reported in Figure 2.23. It is possible to decompose the machining force R, acting on the tool, along the cutting direction and orthogonally to it, obtaining the cutting force F_c and the thrust force F_t, respectively. The resultant force can also be decomposed along the tool rake face F_f, and in the normal direction to it, obtaining the normal force F_n. The former component F_f represents the friction force due to chip sliding on the tool rake face. Instead, resolving the resultant force along the shear plane and orthogonally to it, shear force F_s and normal component F_{ns} are obtained, respectively.

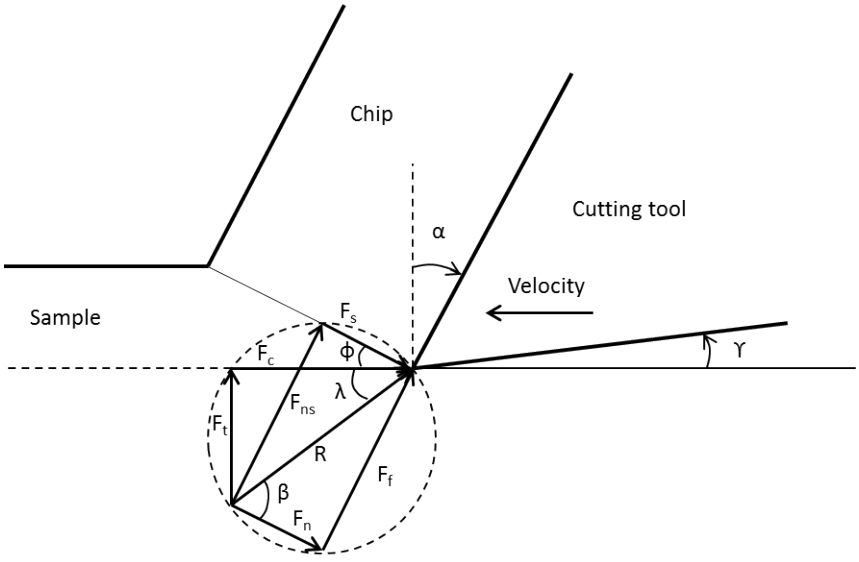

Figure 2.23: Schematic representation of the orthogonal cutting condition [11].

The machining force detected during cutting of FRPs exhibits a high level of fluctuation, which is related to the fibre orientation. In fact, fibre angle represents the most important parameter affecting the chip formation mechanisms. Hence, cutting force and thrust force profiles are representative of repetitive failure of the phases (fibre, matrix, interface), through

which the chip is formed.

The trend of the cutting force with the fibre angle is shown in Figure 2.24(a) for machining parameters listed in Table 2.1.

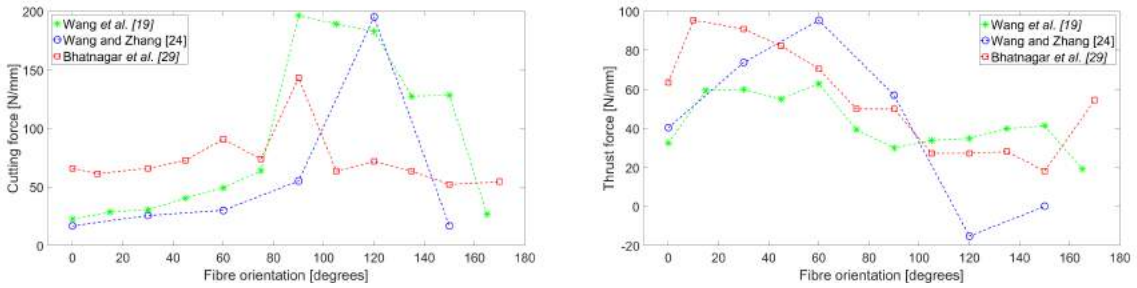

(a) *(b)*

Figure 2.24: Effect of fibre orientation on (a) cutting force; and (b) thrust force [18, 24, 29].

Table 2.1: Machining parameters.

Source	DOC [mm]	Vel [m/min]	Cutting tool	α [°]	γ [°]	r [μm]
[18]	0.25	4	Polycrystalline diamond	10	17	-
[24]	0.05	1	Tungsten carbide	20	7	50
[29]	0.25	1.18	Tungsten carbide	12	-	-

For all conditions, the cutting force increases slowly up to a critical angle. After that an abrupt increase can be observed, followed by a decrease of the force. Furthermore, comparing Wang and Zhang's [24] results (depth of cut of 0.05 mm) with the others (depth of cut of 0.25 mm), the depth of cut variation seems to cause also a shift in the cutting force curve along the horizontal axis.

The thrust force variation with fibre orientation presents a peak for $0°<\theta<90°$ and a minimum for $\theta>90°$; after which an increase with the fibre orientation is detected (Figure 2.24(b)). Similar to the cutting force, a variation in the location of the peak and minimum points seems to be associated with the depth of cut. For a depth of cut of 50μm, a sign

change in the thrust force was found by Wang and Zhang [24] when machining with large rake angles (α=20° and α=40°) and high fibre orientation (90°<θ<120°).

The influence of the depth of cut on cutting force and thrust force was also analysed independently from the effect of the fibre angle by Li *et al.* [26]. Considering a specific value of the fibre orientation, the increase of the cutting force is almost proportional to the increase of the depth of cut (Figure 2.25).

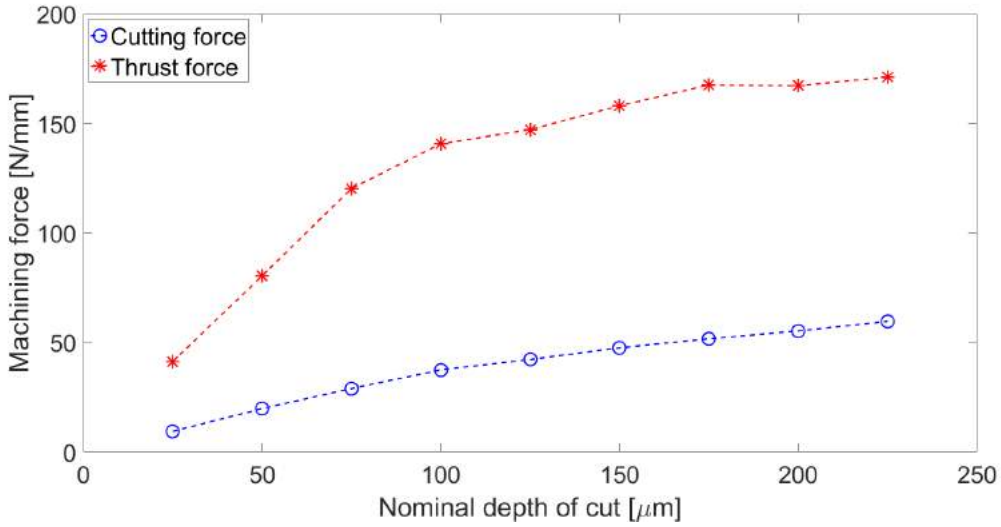

Figure 2.25: Variation of cutting force and thrust force with depth of cut for fibre orientation θ=0° [26].

The effect of the depth of cut on the thrust force is strictly connected with the bouncing back concept previously introduced. When increasing the depth of cut, the thrust force rises rapidly until a depth of cut of 100 μm, after which the slope reduces. This behaviour could be due to the high amount of elastic recovery exhibited by the workpiece on the clearance face for a low depth of cut, where material pressing predominates on cutting. Increasing the depth of cut, the amount of bouncing back becomes stable and the increase is mostly due to the cutting effect.

The effect of the rake angle on cutting force and thrust force was studied by Wang and Zhang [24] and is shown in Figure 2.26. The variation of the rake angle was found negligible for the former for fibre angles up to θ=90°, as also confirmed by Bhatnagar *et al.* [29]. However, an increase of the cutting force was detected increasing the rake angle at fibre orientation θ=120°. Afterwards, the effect seems to be again negligible for fibre orientation θ=150°. Similarly, the effect on the thrust force is particularly visible at fibre orientation θ=120°, but with a thrust force increase when the rake angle is reduced.

The influence of the rake angle was also studied by Kaneeda *et al.* [36] for fibre angles 0°≤θ≤90°and reported in Figure 2.27. It is clear that the reduction rate of the cutting force

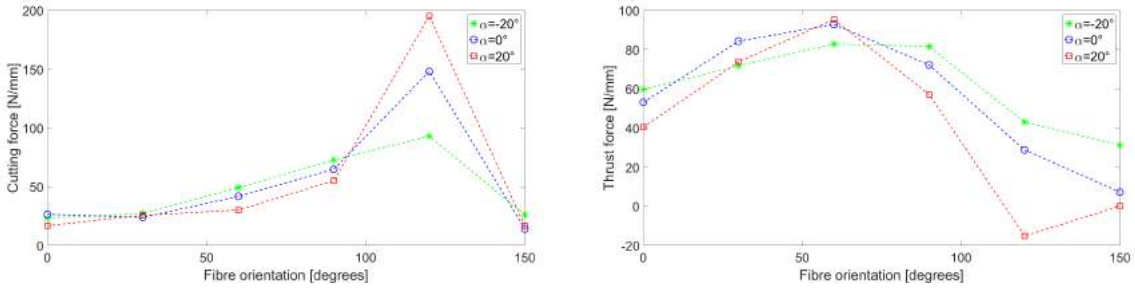

(a) *(b)*

Figure 2.26: Effect of the rake angle on (a) cutting force; and (b) thrust force for 0°≤θ≤150° [24].

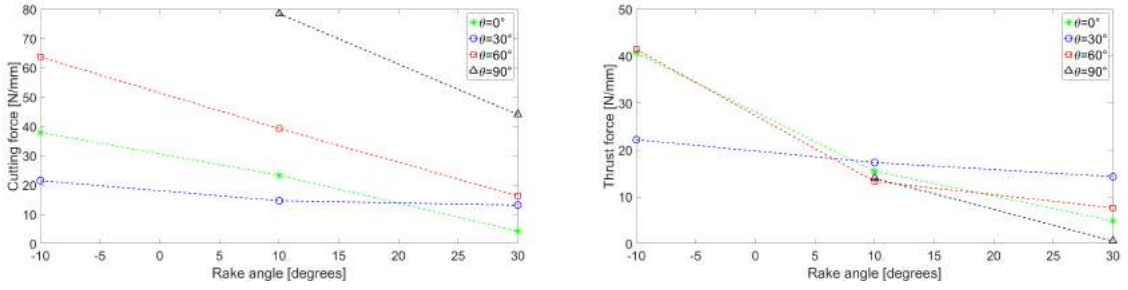

(a) *(b)*

Figure 2.27: Effect of fibre orientation on (a) cutting force; and (b) thrust force for -10°≤α≤30° [18, 29, 36].

depends on the fibre orientation with the maximum value at θ=60°; while the effect on the thrust force magnitude is much less significant, exhibiting a smaller reduction with the rake angle.

The effect of the clearance angle on the cutting force and thrust force was investigated by Wang *et al.* [18] and reported in Figure 2.28. While the influence on the cutting force is negligible, the thrust force shows a reduction with the clearance angle increase. This behaviour is due to the bouncing back. In fact, due to the elastic recovery after the tool is passed, the machined surface comes in contact with the clearance face, exerting pressure on it, which contributes to the thrust force. It is clear that for a higher clearance angle the clearance face undergoes a smaller force.

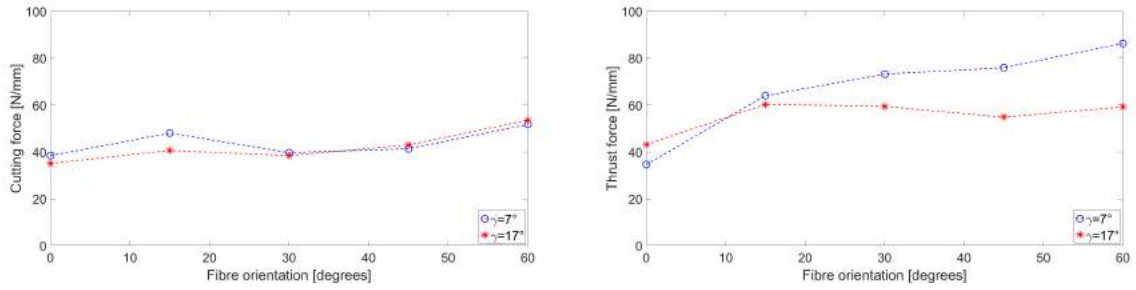

(a) *(b)*

Figure 2.28: Effect of the clearance angle on (a) cutting force; and (b) thrust force for 0°≤θ≤60° [18].

2.6 Modelling of the orthogonal cutting of UD-FRPs

Experimental studies on machining of FRPs represent a fundamental step to assess the tool-workpiece interaction and the material deformation and failure under specified machining conditions. However, the experimental approach can be expensive, e.g. because

of the cost of the material itself, and because it usually requires the availability of expensive equipment to obtain and analyse the information on the process. In addition, the equipment available and the current technology also determine the level at which it is possible to analyse the process, representing often a limit in the ability to obtain the required and desired information, in particular at micro-scale level. For these reasons, predictive models could help to overcome some of the limits, even if they still require the necessary experimental tests for validation purposes and assessing the degree of reliability. In particular, different approaches, encompassing analytical, empirical and numerical methods, have been utilised to investigate the machining of composite materials [37].

2.6.1 Analytical and empirical approaches

There are few analytical studies on the orthogonal cutting of FRPs in the literature. The first attempts were based on applying Merchant's shear plane theory (minimum energy principle), widely used in metal cutting, to the machining of FRPs. According to the theory, the shear plane angle assumes the value at which the energy to realise the cut is minimum. For instance, using this theory, Takeyama and Iijima [38] proposed that the chip formation mechanism consists of material shearing along a shear plane, forming an angle ϕ with the cutting plane. The model is based on several assumptions such as two-dimensional type of cut, temperature effect neglected, and the fibre orientation limited to $\theta \leq 90°$.

According to this model cutting force and thrust force can be calculated by means of

Equation (2.1) and Equation (2.2).

$$F_c = \frac{\tau(\theta^{'})a_c a_w}{sin(\phi)} \frac{cos(\beta - \alpha)}{cos(\phi + \beta - \alpha)} \tag{2.1}$$

$$F_t = \frac{\tau(\theta^{'})a_c a_w}{sin(\phi)} \frac{sin(\beta - \alpha)}{cos(\phi + \beta - \alpha)} \tag{2.2}$$

where a_c and a_w represent the depth of cut and the cutting width, respectively. In addition β is the friction angle; and $\tau(\theta^{'})$ represents the in-plane shear strength. The latter needs to be determined experimentally by means of a shear test carried out varying the shear fibre angle $\theta^{'}$.

Cutting force and thrust force obtained using the analytical approach are compared with experimental values in Figure 2.29 for friction angle either β=40° and variable with fibre angle $\beta = f(\theta)$. The model shows very good prediction capability for 15°≤θ≤60°, where it is possible to affirm that there is a resemblance to shearing with homogeneous material. It is important to notice that analytical results obtained using a variable friction angle deviate more from the experimental values.

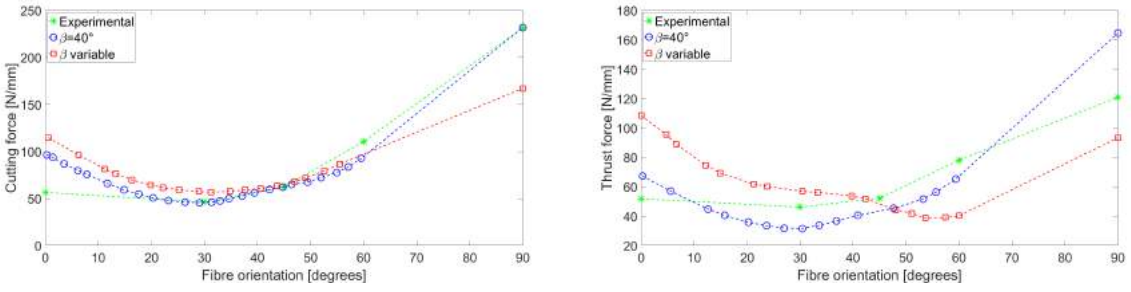

(a) *(b)*

Figure 2.29: Comparison for (a) cutting force; and (b) thrust force, between experiments and results of analytical model of Takeyama and Iijima [11, 38].

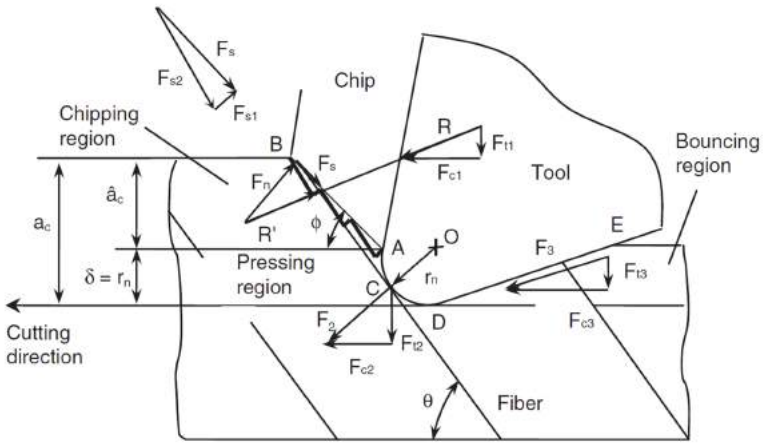

Figure 2.30: Schematic of the cutting mechanism on which the Zhang et al.'s [39] analytical model is based.

A more complex model was developed by Zhang *et al.* [39] for fibre orientations varying in the range $0°{\leq}\theta{\leq}90°$, which is also able to account for the effect of the tool geometry (rake angle, clearance angle and cutting edge radius) on the machining process. The analytical model considers three different regions during cutting (Figure 2.30): chipping, pressing and bouncing. Further assumptions are made, such as considering complete bouncing back and a two-dimensional cut. Cutting force and thrust force during cutting are calculated for each region, and then summed, applying the principle of superposition; thus, the total cutting force and thrust force are obtained:

$$F_c = F_c(chipping) + F_c(pressing) + F_c(bouncing) \tag{2.3}$$

$$F_t = F_t(chipping) + F_t(pressing) + F_t(bouncing) \tag{2.4}$$

As in the previous model, experiments are still necessary in order to determine values of the parameters involved in the developed equations.

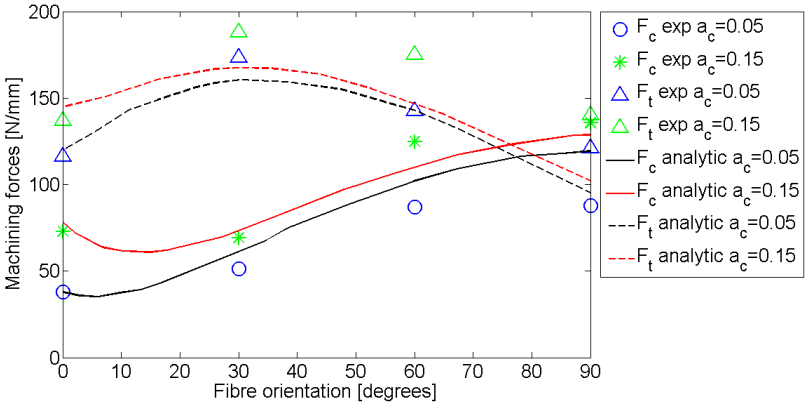

Figure 2.31: Comparison between experimental and analytical cutting force and thrust force obtained using Zhang et al.'s [39] model.

.

The comparison between the model's prediction and the experimental results is shown in Figure 2.31 for two different depths of cut (a_c). A good agreement with the experimental values can be observed for fibre orientations $0°\leq\theta<60°$, with the cutting force showing a trend closer to the experimental values. In fact, the maximum errors in predicting cutting force and thrust force are 27% and 37%, respectively. Taking into account also the clearance angle and cutting edge radius of the tool, and above all considering the three regions experimentally observed by Wang and Zhang [24], an improvement in the prediction of the cutting force and thrust force for fibre orientation $0°\leq\theta<15°$ can be observed when compared with the previous model.

An analytical model for fibre orientations $\theta>90°$ was developed by Jahromi and Bhar [40] based on the suggestion of the cutting mechanism reported by Zhang *et al.* [39] and is shown in Figure 2.32. In fact, they observed that cutting force and thrust force could be considered due to microbuckling, fibre-matrix debonding, and fibre bending [39]. Jahromi and Bhar [40] then calculated the cutting force as a sum of the following contributors: fibre microbuckling,

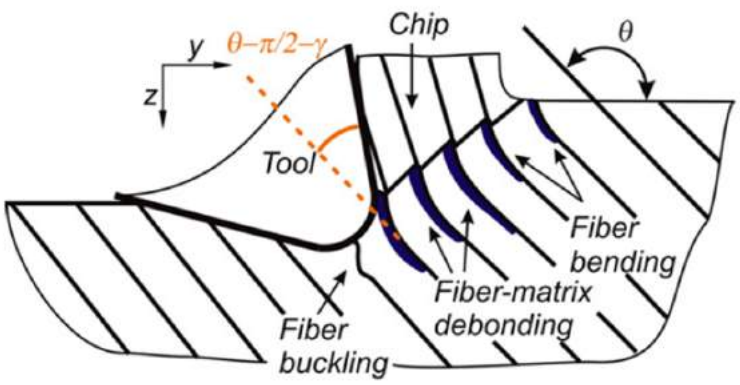

Figure 2.32: Schematic of the cutting mechanism on which the Jahromi and Bhar [40] analytical model is based.

.

fibre bending-matrix shearing and friction force on the tool rake face. Instead, only the first two mechanisms contribute to the thrust force. The analytical expression of the forces is reported in Equation (2.5) and Equation (2.6):

$$F_c = -G_{LT}\frac{\pi {d_\mathrm{f}}^2}{4}\frac{t}{2c+d_\mathrm{f}}\cos\theta + \frac{\max(|s^{\mathrm{shear}}|,|s^{\mathrm{bend}}|)}{cos\gamma} n_{\mathrm{RVE}}(1+\mu)\nu_\mathrm{f} \tag{2.5}$$

$$F_t = G_{LT}\frac{\pi {d_\mathrm{f}}^2}{4}\frac{t}{2c+d_\mathrm{f}}\sin\theta - \max(|s^{\mathrm{shear}}|,|s^{\mathrm{bend}}|)\tan\gamma n_{\mathrm{RVE}}\nu_\mathrm{f} \tag{2.6}$$

where G_{LT} represents the shear modulus of a circular fibre reinforced composite; $t/(2c+d_f)$ is the number of fibres along the width of cut; θ is the fibre orientation; γ is the tool rake angle; $\mathrm{s}^{\mathrm{shear}}$ is the critical lateral force due to matrix shearing; $\mathrm{s}^{\mathrm{bend}}$ is the critical lateral force due to fibre bending; $\mathrm{n_{RVE}}$ is the number of representative volume elements; μ is the friction coefficient; and ν_f is the fibre volume fraction.

Assumptions on which the model is based include: two-dimensional deformation, shear

stress in the fibre is negligible compared to the normal stress, no matrix extension or compression, normal stress in the fibre that produces no mechanical work during deformation of the fibre.

The analytical model was validated against experimental values, as shown in Figure 2.33. The model seems to be adept in capturing the chip formation mechanism change

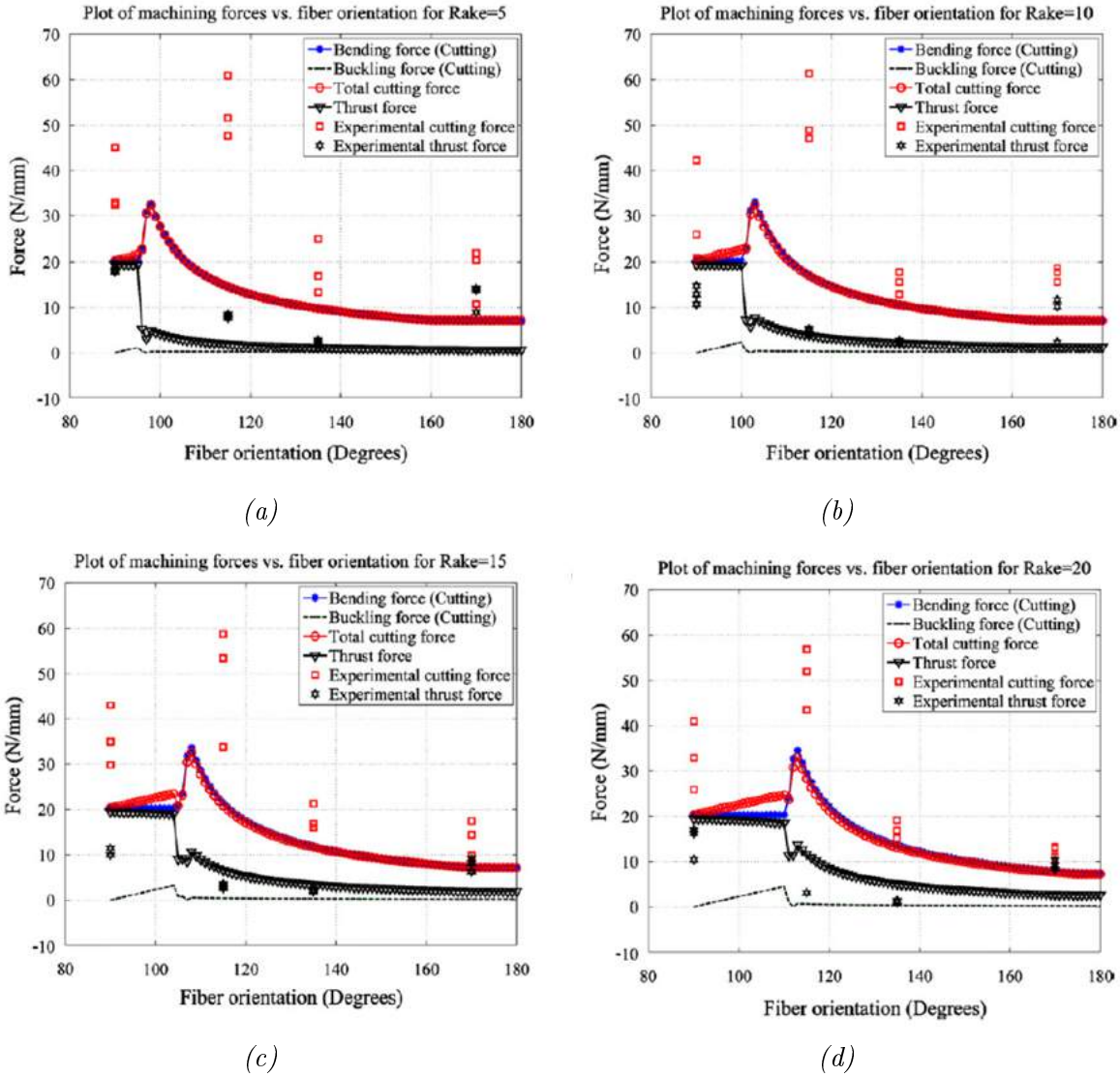

Figure 2.33: Comparison of machining forces between experiments and Jahromi and Bhar's [40] analytical model for different tool rake angles: (a) α=5; (b) α=10; (c) α=15; (d) α=20.

moving from θ=90° to higher fibre orientations, which is represented by a discontinuity in the curve. Deviation of the model from the experimental results reduces when the rake angle increases. However, a significant discrepancy in the cutting force prediction can be observed for 90°<θ<135°.

Moreover, other analytical models were developed to investigate a specific fibre orientation. For instance, a model for fibre orientation θ=0° was developed by Everstine and Rogers [41]. Other than the cutting force and thrust force usually provided by previous models, this model presents a method for estimating the deformation and the stress field. The deformation of the machined component was found to be dependent on the tool shape. Pwu and Hocheng [27] focused on the chip formation when cutting orthogonally to the fibre direction. They used the beam theory and the laminate mechanics to establish the correlation between cutting force, chip length and thickness.

Finally, it is possible to observe how the analytical models are based on strong assumptions, and are not able to handle numerous parameters involved in the process. In addition, they provide information mainly on cutting force and thrust force.

A different approach is represented by models that try to empirically predict the machining force based on specific cutting energy functions. They have been widely used when machining FRPs [42–47]. Specific cutting energy functions represent the amount of energy necessary to remove a unit volume of material during machining; and they are mainly dependent on chip, tool and workpiece geometries, sample material strength, tool-workpiece interaction, and can also include the effect of tool wear and workpiece material inhomogeneity [48]. Generally, specific cutting energy coefficients K_c and K_t are

defined for the principal directions and they need to be determined experimentally for a tool-workpiece pair. Edge coefficients (K_{ce} and K_{te}), which are functions of the tool wear or chipping, can be also added. Cutting force and thrust force can be basically expressed by Equation (2.7) and Equation (2.8) [11]:

$$F_c = K_c(a_c, \theta)a_c a_w + K_{ce}a_w \tag{2.7}$$

$$F_t = K_t(a_c, \theta)a_c a_w + K_{te}a_w \tag{2.8}$$

where a_c represents the depth of cut; a_w the width of cut; and the term $a_c a_w$ the undeformed chip cross-sectional area.

The trend of the specific cutting energy coefficients K_c and K_t with fibre orientation for orthogonal cutting of UD-CFRP is shown in Figure 2.34. It is possible to observe the strong dependence of the specific cutting energy coefficients from the fibre orientation. The coefficient K_c increases slowly for $\theta<75°$, after which an abrupt increase is present until $\theta=90°$, followed by a decrease with further fibre orientation increase. Instead, the coefficient K_t presents a sinusoidal shape.

This approach requires an experimental calibration, and results provided are reliable only in the range where the model has been calibrated.

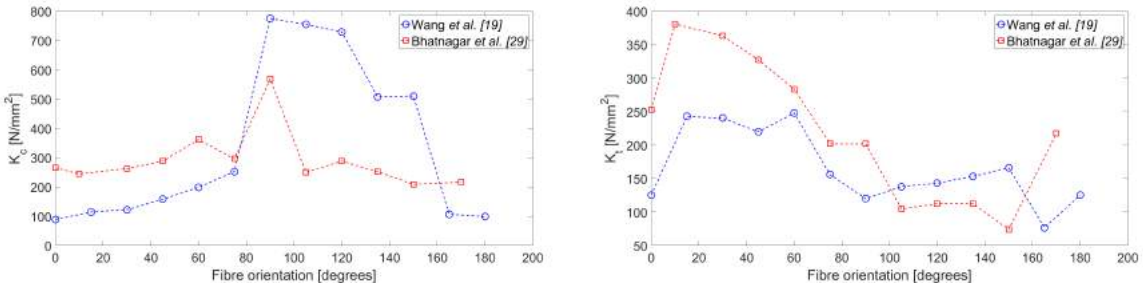

(a) *(b)*

Figure 2.34: Specific cutting energy coefficients as function of fibre orientation [11, 18, 29].

2.6.2 Numerical approach

Numerical studies carried out on the machining of metals are numerous in the literature [49–52], unlike simulations of composite materials' machining, which are still limited. Three different approaches have been used in order to model the composite material in a numerical analysis [37, 53]: macro-mechanical, micro-mechanical and macro-micro combined (meso-scale) approach. The former involves representing the composite workpiece as an equivalent homogeneous material (EHM), whose properties can be derived by means the rule of mixtures [54] and provides only general information on the chip formation mechanism [31, 55–57].

In contrast, the microscopic or micro-mechanical approach accounts for each material phase separately [15, 33, 58], thus enabling more detailed simulation/analysis of material deformation and defect formation during machining. The micro-mechanical model represents a powerful approach to analysing processes at the microscopic level. However, it is still computationally prohibitive for simulating machining operations involving a large amount of material, such as drilling, where the EHM approach has been used [59–61]. This led several researchers to develop a meso-scale formulation [25, 62, 63]. Here, the microscopic model is

implemented in the vicinity of the tool, while the EHM approach is used for the rest of the model, in order to provide the necessary stiffness while minimising the computational cost.

The advantage of using the meso-scale approach was highlighted in Rentsch *et al.*'s [64] work, where a comparison with the EHM approach was realized for the orthogonal cutting of UD-CFRP, as shown in Figure 2.35. They highlighted that the meso-scale approach provides a further insight into the material removal mechanisms and it was used to investigate the matrix deformation and failure that plays an important role in the material removal process.

Material models and failure criteria implemented in simulations depend on the approach chosen; there are many material models incorporating failure criteria that can be used [65–70].

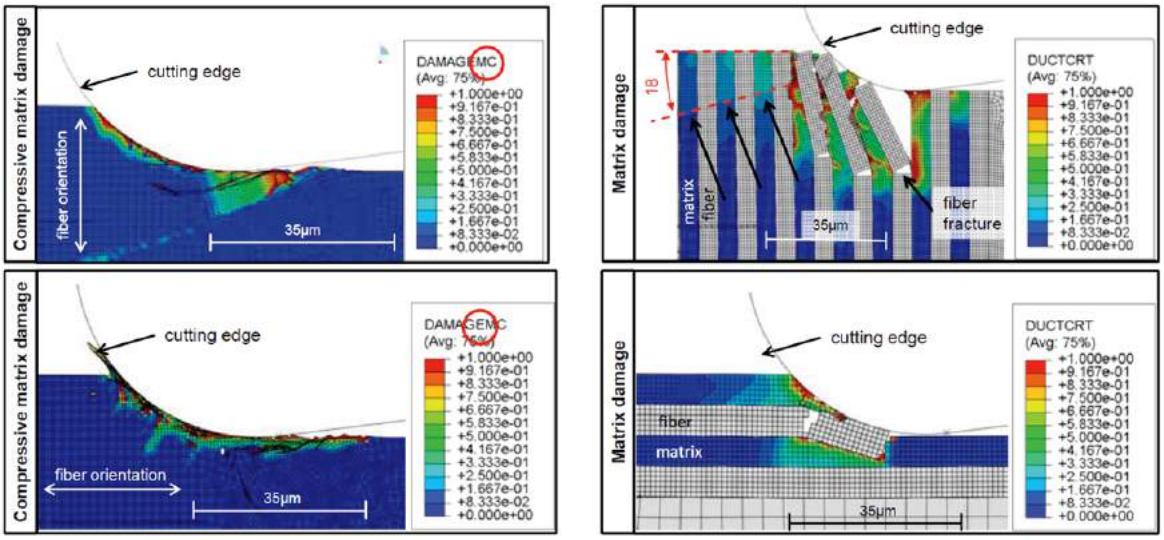

(a) *(b)*

Figure 2.35: Matrix damage distribution during orthogonal cutting of UD-CFRP for (a) the macroscopic approach; and (b) the meso-scale approach [64].

2.6.2.1 Macro-mechanical approach

When the macro-mechanical approach is employed, an orthotropic homogeneous material with a pre-defined crack path to allow the chip formation was used by several researchers. Two fracture planes were considered by Arola *et al.* [71] as shown in Figure 2.36, where the secondary shear plane was located ahead of the cutting tool at a distance equal to the mean primary fracture length.

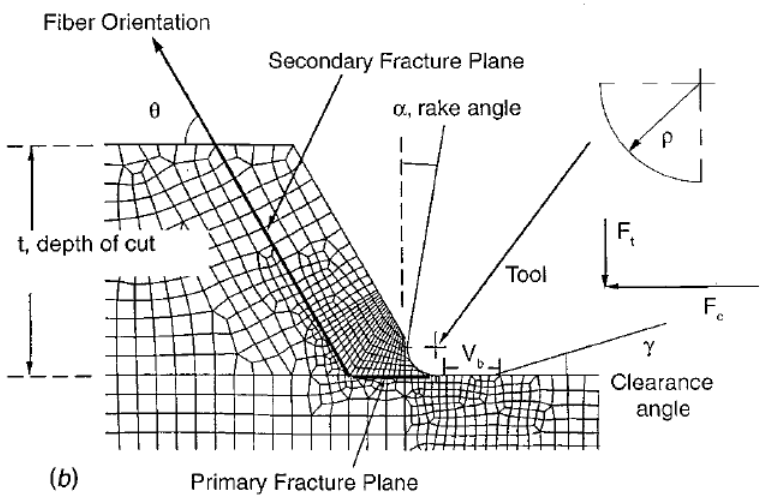

Figure 2.36: Macro-mechanical finite element model implementing pre-defined fracture planes [71].

Fracture planes were modelled with double nodes initially bonded together in pairs. Debonding occurred when the fracture criterion, reported in Equation (2.9), was satisfied:

$$f = \sqrt{\left(\frac{\sigma'_n}{\sigma^{\mathrm{f}}}\right)^2 + \left(\frac{\tau_1}{{\tau_1}^{\mathrm{f}}}\right)^2 + \left(\frac{\tau_2}{{\tau_2}^{\mathrm{f}}}\right)^2}; \qquad \sigma'_n = max(\sigma_n, 0) \tag{2.9}$$

where σ_n, τ_1 and τ_2 represent the in-plane normal and shear stress across the interface and the transverse shear stress, respectively. Instead, σ^{f}, ${\tau_1}^{\mathrm{f}}$ and ${\tau_2}^{\mathrm{f}}$ are the in-plane normal and shear strength and the transverse shear strength (out of plane) of the composite material.

When the failure criterion ratio (f) reached the unit value, the overlapping nodes underwent debonding.

A similar approach was used by Bhatnagar *et al.* [35] and Nayak *et al.* [72] who developed two-dimensional simulations of orthogonal cutting on GFRP for fibre angles $0°\leq\theta\leq90°$. Duplicate nodes were positioned along the trim plane. Different to Arola *et al.*'s [71] model, where a pre-defined secondary shear plane was located ahead of the cutting tool, a contour plot of the Tsai-Hill failure criterion was used to visualise the crack propagation in the workpiece. Chip release took place where the Tsai-Hill contour met the free edge of the sample when two consecutive nodes experienced debonding on the trim plane.

Some drawbacks of approaches based on a pre-defined sacrificial layer to simulate the chip formation include knowledge a priori of the chip formation mechanisms and of the path followed by the crack during cutting. However, this information is generally desired as output in a numerical model.

No pre-defined fracture plane was used by Lasri *et al.* [73] where material stiffness properties' degradation was also implemented when using the Hashin-Rotem's failure criterion [74] according to the failure condition satisfied [73, 75]. Analysis results show the damaged area and the failure mode responsible for it (Figure 2.37). Since a user-defined subroutine was used to implement the constitutive model of the material, user-defined field variables were used and linked with different failure mechanisms. In particular, variables SDV2 and SDV3, reported in Figure 2.37, were associated with fibre-matrix shear failure and fibre failure, respectively. The model is able to predict the primary fracture plane formation, which propagates in a direction orthogonal to the fibre axis, and the secondary

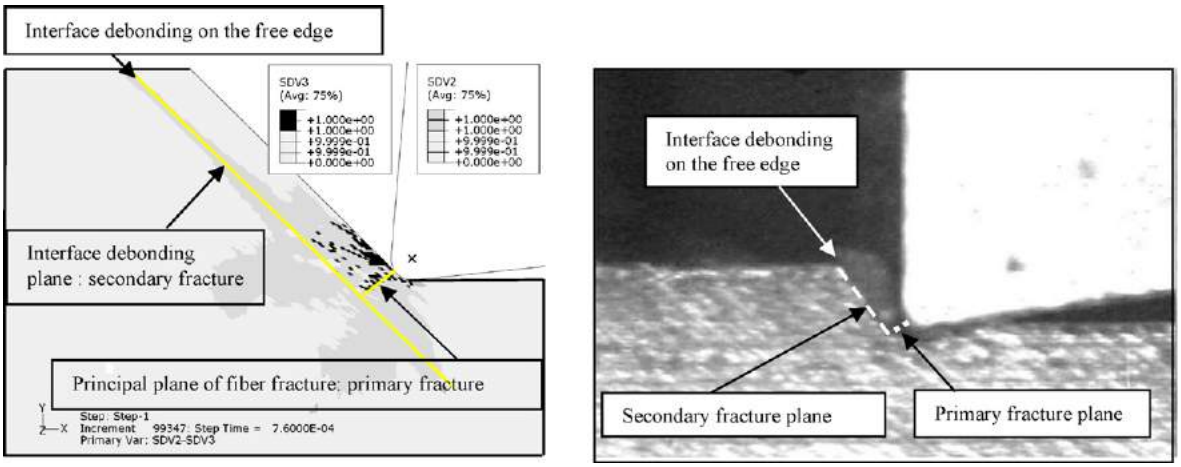

(a) *(b)*

Figure 2.37: Comparison of the damage when machining at θ=45° between (a) numerical model implementing Hashin-Rotem's failure criterion; and (b) experimental image [75].

fracture plane, whose formation is due to the shear failure of the fibre-matrix interface.

In the models previously described, tool advancement during simulation could cause excessive elements deformation and subsequent analysis interruption. Two different techniques have been used to avoid it. In fact, the adaptive mesh technique was used by Mkaddem *et al.* [76, 77]. Instead, Soldani *et al.* [78] and Santiuste *et al.* [57] implemented properties' stiffness degradation once damage had taken place with subsequent deletion of failed elements from the analysis, as shown in Figure 2.38.

In addition, the latter technique makes it easier to visualise the path along which the cracks propagate. Nowadays, deletion of failed elements from the analysis is generally used.

Three-dimensional models have been developed by several researchers, simulating the composite as homogeneous orthotropic material. The necessity of three-dimensional models was highlighted by Cantero *et al.* [55] when simulating cutting on quasi-isotropic laminates $[45/\text{-}45/0/90]_s$. Results showed significant out of plane stresses leading to delamination

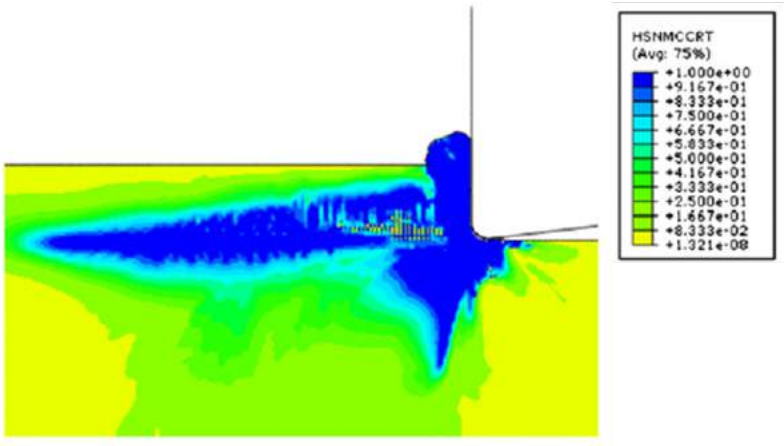

Figure 2.38: Matrix crushing damage in the workpiece during machining using Hashin's failure criterion for fibre orientation θ=0° [78].

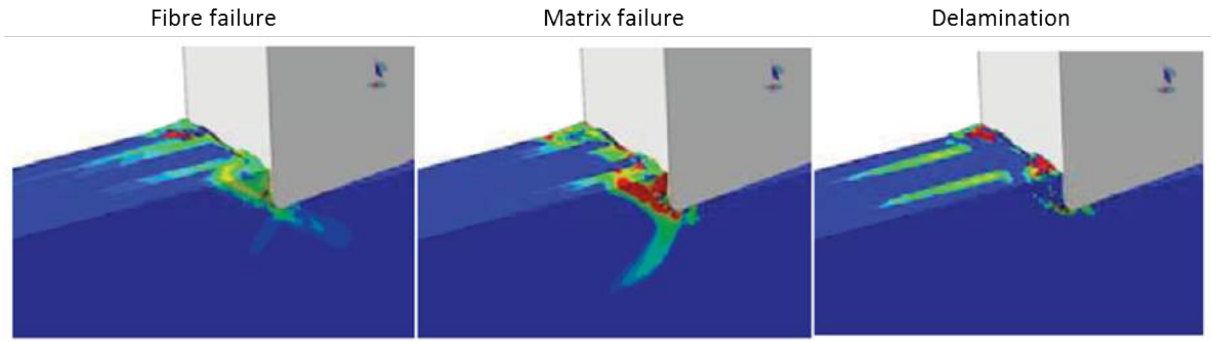

Figure 2.39: Material damage during machining using a three-dimensional numerical model [55].

between different layers, which represents a critical issue that can be studied only by means of a 3D model. Damages in fibre, matrix and delamination during analysis are shown in Figure 2.39.

A comparison between two-dimensional and three-dimensional models was carried out by Santiuste *et al.* [79]. It was found that the difference between 2D and 3D models' results reduces when decreasing the laminate thickness. The three-dimensional model was able to predict significant delamination, which is one of the most important causes for component rejection at the final stage of composite component manufacture.

A three-dimensional Tsai-Hill criterion, followed by material degradation till failure with element deletion from the analysis, was used by Venu Gopala Rao *et al.* [31]. Cutting force and thrust force obtained for fibre orientation of $15° \leq \theta \leq 90°$ was compared with experimental results, showing good agreement, as reported in Figure 2.40.

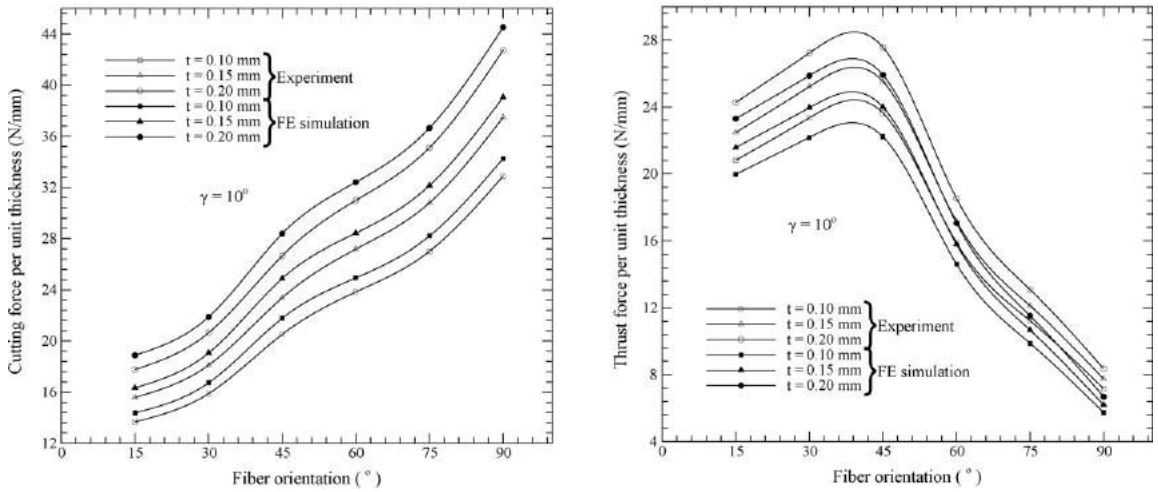

Figure 2.40: Comparison between a three-dimensional numerical model and experimental results in terms of (a) cutting force; and (b) thrust force [31].

Santiuste *et al.* [56], implemented a three-dimensional model using Hou's theory, followed by material degradation till failure with element deletion from the analysis. Differently from the models previously mentioned, delamination between plies was modelled by means of both Hou's criterion and cohesive elements. Cohesive elements' implementation is shown in Figure 2.41. They are positioned between consecutive plies. They are used to simulate the adhesion between the plies, and their eventual detachment during cutting (delamination). Results showed significant improvement in delamination damage prediction using cohesive elements instead of the classical formulation previously mentioned. In particular, it was highlighted how Hou's model underestimates the levels and extension of the delamination damage. For

this reason, the cohesive elements are usually used nowadays for simulating the interface between different plies or phases in a single ply (fibre-matrix interface). Santiuste *et al.* [56] showed also the capability of the three-dimensional model to investigate the influence of the plies' staking sequence on the delamination damage.

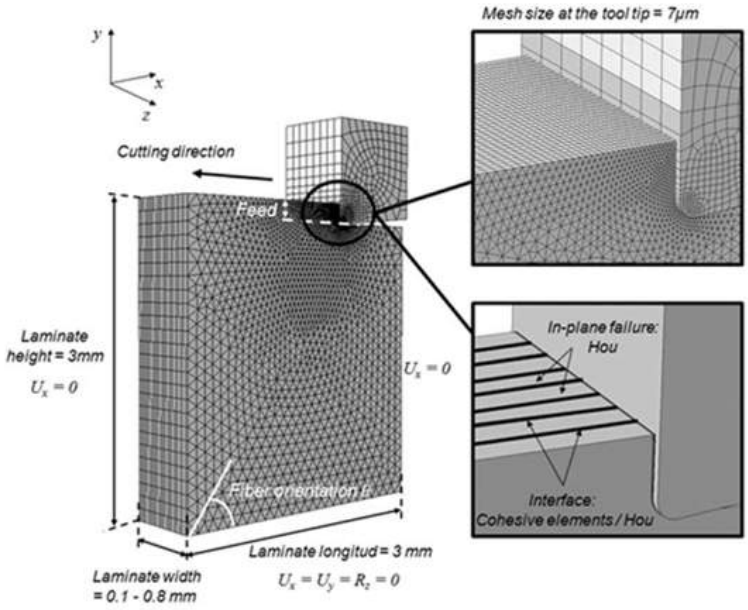

Figure 2.41: Cohesive elements implementation for orthogonal cutting of UD-CFRP material [56].

Generally numerical models are based on the Lagrangian approach, as with those described above. Recently, an Eulerian model for simulating the cutting of unidirectional fibre reinforced polymer was developed by Zhang [80]. It was able to predict the cutting force trend as a function of fibre orientation with a slight phase shift (Figure 2.42). However, the model did not account for fibre buckling and the clearance face was not included in the cutting model. The former limits the usability of the model; for instance, it is well known that buckling represents the main failure mechanism when machining with a negative rake angle at θ=0°. In addition, the absence of the clearance face can cause an

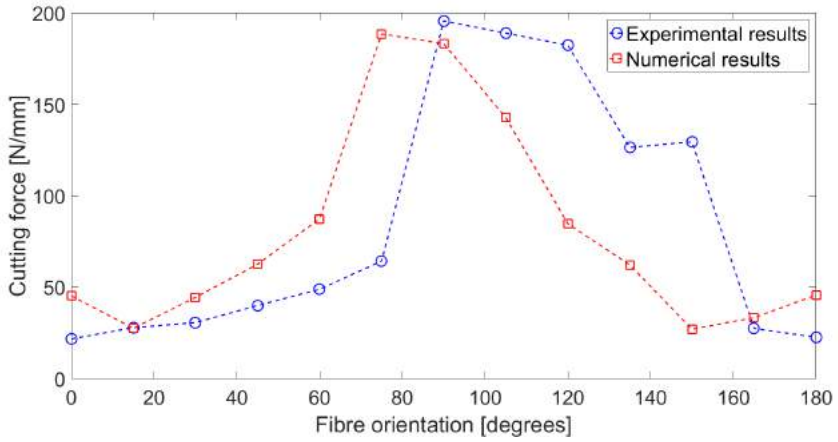

Figure 2.42: Comparison between experimental and numerical cutting force obtained using an Eulerian model [80].

error in the prediction of the thrust force due to the absence of the contact between the clearance face and the machined surface. However, the potential for much higher computational efficiency compared to the traditional Lagrangian approach was highlighted.

2.6.2.2 Micro-mechanical and meso-scale approaches

Unlike the macro-mechanical approach, the micro-mechanical and meso-scale approaches require implementation of material models also in terms of failure criteria and stiffness degradation for each phase of the composite material. Models developed up to date are generally two-dimensional [62–64, 81], and are few compared with models implementing the EHM approach. The composite materials considered present mainly glass or carbon fibres and epoxy matrix. As previously discussed, the mechanical properties of the epoxy matrix are highly dependent on strain rate, temperature and loading conditions [82–85]. This can usually be simplified and represented by a static stress-strain curve if the cutting speed is sufficiently low [62, 81]; which assures a low strain rate and low heat generation between

tool and workpiece. It is generally described as an elasto-plastic curve to failure, where the plastic region is defined by means of Von Mises yield criterion and isotropic hardening [81, 86–88]. Material stiffness degradation is also implemented until material failure takes place [25, 62, 63].

While glass fibres are isotropic and strain rate dependent [63], carbon fibres are orthotropic in nature and strain rate independent [15, 89, 90]. Over the past years few experimental works have been carried out in order to assess fibre properties to be implemented in numerical analysis [91–93]. The Marigo model was used to describe the brittle failure of carbon fibres by Dandekar and Shin [15]; while transversely isotropic and perfectly elastic behaviour, followed by maximum principal stress failure criterion was implemented by Abena *et al.* [81] and Venu Gopala Rao *et al.* [62]. Calzada *et al.* [25] imposed fibre failure occurring when stress along the fibre direction exceeds the fibre tensile strength (θ=0°, θ=135°) or compressive strength (θ=45°, θ=90°). A progressive damage model by Hashin was used for both the matrix and fibre by Rentsch *et al.* [64]; close resemblance was found in terms of matrix-fibre failure mode, but the significant discrepancy between numerical and experimental cutting force and thrust force was attributed to the chosen material model.

The bond between fibre and matrix is usually realized by implementing a *cohesive zone model*. It was already utilised in a macro-mechanical approach by Santiuste *et al.* [56] to study the out-of-plane failure during orthogonal cutting of LFRP composites. It was also implemented to simulate delamination both for more complex machining operations, such as drilling [94, 95] and for impact problems on composites [96, 97]. Despite a decohesion element with mixed mode capability proposed by Camanho and Davila [98], recently several

studies have focused on the development of more accurate and realistic cohesive models. For instance, a dependence on strain rate has been introduced by May [99], and an elasto-plastic phase in the constitutive law has been developed by Salih *et al.* [100]. Furthermore, new approaches for the interface simulation, such as the smoothed particle hydrodynamics (SPH) method [101], have been implemented.

In the micro-mechanical approach, modelling of the matrix-fibre link is crucial for simulating the debonding of the phases. It can be realized either using cohesive elements [15, 62, 63, 81] or defining the cohesive property in the contact between the fibre and the matrix [102]. Cohesive elements based on the traction-separation law are generally used to simulate very thin adhesive layers of bonded surfaces; implemented with a thickness value of zero [62, 63]. The limitation of this approach has been highlighted by different works [25, 81, 103] and resides in the excessive distortion that cohesive elements can experience during the analysis. Recent research has tried to overcome these drawbacks by extending the constitutive behaviour of the cohesive elements already implemented in Abaqus software [81]; or using traditional continuum elements for the interface [25, 103].

In order to adequately simulate the matrix-fibre interface behaviour in composite material, a few experimental works have been carried out to determine the interface constitutive behaviour and properties. In particular, Pitkethly and Doble [104] used a single fibre pull-out test to evaluate the maximum interfacial shear stress between the fibre and the matrix for carbon fibre reinforced composites. Instead Meurs *et al.* [105] determined the interfacial normal strength, combining scanning electron microscope measurements and finite element analysis.

Comparisons between macro-mechanical and micro-mechanical approaches have been carried out by some studies [34, 64, 72]; where the advantages of the latter approach have been highlighted. Indeed, significant improvement in machining force prediction was observed by Venu Gopala Rao *et al.* [34], as shown in Figure 2.43.

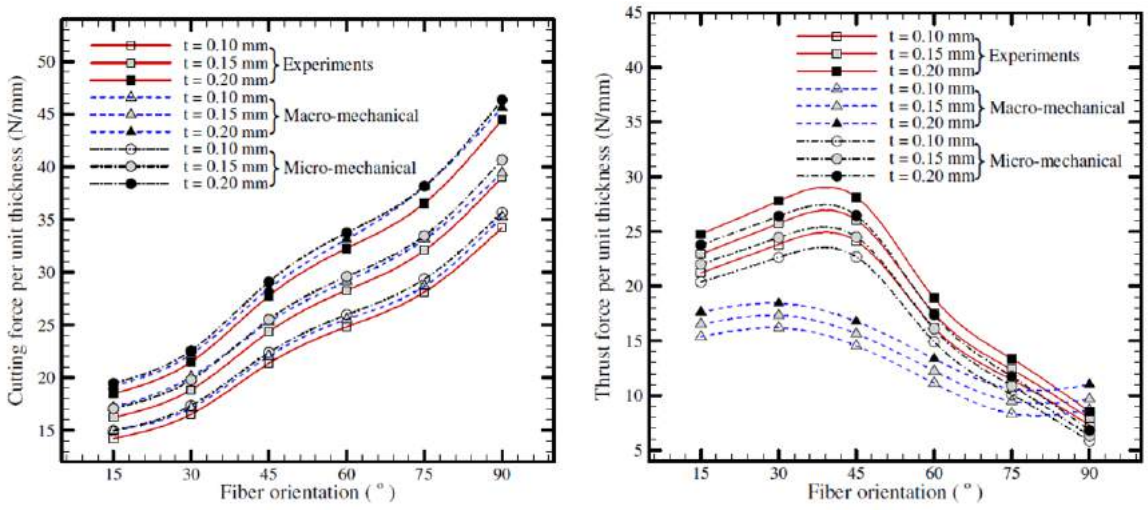

Figure 2.43: Comparison between macro-mechanical and micro-mechanical approaches for (a) cutting force; and (b) thrust force [34].

A better agreement of the micro-mechanical model with the experimental results was detected in terms of thrust force prediction (Figure 2.43(b)), highlighting the importance of modelling composite material considering each phase separately. In fact, the macro-mechanical approach presents a maximum error on the thrust force prediction of $\sim$11 N/mm at fibre orientation of θ=45°; while the micro-mechanical approach differs only by $\sim$2 N/mm. Finally, comparisons show the power of the micro-mechanical approach in analysing the chip formation mechanisms through single phases, providing detailed information on material deformation and failure mechanism during cutting, as shown in

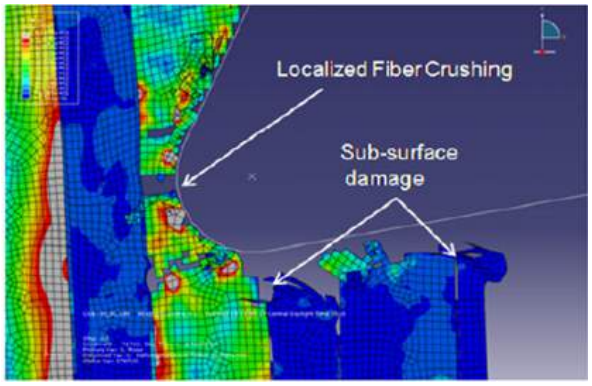

Figure 2.44: Micro-mechanical approach developed by Calzada et al. [25].

Figure 2.44.

A three-dimensional model obtained extruding a two-dimensional model along the third direction was realized by Chennakesavelu [102]. This represents an intermediate step between two-dimensional models previously described and the actual geometry of the composite material, where cylindrical fibres are present. In Chennakesavelu's model the tool encounters different phases sequentially, one after the other. This differs from reality where the fibres are totally embedded in the matrix and the tool comes in contact with all phases at the same time. However, Chennakesavelu's approach allows the taking into account of the three-dimensional effects using a simplified geometry. Alternatively, a three-dimensional model with cylindrical fibres was developed by Xu *et al.* [103] for studying the elliptic vibration-assisted (EVA) technique when cutting unidirectional carbon fibre reinforced polymer (Figure 2.45). In this model the number of fibres implemented is still limited due to the high computational cost when developing a three-dimensional model.

While cutting force is usually in good agreement, thrust force is generally underestimated. Indeed, a significant underestimation of thrust force has been observed and highlighted in

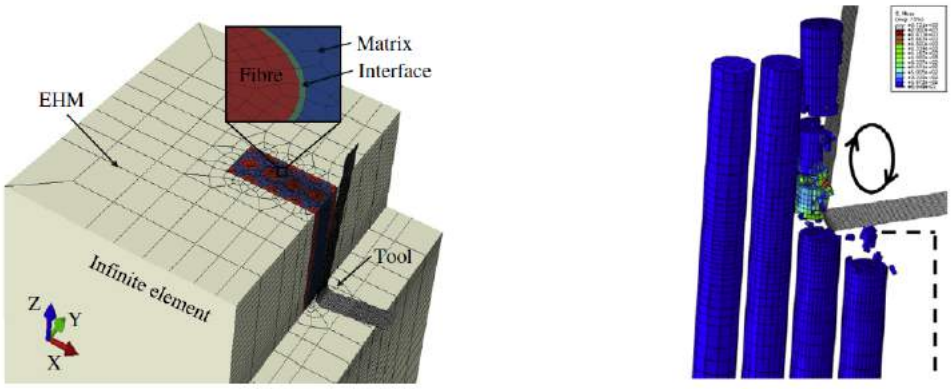

(a) (b)

Figure 2.45: (a) Schematic of three-dimensional model developed by Xu et al. [103]; and (b) fibre damage during cutting using EVA technique for fibre orientation θ=90°.

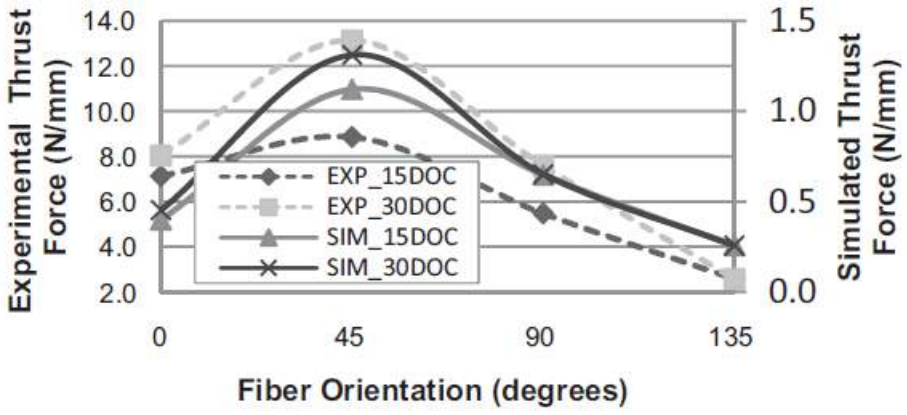

Figure 2.46: Comparison of machining forces between experiment and numerical model developed by Calzada et al. [25].

.

several works [25, 81, 103]. For instance, in Figure 2.46 the comparison between numerical and experimental results obtained by Calzada *et al.* [25] is reported. The numerical thrust force values reported on the right vertical axis are one order of magnitude lower than the experimental values. This underestimation has been attributed to the failure and subsequent deletion of elements during the analysis along the cutting path; thereby causing a relaxation in the force component due to the loss of contact between the tool and the workpiece [25, 81].

Quasi-static and explicit simulations have been carried out. In particular, a quasi-static simulation, involving the orthogonal cutting of UD-FRP at different fibre orientations and machining parameters, was developed by Venu Gopala Rao *et al.* [34, 62]. A tool displacement boundary condition was specified. The drawback of implementing a quasi-static analysis is that the model is limited to predicting failure only in the first fibre via an iterative approach, and is therefore unable to simulate chip formation progression. Unlike quasi-static analysis, dynamic simulations can predict the failure mechanism and illustrate material deformation during the chip formation process [15, 25, 81]. In such cases, a boundary condition based on tool velocity is typically implemented.

The cutting tool is usually simulated as a rigid body [25, 62, 63, 81] as its elastic modulus (e.g. Young's modulus for tungsten carbide tool is in the range 500-700 GPa [106]) is much bigger than that of the fibres (e.g. Young's modulus along fibre direction for carbon fibre is 230 GPa [11]) and the matrix (Young's modulus for epoxy matrix is in the range 2.6-3.8 GPa [11]). Instead, an elastic material model was used by Ramesh *et al.* [107] in order to investigate the stress level in the tool during cutting. However, this model represents a simplistic approach; in fact, an appropriate elasto-plastic material model should be associated to the tool in order to obtain more reliable information on deformation and stress, to which deletion of failed elements could be add to simulate the tool wear during cutting.

All models previously described are based on finite element analysis. A mesh-free approach was used by Iliesu *et al.* [33]; where a discrete element method (DEM), first introduced by Cundall and Strack [108] was implemented for the orthogonal cutting of UD-CFRP. The model's behaviour during analysis is reported in Figure 2.47. The

developed model was able to capture the physical mechanism of chip formation. The trends of the cutting force and thrust force were similar to the experimental results. However, it was highlighted that 80% of the computational time was spent on searching for particles' contact and resulting forces.

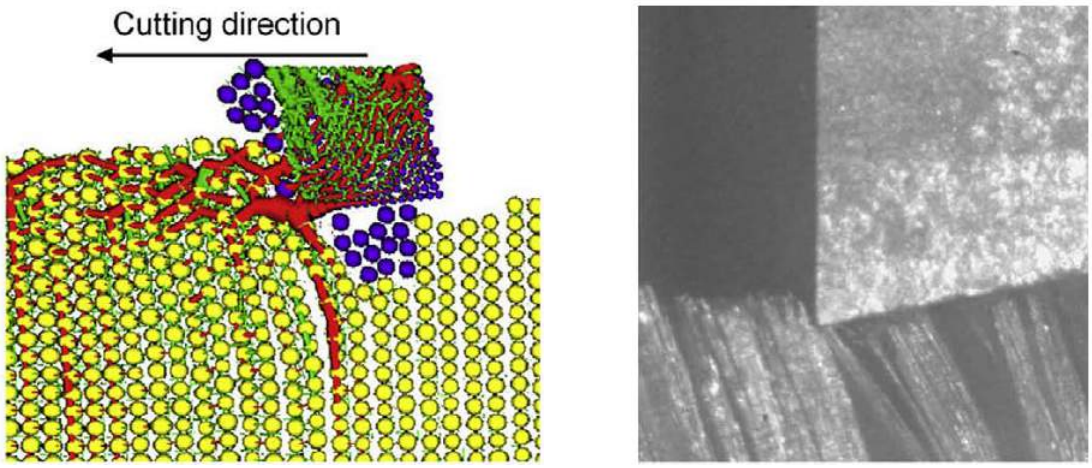

(a) *(b)*

Figure 2.47: Chip formation mechanism for fibre orientation θ=90° obtained by (a) DEM method; and (b) experimental high-speed camera images [33].

2.7 Summary

The literature review highlights that the study of the orthogonal cutting on composites can help to understand the tool-workpiece interaction and its effect on the machined component during complex machining processes. It can be realised using different approaches: experimental, analytical, empirical, and numerical.

Several works focused on the experimental aspects, trying to fully understand the mechanisms on which the process is based. This approach requires specific equipment in

order to obtain and process the desired information. This can represent also a limit in the capacity to analyse the process. For instance, it is still very challenging to obtain images during cutting at micro-scale level, analysing also the material deformation near the tool tip; and it is extremely hard to obtain information on deformation and stresses in a single fibre, interface, and matrix. However, this approach represents a mandatory step since it is used to validate analytical and numerical models and calibrate the empirical models.

Analytical approaches are usually based on strong assumptions limiting their application. Material removal complexity, due to different phases, with which different failure mechanisms are connected, and the strong influence of the fibre orientation, is difficult to capture using an analytical model. The large number of parameters involved and the complexity of their interaction make the development of an analytical model very hard. For this reason, a few models have been developed; they were mainly able to predict cutting force and thrust force. Empirical approaches require experimental calibration. This restricts the application to the range used for calibration. In addition, only cutting force and thrust force can be obtained.

In contrast to previous approaches, the numerical models represent a powerful tool, able to analyse the process at different levels of complexity. For this reason it will be employed in this thesis. Up-to-date, mainly two-dimensional models implementing an equivalent homogeneous material have been developed. This approach can provide only general information on the chip formation mechanisms during cutting. Conversely, local information can be obtained for each phase and the chip formation mechanisms can be observed on a micro-scale level when the microscopic approach is used. However, such models require detailed material data for each phase, which are not always available in the literature. Furthermore, existing

material models already implemented need to be improved. In particular, the limitations in simulating the fibre-matrix interface using current models have been highlighted in several works. Also, a paucity in the description of different cohesive models available has been observed. In addition, the usually used finite element method underestimates the thrust force due to element deletion during the analysis, which also causes the absence of bouncing back in the model. Finally, when using the microscopic approach, few models take into account the cylindrical geometry of the fibre.

Numerical models still require validation by means of experiments. For this purpose, the information needed is not always available in the literature. Hence, in-house experiments are usually carried out in order to support the numerical results.

Finally, this thesis will employ numerical models to study the orthogonal cutting of composite materials using a microscopic approach, as suggested by the literature review. As the current model capability presents the limitations described above, this thesis will focus on the development of a novel cohesive model for the matrix-fibre interface simulation, and on the implementation of a mesh-free method to improve the thrust force prediction avoiding the element deletion during the analysis. Furthermore, the latter approach will also be used to simulate the bouncing back during machining.

Chapter 3

Development of a novel cohesive model

3.1 Introduction

The literature review highlighted that cohesive models generally used to link the fibre and matrix, employ zero thickness cohesive elements based on the traction-separation law. This approach is limited due to the high distortion that the cohesive elements can undergo when the surrounding elements, representing the matrix or fibre phases, fail earlier [25, 81]. The drawbacks shown by interface elements can be overcome by implementing *surface-based cohesive behaviour*; where the cohesive behaviour is defined in terms of surface interaction property avoiding the implementation of interface elements between the fibre and matrix phases. This approach was employed by Chennakesavelu [102] to simulate the orthogonal cutting of UD-CFRP. This method was chosen over the implementation of cohesive elements at the interface because of its simple set-up in the model.

It is clear from the literature that different methods were used in order to simulate the

interface between the matrix and the fibre when the micro-mechanical approach is chosen. However, when using these methods only general information on the interface is reported in the literature. Hence, a comparison attempting to provide a better understanding of the cohesive models usually used, highlighting the advantages and drawbacks, is presented in this chapter. In order to overcome the limitations observed, a three-dimensional model of the orthogonal cutting of unidirectional carbon fibre reinforced polymer composite is realized by introducing, via a bespoke subroutine, a novel fibre-matrix interface approach. In particular, zero thickness cohesive elements based on the traction-separation law are employed and deleted from the simulation if any of the surrounding elements, matrix or fibre fails. The 3D model is developed by means of the extrusion of a two-dimensional model, obtaining the so-called *2D-extruded model*. In addition, for different fibre orientations (θ=0°,45°,90°,135°), a comparison of the proposed new approach against previously published models is carried out.

3.2 Novel approach for cohesive zone modelling

The cohesive zone model incorporating zero thickness cohesive elements based on the traction-separation law is an approach that can potentially represent the actual interface behaviour. This is due to its ability in describing very thin adhesive phases, such as those present between the matrix and fibre of composite materials. This method was used as the basis to develop a novel interface model. A detailed description relating to the constitutive law of the proposed approach is presented in the following sections.

3.2.1 Elastic behaviour

For a three-dimensional problem the cohesive element possesses three components of separation: one acting along the thickness direction and representing the normal behaviour of the element; and two acting in the plane orthogonal to the thickness direction and representing the shear behaviour of the element [109]. The mechanical response, for normal (tensile and compressive) and tangential (shear) behaviour, is shown in Figure 3.1.

Normal and shear behaviour are composed by a linear elastic response, where the strains ϵ (tensile, compressive and shear) are related to displacements δ by means of Equation (3.1):

$$\epsilon_n = \frac{\delta_n}{T_0}, \qquad \epsilon_s = \frac{\delta_s}{T_0}, \qquad \epsilon_t = \frac{\delta_t}{T_0} \tag{3.1}$$

where T_0 represents the constitutive thickness assumed to be unitary to make the strains and displacements coincident; while the subscripts n, s and t indicate the normal and the two shear directions, respectively. So, the linear elastic behaviour can be expressed by means of Equation (3.2):

$$\bar{t} = \begin{Bmatrix} t_n \\ t_s \\ t_t \end{Bmatrix} = \begin{bmatrix} P_n & 0 & 0 \\ 0 & P_s & 0 \\ 0 & 0 & P_t \end{bmatrix} \begin{Bmatrix} \epsilon_n \\ \epsilon_s \\ \epsilon_t \end{Bmatrix} = \overline{\overline{P}}\bar{\epsilon} \tag{3.2}$$

where $\bar{t}$, $\overline{\overline{P}}$ and $\bar{\epsilon}$ represent the stress vector, the stiffness matrix and the strain vector, respectively.

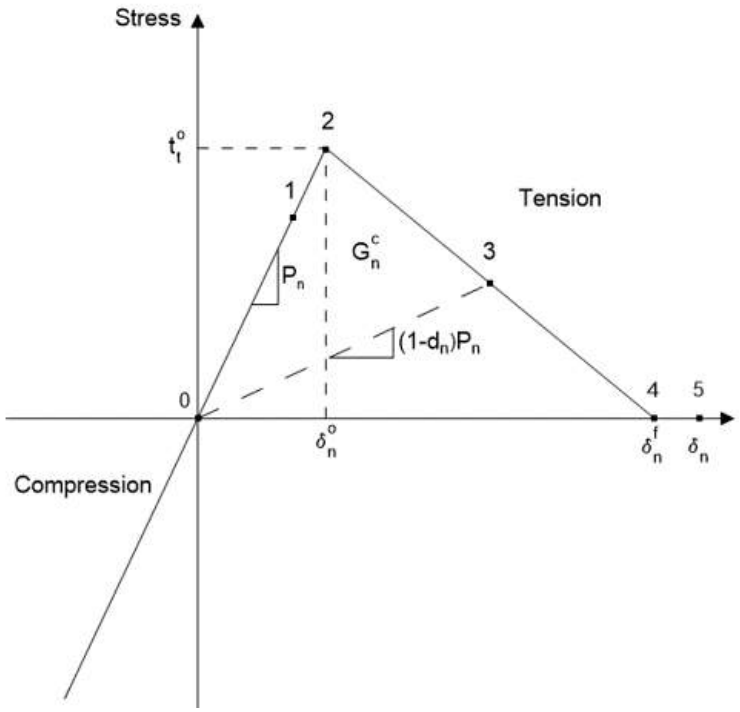

(a)

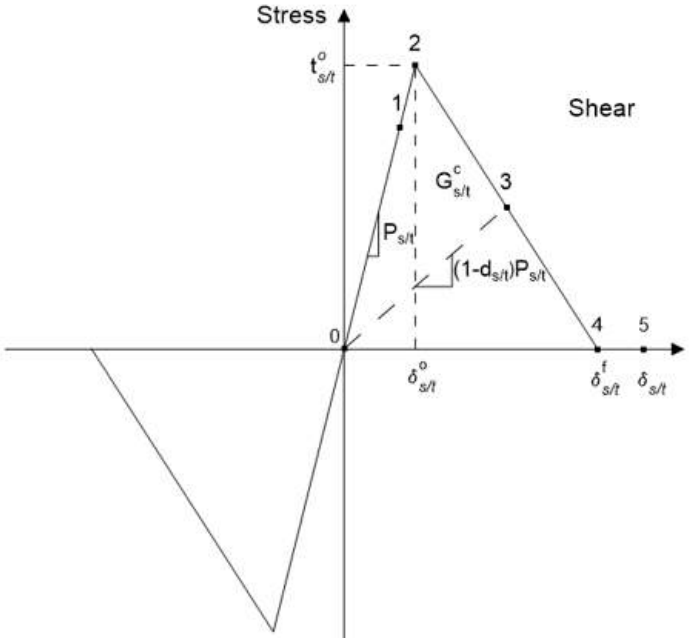

(b)

Figure 3.1: Cohesive model based on traction-separation law, mechanical response for (a) normal behaviour; and (b) tangential behaviour.

In addition to the elastic behaviour, during the analysis the cohesive element can fail, and the failure can be promoted by:

- damage initiation and evolution;
- a surrounding element failure.

3.2.2 Damage initiation and evolution

The end of the linear elastic behaviour is indicated by the initial damage condition (point 2 in Figure 3.1), which is followed by the damage evolution. The latter represents the degradation of the adhesive phase until failure (point 4) and is obtained through the reduction of its stiffness according to Equation (3.3):

$$P^d_{n/s/t} = P_{n/s/t}(1 - d_{n/s/t}) \tag{3.3}$$

where $d_{n/s/t}$ represents the damage variable introduced for each failure mode. It is expressed by the Camanho and Davila law [98] describing a linear damage evolution:

$$d_{n/s/t} = \frac{\delta^f d_{n/s/t}(\delta^{max}_{n/s/t} - \delta^0_{n/s/t})}{\delta^{max}_{n/s/t}(\delta^f_{n/s/t} - \delta^0_{n/s/t})}, \qquad d_{n/s/t} \in [0, 1] \tag{3.4}$$

where $\delta^0_{n/s/t}$, $\delta^f_{n/s/t}$ and $\delta^{max}_{n/s/t}$ represent the displacement at the damage initiation, the displacement at failure, and the maximum displacement reached during the analysis until the time considered, respectively. The segment $\overline{03}$, reported in Figure 3.1, represents the unloading condition once initiation of damage occurs. As implemented by Venu Gopala Rao

et al. [63], in the present work the damage initiation condition was chosen to be based on the quadratic nominal stress criterion, coupling traction and shear behaviour as in Equation (3.5):

$$\left\{\frac{\langle t_n \rangle}{t_n^0}\right\}^2 + \left\{\frac{\langle t_s \rangle}{t_s^0}\right\}^2 + \left\{\frac{\langle t_t \rangle}{t_t^0}\right\}^2 = 1 \tag{3.5}$$

where the Macaulay brackets $\langle\rangle$ mean that no damage initiation is possible under compressive behaviour. With this assumption, the softening behaviour in the cohesive element may start before each mode reaches its damage initiation condition.

Traction and shear behaviour interaction was considered also in terms of failure condition, implementing the power law criterion:

$$\left\{\frac{G_n}{G_n^C}\right\}^\alpha + \left\{\frac{G_s}{G_s^C}\right\}^\alpha + \left\{\frac{G_t}{G_t^C}\right\}^\alpha = 1 \tag{3.6}$$

where G^C represents the fracture energy, i.e. the area below the stress-displacement curve in Figure 3.1. When Equation (3.6) is satisfied, the integration point of the cohesive element is considered as failed. The cohesive element is deleted from the analysis when all the integration points fail.

3.2.3 Failure due to connectivity

Cohesive element failure during the analysis could be also due to surrounding element failure. As the analysis starts, the connectivity matrices $\overline{\overline{CM}}$ and $\overline{\overline{CF}}$, storing the connection between

cohesive elements and surrounding elements (matrix and fibre), are created by means of a user-defined field subroutine (VUSDFLD). For that goal, the VUSDFLD subroutine calls the appositely created connectivity subroutine for the matrices generation, starting from the input file created by the Abaqus/CAE. In fact, the subroutine reads the input file looking for the sections where nodes and elements' information for cohesive, fibre and matrix phases are stored. Afterwards, it creates two different matrices for each phase: elements matrix $\overline{\overline{El}}_{phase-name}$; and the nodes matrix $\overline{\overline{Nd}}_{phase-name}$. For each element of the considered phase, the elements matrix $\overline{\overline{El}}_{phase-name}$ stores the ID element number and the ID numbers of the eight nodes forming the 3D element. The matrix is composed of nine rows and the number of columns is equal to the total number of elements in the considered phase. For each column, the first row represents the element ID number, while the following eight ID numbers of all nodes form the element. For each node of the considered phase, the $\overline{\overline{Nd}}_{phase-name}$ matrix stores the ID node number and its three spatial coordinates. The matrix is composed of four rows and the number of columns is equal to the total number of nodes in the considered phase. For each column, the first row contains the node ID number, while the following three, the spatial coordinates of the node. It is possible to observe that the $\overline{\overline{El}}_{phase-name}$ and $\overline{\overline{Nd}}_{phase-name}$ matrices dimension changes depending on the phase considered. At the end, six matrices are built: $\overline{\overline{El}}_{cohesive}$, $\overline{\overline{El}}_{fibre}$, $\overline{\overline{El}}_{matrix}$, $\overline{\overline{Nd}}_{cohesive}$, $\overline{\overline{Nd}}_{fibre}$, and $\overline{\overline{Nd}}_{matrix}$. Starting from these matrices, the connectivity subroutine compares each cohesive element with all fibre and matrix elements at the node coordinates level. Finally, the subroutine is able to create two different connectivity matrices for fibre and matrix phases, having a number of rows equal to the cohesive elements' number in the model and two columns. The first column contains

the cohesive elements' ID number, while the second reports the correspondent connected surrounding elements. The connectivity matrices are afterwards available in the VUSDFLD subroutine.

During the analysis the cohesive elements follow the elastic behaviour and damage evolution. Meanwhile, matrix and fibre deform under the loads applied during the machining, and eventually fail. As one matrix/fibre element fails, the VUSDFLD subroutine searches in the connectivity matrices for the possible corresponding cohesive element, deleting it from the analysis.

This criterion prevents the cohesive element from remaining in the model after the surrounding element fails, losing its purpose and potentially experiencing excessive deformation.

3.3 Implementation of cohesive models in a finite element analysis: 2D-extruded model

A 3D finite element analysis of orthogonal cutting on UD-CFRP was developed using Abaqus/CAE software and referring to Calzada *et al.*'s [25] work. The three-dimensional model was obtained by means of the extrusion of the two-dimensional model presented in Abena *et al.*'s [81] work, where a meso-scale approach was implemented. A schematic of the FEM model and the boundary conditions applied are reported in Figure 3.2.

The material models representing different phases were implemented as reported in Abena *et al.* [81]. The epoxy matrix was implemented according to a static compressive stress-strain

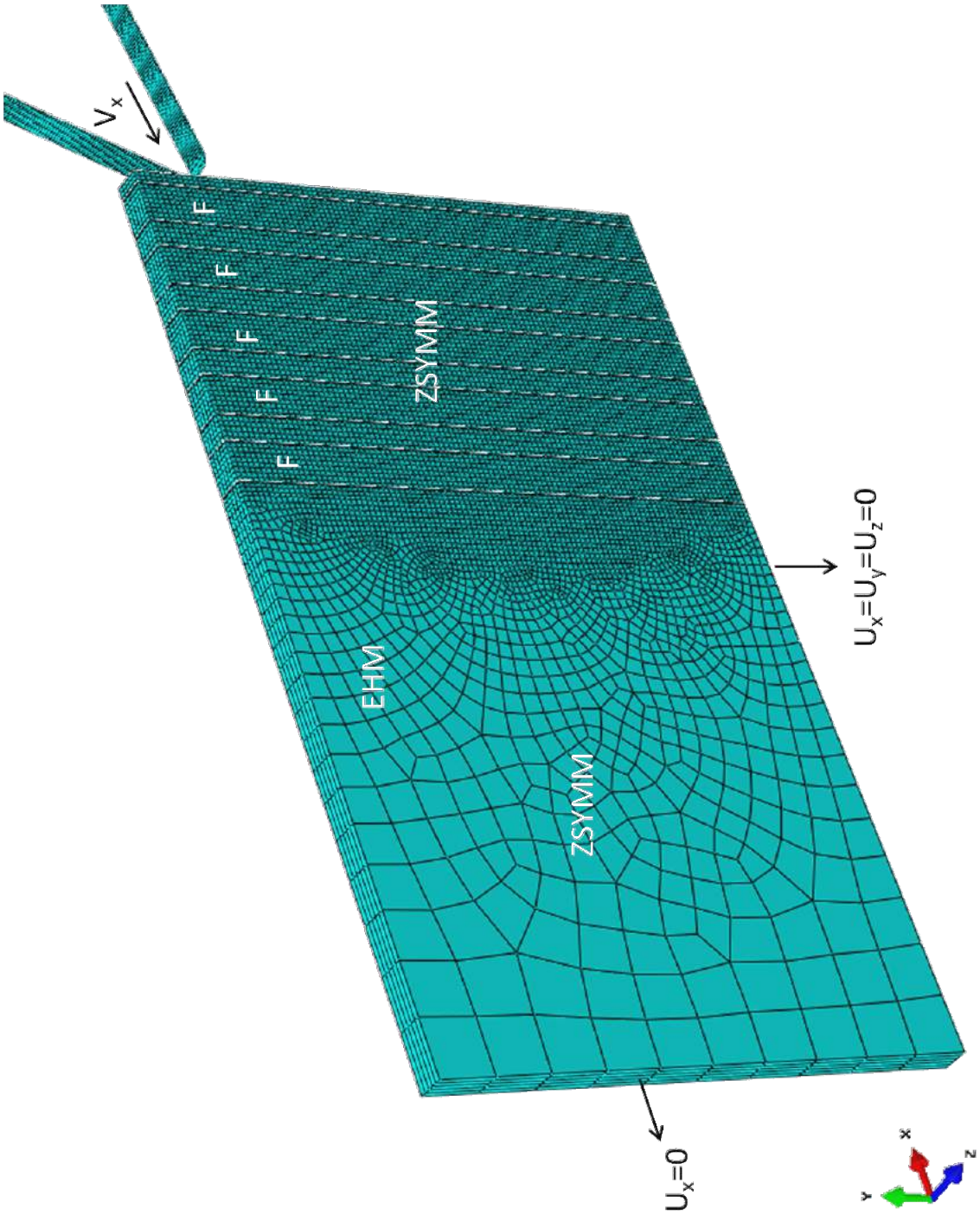

Figure 3.2: Schematic representation of the FEM model and of the boundary conditions applied.

curve at room temperature; the element in the model was considered as failed when the Von Mises stress reached the ultimate stress level. Instead, the carbon fibres were simulated as transversely isotropic and perfectly elastic to failure with failure criterion based on the maximum principal stress. Both failure criteria have been already used in the literature to study the orthogonal cutting on FRPs' material [62, 63, 81]. The material properties are reported in Table 3.1.

Table 3.1: Material properties for carbon fibre and epoxy matrix implemented in the numerical model [25, 62, 84, 98].

Material	Property	Value
Carbon fibre	Elastic constants	E_1=235 GPa, E_2=E_3=14 GPa
		ν_{12} = ν_{13}=0.2, ν_{23}=0.25
		G_{12}=G_{13}=28 GPa, G_{23}=5.5 GPa
	Longitudinal strength	X_t=3.59 GPa, X_c=3 GPa
	Diameter	7.5 μm
	Volume percentage	60 %
Epoxy	Elastic constants	E=2.96 GPa, ν=0.4
	Yield strength	σ_y=74.7 MPa
Interface	Normal strength	σ_{max}=167.5 MPa
	Shear strength	τ_{max}=25 MPa
	Fracture energy	G^c=0.05 N/mm^2
EHM	Elastic constants	E_1=142.184 GPa, E_2=E_3=7.606 GPa
		ν_{12} = ν_{13}=0.28, ν_{23} ==0.347
		G_{12}=G_{13}=4.151 GPa, G_{23}=2.824 GPa

Contact conditions were implemented through a general contact algorithm, where the penalty method was used to enforce the contact constraint between surfaces. The contact property was defined in terms of the Coulomb model considering a constant friction coefficient equal to 0.3 for all fibre orientations, as suggested by Venu Gopala Rao *et al.* [62]. Tie constraint was implemented between the EHM and the micro-mechanical zone, and also between adjacent phases (matrix, fibre and cohesive), except when employing the surface-

based cohesive behaviour. The mesh in the micro-mechanical area was realized by employing 3D stress hex elements and setting the mesh seed on the edges equal to 1 μm. In order to reduce the computational cost of the analysis, coarse mesh was used in the EHM zone with elements having a maximum length of 10 μm in the x-y plane far from the cutting area. In addition, the mass scaling technique was employed to speed up the analysis. Finally, the machining parameters implemented in the simulation are reported in Table 3.2.

Table 3.2: Machining parameters [25].

Tool	5 μm edge radius 10° clearance angle 25° rake angle
Cutting speed	500 mm/min
Depth of cut	15 μm
Fibre orientations	0°, 45°, 90°, 135°

The new proposed approach for the interface simulation (Novel Approach) has been compared with previously published approaches:

- Approach 1: zero thickness cohesive elements based on traction-separation law [63];
- Approach 2: cohesive elements based on traction-separation law presenting a small thickness [81];
- Approach 3: surface-based cohesive behaviour [102].

Abena *et al.* [81] developed Approach 2 to overcome the limitations represented by the excessive deformation of the cohesive elements in the Approach 1, usually implemented in the literature, due to the earlier failure of the surrounding elements (matrix, fibre). A

small thickness (0.25 μm) was introduced in order to accommodate the deformation under compression until failure. Differently from Abena *et al.* [81], in this thesis a linear behaviour under compression was considered. The failure condition was implemented through a user-defined field subroutine (VUSDFLD), allowing the deletion of the cohesive element when the compressive failure stress was reached in each integration point. It is important to notice that the element thickness value is strictly dependent on the compression displacement at failure.

Instead, Chennakesavelu [102] implemented surface-based cohesive behaviour where no elements are present for the interface. Using this approach Chennakesavelu prevented interface elements from eventually remaining in the model, losing their purpose and potentially experiencing excessive distortion.

3.4 Results and discussion

Several analyses were carried out for different fibre orientations and interface approaches. A comparison in terms of cohesive behaviour was performed, and models were validated in terms of chip formation mechanism, cutting force and thrust force against published experimental results [25]. At the end, the computational time was also analysed in order to possibly identify a preferred cohesive model.

3.4.1 Approach 1: zero thickness cohesive elements based on traction-separation law

The zero thickness cohesive elements based on the traction-separation law (Approach 1) were implemented for fibre orientation θ=90°. Figure 3.3(a) shows how matrix and fibre elements ahead of the tool fail mainly because of compressive stress due to the tool progression. Differently, the cohesive elements remain in the model as they do not present any failure criterion under compression. Then, the tool continues to move forward stretching the cohesive elements, which experience excessive deformations, as shown in Figure 3.3(b).

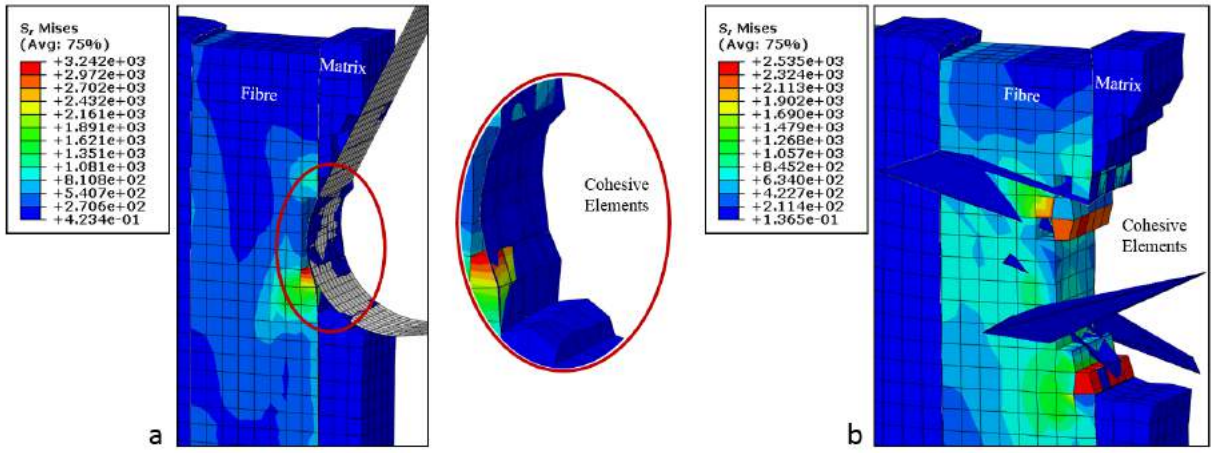

Figure 3.3: Approach 1 for fibre orientation θ=90° at (a) 2.76e-4 seconds; and (b) 7.97e-4 seconds.

The cohesive elements' failure is also due to the tool action, which by pushing the fibres and matrix ahead of it, causes the interface elements to stretch in the already machined area below the cutting plane, originating debonding defects (Figure 3.4). Analysing the failure mechanism of cohesive elements that undergo tensile behaviour, the shear stress represents the main contribution to the damage initiation. This is due to the low shear stress limit required

to reach the shear damage initiation when compared with the normal behaviour. So, small shear deformations can immediately make a big contribution to the damage initiation unlike the normal displacements. Even during the damage evolution, the shear stress contributes mainly to the elements' failure, since the normal stress remains low. However, cohesive failure extends for a few fibres ahead of the tool and also below the cutting plane, near the areas where matrix and fibre damage takes place. It is due to the excessive deformation experienced after the surrounding elements' deletion.

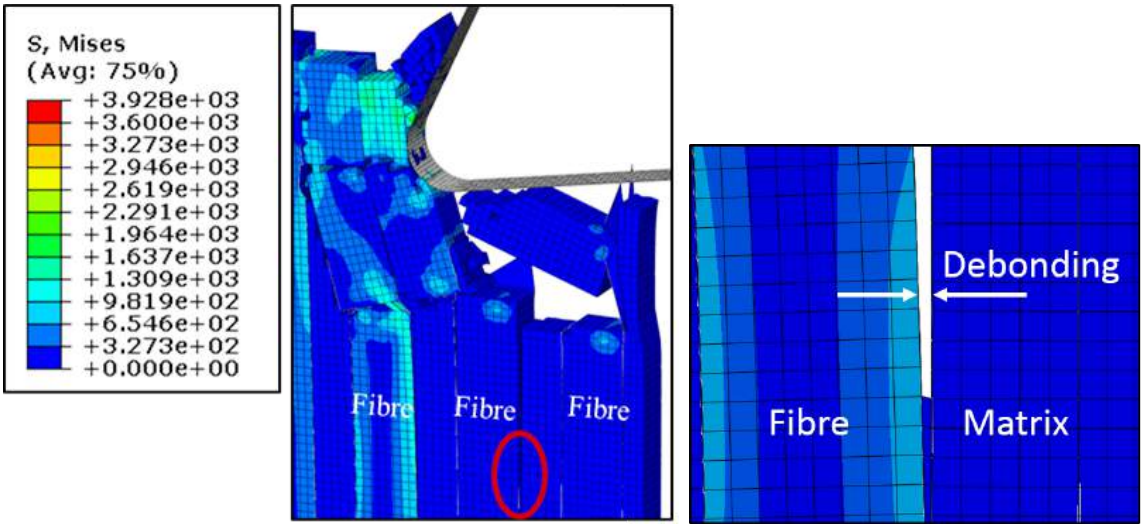

Figure 3.4: Approach 1: cohesive elements' failure and debonding defect formation for (a) the whole model; and (b) the interface between the first matrix and the second fibre.

The results highlight how the cohesive elements allow the debonding defect to be simulated by able to work under tensile and shear behaviour (Figure 3.4). However, their inability to fail under compression, and the assumption the membrane response, does not produce any stress leading to the undesired behaviour highlighted in Figure 3.3, where highly distorted cohesive elements can be observed.

3.4.2 Approach 2: cohesive elements based on traction-separation law having a small thickness (0.25 μm)

In order to overcome the drawback of the previous approach, a small thickness was introduced in the cohesive elements in order to accommodate compressive deformation and failure leading to Approach 2, shown in Figure 3.5.

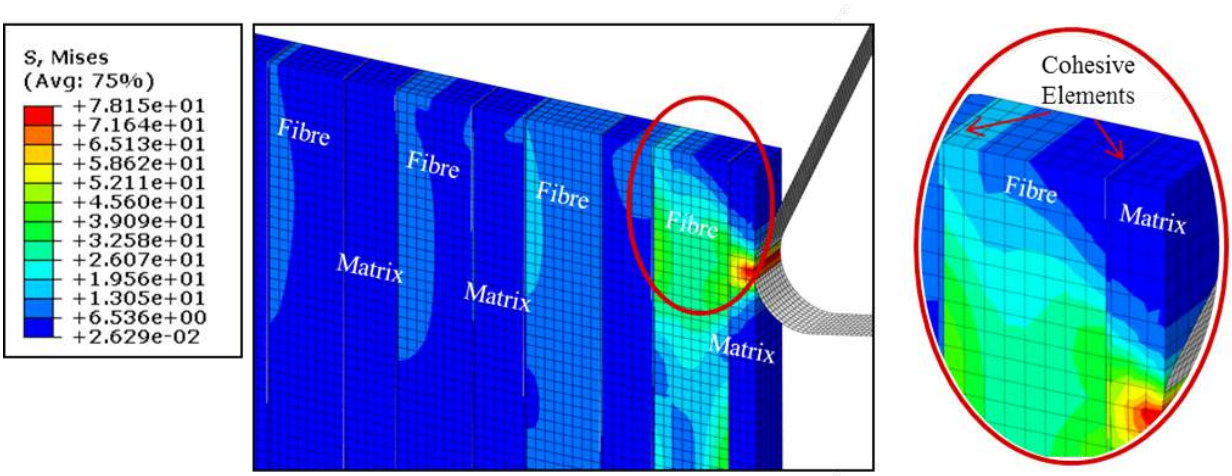

Figure 3.5: Approach 2: numerical model configuration.

Differently from that shown in Figure 3.3(a), the capacity of the cohesive elements to deform and fail under compression can be observed in Figure 3.6, where the red lines mark the depth of the debonding defects for the time-step considered. It is important to notice that the introduction of this new failure condition changes the model's behaviour during the simulation. In fact, the compressive failure of the cohesive elements is not localized, it extends for many fibres ahead of the tool. So, while in the previous approach the link between fibre and matrix was still active ahead of the tool after a few fibres, in this case the fibres and matrix above the red marks are totally separated and able to move independently

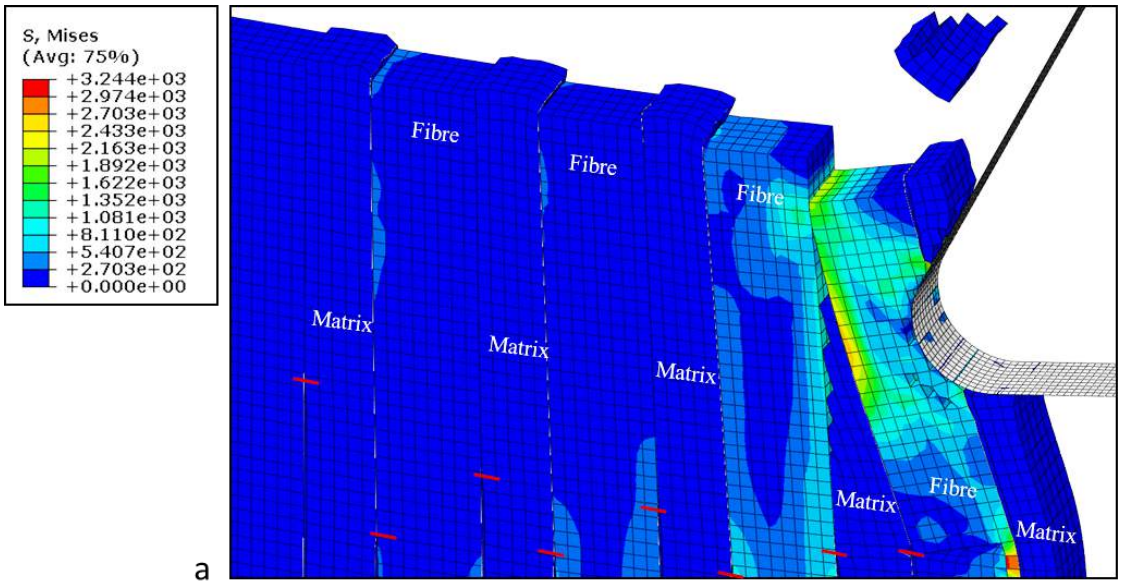

(a)

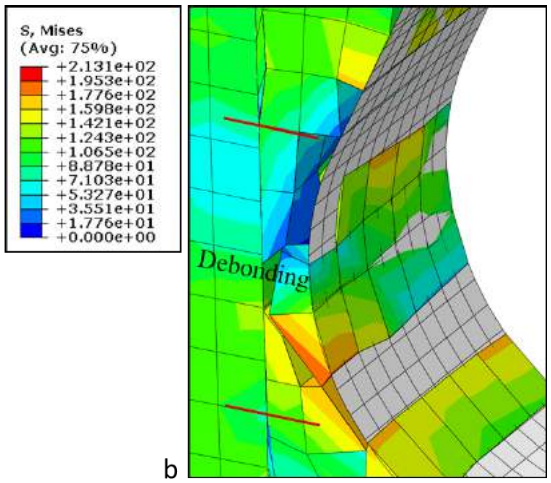

(b)

Figure 3.6: Approach 2: cohesive elements failure for (a) the whole model; and (b) the first matrix-fibre interface.

also very far from the tool (Figure 3.6).

The cohesive damage extends not only in the cutting direction, but also below the cutting plane ahead of the tool, causing the initiating of debonding defects due to compression failure. It is important to underline that during compression the element can still experience shear

deformation that can lead to failure. In this case compressive and shear behaviour are uncoupled in terms of damage initiation and evolution. However, the compressive stress is so high that the compressive failure is generally reached before the shear failure. Further debonding is then formed below the cutting plane after the tool is passed, like in the previous approach. In this case, the shear behaviour is still the main contribution to the damage initiation mechanism; after which the tensile normal stress increases contributing together with shear to reach the failure condition.

The tool movement causes a first crack formation at the contact point with the fibre, since the fibre is compressed between the tool and the following matrix. This crack is not extended for all fibre thickness because, at some point, the matrix behind starts to fail under compression allowing the fibre to increase the bending deformation under the tool movement. Due to bending stresses, a second crack rises and propagates along the whole fibre thickness below the cutting plane. Then the matrix continues to fail until the two consecutive fibres come into contact. When this happens, the first crack in the first fibre continues to propagate through the fibre for all the thickness length. So, the first fibre is divided into three parts (Figure 3.7(a)). A further tool movement causes the fragmentation of the upper part of the first fibre and the bending and failure of the following fibre (Figure 3.7(b)). After that the chip formation mechanism repeats cyclically. Therefore, during the cutting, subsurface damages in terms of fibre and matrix failure are also formed in the machined workpiece as visible in Figure 3.6.

Dissimilarly from θ=90°, when fibre orientation θ=45° is considered, the chip formation mechanism totally changes, as shown in Figure 3.8.

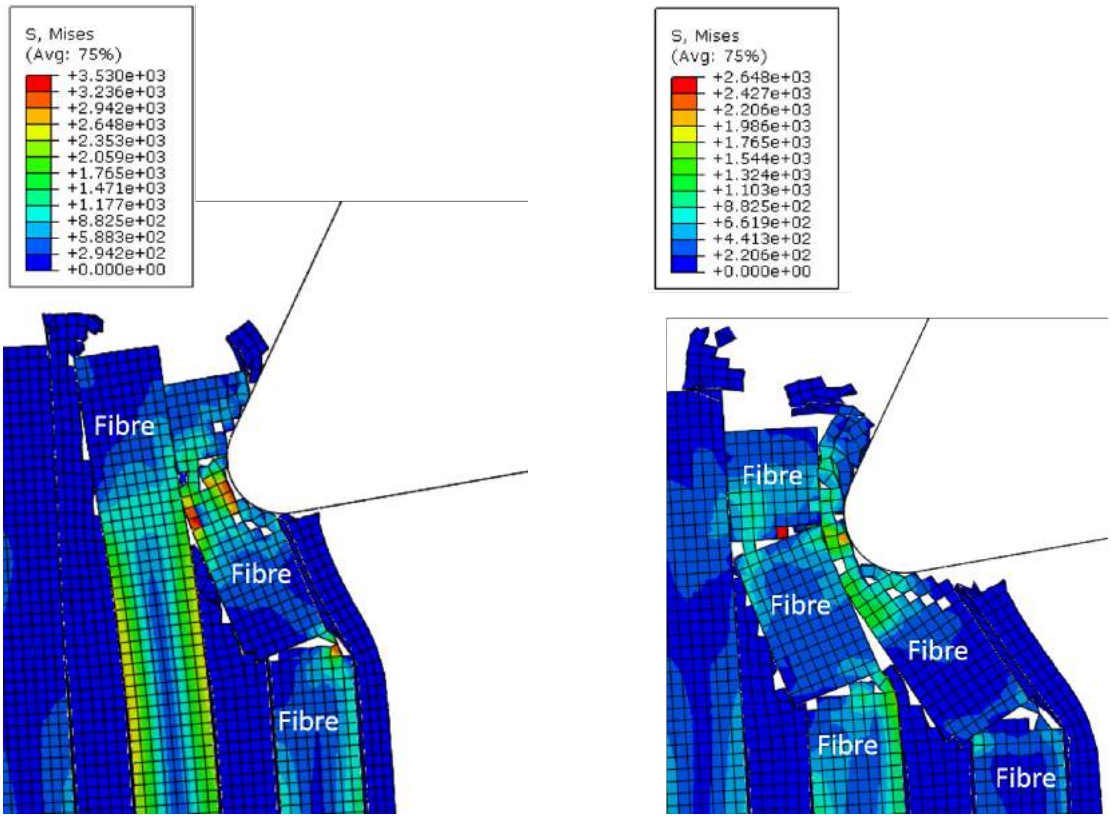

(a) *(b)*

Figure 3.7: Approach 2: model configuration at time (a) 1.96e-3; and (b) 2.68e-3 seconds.

The tool force could be decomposed into two components: one in the fibre direction (F_1), and the other orthogonally to it (F_2). The latter component compresses the different phases leading to a crack formation and propagation along the same direction in the fibre in contact with the tool (Figure 3.8(a)). Also the cohesive elements fail under compression causing debonding formation below the cutting plane in the area highlighted by means of red markers in Figure 3.8(a). This force component, compressing the phases along its direction, causes a bending deformation during failure in the phases nearer to the tool. Thus, the cohesive behaviour changes from compression to tension increasing the distance from the area marked with red lines. Instead, the component acting along the fibre direction introduces shear

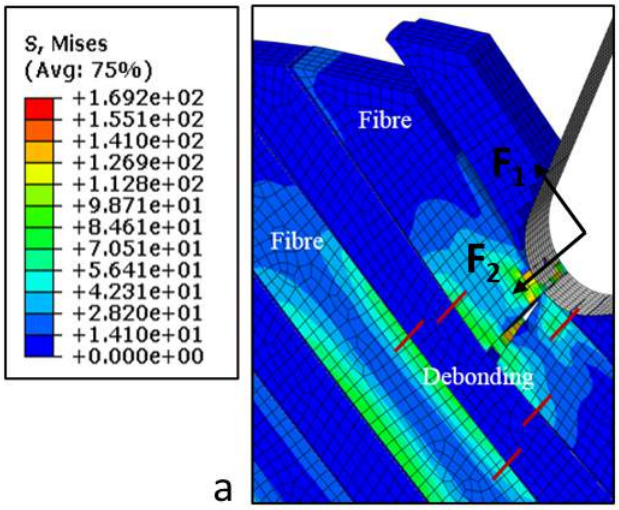

(a)

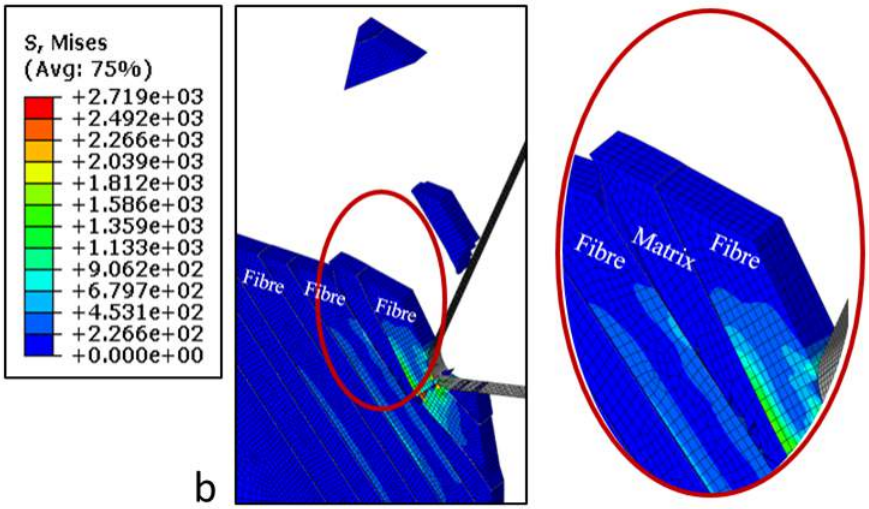

(b)

Figure 3.8: Approach 2: (a) cohesive elements failure; and (b) chip formation mechanism for fibre orientation θ=45°.

behaviour, as can be observed in Figure 3.8(b), leading to the interlaminar shear fracture in the elements, where tensile stresses are also present. The interlaminar shear fracture has been experimentally confirmed by several studies [18, 28, 32], when Type III chip formation

mechanism takes place. Regarding the matrix, it fails under compression starting from the point of the crack location on the previous fibre. So, matrix and fibre are divided by the tool into two different parts below the cutting plane. In addition, as with θ=90° the machined workpiece shows subsurface damages.

For fibre orientation θ=135°, the chip formation mechanism changes again. The fibre engaged by the tool undergoes bending deformation, being peeled from the workpiece and causing huge deformations until failure in the cohesive elements that try to keep the fibre and previous matrix together.

The debonding defect increases with the increase of the fibre deflection, as shown in Figure 3.9, until the fibre failure takes place due to bending stress.

When this happens, the tool exercises pressure only on the upper part of the fibre, which causes the failure under compression of the following matrix. Since the following matrix is still linked by means of cohesive elements with the lower part of the broken fibre, during its failure under compression, it continues to drag with itself the lower part of the fibre increasing the bending deformation and so the debonding defect. At some point, the two consecutive fibres come into contact and the chip formation mechanism described starts again, since the tool pressure is transmitted by means of the first fibre to the second. During the tool displacement, the depth of the fibre failure decreases moving towards the workpiece surface along a direction oriented orthogonally to the fibre direction. Moreover, during the cutting the fibres experience multi-fracture damage. This chip formation mechanism could be classified as Type V.

The cohesive elements show two different kinds of failure. In the upper part of the

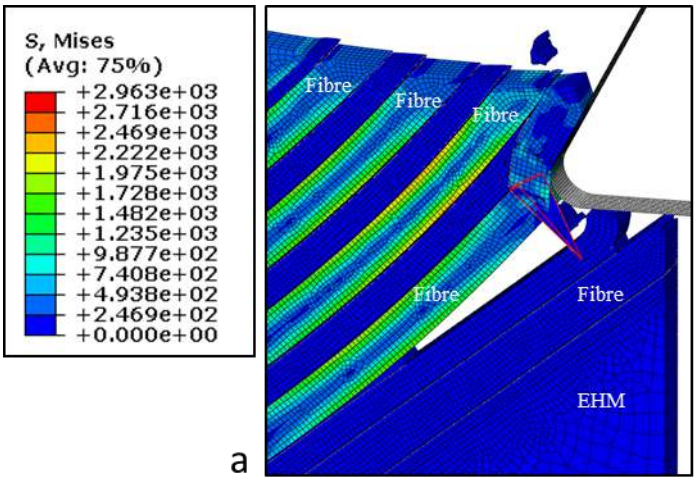

(a)

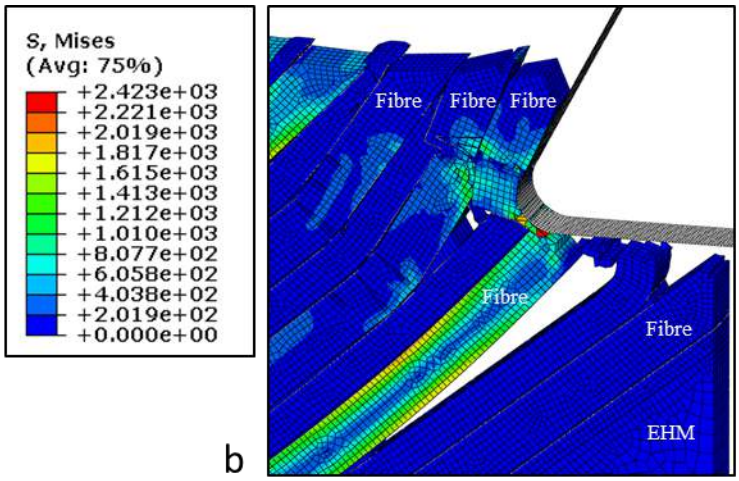

(b)

Figure 3.9: Approach 2: chip formation mechanism at two different time-steps (a) 2.59e-3; and (b) 3.6e-3, for fibre orientation θ=135°.

workpiece, the tool action causes compression of different phases leading to a compressive failure of cohesive elements. Instead, below the cutting plane, the cohesive elements undergo shear and tensile behaviour, with damage initiation and failure caused mainly by shear stress.

Even if the observation of cohesive failure is crucial to estimate the debonding defect in the machined material, the damage level in the cohesive elements that remain in the model

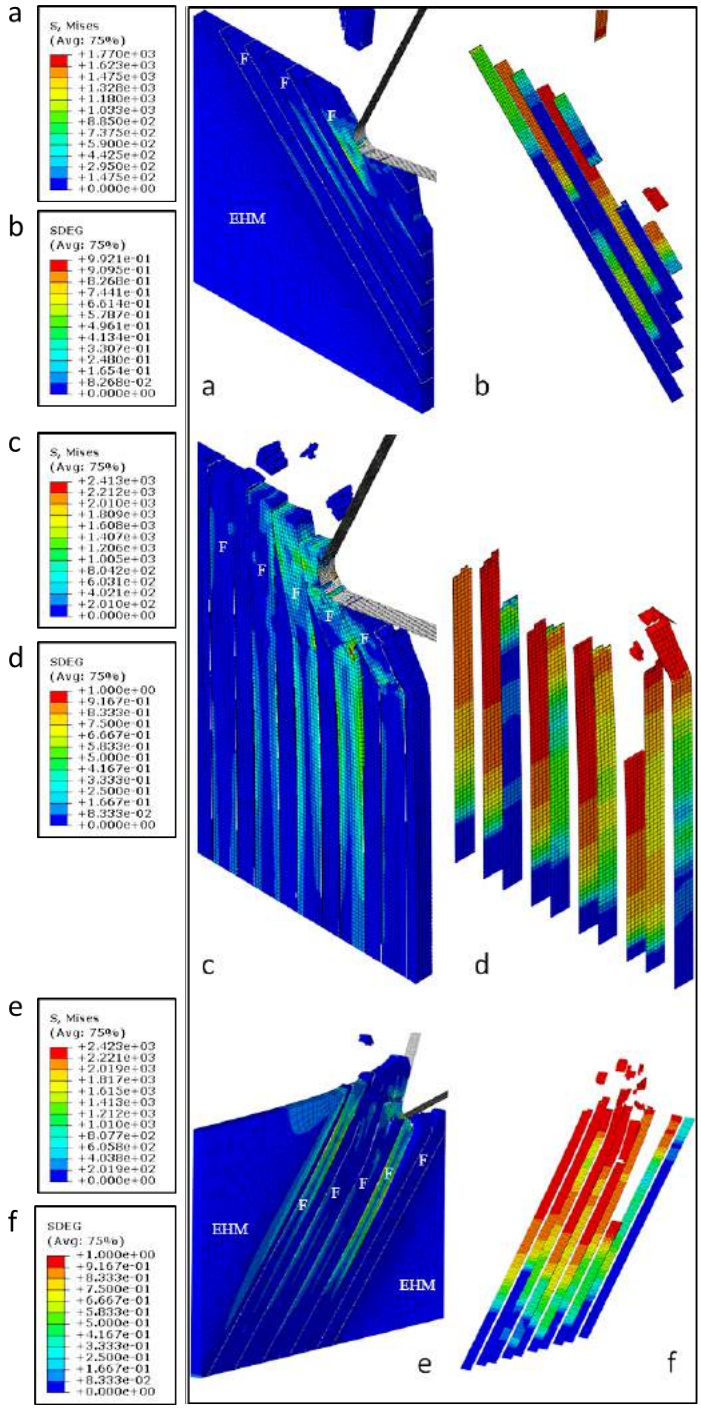

Figure 3.10: Approach 2: chip formation mechanism and cohesive damage for (a-b) θ=45°; (c-d) θ=90°; and (e-f) θ=135°.

after the machining represents also an important parameter that needs to be investigated. In fact, during the in-service condition, the stress in the material could promote additional debonding, compromising the component integrity and performance. For this goal, the SDEG variable representing the overall value of the scalar damage, and the QUADSCRT variable indicating the damage initiation condition, can be used. In Figure 3.10 it is possible to observe how the damage in the cohesive elements reaches areas that are very far from the tool. For all fibre orientations investigated the amount of damage decreases moving away from the cutting plane; it is possible to observe a considerably expanded zone which is subject to a medium/high damage value ($0.6<\text{SDEG}<1$), prone to fail if subjected to further stresses.

The approach previously described still presents some failing of cohesive elements due to excessive distortion caused by surrounding element failure, as shown in Figure 3.9(a), where a highly deformed cohesive element is highlighted in red.

3.4.3 Approach 3: surface-based cohesive behaviour

As described, the problem of the excessive distortion of the cohesive elements was limited implementing the failure condition under compression. It needed the introduction of a thickness in the cohesive elements. This thickness in the cohesive elements and the capacity to fail under compression could not represent properly the real interface behaviour.

Alternatively to the previous approaches it is possible to implement the cohesive behaviour as a contact property (Approach 3). This approach allows the elimination of the problem related to excessive deformation of cohesive elements without implementing compressive failure and thickness. If the absence of cohesive elements represents an

advantage from a practical point of view, on the other hand it makes it very difficult to recognise the interface failure, and analyse the interface behaviour. In order to understand the interface behaviour during the cutting, two variables can be used: the CSDMG variable, which represents the overall value of the damage; and the CSQUADSCRT variable, which indicates if the damage initiation condition chosen has been satisfied.

For fibre orientation θ=90°, the chip formation mechanism is similar to that previously described from the failure mechanism point of view, but the velocity at which the damage propagates ahead of the tool along the cutting plane is much higher. In fact, in Figure 3.11(b) it is possible to notice that more fibres and matrix phases are involved in the damage at the end of the analysis when compared with Figure 3.10(c). Analysing the cohesive behaviour at the fibre-matrix interface, also in this case the damage propagates deeply inside the material affecting areas very far from the tool (Figure 3.11(b)).

The debonding defect in the model is represented by nodes where the damage variable CSDMG reaches the unitary value. During the analysis, this value is reached only in a few nodes, indicating that the fibre-matrix link is still active for most of the interfaces in the model. This is shown in Figure 3.12, where areas with CSDMG variable values between 0.99 and 1 have been highlighted. It represents a difference to the previous approaches, where cohesive elements' failure was observable during the cutting at the end of the analysis. So, using the surface-based cohesive behaviour, the link between the fibre and matrix appears stronger compared with the cohesive elements, even if the same properties are implemented. Finally, not as expected, no debonding was detected using the present approach. Indeed, Dandekar *et al.* [15] observed experimentally debonding after machining at fibre angle θ=90°.

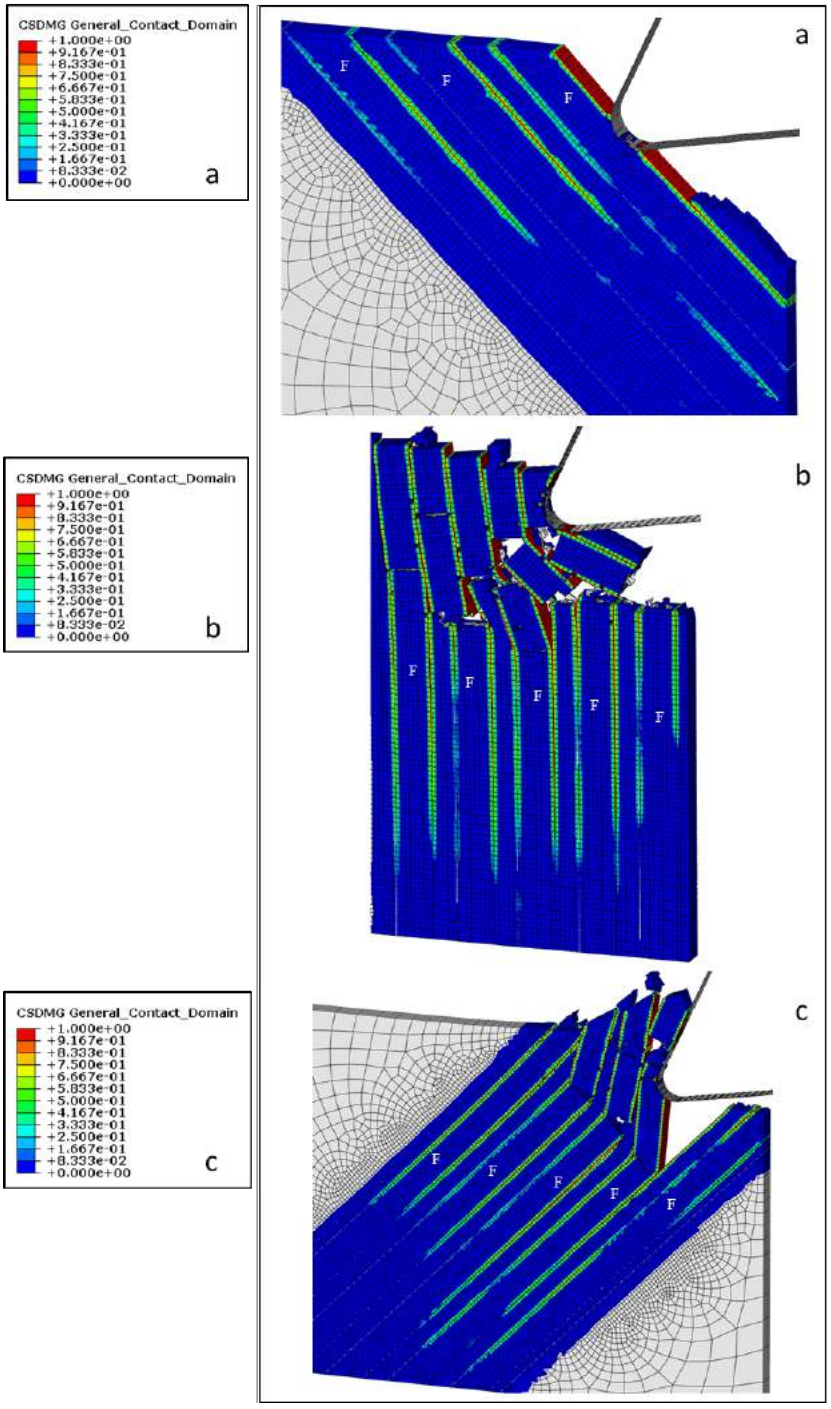

Figure 3.11: Approach 3: chip formation mechanism and cohesive damage for (a) θ=45°; (b) θ=90°; and (c) θ=135°.

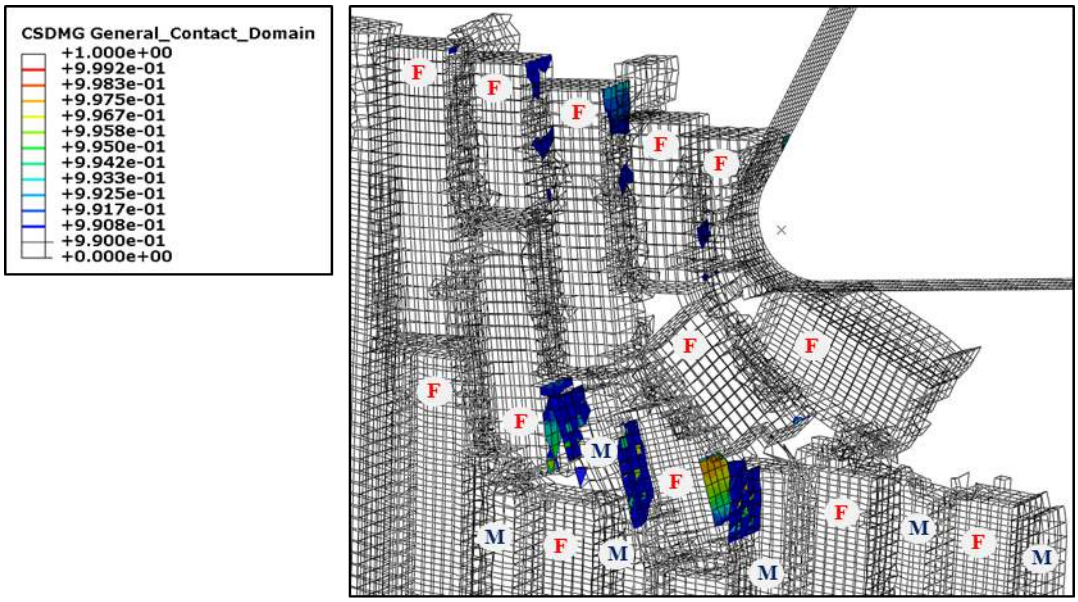

Figure 3.12: Approach 3: debonding and damage variable for fibre orientation θ=90°.

For fibre orientation θ=45°, the chip formation mechanism is similar to that observed in the previous approach. In fact, crack propagation takes place in the direction orthogonal to the fibre axis at the tool tip, with chip release due to fibre-matrix interface shear failure. In Figure 3.11(a) it is possible to observe the damage at the fibre-matrix interface taking place ahead of the tool reaching the EHM phase. However, the amount of damage experienced does not lead to debonding. Even in this case the CSDMG variable can reach high values but less than the unit leading to an absence of debonding during cutting.

For fibre orientation θ=135°, the chip formation mechanism remains similar to the previous approach. It is possible to notice that the fractures in the fibres, orthogonal to the fibre orientation, take place earlier than in the previous approach, and at the same time-step for all fibres (Figure 3.11(c)). Instead, a progressive failure propagating through the fibres towards the sample surface with the time was observed in Approach 2. Differently

from fibre orientation θ=45° and θ=90°, debonding formation is observed in the model on the right side of the second fibre with an extension of about 15 μm (Figure 3.13). This is due to the opening action exerted by the tool during its advancement until fibre failure due to bending taking place below the cutting plane.

In addition, also for θ=45° and θ=135°, interface damage extends below the cutting plane far from the tool.

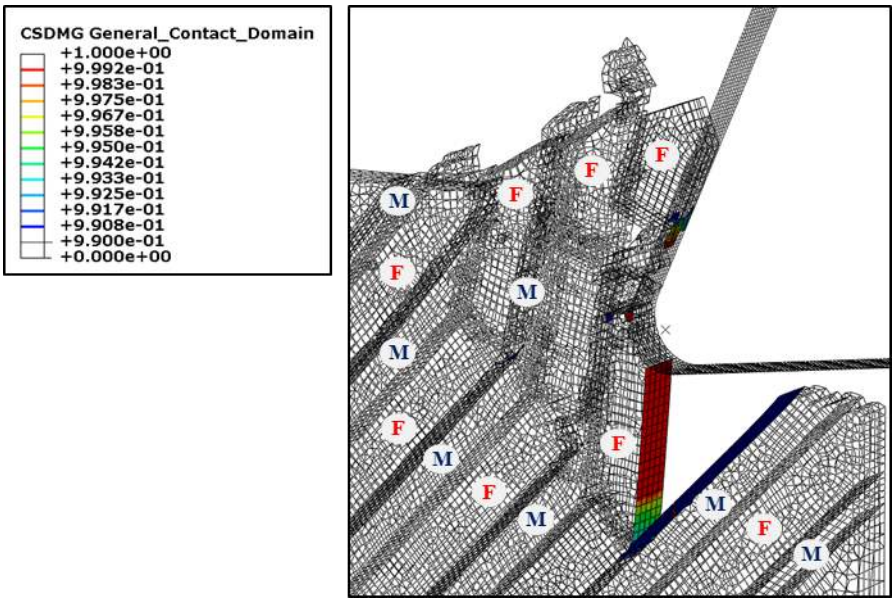

Figure 3.13: Approach 3: debonding and damage variable for fibre orientation θ=135°.

For the surface-based cohesive method the fibre orientation θ=0° was also investigated. In Figure 3.14 the configuration of the model, showing also the chip formation mechanism, at the end of the analysis is reported. During the cutting the first matrix and fibre are compressed by the tool, which also tends to lift up and bend them because of the rake angle. Conversely, the cohesive behaviour at the interface tends to keep the different phases together. The cohesive effect seems to predominate, causing failure under compression of the

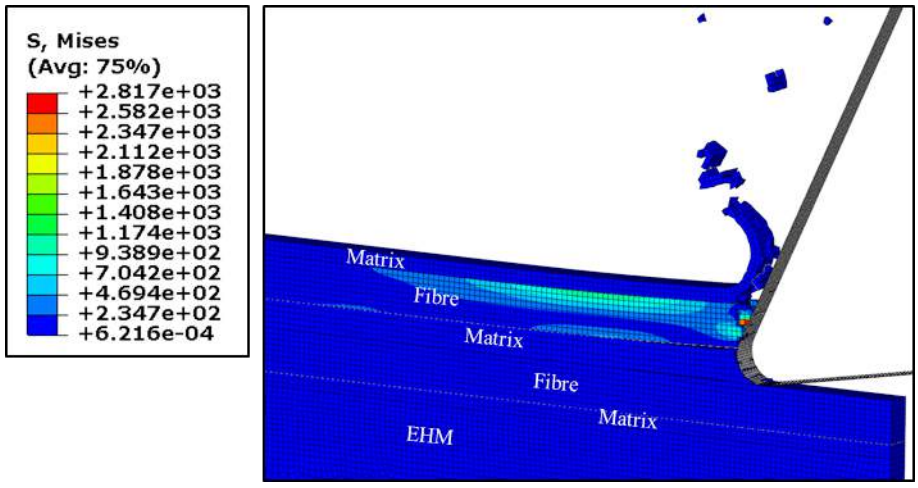

Figure 3.14: Approach 3: chip formation mechanism for fibre orientation θ=0°.

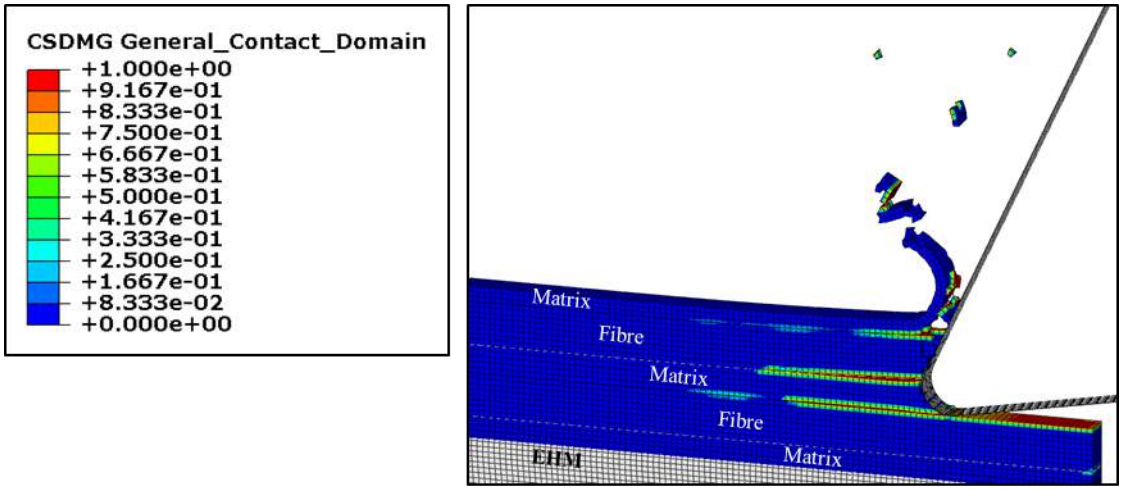

Figure 3.15: Approach 3: cohesive damage for fibre orientation θ=0°.

first brittle fibre and bending of the first ductile matrix, which tends to produce a curling chip as shown in Figure 3.14. The second matrix fails under compression, while the second fibre is weakly pushed down by the tool. The chip formation mechanism described does not represent the real chip formation mechanism during cutting. In fact, interface debonding and consequent fibre bending and fracture were expected, according to Calzada *et al.* [25]. Figure 3.15 shows the damage at the interfaces in the model. Damage extends ahead of the tool far

away from it and differently from the other fibre orientations, it remains mainly contained above the cutting plane slightly affecting the next interface. So, in this case debonding in the machined work-piece is totally absent.

3.4.4 Novel cohesive model

Despite the capacity of the surface-based cohesive method to avoid the drawbacks observed when using zero thickness cohesive elements based on the traction-separation law, difficulty in the interface behaviour analysis and debonding evaluation were experienced. Also, a general absence of debonding was detected. So, a new approach for the interface simulation was developed in order to obtain a robust interface model that can overcome the listed drawbacks.

For fibre orientation θ=90°, failure modes experienced by fibres and matrix are similar to those described in Approach 2. So, the fibres show multi-fracture failure mode due to bending stresses, and to the action of the tool that pushes the fibres against each other. The matrix failure is due to compressive stresses exercised by the surrounding fibres. Since the classical zero thickness cohesive element approach based on the traction-separation law was implemented, the cohesive elements cannot undergo compression. In this case, it does not represent a limit in the cohesive elements' behaviour because even if the surrounding matrix and fibre elements fail due to compression, the cohesive element connected with them is recognized by means of a user-defined field subroutine and is eliminated from the analysis. Therefore, results show that no excessive deformations are experienced by cohesive elements. Figure 3.16 shows the area where cohesive elements were deleted by the subroutine due to

matrix failure under compression, and the cohesive elements still active in the model near that area. The failure of the cohesive elements is similar to that described in the Approach 1, where generally the shear stress represented the main contribution to the damage initiation. Also during the damage evolution phase, the shear stress contributes mainly to the elements' failure, since the normal stress remains low.

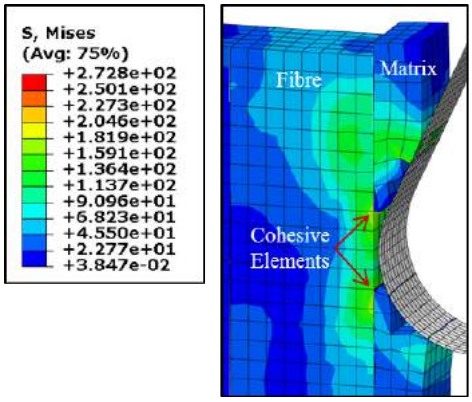

Figure 3.16: Novel Approach: cohesive elements' deletion due to surrounding element failure.

For fibre orientation θ=45°, even if the fibres and matrix failure mechanism is quite similar to that described in Approach 2, in this case the cohesive elements in the area undergoing compression remain active until a surrounding element fails. For this reason the different phases are kept together longer by the interface. The cohesive element failure in the model is mainly due to shear stresses originated during the cutting (Type III).

For fibre orientation θ=135°, as for the others fibre orientations, the failure modes in the fibres and the matrix are similar to that observed in Approach 2, where matrix failure was mainly due to compression and fibre failure to bending. Instead, the cohesive elements undergo shear and tensile behaviour, with damage initiation and failure caused mainly by shear stress (Type V).

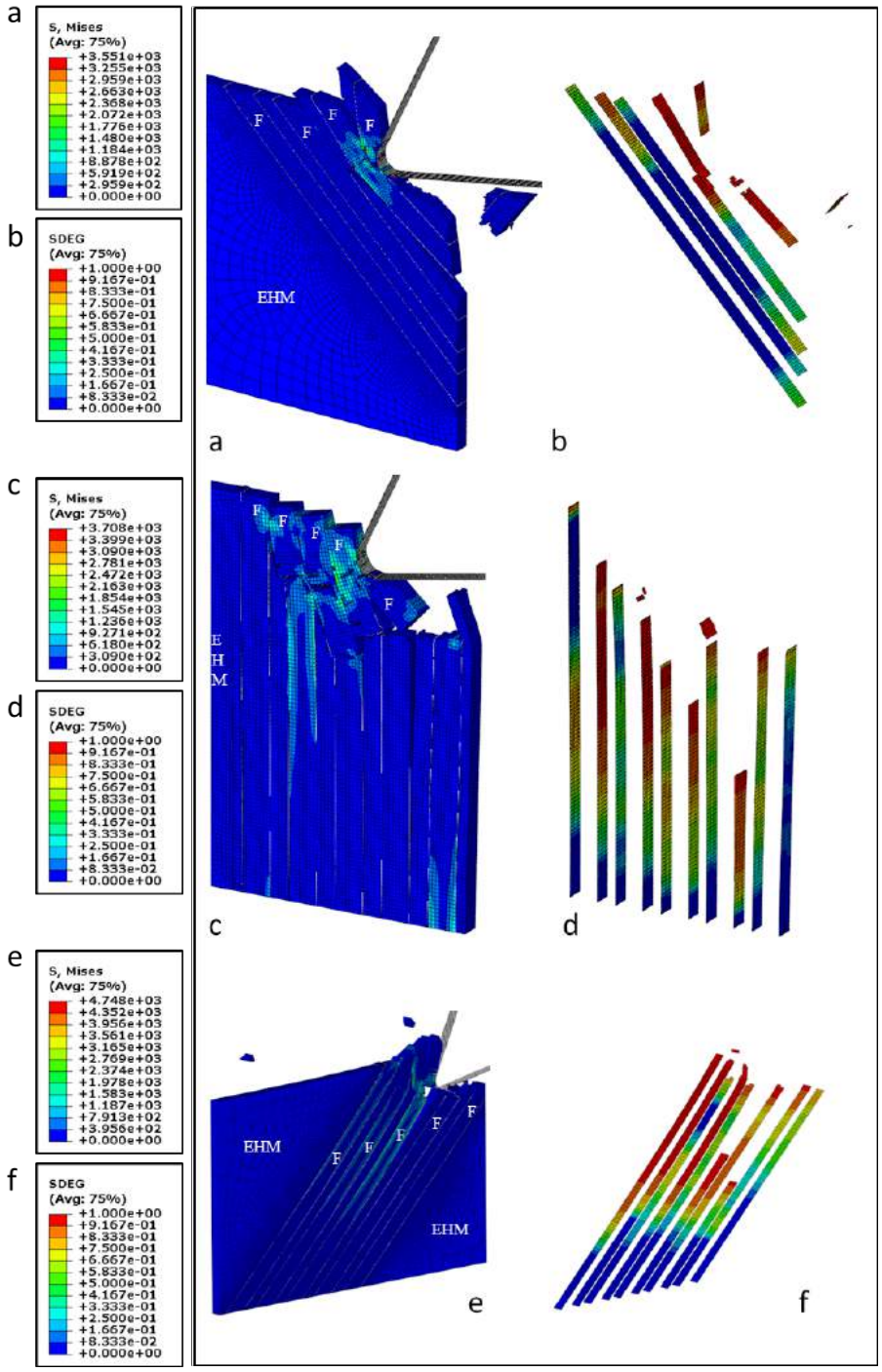

Figure 3.17: Novel Approach: chip formation mechanism and cohesive damage for (a-b) θ=45°; (c-d) θ=90°; and (e-f) θ=135°.

Figure 3.17 shows the amount of damage in the cohesive elements at the end of the analysis for θ=45°, θ=90° and θ=135°. The area affected by damage extends very far from the tool, making the interface more prone to fail if subjected to further loads during the in-service conditions.

In order to compare the Novel Approach and Approach 3, fibre orientation θ=0° was also investigated. The chip formation mechanism for the Novel Approach proposed is quite different from the previous approach, as shown Figure 3.18. Even in this case the tool tends to lift up the fibre and the matrix in contact with the tool rake face and to push down the phases located below the cutting plane. The difference with the previous approach is due to the cohesive elements' behaviour. In fact, they tend to oppose bending deformation trying to

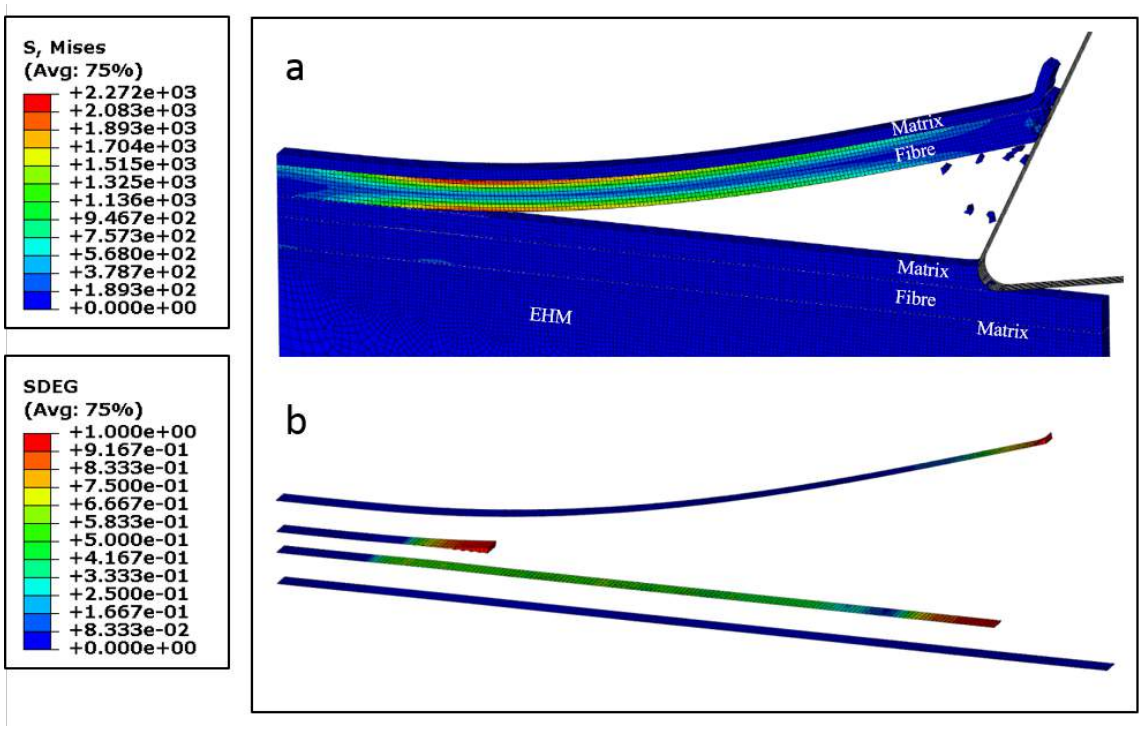

Figure 3.18: Novel Approach: (a) chip formation mechanism; and (b) cohesive damage for fibre orientation θ=0°.

keep all phases together until they reach the failure condition. The tool progression causes an increase in the bending deformation and the propagation of cohesive failure along the cutting direction. In the cohesive elements shear and tensile stresses contribute together to damage initiation and evolutions until failure with a bigger contribution of the shear for the damage initiation. The chip formation mechanism described is in agreement with findings in the literature [25, 26] and representative of Type I.

Differently from the other orientations, no damage was detected below the cutting plane in the machined material. Indeed, in the literature the absence of damage or a very small damage depth has been experimentally observed [16, 20].

Results obtained for fibre orientation θ=0° and θ=135° with the Novel Approach and Approach 3 were compared with high-speed camera images obtained by Calzada *et al.* [25] (Figure 3.19 and Figure 3.20). The chip formation mechanism observed experimentally shows a bending failure of the fibre for fibre orientation θ=0° with chip formed by fibre length between 100-150 μm. It agrees well with that obtained implementing the Novel Approach, even if fibre failure is not reached during the analysis; while Approach 3 shows a compressive fibre failure due to a strong bond between different phases.

For fibre orientation θ=135°, Approach 3 shows a depth at which the fibre failure occurs more similar to the experimental depth; while the Novel Approach agrees well in terms of the cohesive behaviour. In fact, in the latter approach, the cohesive elements' failure propagates very far from the tool as expected by the experimental results, but the fibre failure location seems to be too near to the cutting plane.

For the Novel Approach proposed it is worth calculating the amount of debonding for

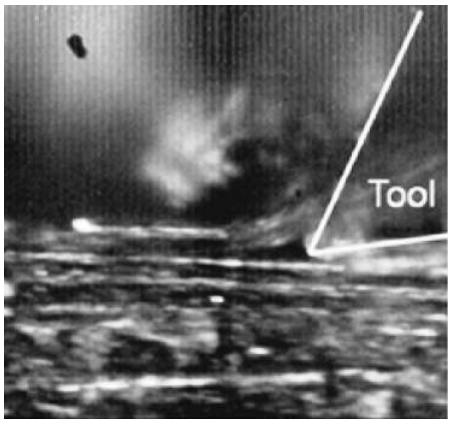

(a) Experiment

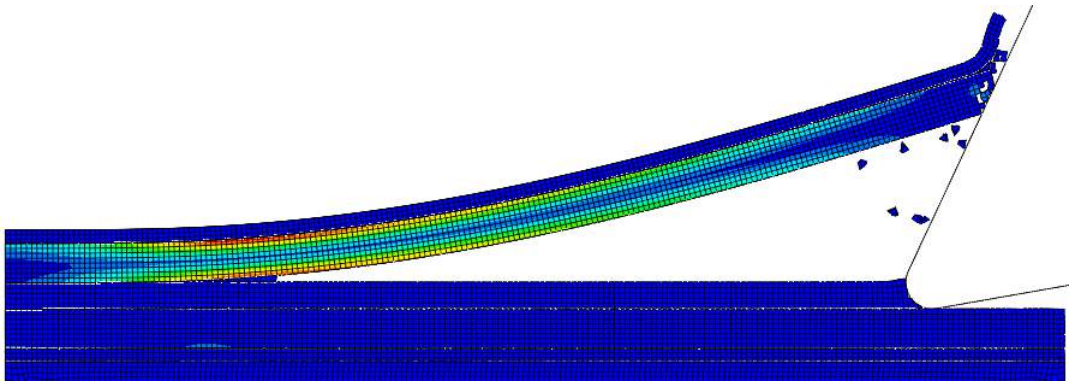

(b) Novel Approach

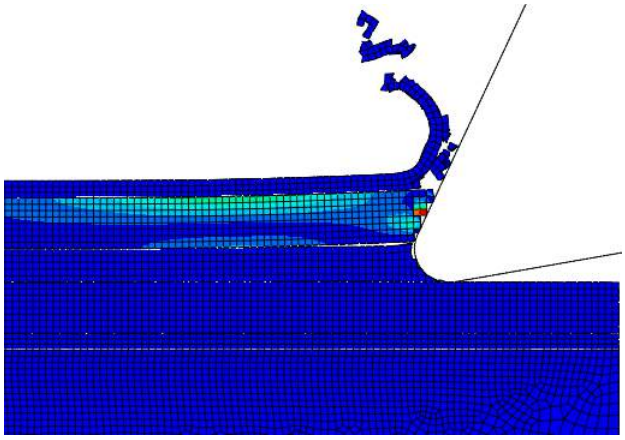

(c) Approach 3

Figure 3.19: Comparison of the chip formation mechanism for the Novel Approach, Approach 3 and experimental results [25] for fibre orientation θ=0°.

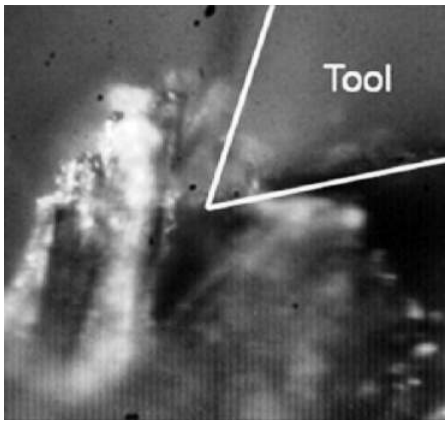

(a) Experiment

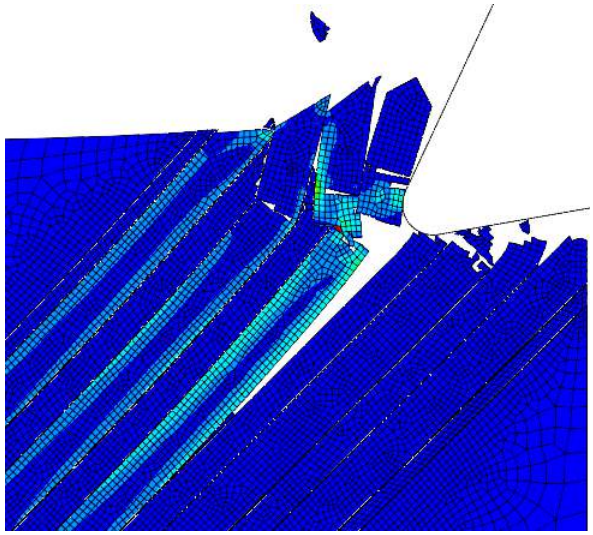

(b) Novel Approach

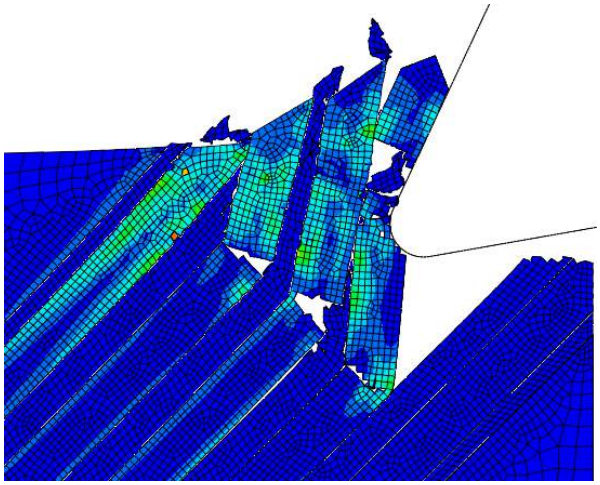

(c) Approach 3

Figure 3.20: Comparison of the chip formation mechanism for the Novel Approach, Approach 3 and experimental results [25] for fibre orientation θ=135°.

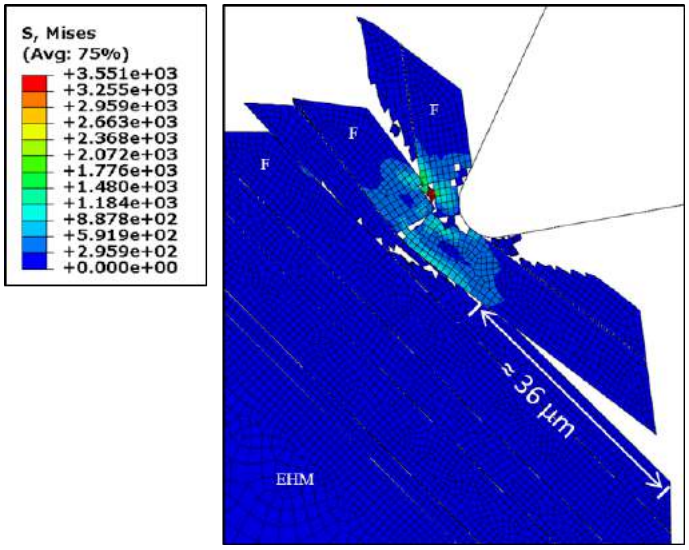

Figure 3.21: Novel Approach: maximum debonding length for fibre orientation θ=45°.

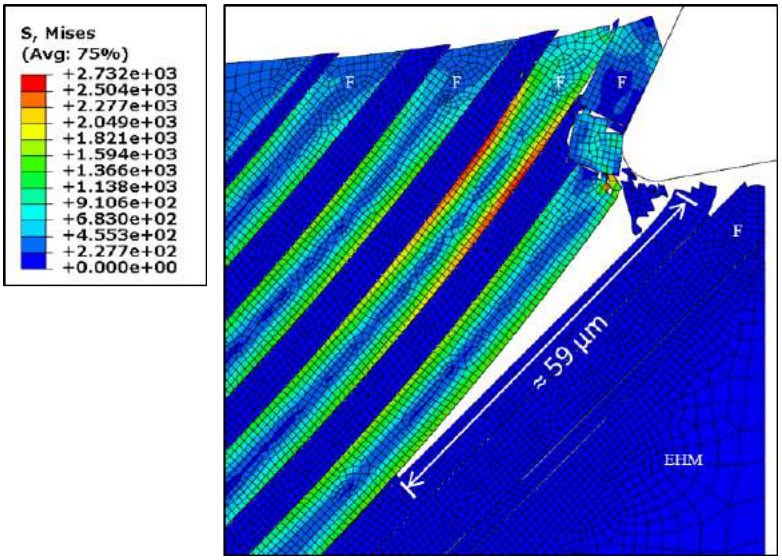

Figure 3.22: Novel Approach: maximum debonding length for fibre orientation θ=135°.

each fibre orientation. For fibre orientation θ=0°, debonding is experienced among different phases ahead of the tool, but no debonding is visible below the cutting plane, as Figure 3.18(b) shows. For fibre orientation θ=45°, θ=90° and θ=135° the maximum debonding detected during the analysis is about 36 μm, 33 μm and 59 μm, respectively, leading to subsurface damages in the machined workpiece, as shown in Figure 3.21 and Figure 3.22.

3.4.5 Validation of cutting force and thrust force

The numerical cutting force and thrust force for the Novel Approach and Approach 3 are reported and compared with the experiments carried out by Calzada *et al.* [25] in Figure 3.23 and Figure 3.24, respectively. The experimental data present a force increase for fibre orientation between θ=0° and θ=45°, and a reduction after θ=45° until θ=135°.

In both approaches the numerical cutting force and thrust force were calculated as the average value over the entire analysis for each fibre orientation, as shown in Figure 3.25 and Figure 3.26. In terms of cutting force, the Novel Approach shows closer values to the experimental data for all fibre orientations except for θ=0°. For this orientation the Novel Approach predicts a cutting force of 1.81 N/mm while Approach 3 predicts 2.24 N/mm, which is closer to the experimental value of 3.2 N/mm. The prediction of the cutting force for θ=90° and θ=135° implementing the Novel Approach is very good.

Even if both models underestimate the cutting force for θ=0° and θ=45°, the new model proposed is able to show a more similar trend to the experimental result. Differently, the thrust forces are widely underestimated for all fibre orientations independently by the approach, even if the Novel Approach seems to provide slightly better results, except for

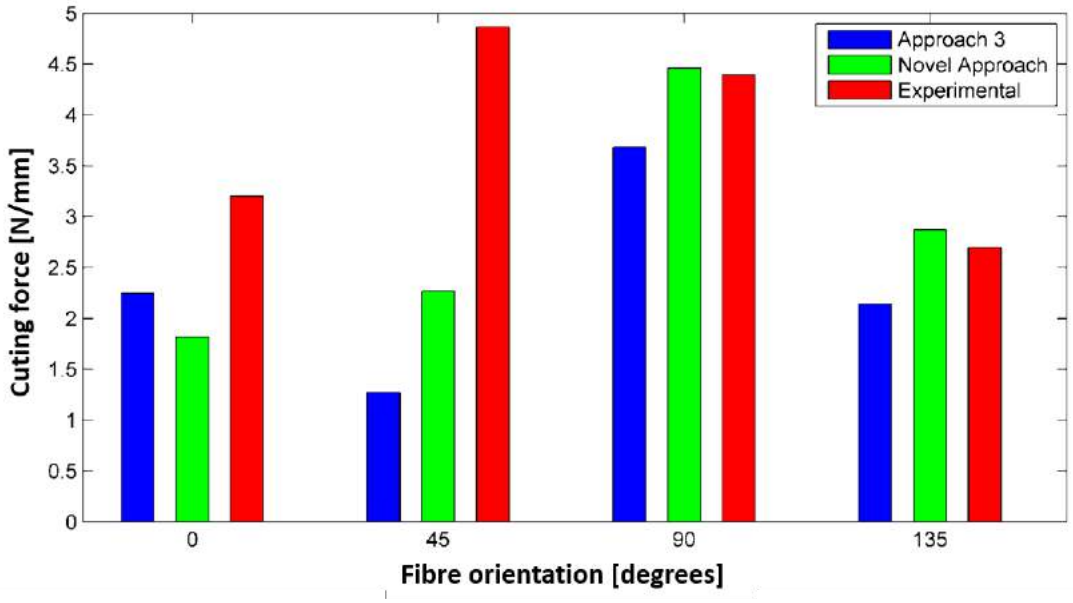

Figure 3.23: Comparison of cutting force for Novel Approach and Approach 3 against experimental results [25].

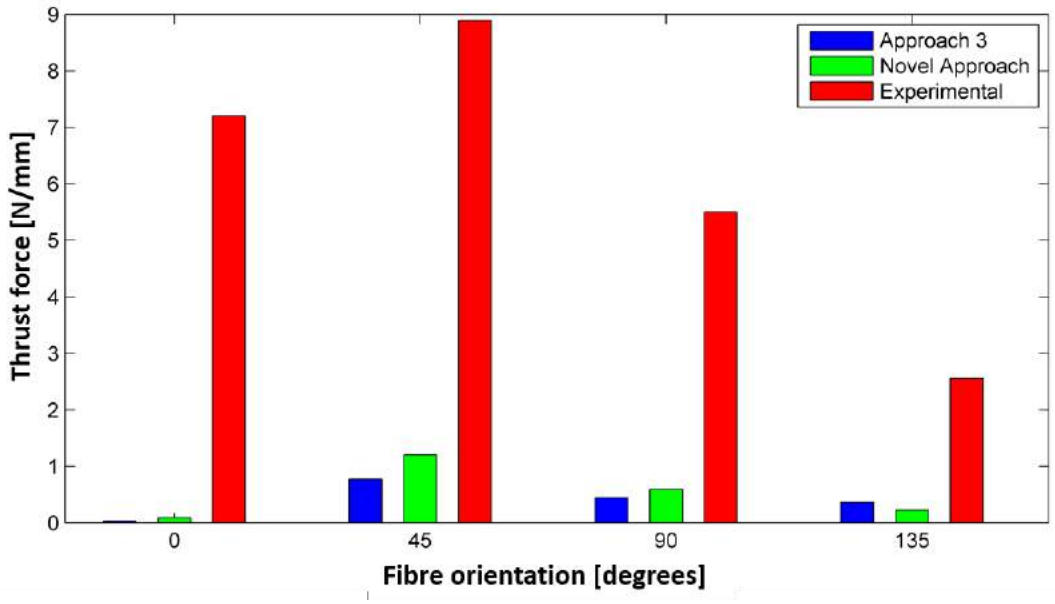

Figure 3.24: Comparison of thrust force for Novel Approach and Approach 3 against experimental results [25].

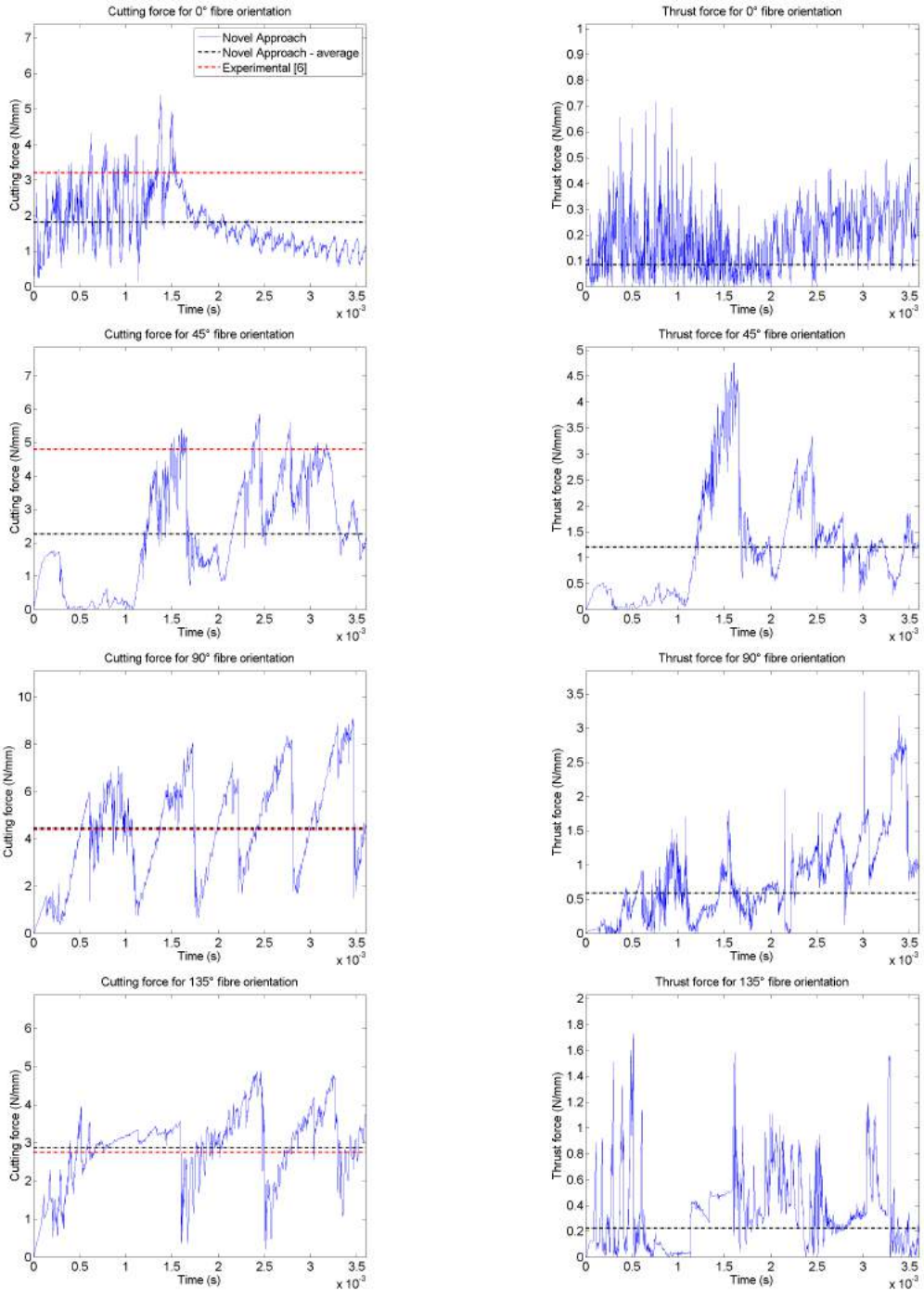

(a) *(b)*

Figure 3.25: Novel Approach: (a) cutting force; and (b) thrust force, for different fibre orientations (experimental results [25]).

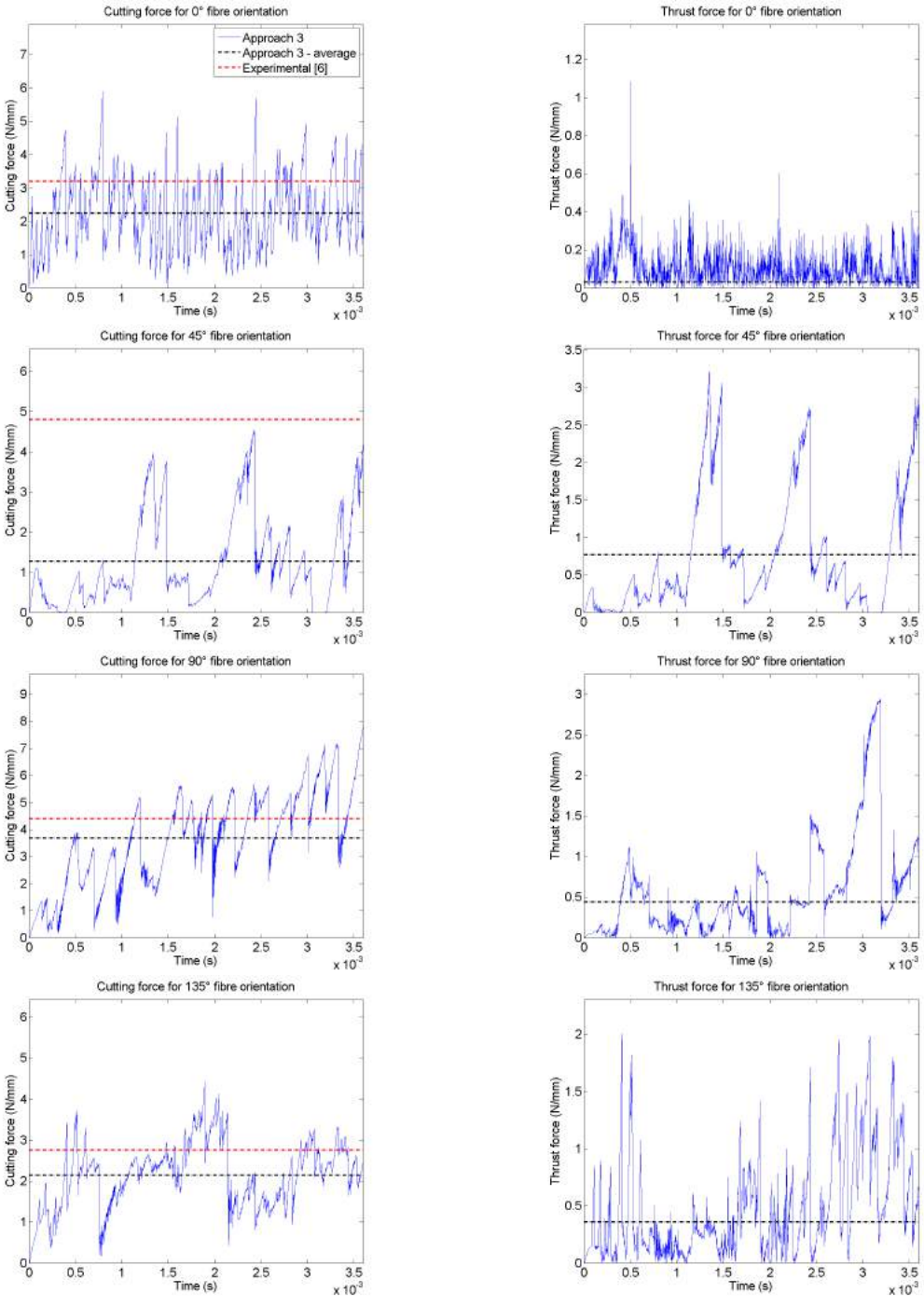

(a) *(b)*

Figure 3.26: Approach 3: (a) cutting force; and (b) thrust force, for different fibre orientations (experimental results [25]).

θ=135°. In fact, the thrust force predicted for θ=45° is 0.4 N/mm higher than that predicted using Approach 3. The difficulty in the thrust force prediction can be observed in the literature. This challenge can be explained considering that the material is divided into two regions by the tool: pressing and chipping. The material in the former region is pushed under the tool, and when the tool has passed it springs back due to the elastic recovery exerting a pressure on the clearance face, and so contributing in this way to the thrust force [24]. The difficulty in replicating this behaviour in the FEM model can explain the big gap usually observed between the experimental and numerical thrust force.

3.4.6 Analysis time and computational cost

The analysis time also represents an important factor that could contribute in the choice of the assumptions and approaches used in the simulation. For this reason the computational time, using an Intel(R) core(TM) i7-3770 CPU with 3.4 GHz and 32 GB of RAM, was calculated and compared for the Novel Approach and Approach 3 and reported in Figure 3.27. Job settings in Abaqus software were left as default options. The computational time follows a similar trend for both approaches and it is dependent on the fibre orientation, showing a considerable increase when fibre orientation θ=135° is simulated. Figure 3.27 also highlights how the Novel Approach proposed reduces the analysis time of about 12, 1.5 and 20 hours for θ=0°, θ=90° and θ=135°, respectively. Only for fibre orientation θ=45° was an increase of about 15 hours detected. Moreover, the analysis time was generally very high independent of the approach employed, despite mass scaling being used.

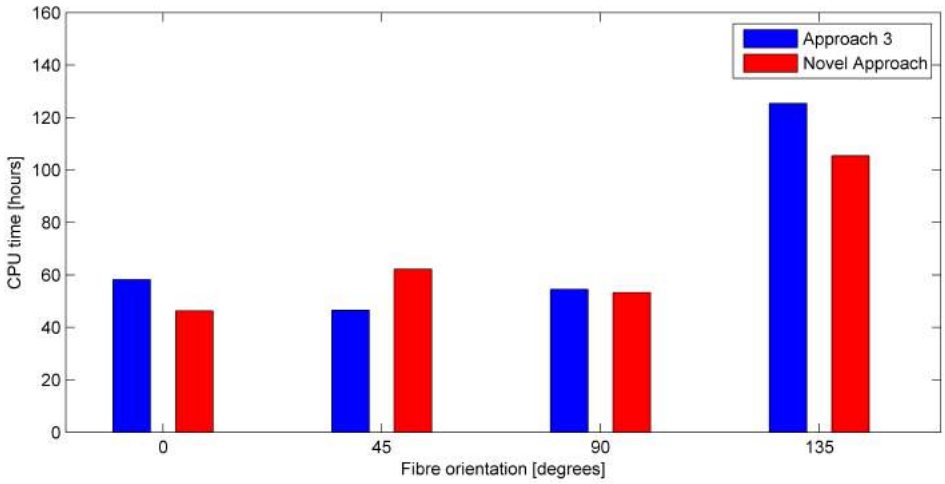

Figure 3.27: Analysis time for the Novel Approach and Approach 3.

3.5 Summary

A 3D model of the orthogonal cutting on CFRP composite material has been developed by means of a meso-scale model, introducing a new approach for the interface simulation. The interface behaviour proposed has been compared against three different approaches used in the literature for different fibre orientations:

- zero thickness cohesive elements based on the traction-separation law [63];
- cohesive elements based on the traction-separation law presenting a small thickness [81];
- surface-based cohesive behaviour [102].

Implementing Approach 1 the inability of the cohesive elements to fail under compression, and the assumption that the membrane response does not produce any stress could lead to excessive element deformation during the analysis when surrounding elements fail.

In order to include compressive behaviour until failure in the cohesive elements, a small thickness has been introduced. Approach 2 is capable of limiting the excessive deformation that cohesive elements can experience, making them fail generally before their surrounding elements. When this does not happen the cohesive elements remain in the model showing much deformation. In addition, the introduction of a thickness could not reflect the physical reality, and it could also change the chip formation mechanism.

The surface-based cohesive behaviour allows the overcoming of the drawbacks shown by previous approaches. Despite that, it makes the interface behaviour analysis very hard. Also, debonding defect formation is almost absent or very low for all fibre orientations, making the matrix-fibre link stronger when compared with cohesive elements based on the traction-separation law and high-speed camera images [25].

Among the approaches investigated, the approach that could potentially represent the real interface behaviour is Approach 1. For this reason improvements to it have been attempted; proposing a novel fibre-matrix interface behaviour. It is capable of totally avoiding excessive distortion of the cohesive elements, connecting their failure with the surrounding elements' failure.

The new approach shows that, for fibre orientation θ=0°, shear and tensile stresses contribute together to damage initiation and evolution until failure in the cohesive elements, with a bigger contribution of the shear to the damage initiation. Instead for fibre orientation θ=45°, θ=90° and θ=135° the damage initiation and failure are generally mainly caused by the shear stress.

Cutting force has also been calculated for the new approach and the approach implementing the surface-based cohesive behaviour for comparison purposes. Globally the new proposed approach shows closer values with the experimental published data [25]. The predicted thrust force has been underestimated for both approaches. This behaviour has been linked to the element deletion due to failure in the finite element model.

In addition, the novel approach shows also a lower CPU time for all simulations, except for θ=45°.

Finally, the new proposed approach can be implemented also in a 2D analysis, differently from the surface-based cohesive behaviour that requires a 3D model.

The 2D-extruded model does not represent the real geometry at micro-scale level. Therefore, in the following chapter the novel cohesive approach will be implemented in a model where cylindrical fibres are considered.

Chapter 4

Three-dimensional finite element model implementing cylindrical fibres

4.1 Introduction

In the previous chapter, a novel cohesive model was developed and compared with those published in the literature. The Novel Approach showed its ability to overcome the drawbacks of existing models. To this end, a 2D-extruded model was used. It presents fibre and matrix having a parallelepiped shape that does not represent the real geometry of the component. Therefore, a three-dimensional FE model, having cylindrical fibres, and deploying the novel cohesive model presented in the previous chapter is developed and presented in the following sections.

4.2 Development of the three-dimensional finite element model

The three-dimensional finite element model was developed in the same manner as the 2D-extruded model, implementing a meso-scale approach in order to simulate the composite material. The material properties and model parameters' set-up remain the same, as reported in Table 3.1 and Table 3.2. Only the geometry was modified in order to be more realistic, implementing cylindrical fibres. The novel cohesive model developed in the previous chapter was implemented. The depth of cut was set to 15 μm. In order to reduce the computational time, the developed model considered half of the fibres' geometry, assuming the symmetry.

A schematic of the FEM model and of the boundary conditions applied are reported in Figure 4.1. Unlike the 2D-extruded model, it is possible to notice that the fibre is totally embedded in the matrix, and the cohesive elements surrounding the fibre are no longer aligned in the same direction.

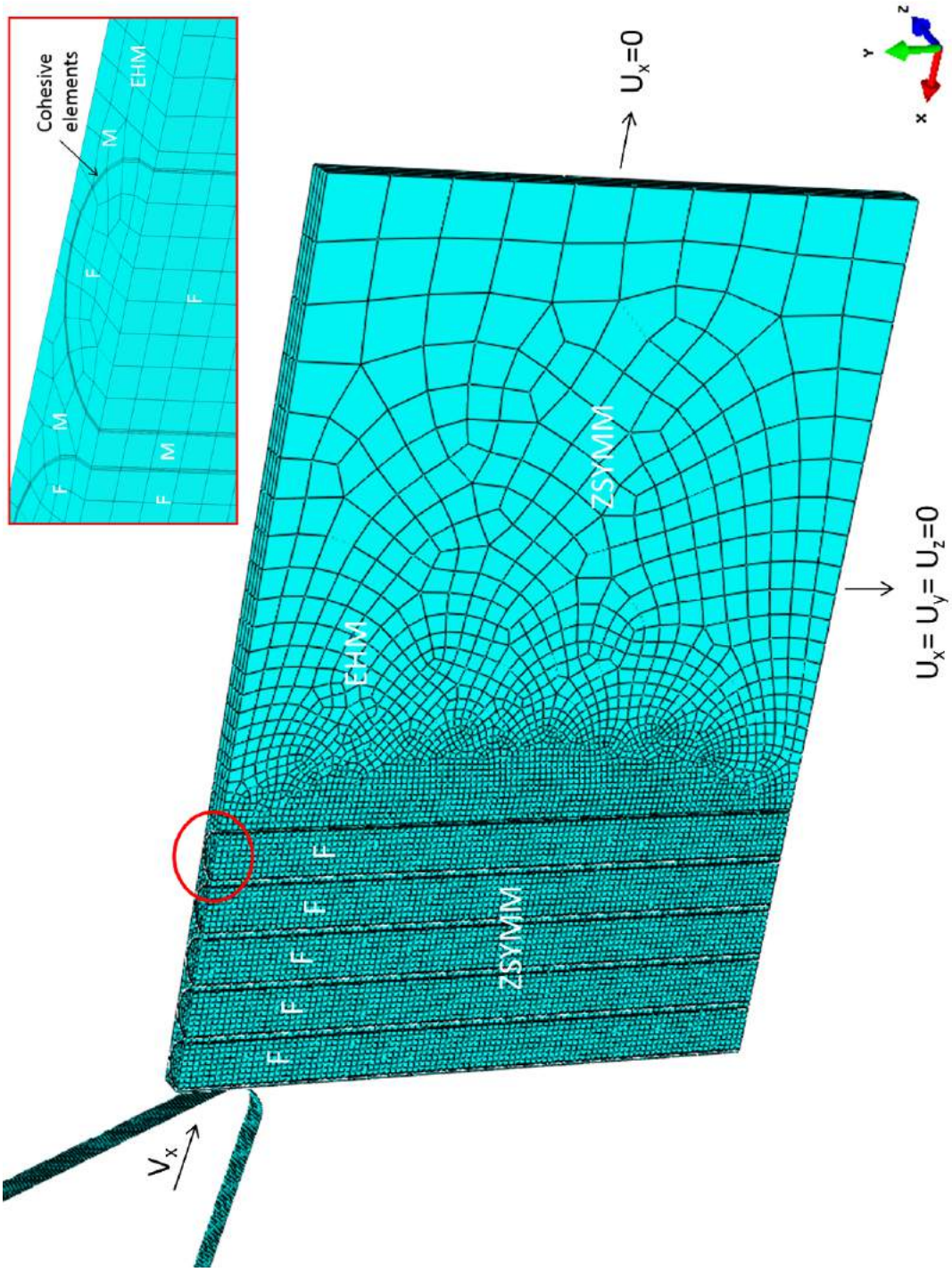

(a)

Figure 4.1: Schematic of the three-dimensional FEM model for fibre orientation θ=90°with applied boundary conditions.

4.3 Results and discussion

Different fibre orientations were simulated (θ=0°,45°,90°,135°) in order to study machining forces, the chip formation mechanisms and damages in the workpiece during orthogonal cutting of UD-CFRP. The model was validated against experiments carried out by Calzada *et al.* [25] and compared with results obtained in the previous chapter for the 2D-extruded model. Since the majority of the models in the literature are two-dimensional, the comparison is also able to highlight the degree of reliability of such models.

4.3.1 Chip formation mechanisms and damage at various fibre orientations

For fibre orientation θ=0°, a model implementing three fibres, having length of 200 μm, was developed. Below them, an EHM phase was positioned in order to introduce the necessary stiffness (Figure 4.2).

As in the previous chapter, the SDEG variable, representing the overall value of the scalar damage, and the QUADSCRT variable, indicating the damage initiation condition, can be used to study the cohesive behaviour during machining (Figure 4.3).

Similar to the 2D-extruded model, damages in the workpiece remain close to the trim plane. A small amount of subsurface damages was observed ($\sim$5 μm). Due to the change in geometry, cohesive elements behave differently when compared with the 2D-extruded model. They experience damage initiation far ahead of the tool, as visible in Figure 4.3. However, they fail only when they come close to the tool, due to surrounding element failure. In the

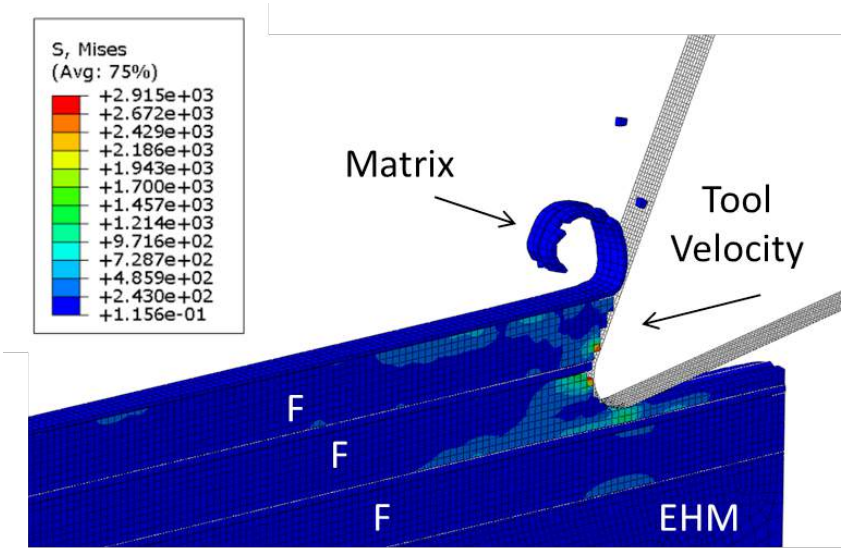

Figure 4.2: Model configuration during cutting for fibre orientation θ=0°.

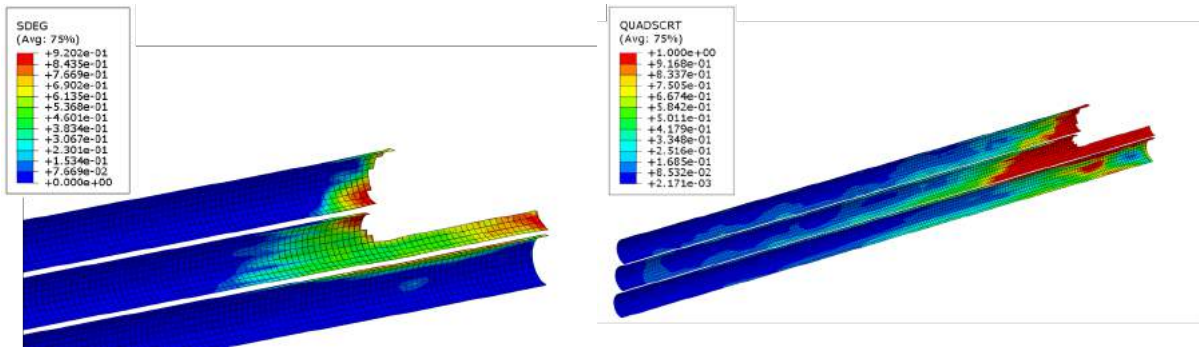

(a) *(b)*

Figure 4.3: (a) Overall value of scalar damage SDEG; and (b) damage initiation variable QUADSCRT for cohesive elements at fibre orientation θ=0°.

2D-extruded model, cohesive elements separated completely the fibre from the matrix, and they were all oriented in the same direction. Hence, tool action, which tended to lift the fibres, mainly produced an opening load type for all cohesive elements. With cylindrical fibre geometry, the action exerted by the tool is absorbed diversely by each cohesive element depending on its location. In fact, the cohesive elements' location causes a variation in the cohesive elements' thickness directions, as shown in Figure 4.4. Cohesive elements C_1 and

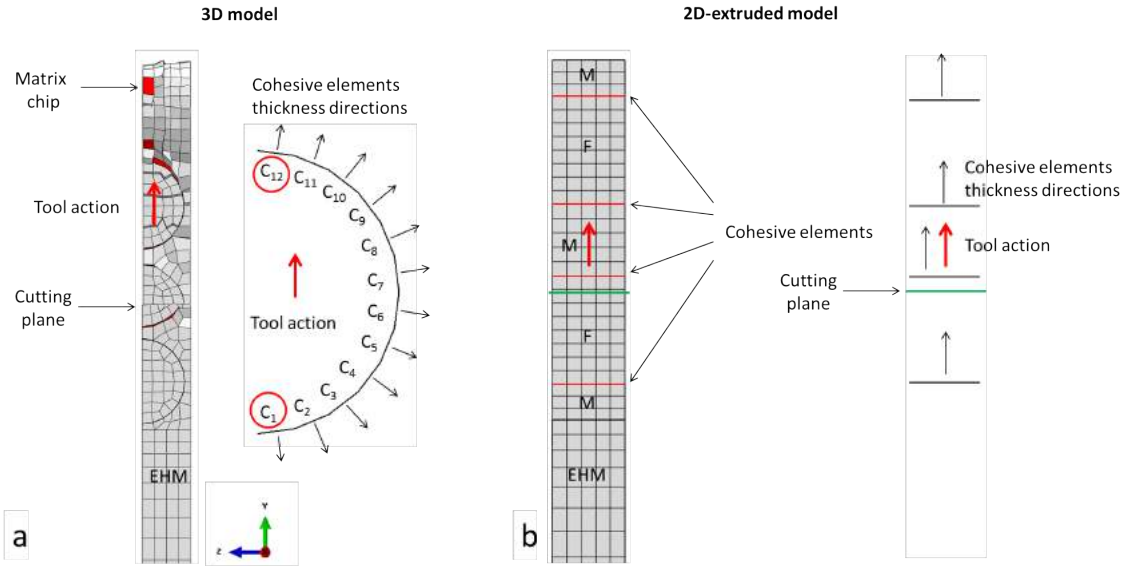

Figure 4.4: Tool action exerted on cohesive elements, and cohesive elements configuration for (a) 3D model; and (b) 2D-extruded model.

C_{12}, highlighted in red, are the cohesive elements which during cutting experience the most similar deformation to those in the 2D-extruded model.

In addition, since the fibre is surrounded by the matrix, debonding is not enough to make the fibre free to bend. In the 2D-extruded model phases were totally separated and arranged sequentially. Finally, damage initiation is visible for cohesive elements below the machined surface, reaching a higher depth compared to the 2D-extruded model. In fact, due to the cylindrical geometry of the cohesive zone, damages propagate $\sim$11 μm deeper in the workpiece. Differently, in the 2D-extruded model they mainly propagated ahead of the tool since they were represented by a flat layer between the matrix and the fibre.

Variation of cohesive element behaviour causes a change in the fibre failure as visible in Figure 4.2. In fact, it is due to compression exerted by the tool instead of bending. Matrix crushing is also observed, with curling chip formed by a thin matrix material, once the fibre

elements are deleted during tool advancement. This material removal mechanism differs from Type I, which is the expected type. This could be due to deletion of elements once the failure criterion has been reached. Variable PEEQ, representing the equivalent plastic strain, was considered to analyse the matrix condition after machining (Figure 4.5). Plastic deformation remains close to the cutting plane, reaching a few micrometres in depth. In the 3D model, the matrix is represented by a single continuous phase, in which fibres and cohesive elements are embedded. Hence, damages can propagate easier compared with the 2D-extruded model, where the matrix was represented by different separated phases, each one positioned between two consecutive fibres.

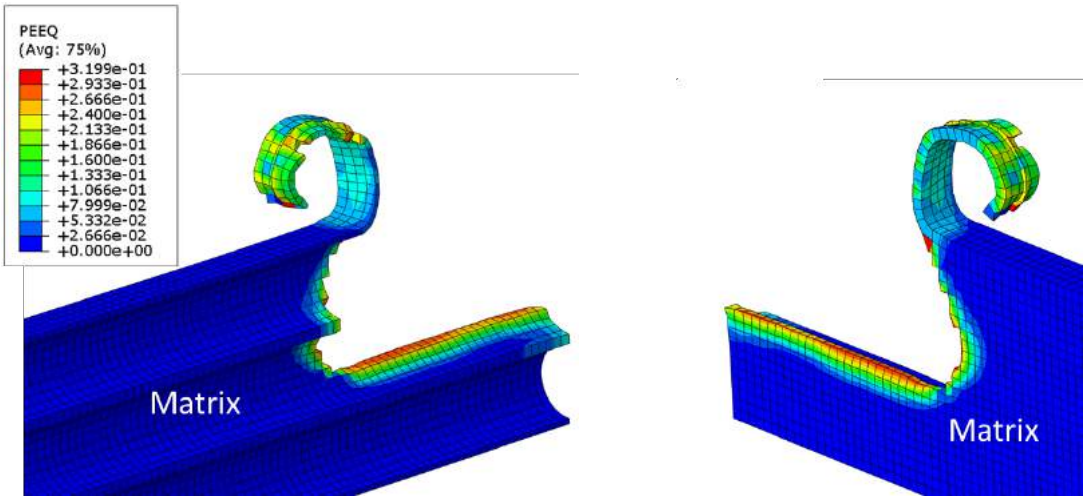

(a) Fibre side *(b) Matrix side*

Figure 4.5: Equivalent plastic strain in the matrix when machining at fibre orientation θ=0°.

For fibre orientation θ=45°, configuration of the model during cutting is reported in Figure 4.6, where the chip formation mechanism can be observed. Due to tool advancement, a crack propagates from the contact point across the fibre, orthogonally to the axis (Figure 4.6(a)). Further tool displacement causes a fibre failure due to compression with fibre release along its

axis (Figure 4.6(b)). Matrix crushing takes place between two consecutive fibres and at the contact point with the tool. During tool advancement less bending deformation is observed in the fibres compared with the 2D-extruded model. In fact, in the latter, debonding was observed starting from the vertical free edge of the sample and propagating towards the tool-fibre contact point, due to fibre bending. Instead in a 3D model, the material becomes more compact, producing a cleaner cut.

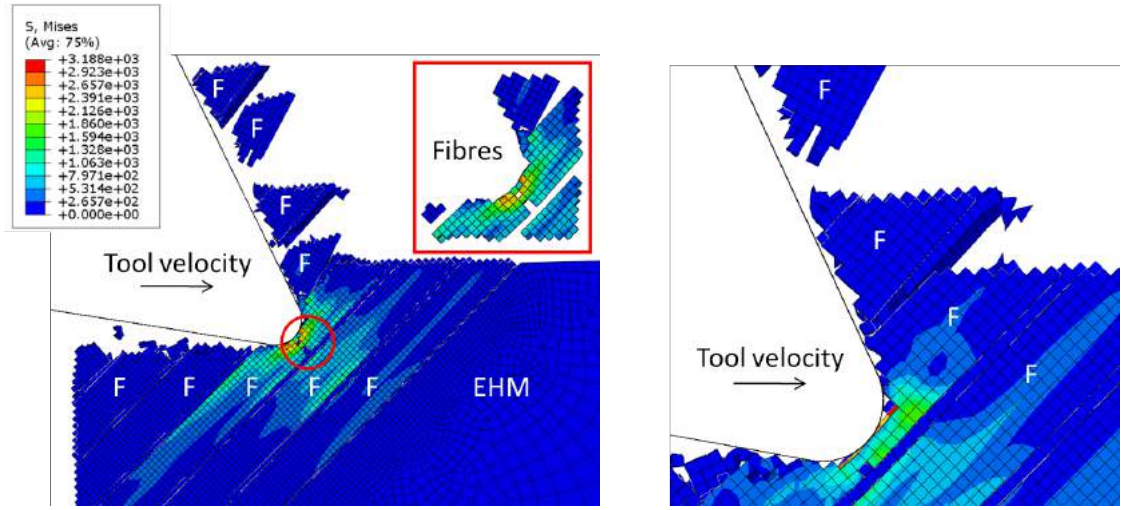

Figure 4.6: (a) Model configuration during cutting; and (b) tool tip - workpiece interaction for fibre orientation θ=45°.

Variable PEEQ was considered to analyse the matrix condition after machining (Figure 4.7). It is possible to observe that plastic deformations extend below the cutting plane, reaching a maximum depth (∼4.2 μm) between two consecutive fibres. Plastic deformations are also visible ahead of the cutting tool, which start from the tool tip and propagate along the fibre axis due to the shear.

The cohesive elements' behaviour during cutting is shown in Figure 4.8. Due to tool

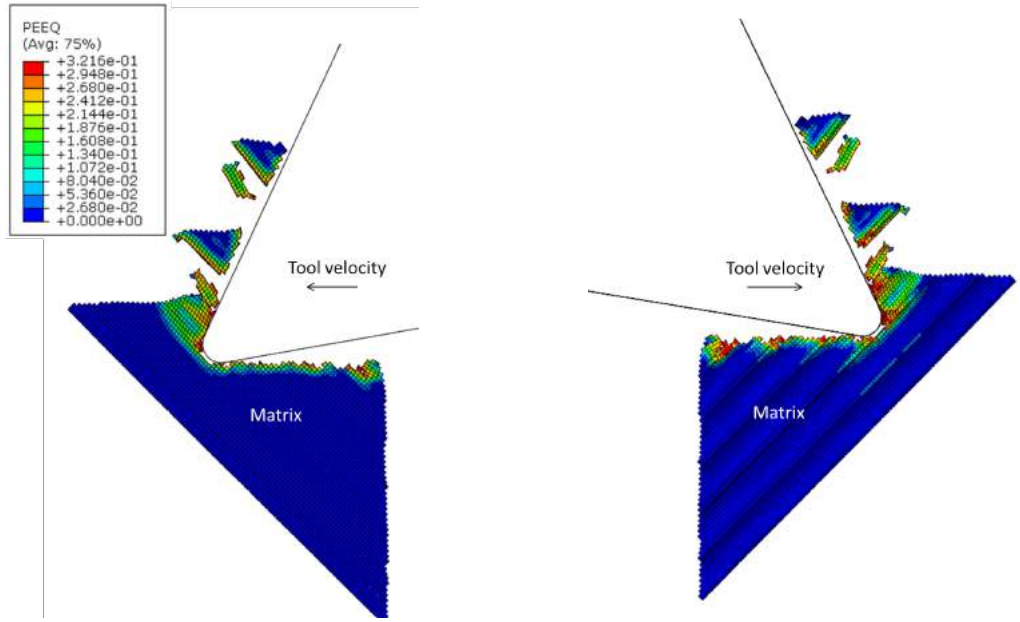

(a) Matrix side *(b) Fibre side*

Figure 4.7: Equivalent plastic strain in the matrix when machining at fibre orientation θ=45°.

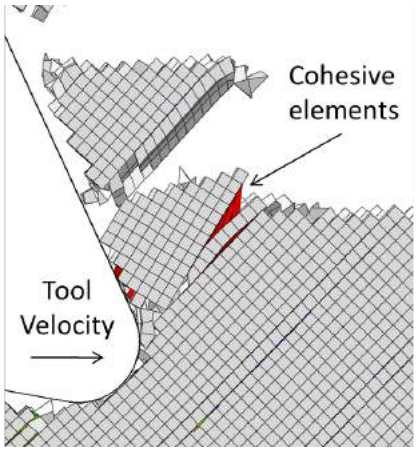

Figure 4.8: Cohesive elements' behaviour during cutting at fibre orientation θ=45°.

advancement, fibres undergo displacement along their axis. Hence, cohesive elements experience shear and normal deformation until failure, which is mainly due to the former. This behaviour, identified as Type III, is similar to that observed in the 2D-extruded model (Figure 3.17(a-b) and Figure 3.21).

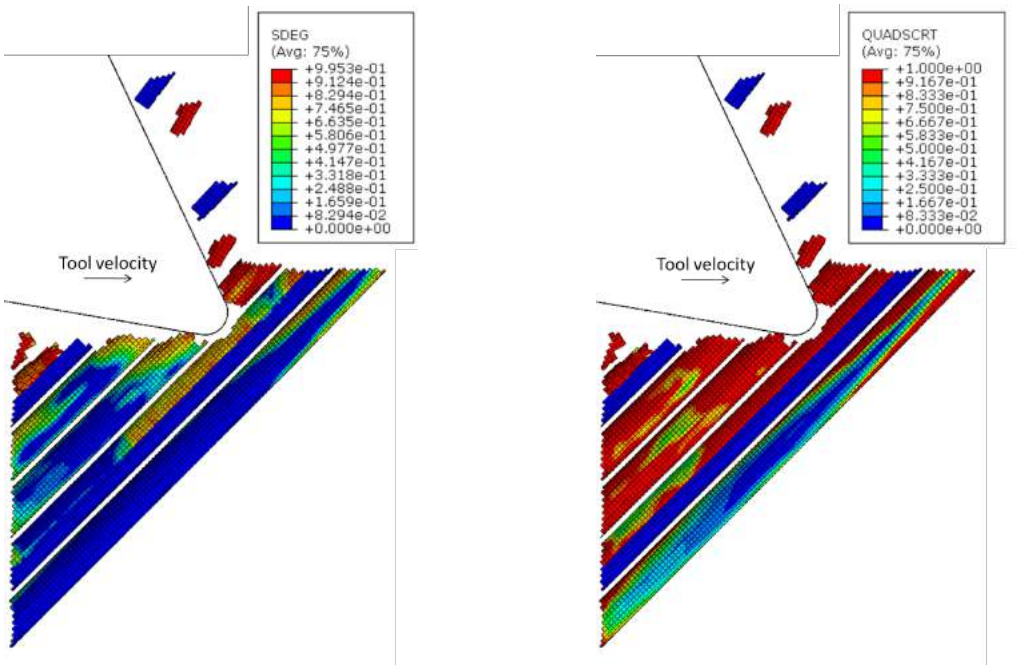

(a) *(b)*

Figure 4.9: (a) Overall value of scalar damage SDEG; and (b) damage initiation variable QUADSCRT for cohesive elements at fibre orientation θ=45°.

Fibre-matrix interface damage below the cutting plane can be observed in Figure 4.9. It is due to the normal and shear deformations they undergo during cutting. It is worth noticing that, except for small zones, the values assumed by the QUADSCRT variable are very high almost everywhere, being equal or close to unity. It highlights how almost all cohesive elements present in the model experience or are very close to experiencing damage. However, only a few cohesive elements fail below the cutting plane. Whereas a large amount of cohesive elements below the cutting plane were deleted from the analysis due to fibre bending in the 2D-extruded model.

The chip formation mechanism when machining at θ=90° is shown in Figure 4.10. The cylindrical geometry of the fibres strongly affects the material removal mechanism when

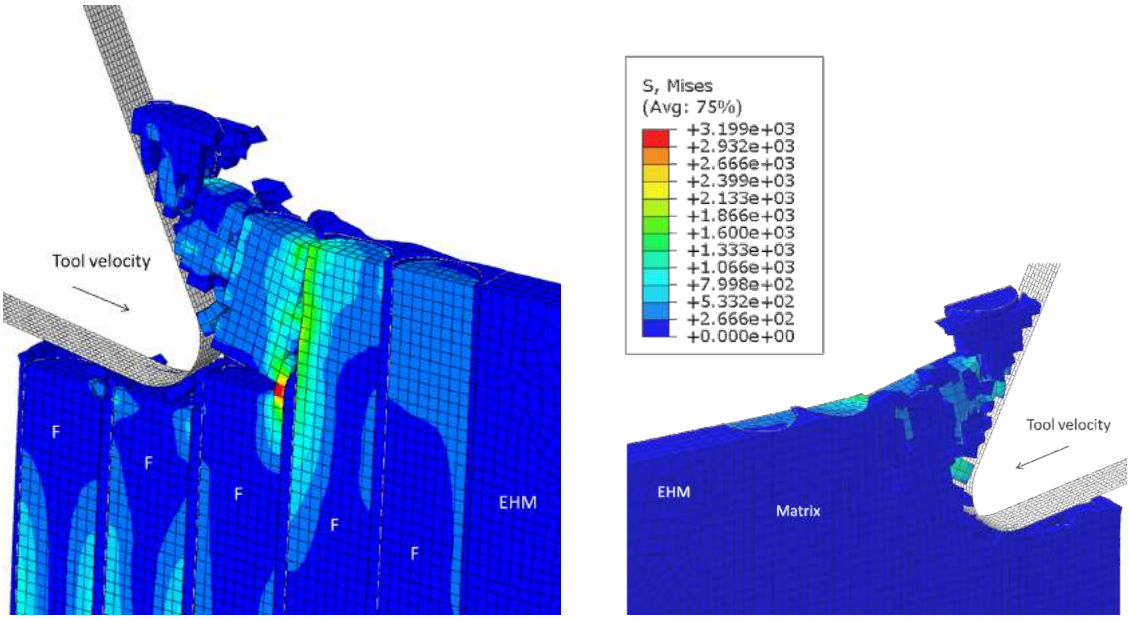

(a) Fibre side *(b) Matrix side*

Figure 4.10: Model configuration during cutting for fibre orientation θ=90°.

compared with the 2D-extruded model. In fact, in the latter, the fibre failure was mainly due to bending stresses arising in the fibres during tool advancement below the cutting plane. Multi-fracture was experienced also due to the compression exerted by the tool at the contact point. When a 2D-extruded model was considered, different phases were located sequentially, and during cutting the tool encountered them one after another singularly. In contrast, in a proper 3D model the fibre is embedded in the matrix. Hence, all phases interact at the same time with the tool, the fibre being totally surrounded by matrix and connected to it by means of cohesive elements. This change makes the material more compact experiencing a cleaner cut. Crack formation takes place at the contact point with the tool. It propagates in a direction orthogonal to the fibre axis, cutting the fibre into two parts. Due to tool advancement, the upper part of the cracked fibre is lifted and compressed against the next fibre, experiencing further compression failure and forming the chip. No bending failure was

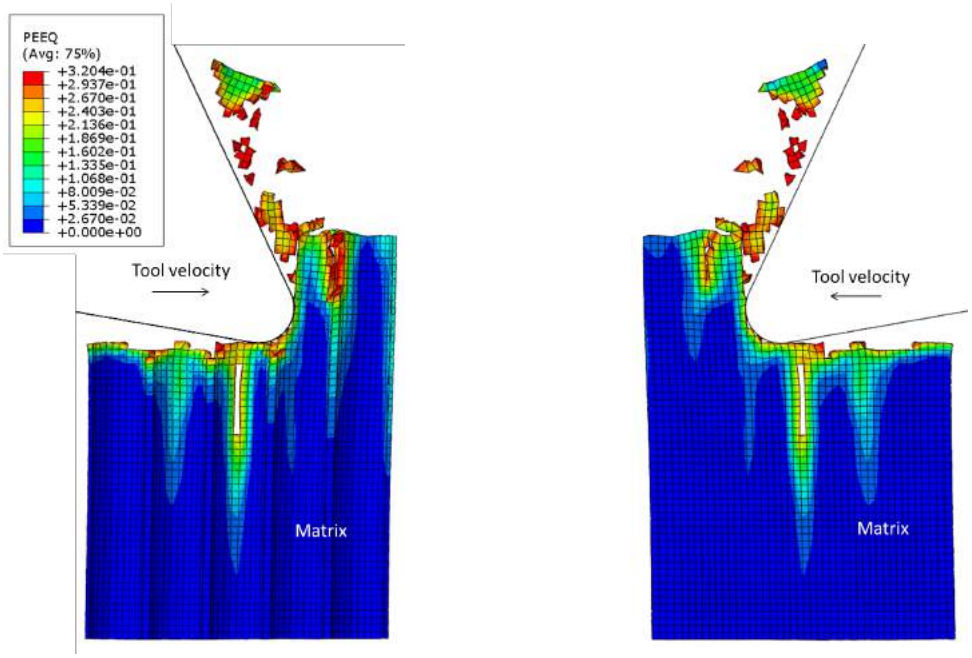

(a) Fibre side *(b) Matrix side*

Figure 4.11: Equivalent plastic strain in the matrix when machining at fibre orientation θ=90°.

observed. This behaviour better represents the expected chip formation mechanism, typical of Type IV.

Matrix failure is due to compression. A crack extending vertically for ∼10 μm corresponding to the third fibre can be observed in Figure 4.11. The PEEQ variable shows how plastic deformations are experienced by the matrix far below the trim plane (∼30 μm) after machining and ahead of the cutting tool. However, elements representing the matrix fail mainly above the cutting plane. In the 2D-extruded model the matrix elements' failure extended far below the tool (∼21 μm) due to fibre bending failure below the cutting plane.

The cohesive elements' damage after machining is reported in Figure 4.12. Damage depth reaches almost the end of the finite element model, hence having a length of about 100 μm. However, the variable SDEG generally does not reach the unitary value, so debonding is not

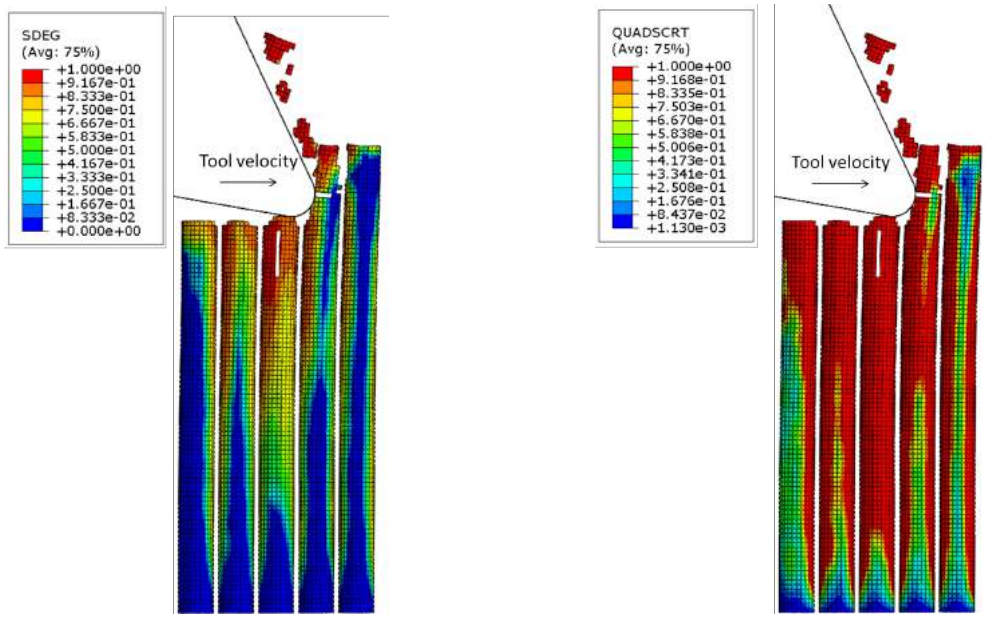

(a) *(b)*

Figure 4.12: (a) Overall value of scalar damage SDEG; and (b) damage initiation variable QUADSCRT for cohesive elements at fibre orientation θ=90°.

generated.

During machining, cohesive elements undergo shear, as shown in Figure 4.13. However, cohesive elements' failure is caused by surrounding element failure. Differently, in the 2D-extruded model cohesive failure was mainly due to shear; cohesive element deletion below the cutting plane was also due to the large amount of fibre and matrix failure.

The chip formation mechanism for fibre orientation θ=135° is shown in Figure 4.14. The cutting tool engages the fibre causing bending deformation until failure. Fibre fracture occurs a few micrometres below the trim plane. Due to matrix compression failure, two consecutive fibres come into contact. In particular, the upper part of the fractured fibre pushes against the top part of the next fibre, causing a crack formation at a higher position. Hence, the crack propagates orthogonally to the fibres' axis towards the free surface of the sample. At

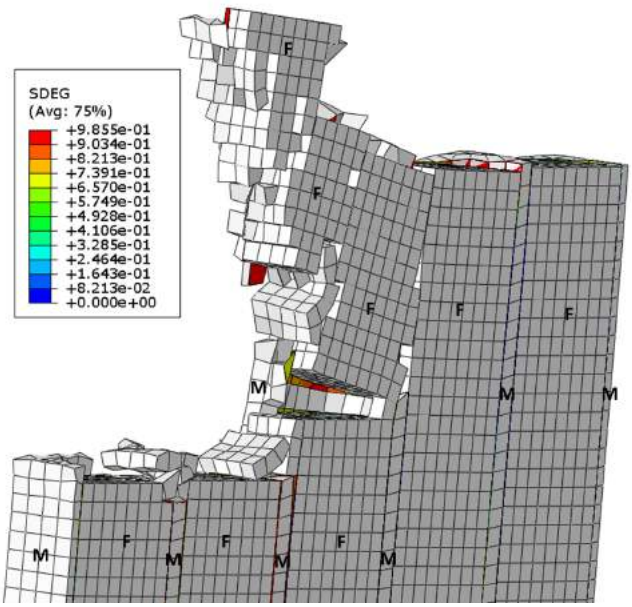

Figure 4.13: Cohesive elements' behaviour during cutting at fibre orientation θ=90°.

the end of the analysis a crack is visible below the cutting plane in the fourth fibre. It is due to further bending caused by tool advancement in the already fractured fibre.

Due to fibre bending and to the pushing action of the tool, debonding takes place at the fibre-matrix interface, as shown in Figure 4.15. The cohesive elements fail sequentially with fibre bending increase, with damage extending deeper in the workpiece. Information on damage experienced by cohesive elements is reported in Figure 4.16. Damage extends along the fibre direction deep in the workpiece (∼48 μm below the cutting plane) similarly to the 2D-extruded model (∼66 μm), as visible in Figure 3.17(e) and Figure 3.22. In the 3D model a maximum debonding length of ∼17 μm was observed, which was smaller than that measured in the 2D-extruded model (∼59 μm).

Matrix failure and plastic deformations after machining are shown in Figure 4.17. Matrix failure due to compression takes place between two consecutive fibres above the cutting plane.

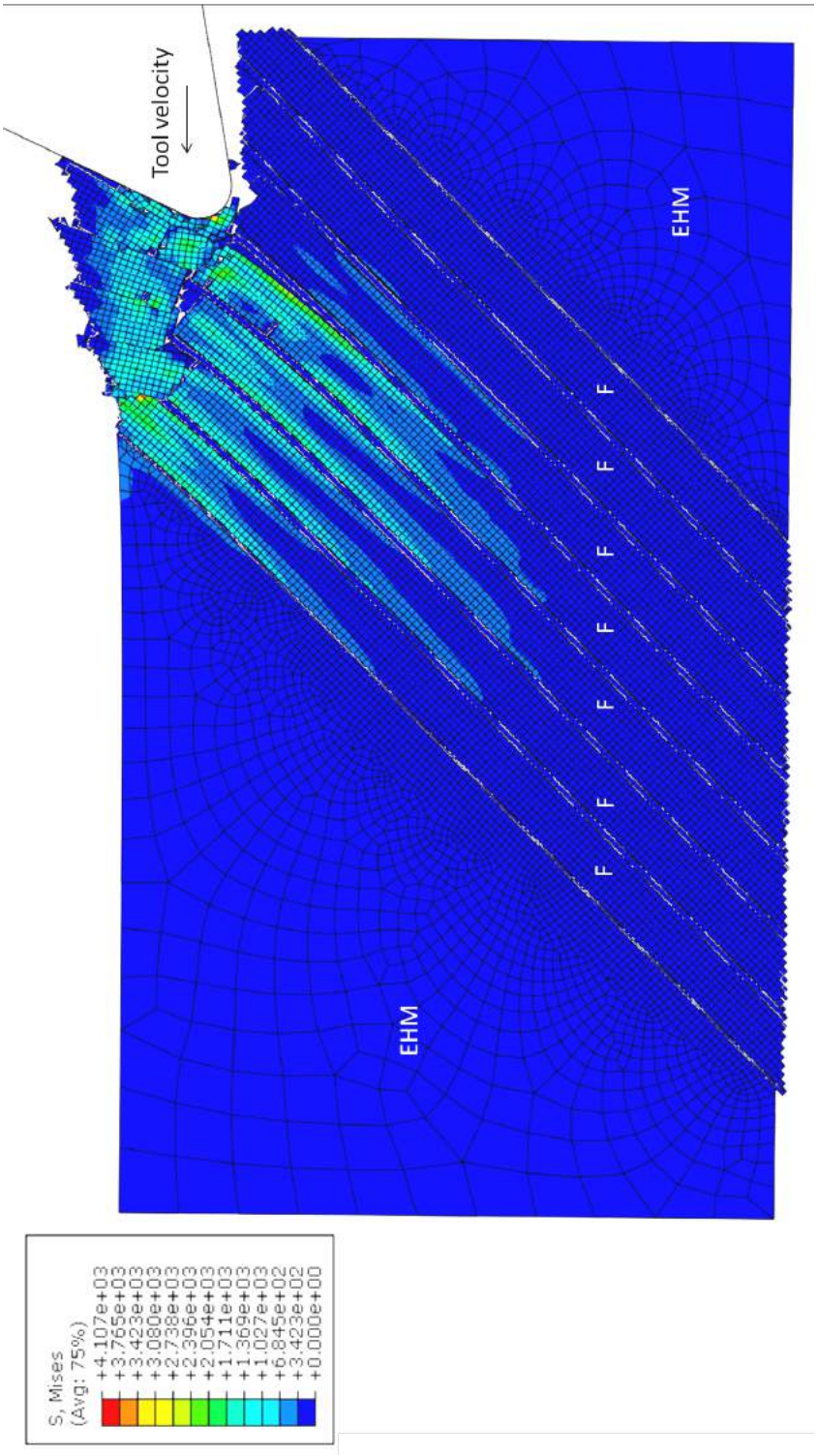

Figure 4.14: Model configuration during cutting for fibre orientation θ=135°.

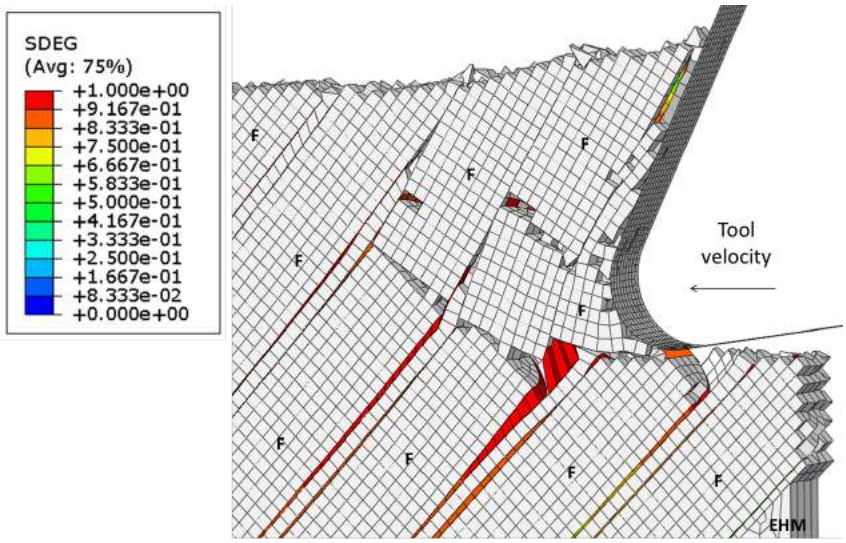

(a)

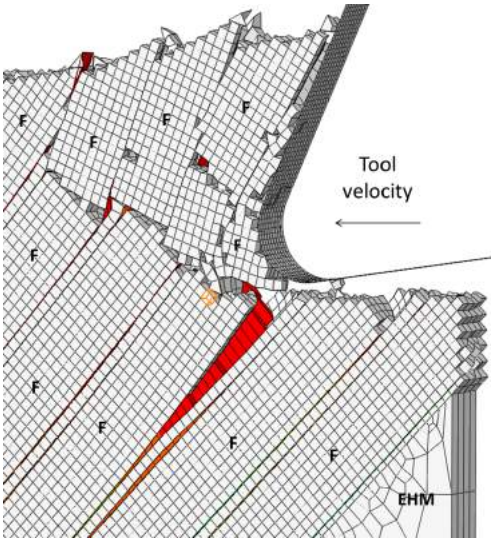

(b)

Figure 4.15: Debonding when machining at fibre orientation θ=135° at time-step (a) 2.56e-3 seconds; and (b) 2.87e-3 seconds.

Due to fibre bending, a region where the matrix experiences tensile failure is visible below the cutting plane, generating a crack that penetrates deep in the workpiece (∼12 μm below the cutting plane). Since in the 2D-extruded model the matrix was composed of more phases, each positioned between two consecutive fibres, tensile failure was very difficult to originate.

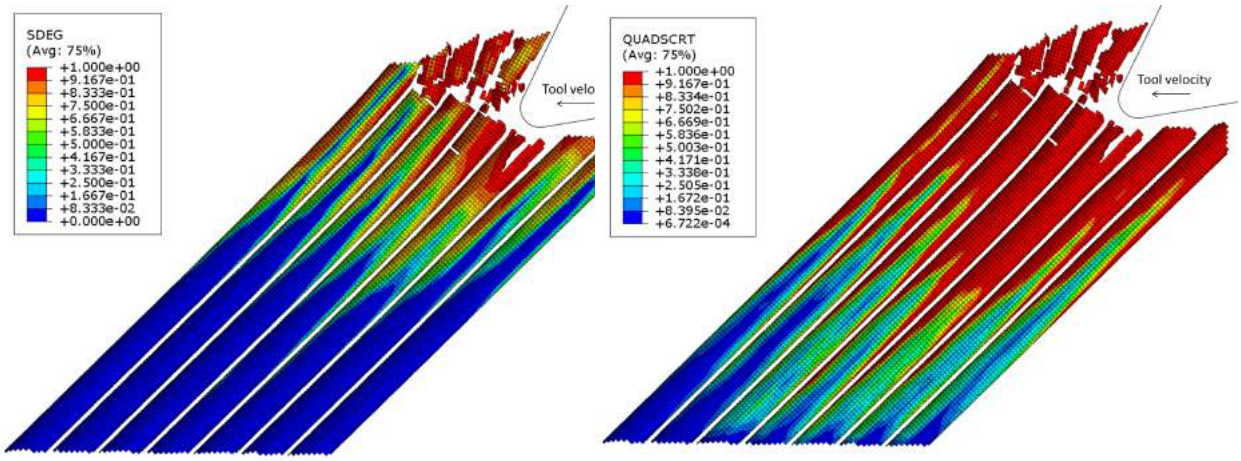

(a) *(b)*

Figure 4.16: (a) Overall value of scalar damage SDEG; and (b) damage initiation variable QUADSCRT for cohesive elements at fibre orientation θ=135°.

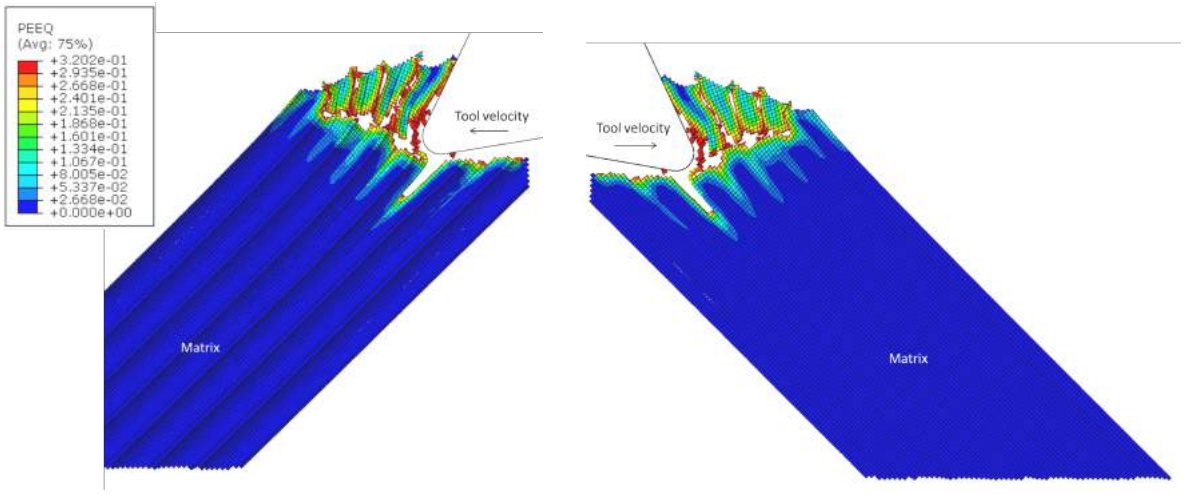

(a) Fibre side *(b) Matrix side*

Figure 4.17: Equivalent plastic strain in the matrix when machining at fibre orientation θ=135°.

In fact, cohesive elements failed earlier allowing the separation of fibre from the matrix with a consequent reduction of the stress in the latter. For this reason, matrix element deletion remained very close to the cutting plane in the 2D-extruded model (∼2 μm).

4.3.2 Validation of cutting force and thrust force

Cutting force and thrust force were calculated for each fibre orientation; and compared with those obtained using a 2D-extruded model and with published experimental results [25] in Figure 4.18.

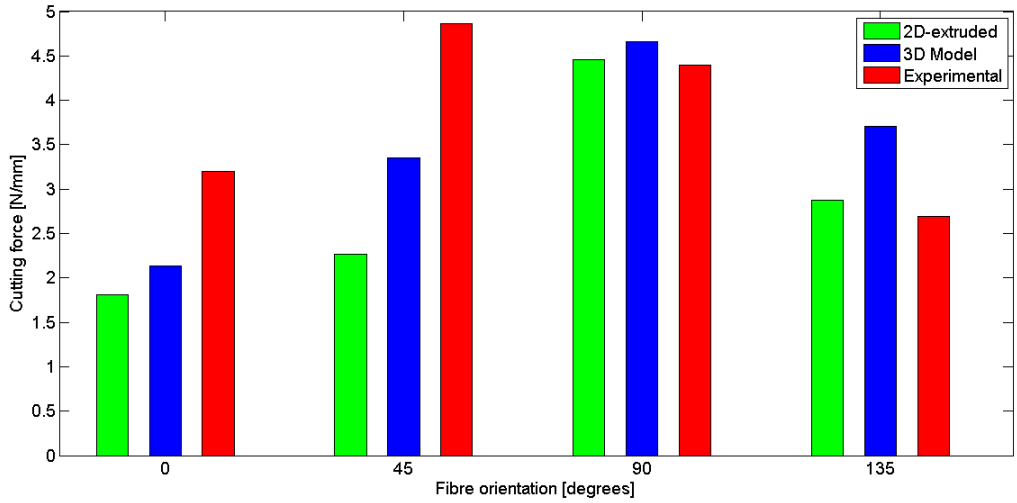

(a)

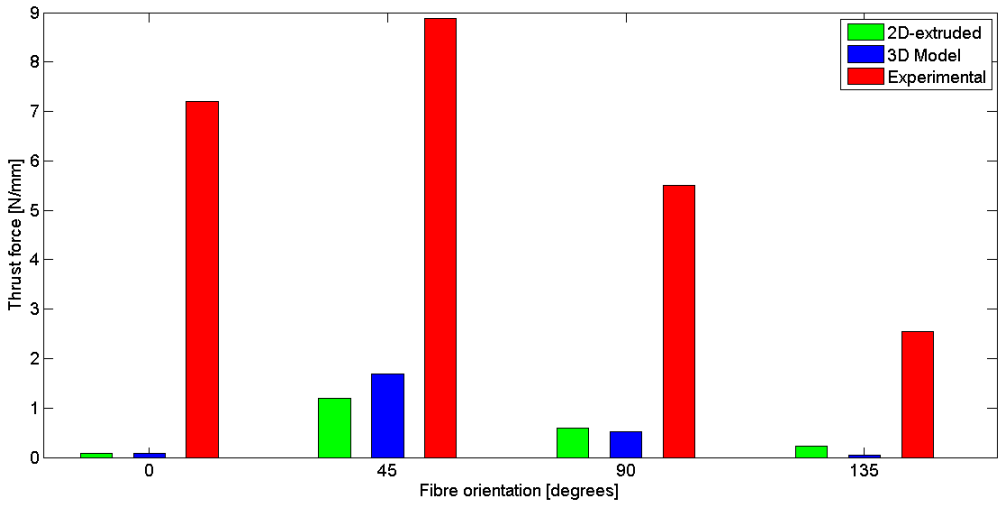

(b)

Figure 4.18: Comparison of (a) cutting force; and (b) thrust force; for the 2D-extruded model, 3D model and published experimental results [25].

In terms of cutting force, it is possible to observe that the 3D model shows a better prediction for fibre orientation θ=0° and θ=45°. In fact, the 3D model shows errors of 33.39% and 30.25% against 43.29% and 52.69% from the 2D-extruded model for θ=0° and θ=45°, respectively. For fibre angle θ=90°, both models show a good agreement with the experimental results. The 2D-extruded model shows a better prediction at fibre angle θ=135° with an error of 6.6%, against an error of 37.52% from the 3D model. Hence, it is possible to conclude that the cutting force is generally higher when a 3D model is used. It could be due to the change in the tool-workpiece interaction. Indeed, the tool does not come into contact with one phase at a time as in the 2D-extruded model, but all phases are cut simultaneously contributing to the cutting force.

In terms of thrust force, both models underestimate the experimental results with errors over than 80%. Hence, considering a geometry more similar to the real component does not improve the thrust force. As previously mentioned, low thrust force could be likely attributed to element deletion during the analysis.

4.4 Summary

A three-dimensional model has been developed and compared with the 2D-extruded model to study the effect of the geometry on the model prediction. Chip formation mechanisms, damages, cutting force and thrust force have been considered for the comparison.

A difference in terms of the material removal mechanism has been found for θ=0° and θ=90°. The former condition does not show debonding with consequent fibre bending until

failure. The absence of debonding can be attributed to the more realistic three-dimensional geometry, where fibres are embedded in the matrix and surrounded by cohesive elements. Due to the different arrangement of cohesive elements, the way they absorb the loads changes, affecting the chip formation mechanism. Hence, in a three-dimensional model tool advancement causes compression failure of the fibre and matrix, with a curling chip generated by the thin matrix layer present on the top of the workpiece. Damages are generally contained near the cutting plane. Fibre orientation θ=90° shows a cleaner cut with a crack propagating ahead of the tool orthogonally to the fibre axis; promoting a more realistic chip formation mechanism. Differently from the 2D-extruded model, no multi-fracture has been observed in the fibres. This was due to fibre bending and compression exerted by the tool. Hence, damages in the fibre are contained compared with the 2D-extruded model.

For fibre orientation θ=45° and θ=135°, the chip formation mechanism becomes similar in both models, but the different arrangement and geometry of the phases make the workpiece more compact, with less bending deformations shown for both orientations.

Generally, the cohesive elements' failure and damaged areas are more extended in the 2D-extruded model than in the 3D model.

The more compact behaviour during cutting of the 3D model causes a general increase in the cutting forces for all fibre angles, allowing to obtain a better prediction at θ=0° and θ=90°. Instead, the thrust force is generally underestimated in both models, due to element deletion during cutting. This represents a limit of the finite element approach, where material loss takes place causing also contact loss between the tool and the machined surface. In order

to overcome this limit, mesh-free methods can be used. Therefore, the smoothed particle hydrodynamic method will be presented in the following chapter.

Chapter 5

Implementation of the smoothed particle hydrodynamics method

5.1 Introduction

When FEM is employed, deletion of failed elements during analysis represents the main cause of inaccurate thrust force prediction, as highlighted in the previous chapters. Material deletion represents a necessity for numerical models, in order to avoid elements becoming highly distorted during tool advancement.

Since mesh-free methods can handle large deformations and material opening without element deletion, smoothed particle hydrodynamics (SPH) is employed in this chapter for simulating orthogonal cutting of UD-CFRP.

5.2 Overview of the SPH method

The smoothed particle hydrodynamics (SPH) method, first developed by Gingold and Monaghan [110], has been used for simulating orthogonal cutting of metals [111–116].

In this method, the workpiece is composed of a number of discrete spherical particles. The value of a variable at a particle of interest can be approximated by summing the contributions from a set of neighbouring particles, denoted by subscript j, for which the kernel function W is not zero [109]:

$$f(x) \backsimeq \sum_j \frac{m_j}{\rho_j} f_j W(|x - x_j|, h) \tag{5.1}$$

where m_j, ρ_j, x_j, f_j are mass, density, location and the value assumed by the variable for the neighbouring particle j. The coefficient h represents the smoothing length for the kernel function W, i.e. the sphere of influence containing all neighbouring particles contributing to the calculation of the variable of interest (Figure 5.1). As for the finite element method, a constitutive model, governing the particles' interaction, needs to be implemented.

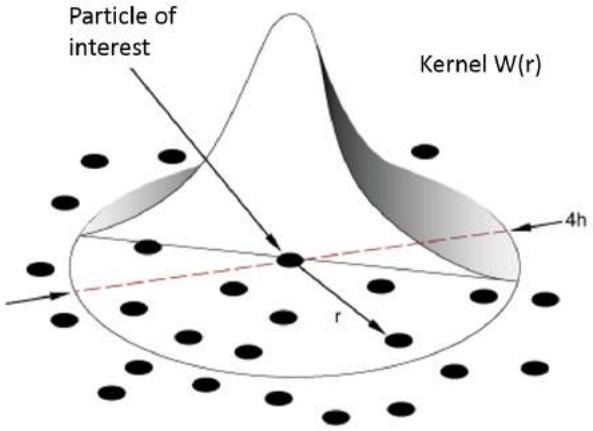

Figure 5.1: Schematic of kernel function W for the generic particle in the SPH model [109].

The SPH method is able to simulate material opening due to tool action without deleting any particle experiencing failure. Degradation of material properties after material failure allows particles to separate.

Unlike the FEM, no cohesive model can be implemented when the SPH method is used. Therefore, information on the fibre-matrix interface cannot be obtained.

5.3 Development of the SPH model

A three-dimensional model with cylindrical fibres was developed to implement the SPH method in Abaqus software, as shown in Figure 5.2. In order to reduce the computational cost, half geometry for the fibres was considered, assuming the symmetry. The model was not entirely composed of SPH elements; in fact the finite element method was used for the EHM phase. The boundary conditions were the same as applied in the models developed in the previous chapters. Tie constraint was applied between the SPH matrix and the EHM phase. Since SPH particles can undergo large displacements, even flying away from the cutting area in case damage is experienced, the imposition of the condition of symmetry on the SPH elements is not sufficient. For this reason, two rigid surfaces were positioned in the model on both sides, avoiding particles moving in z direction out from the simulated strip. Contact with no friction was implemented between particles and rigid surfaces.

The depth of cut set in the model was 15 μm, and a cutting velocity boundary condition was assigned to the tool, realising a dynamic explicit analysis. Moreover, particles were positioned in the model with a relative distance of 1 μm, in order to reduce as much as

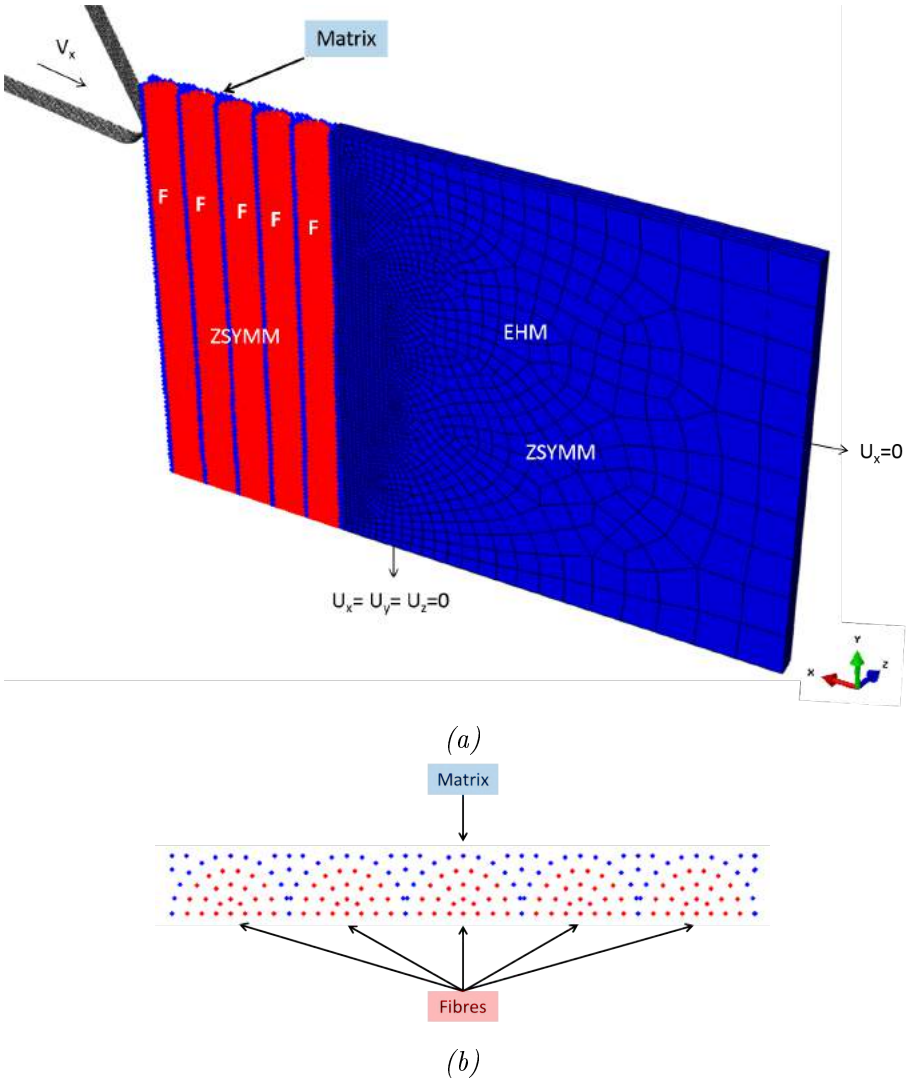

Figure 5.2: Schematic of the three-dimensional SPH model: (a) boundary conditions applied in the case of fibre orientation θ=90°; and (b) details of fibre and matrix (top view).

possible any difference with the models developed in the previous chapter. No condition was needed to be set between the fibres and matrix particles.

In order to simulate two different phases using the SPH model, an user subroutine needed to be developed, which is described in detail below.

Implementation of the user subroutine for the SPH model. The main limitation when using the SPH method in Abaqus exists in the inability to simulate the interaction between two or more parts modelled with that method, to which different material models have been assigned. In the present model, two different phases based on the SPH method are implemented: fibre and matrix. Hence, it is of fundamental importance to overcome this limitation. To this end, a user subroutine has been developed, in which material models for fibre and matrix have been implemented. In fact, fibre and matrix have been developed in the same part in Abaqus/CAE. Afterwards, knowing the ID number of particles belonging to each phase, different properties and constitutive behaviours have been assigned to each particle using a field variable in a VUMAT subroutine to identify fibre and matrix. Using the described method, a unique material card can be used in the analysis, making possible the simulation of the contact between fibre and matrix.

In order to compare results obtained using the SPH method with those observed using a finite element method, the constitutive behaviour coded in the VUMAT has to be the same as implemented using Abaqus/CAE in the latter method for each phase. For each material model, the material damage also needs to be coded together with post-failure behaviour, since elements are not deleted.

Matrix material has been coded having an elasto-plastic behaviour, with the plastic region defined by means of Von Mises yield criterion, and isotropic hardening. The general approach to simulate material damage that can be used for the matrix phase is reported in Figure 5.3(a). The elastic phase identified by the Young's modulus E, and by the yield stress σ_0 can be recognised, followed by the plastic phase. When material damage is introduced in

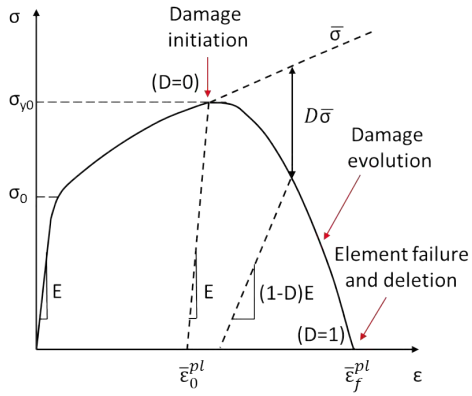

(a) Progressive damage degradation in Abaqus [109]

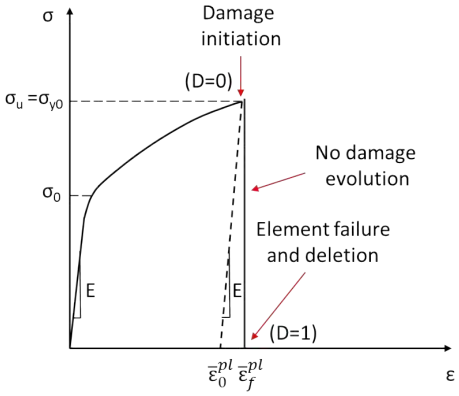

(b) FEM

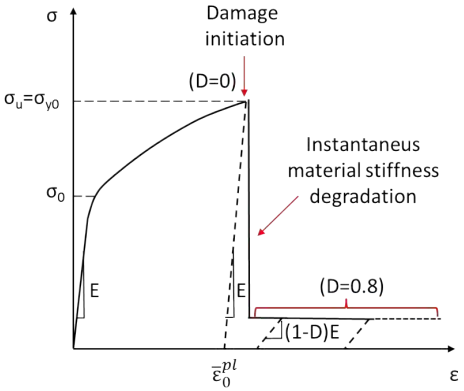

(c) SPH

Figure 5.3: Stress-strain curve considering damage during simulation.

the material model, σ_{y0} and $\bar{\epsilon}_0^{pl}$ identify the damage initiation condition, representing the yield stress and the equivalent plastic strain at the onset of damage, respectively. In order to simulate the damage evolution during the analysis, a damage variable $0 \leq D \leq 1$ has to be considered, simulating the damage through material stiffness degradation. At the damage initiation point, the damage variable assumes value D=0. It rises with the increase of damage experienced by the element till it reaches the unitary value, at which the element loses its load-carry capacity and is deleted from the simulation. The failure condition is identified by the equivalent plastic strain at failure $\bar{\epsilon}_f^{pl}$.

In the FEM model, no damage evolution is set, with the element failing once the Von Mises stress reaches the ultimate stress level (Figure 5.3(b)).

In order to obtain the same behaviour using the VUMAT subroutine, the condition reported in Equation (5.2) [109] has been implemented to identify damage initiation:

$$\omega_D = \int \frac{d\bar{\epsilon}^{pl}}{\bar{\epsilon}_D^{pl}} = 1 \tag{5.2}$$

where ω_D is a state variable increasing with the plastic deformation; and $\bar{\epsilon}_D^{pl}$ represents the equivalent plastic strain at the onset of damage. No damage evolution has been considered after damage initiation. However, differently from the FEM, the element is not deleted from the analysis. The material stiffness is instantaneously degraded considering a value of the damage variable of D=0.8, which has been kept constant over all the analysis after the damage initiation condition was verified in the element. The value of the damage variable (D=0.8) was obtained using an iterative approach aiming to match the experimental cutting force and thrust force values. The constitutive behaviour can be represented as reported in Figure 5.3(c).

As for the FEM model, the fibre has been simulated in the VUMAT as transversely isotropic and perfectly elastic until damage initiation. The latter is represented by the maximum principal stress criterion. It is verified when the maximum compressive/tensile principal stress in an element exceeds the fibre compressive/tensile strength limit. When this happens, the element is deleted by the analysis in the FEM. Differently, material stiffness degradation has been implemented for the SPH method. In particular, the fibre

constitutive model with the associated stiffness matrix is reported in Equation (5.3) [109, 117, 118]:

$$\begin{bmatrix} \sigma_{11} \\ \sigma_{22} \\ \sigma_{33} \\ \tau_{12} \\ \tau_{23} \\ \tau_{13} \end{bmatrix} = \begin{bmatrix} C_{11} & C_{12} & C_{13} & 0 & 0 & 0 \\ C_{21} & C_{22} & C_{23} & 0 & 0 & 0 \\ C_{31} & C_{32} & C_{33} & 0 & 0 & 0 \\ 0 & 0 & 0 & C_{44} & 0 & 0 \\ 0 & 0 & 0 & 0 & C_{55} & 0 \\ 0 & 0 & 0 & 0 & 0 & C_{66} \end{bmatrix} \begin{bmatrix} \epsilon_{11} \\ \epsilon_{22} \\ \epsilon_{33} \\ \gamma_{12} \\ \gamma_{23} \\ \gamma_{13} \end{bmatrix}$$

$$N = 1 - \nu_{12}\nu_{21} - \nu_{23}\nu_{32} - \nu_{31}\nu_{13} - 2\nu_{21}\nu_{32}\nu_{13}$$

$$C_{11} = (1 - \nu_{23}\nu_{32})E_1/N \qquad C_{12} = (\nu_{12} + \nu_{13}\nu_{32})E_2/N \qquad C_{13} = (\nu_{13} + \nu_{12}\nu_{32})E_3/N$$

$$C_{21} = (\nu_{21} + \nu_{31}\nu_{23})E_1/N \qquad C_{22} = (1 - \nu_{13}\nu_{31})E_2/N \qquad C_{23} = (\nu_{23} + \nu_{13}\nu_{21})E_3/N$$

$$C_{31} = (\nu_{31} + \nu_{21}\nu_{23})E_1/N \qquad C_{32} = (\nu_{32} + \nu_{31}\nu_{12})E_2/N \qquad C_{33} = (1 - \nu_{12}\nu_{21})E_3/N$$

$$C_{44} = 2G_{12} \qquad C_{55} = 2G_{23} \qquad C_{66} = 2G_{13}$$

$$E_1 = E_1^{DS}(1 - d_1) \qquad E_2 = E_2^{DS}(1 - d_2) \qquad E_3 = E_3^{DS}(1 - d_3)$$

$$\nu_{12} = \nu_{12}^{DS}(1 - d_1) \qquad \nu_{21} = \nu_{21}^{DS}(1 - d_2) \qquad \nu_{13} = \nu_{13}^{DS}(1 - d_1)$$

$$\nu_{31} = \nu_{31}^{DS}(1 - d_3) \qquad \nu_{23} = \nu_{23}^{DS}(1 - d_2) \qquad \nu_{32} = \nu_{32}^{DS}(1 - d_3)$$

$$G_{12} = G_{12}^{DS}(1 - d_{s12}) \qquad G_{13} = G_{13}^{DS}(1 - d_{s13}) \qquad G_{23} = G_{23}^{DS}(1 - d_{s23})$$

$$d_{s12} = 1 - (1 - d_1)(1 - d_2) \qquad d_{s13} = 1 - (1 - d_1)(1 - d_3) \qquad d_{s23} = 1 - (1 - d_2)(1 - d_3) \tag{5.3}$$

where the superscript DS stands for data-sheet, i.e. terms associated with this symbol represent the material properties without damage.

Three damage variables have also been introduced: d_1, d_2, d_3. The former is linked with the damage along the fibre direction 1, while the other two govern the damage in the plane of isotropy 2-3. Hence, d_2 and d_3 have the same value. The damage variables can be implemented straightforwardly to calculate the damaged Young's modulus for each direction; and used to calculate the damaged Poisson's ratio. In fact, even for the damaged material, Equation (5.4) has to be satisfied [118]:

$$\frac{\nu_{ij}}{E_i} = \frac{\nu_{ji}}{E_j} \tag{5.4}$$

In addition, d_{s12}, d_{s13}, d_{s23} represent the damage variables to shear in the planes 1-2, 1-3, and in the plane of isotropy 2-3, respectively. Similarly to what is reported in the Abaqus manual on damage and failure for fibre-reinforced composites [109], the generic shear damage variable d_{sij} is calculated as a function of the damage variables in direction i and j, i.e. d_i and d_j, respectively.

The damage variables' values are set to zero if the damage initiation condition has not been satisfied ($d_1 = d_2 = d_3 = 0$). Otherwise, material degradation takes place instantaneously, without damage evolution, and damage variables are set directly to the maximum and final values considered: $d_1 = 0.4$, $d_2 = 0.8$, $d_3 = 0.8$. A different coefficient has been assigned to damage variables in the plane of isotropy from that associated with the direction along the fibre. The values of the damage variables (d_1, d_2, d_3) were obtained using an iterative

approach aiming to match the experimental cutting force and thrust force values.

Material properties implemented for each phase in the SPH model are the same as those used in the FEM model (Table 3.1).

5.4 Results and discussion

The SPH method was implemented considering different fibre orientations (θ=0°, 45°, 90°, 135°) to analyse the tool-workpiece interaction and the material deformation during the orthogonal cutting, and to predict the cutting force and thrust force. The model was validated against experiments [25] and compared with the three-dimensional finite element model (3D-FEM) developed in the previous chapter. The results obtained are reported and discussed below.

5.4.1 Chip formation mechanisms and damage at various fibre orientations

The deformed configuration of the model during cutting at fibre orientation θ=0° is reported in Figure 5.4. The field variable FV1 is used to distinguish fibres (FV1=1) from matrix (FV1=0). It is possible to observe the absence of element deletion during the analysis totally changes the chip formation mechanism when compared with the 3D-FEM model (Figure 4.2). In particular, when the SPH method is employed, the bouncing back is observed during cutting due to the elastic recovery of the material. In fact, the contact between the tool clearance face and the workpiece machined surface is clearly visible. This was not possible

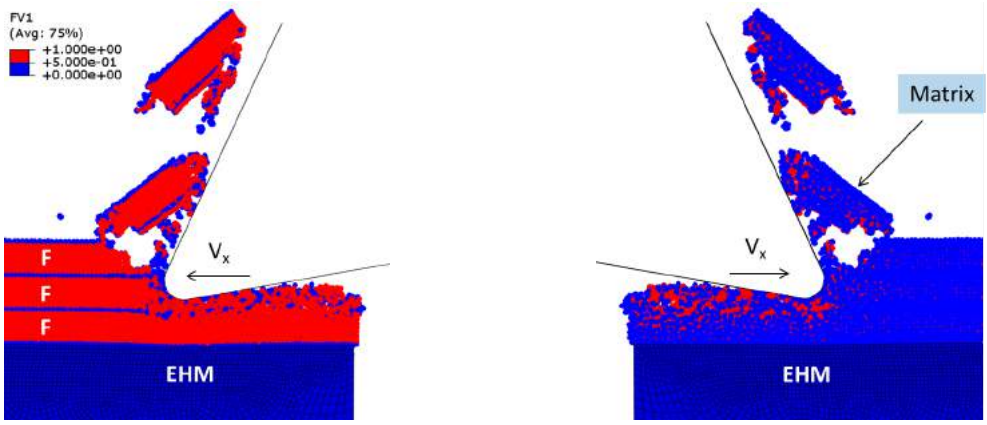

(a) Fibre side *(b) Matrix side*

Figure 5.4: Model configuration during cutting implementing the SPH method for fibre orientation θ=0°.

to detect in the 3D-FEM model due to the deletion of failed elements.

The tool causes fibre and matrix compression in the direction of the fibre axis during advancement, with consequent material damage around the tool-workpiece contact area. Differently from the 3D-FEM model, elements are not deleted from the analysis, but they experience degradation of the material properties. Hence, the damaged material cannot leave the cutting zone, as it is entrapped between the tool and the upper part of the material which is still not affected by damage. The damaged area expands with further tool advancement and a crack propagates horizontally ahead of it, affecting the elements located on the fibre-matrix border. In addition, the damaged material helps in transferring the tool action to the undamaged elements, favouring material opening. During crack propagation fibre bending takes place. When the crack reaches a length of ∼30 μm, it suddenly changes direction, moving through the fibre towards the free surface of the sample. In addition, the crack also moves through the matrix at the same time. When it reaches the free surface, the chip, composed of the cut fibre and matrix, is released and the process repeats again. Differently,

in the 3D-FEM model a thin curl chip was formed by a small amount of matrix material located on the upper free edge of the sample. Almost the totality of the material in front of the tool, that was supposed to form the chip, was deleted from the analysis due to failure. This represents a non realistic behaviour, while that observed in the 3D-SPH model is closer to that observed by Calzada *et al.* [25] and representative of Type I chip formation mechanism.

Solution-dependent state variables (SDVs), defined for material model implementation in the VUMAT subroutine, provide additional information. In particular, the variable SDV13 is associated with the damage experienced by the material, which is shown in Figure 5.5.

Damaged particles are identified by values of SDV13=1. The damage extension tends to reach the EHM phase ($\sim$12 μm below the cutting plane). The damaged material can also be observed until $\sim$8 μm ahead of the cutting tool. Considering the fibres (Figure 5.5(c-d)), damage is mainly concentrated along the crack propagation path in the external fibre, which allows the formation of the chip. The second fibre presents large amounts of damage being almost totally crushed by the round tool cutting edge. The third fibre, located near the EHM phase, shows damages mostly in the upper part. Damages in the matrix (Figure 5.5(a-b)) are more spread out, reaching the EHM phase.

The 3D-SPH model shows larger damaged areas both for fibre and matrix phases compared to the 3D-FEM model.

The equivalent plastic strain in the matrix is identified by the variable SDV7 and shown in Figure 5.6. A scale with a minimum value of 1.0e-3 has been set, while a maximum value of 0.32 has been considered. The latter represents the value of the plastic deformation at the onset of damage. Hence, all areas coloured in the considered figures represent zones

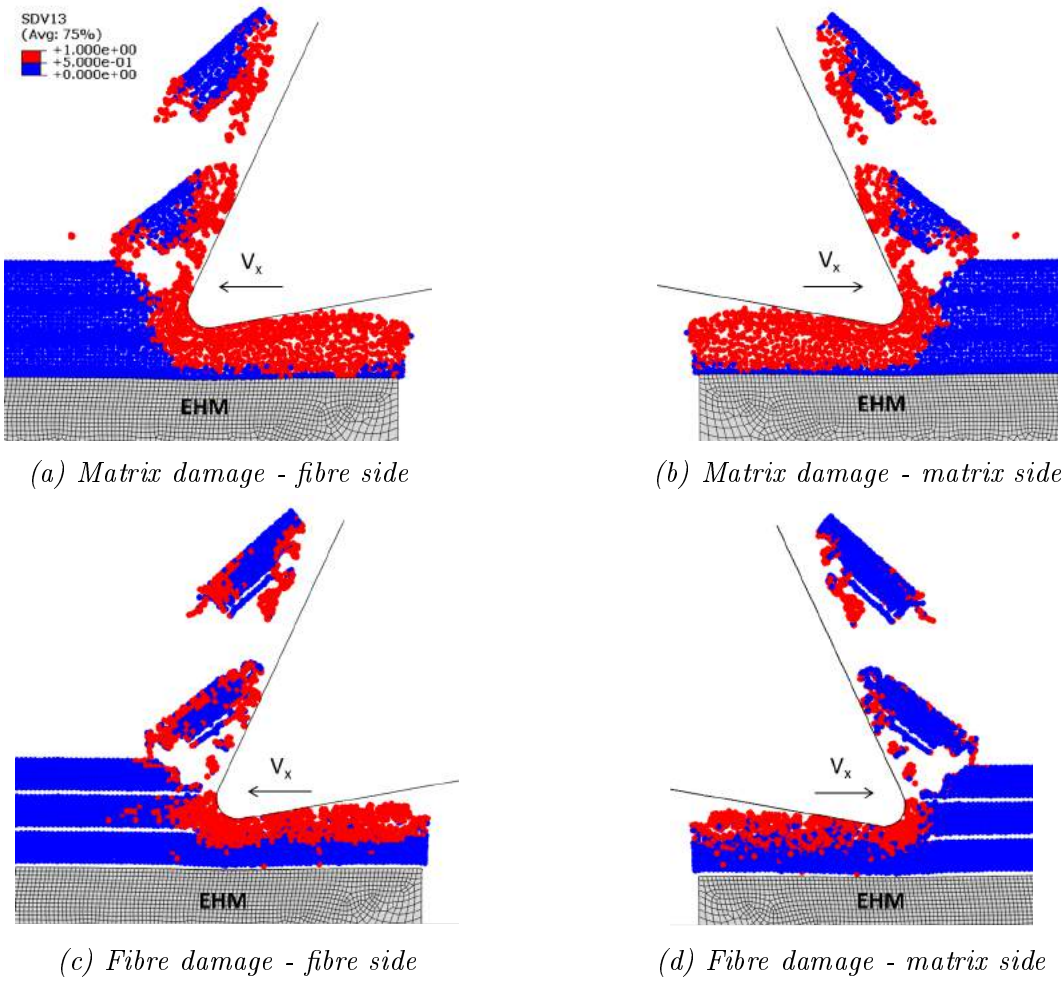

(a) Matrix damage - fibre side

(b) Matrix damage - matrix side

(c) Fibre damage - fibre side

(d) Fibre damage - matrix side

Figure 5.5: Damage in fibre and matrix material identified by the variable SDV13 in the VUMAT subroutine for fibre orientation θ=0°.

where no damage has been experienced yet. Instead, grey areas represent damaged material, where very large plastic deformation can occur. The magnitude of the plastic deformations reduces, moving far from the tool and showing values near to the maximum set around the damaged area, indicating imminent degradation of material properties. Plastic deformations rise in the matrix ahead of the tool and deep in the material reaching the EHM phase (∼12 μm below the cutting plane). This behaviour represents a big difference to that observed in the 3D-FEM model, where plastic deformations in the matrix remain contained around the

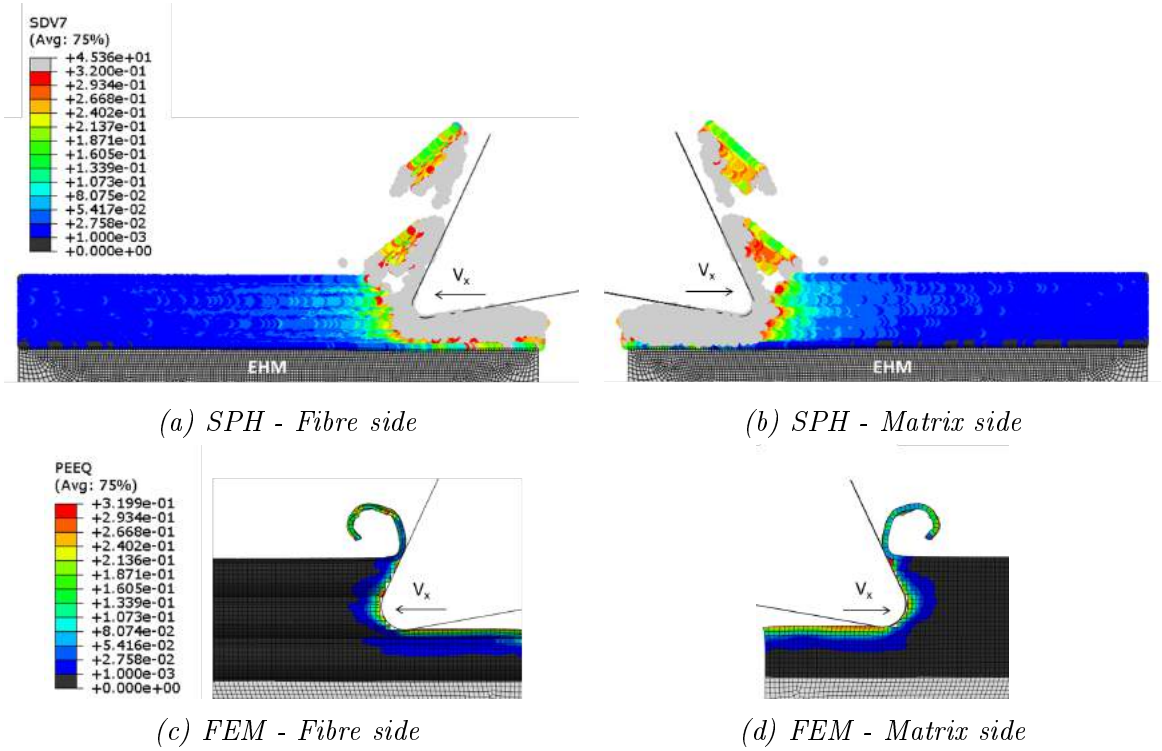

(a) SPH - Fibre side *(b) SPH - Matrix side*

(c) FEM - Fibre side *(d) FEM - Matrix side*

Figure 5.6: Equivalent plastic strain in the matrix material for fibre orientation θ=0°.

cutting area, as shown in Figure 5.6(c-d). It is due to the presence of damaged material that, reaming in the model, causes a bigger amount of material involved during cutting.

For fibre orientation θ=45°, the model configuration at the end of the analysis is reported in Figure 5.7. At the beginning of the analysis, the tool pushes the material along the cutting direction, causing damage in the particles in contact with the cutting edge. During tool advancement, material experiences shear with fibres undergoing displacement along their axis. Due to this behaviour, shear damage takes place in the weaker phase, the matrix. Further tool displacement causes an increase in the shear damage and damage propagation in a direction orthogonal to the fibre axis from the cutting edge.

A few damaged particles are also visible in the area located between the second and third

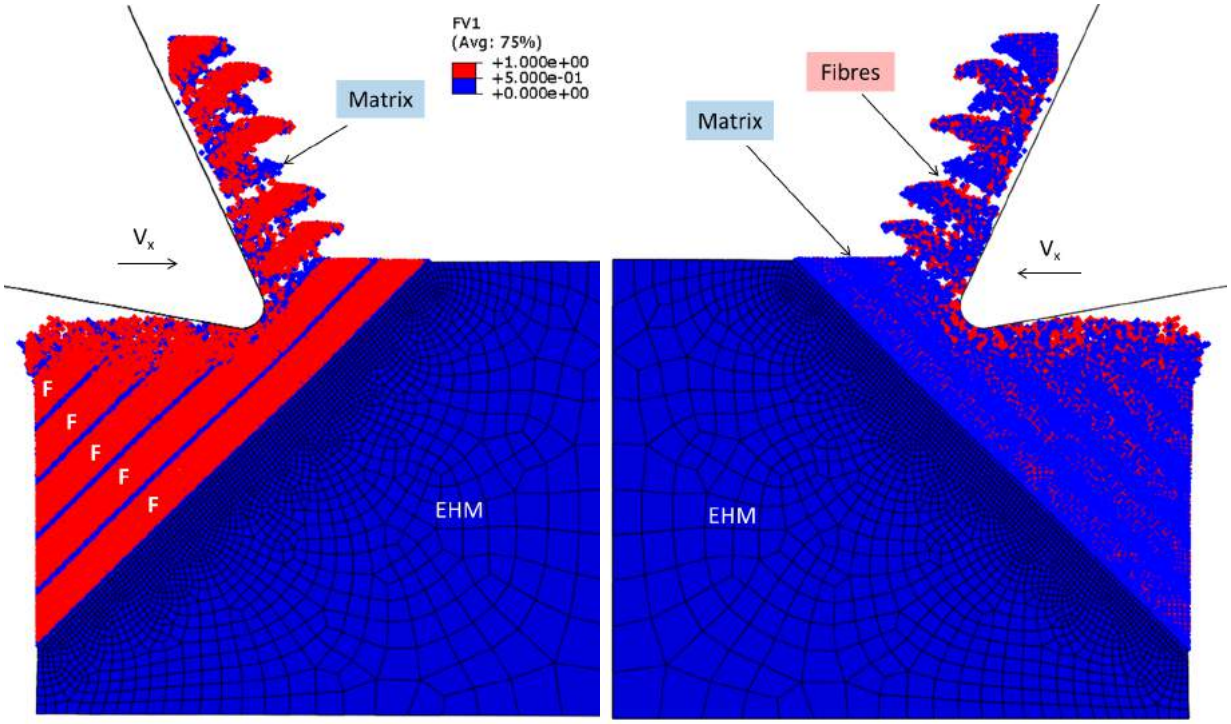

(a) Fibre side *(b) Matrix side*

Figure 5.7: Model configuration implementing the SPH method for fibre orientation θ=45°.

fibre, due to the matrix starting to experience shear. The amount of damage increases as the tool advances, with the material being divided into two parts: the upper, forming the chip through shear deformation sliding on the rake face; and the lower, undergoing compression below the tool. As for fibre angle θ=0°, bouncing back due to elastic recovery after the tool has passed is clearly visible in Figure 5.7, as the clearance face and the workpiece machined surface are in contact. In addition, chip formation through shear deformation is highly visible at the end of the analysis, showing the chip shape. In general, the chip formation mechanism seems similar to that observed for the 3D-FEM model. It is representative of Type III chip formation mechanism.

Material damage is shown in Figure 5.8, by means of variable SDV13.

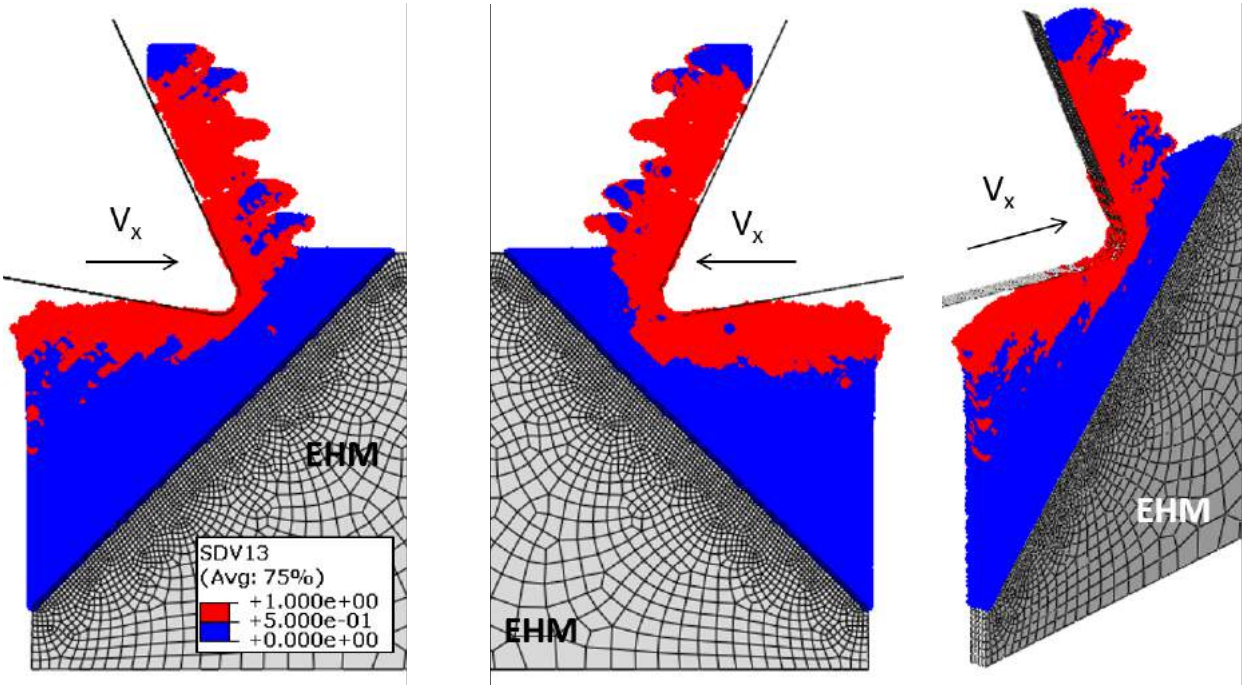

(a) Fibre side *(b) Matrix side* *(c) 3D view*

Figure 5.8: Damage in fibre and matrix material identified by the variable SDV13 in the VUMAT subroutine for fibre orientation θ=45°.

Material forming the chip experiences damage due to shear and compression. The latter is exerted by the tool on the area in front of the cutting edge; the consequent damage is transported by the material in the chip and in the machined surface. Damage extends below the cutting plane (∼24 μm), reaching also the vertical free edge of the workpiece, propagating along the border area between the matrix and fibres (Figure 5.8(c)).

Matrix damage extends ahead of the cutting tool, especially at the border with the fibres due to shear deformation. Moreover, subsurface damages can also be observed in Figure 5.9. The path of the damage in the matrix seems to be influenced by the presence of fibres, travelling around them deep in the workpiece. Damage depth in the matrix (∼19 μm) is higher than that experienced in the 3D-FEM model, where it remains very close to the

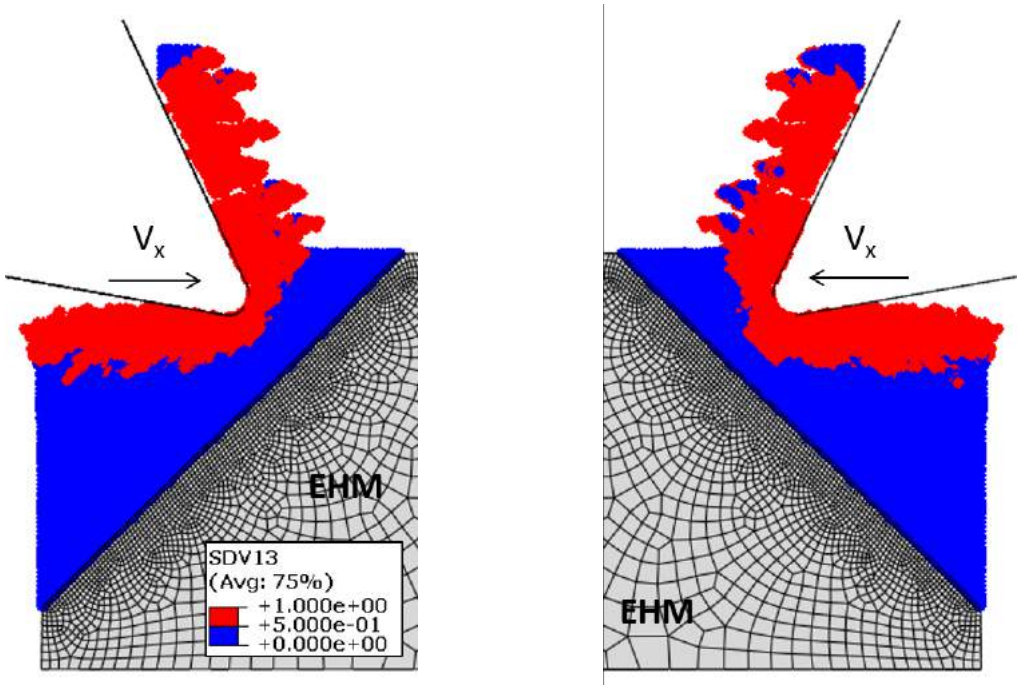

(a) Fibre side *(b) Matrix side*

Figure 5.9: Damaged matrix material identified by the variable SDV13 in the VUMAT subroutine for fibre orientation θ=45°.

cutting plane (a few micrometer).

During advancement, the tool comes into contact with different fibres sequentially. For each of them damage firstly propagates in a direction orthogonal to the fibre axis, and then it extends along the fibre-matrix border mainly towards the free surface. Further advancement of the tool causes damage propagation within the fibre, as visible in Figure 5.10. As for the matrix, the extension of damage in the fibres is larger when the SPH method is employed. In fact, it extends ∼24 μm below the cutting plane in the SPH model, while in the FEM model it extends a few micrometer.

The equivalent plastic strain for the matrix is reported in Figure 5.11. Very high plastic deformations ($\bar{\epsilon}^{pl}$=51.77) are located in the areas that have experienced damage. As

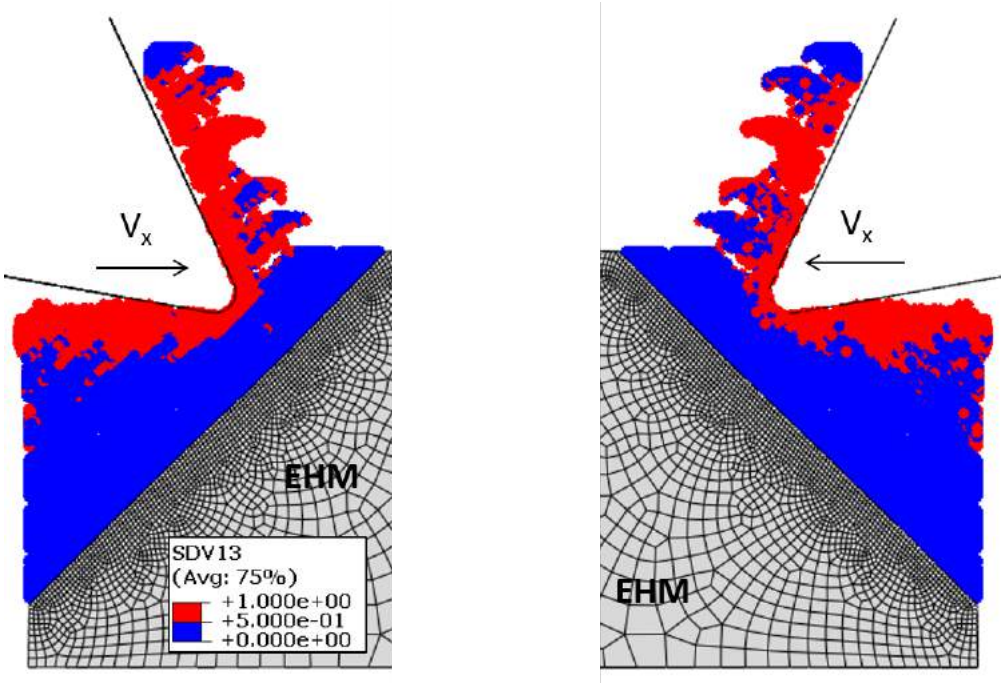

(a) Fibre side *(b) Matrix side*

Figure 5.10: Damaged fibre material identified by the variable SDV13 in the VUMAT subroutine for fibre orientation θ=45°.

observed for fibre angle θ=0°, plastic deformations are not contained near the tool and the cutting plane, but they reach the EHM phase, assuming values ∼1.0e-3 in its vicinity. Plastic deformations are much more contained in the 3D-FEM model as shown in Figure 5.11(b).

For fibre orientation θ=90°, the model configuration at the end of the analysis is shown in Figure 5.12. The cutting tool advancement causes a fibre failure due to compression at the contact point. The damaged area extends all around the cutting edge. Afterwards, the fibre is divided into two parts, with the upper part being lifted while sliding on the tool rake face, and compressed against the next fibre. The lifting causes a shear deformation in the material during chip formation. It is possible to observe that the machined surface exhibits

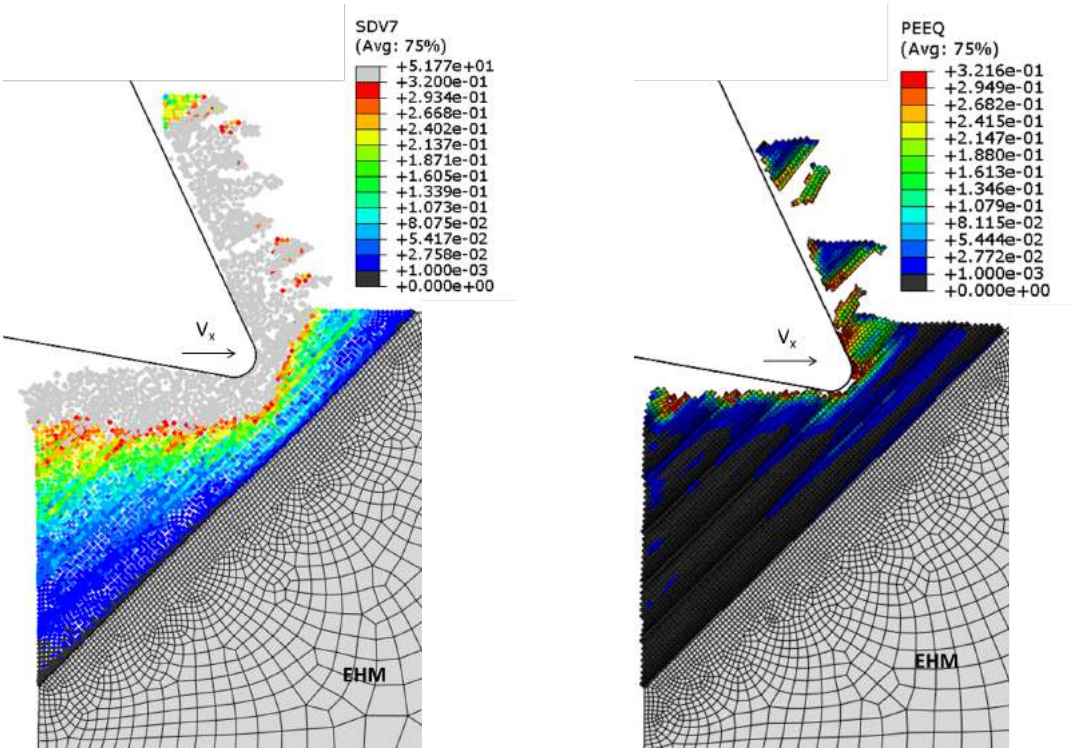

(a) SPH - Fibre side *(b) FEM - Fibre side*

Figure 5.11: Equivalent plastic strain in the matrix material for fibre orientation θ=45˚.

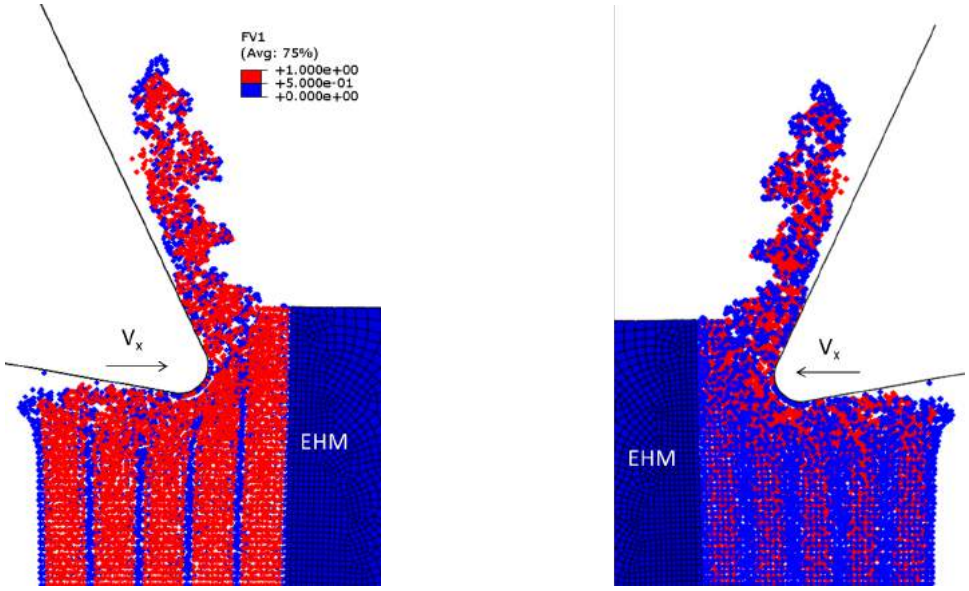

(a) Fibre side *(b) Matrix side*

Figure 5.12: Model configuration implementing the SPH method for fibre orientation θ=90˚.

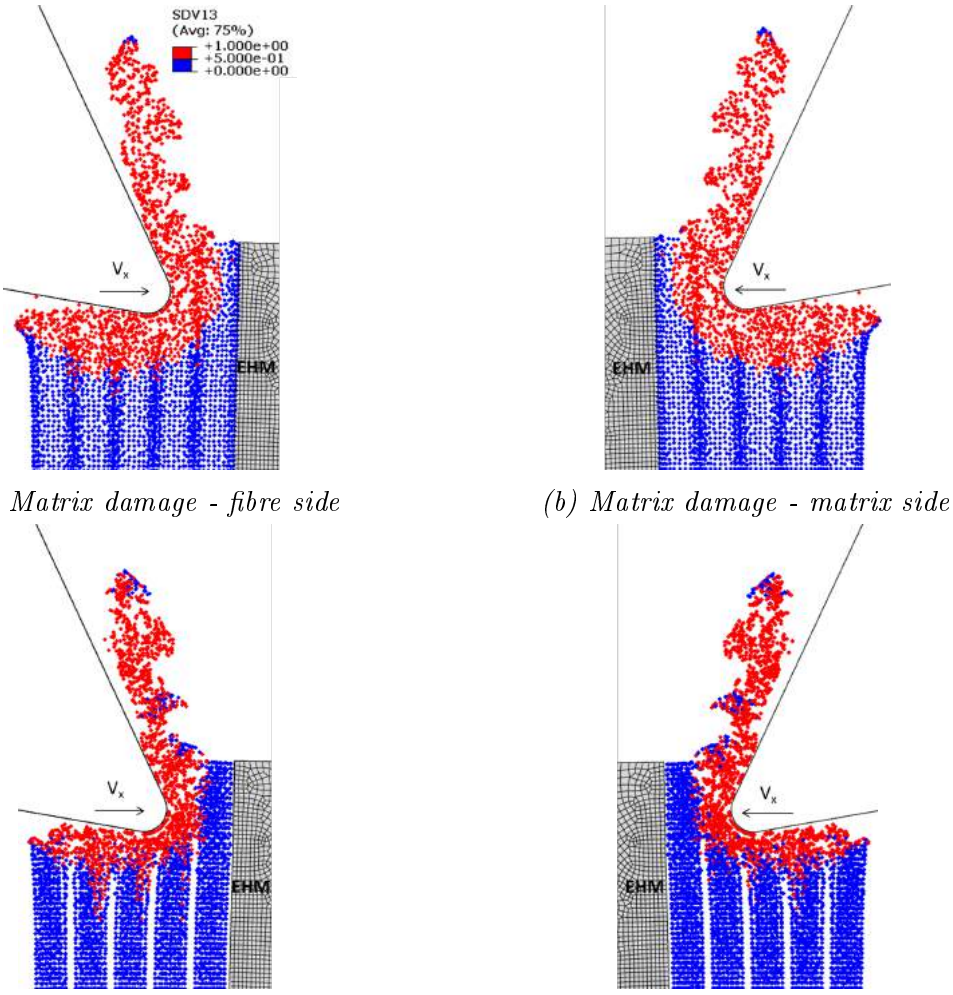

(a) Matrix damage - fibre side

(b) Matrix damage - matrix side

(c) Fibre damage - fibre side

(d) Fibre damage - matrix side

Figure 5.13: Damage in fibre and matrix material identified by the variable SDV13 in the VUMAT subroutine for fibre orientation θ=90°.

elastic recovery after the tool has passed. The chip formation mechanism is similar to that observed in the 3D-FEM model (Type IV).

Material damage during cutting is shown in Figure 5.13. Damage extends ahead of the tool and below the cutting path (∼24 μm). In particular, it seems to propagate equally in all directions starting from the cutting edge in the matrix phase (Figure 5.13(a-b)). This behaviour produces a damaged area having a circular shape around the tool. Damage

extension is less expanded in the fibre phase (Figure 5.13(c-d)). Damage below the trim plane can be observed with the damage propagating along the fibre direction near the fibre-matrix border. In Figure 5.12(a) and Figure 5.13(c) it is also possible to notice as the first fibre, undergoing the cut, experiences a bending deformation in the opposite direction to the tool velocity. In fact, the tool compresses the fibres causing a bending deformation in the same direction as its displacement. After the fibre is cut, the lower part experiences an elastic recovery, which causes a fibre oscillation around the vertical position and an increase in the material damage. In fact, while the first fibre experiences the elastic recovery, the second one is pushed forward by the tool. This double action causes further damage propagation in the machined material near the fibre-matrix boarder. Similar to the previous fibre orientations analysed, the damaged area is greater for the SPH model.

The equivalent plastic strain in the matrix phase has been reported in Figure 5.14. The plastic deformation experienced by the matrix is more extended in the 3D-SPH model. In fact, the particles having a grey colour in Figure 5.14(a) represent damaged areas, below which plastic deformation is visible. It reduces in magnitude moving away from the tool, deep in the workpiece. Differently, in the 3D-FEM model the plastic deformation is more contained near the tool.

The model configuration when cutting at θ=135° is reported in Figure 5.15. Material removal can be studied observing material deformation during cutting combined with damage experienced by the material; these are reported in Figure 5.16 and Figure 5.17. During advancement the tool engages the fibre, exerting a peeling action while pushing forward (Figure 5.16). This causes a bending deformation of the fibre with local compression at

the contact point with the cutting edge. The former causes separation between the fibre and the matrix below the cutting plane; while the latter causes a fibre fracture. Bending deformation is experienced by numerous fibres ahead of the tool, with damage rising far

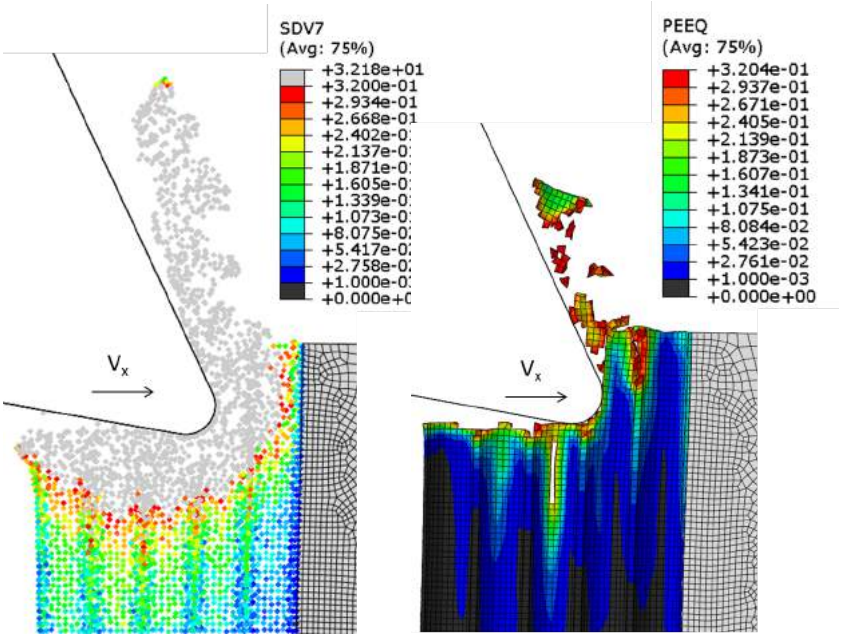

(a) SPH - Fibre side *(b) FEM - Fibre side*

Figure 5.14: Equivalent plastic strain in the matrix material for fibre orientation θ=90°.

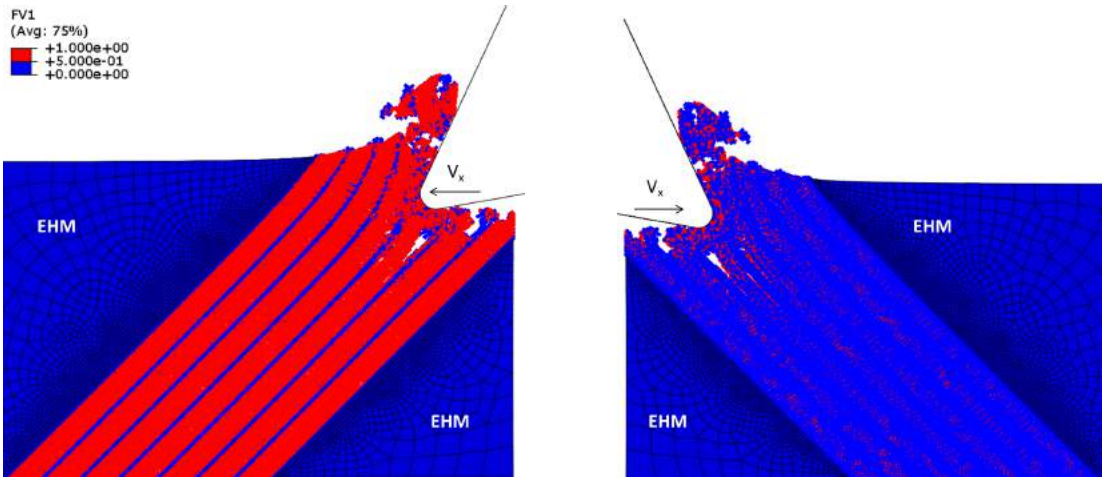

(a) Fibre side *(b) Matrix side*

Figure 5.15: Model configuration implementing the SPH method for fibre orientation θ=135°.

ahead of the tool at the border between the fibre and matrix. A further displacement of the tool causes a fibre failure due to bending, with the upper part fractured into two pieces due to compression. Similar behaviour is experienced by the following fibre which undergoes bending and compression. However, fibre failure is mainly due to compression. The upper parts of fractured fibres fly away in the form of a powder-like chip.

Despite the SPH method not implementing cohesive elements, it is able to predict the fibre-matrix detachment due to the failure of particles near the border along the fibre direction. This behaviour, which can be observed in Figure 5.17, may be interpreted as debonding.

Even if the chip formation mechanism seems similar to the 3D-FEM model, the latter shows a presence of a crack propagating through all fibres towards the workpiece's free edge. Instead, in the SPH method the border of the damaged area ahead of the tool extends in a direction orthogonal to the fibre orientation, towards the free surface of the workpiece.

The equivalent plastic strain in the matrix phase is reported in Figure 5.18 and compared with that obtained in the 3D-FEM results. As for previous orientations, the area affected

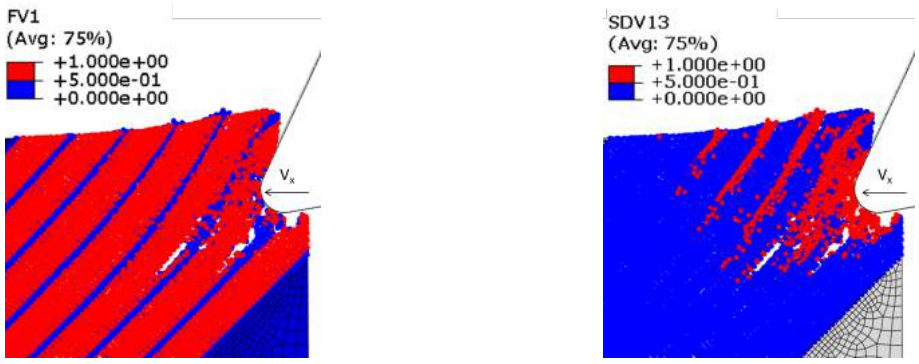

(a) FV1 - Fibre side *(b) SDV13 - Fibre side*

Figure 5.16: (a) Model configuration; and (b) damage at 1.97e-3 seconds for fibre orientation θ=135°.

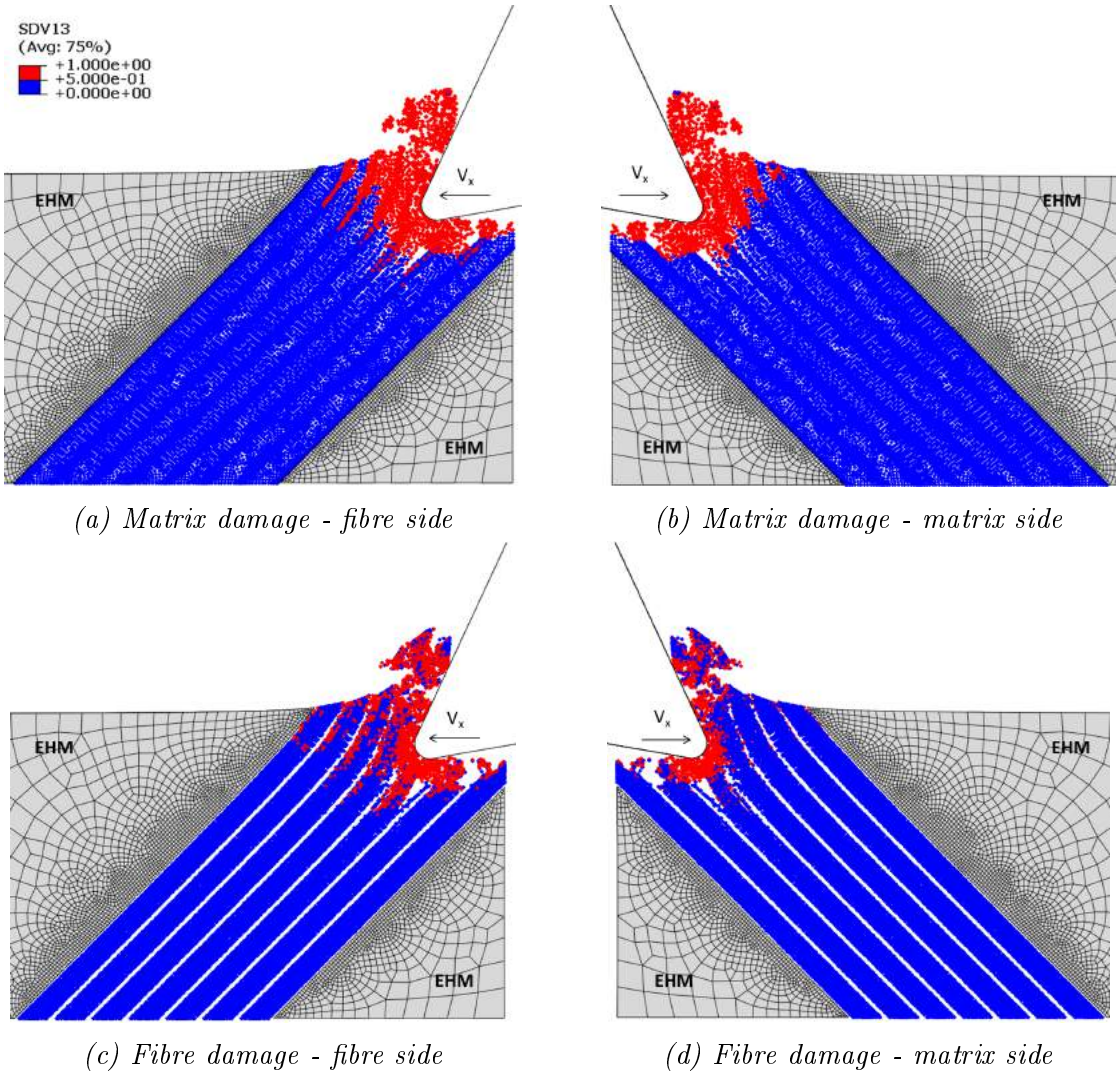

(a) Matrix damage - fibre side

(b) Matrix damage - matrix side

(c) Fibre damage - fibre side

(d) Fibre damage - matrix side

Figure 5.17: Damage in fibre and matrix material identified by the variable SDV13 in the VUMAT subroutine for fibre orientation θ=135°.

by plastic deformation during cutting is more extended in the 3D-SPH model, propagating along the fibre direction. The particles in grey represent the damaged material, which is surrounded by elements where the damage is imminent. Plastic deformation reduces, moving far from the cutting zone.

Since in the 3D-FEM model elements are deleted during the analysis, plastic deformation and damage are contained, compared with the 3D-SPH model. In fact, when an element is

deleted, the tool moves forward until it comes into contact with the next element. Differently, in the latter method the damaged material is still present in the model, interposing between tool and the undamaged material. No loss of contact is generally visible between the tool and the workpiece. It generates larger areas of damage and deformation increasing the volume of material involved during cutting.

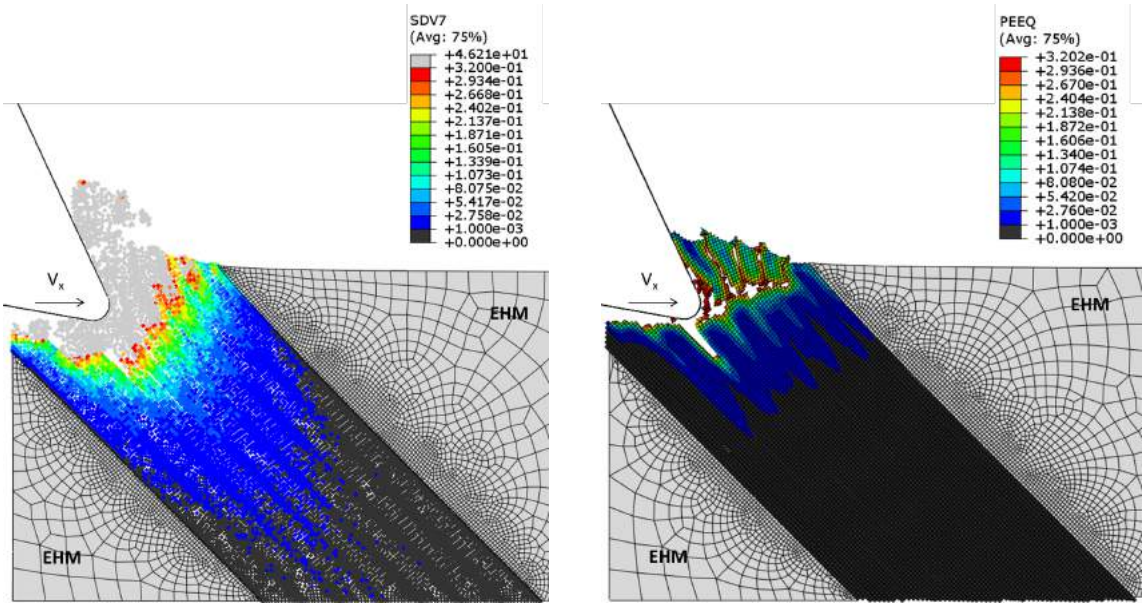

(a) SPH - Matrix side *(b) FEM - Matrix side*

Figure 5.18: Equivalent plastic strain in the matrix material for fibre orientation θ=135°.

5.4.2 Type and morphology of the chip

The chip obtained using the SPH method was compared with that observed in the 3D-FEM model and also in experimental published data (Figure 5.19). For the latter, images obtained by Calzada *et al.* [25], using a high-speed camera, were considered.

Chips obtained from experiments seem to be continuous for all fibre orientations, except for θ=135°. For fibre angle θ=0°, a big difference can be noticed between the 3D-SPH and

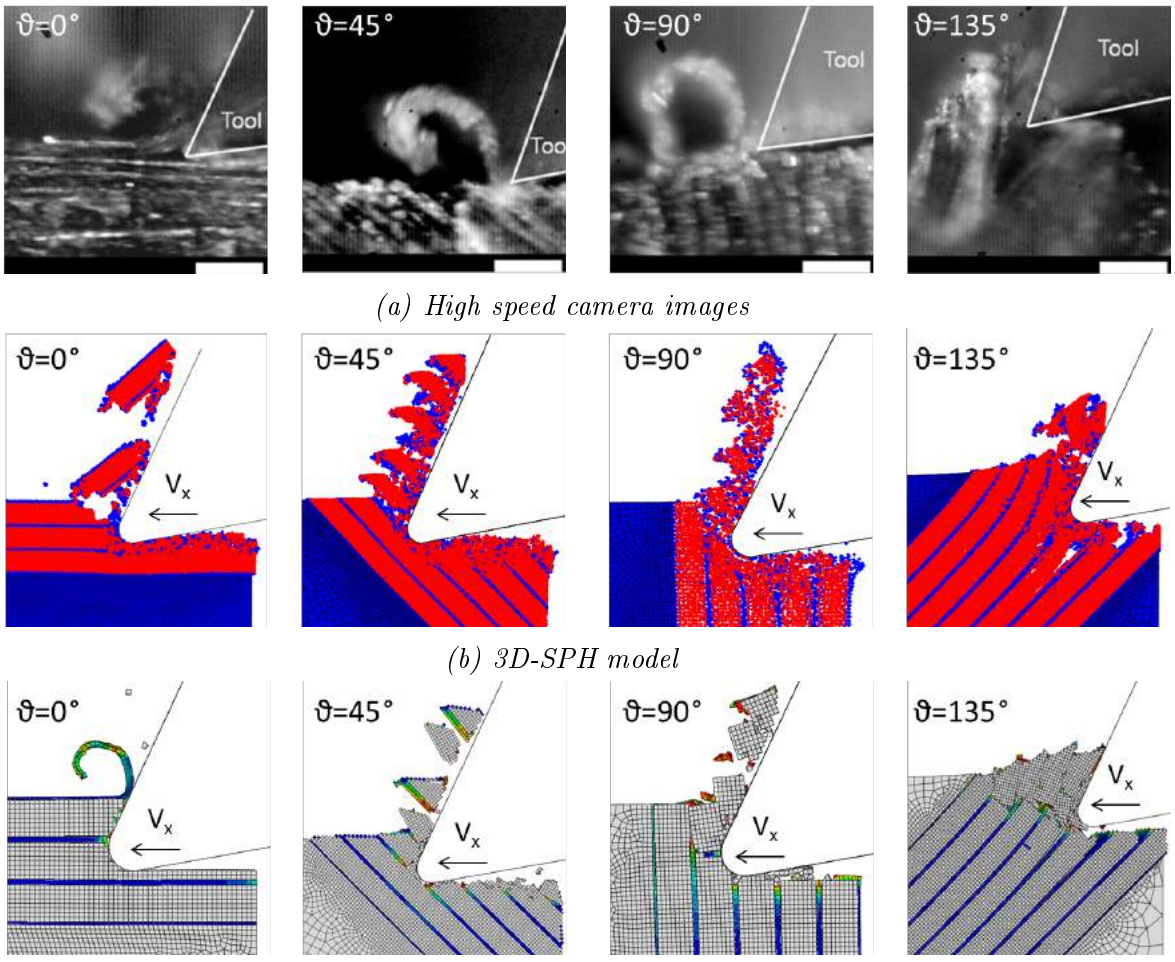

(a) High speed camera images

(b) 3D-SPH model

(c) 3D-FEM model

Figure 5.19: Comparison of chip morphology for different fibre orientations considering: (a) experimental results [25]; (b) 3D-SPH model; and (c) 3D-FEM model.

the 3D-FEM results. Even if the former produces a discontinuous chip, formed by short fibre pieces due to bending failure, the chip formation mechanism is more similar to that observed in the experiments. Differently, in the 3D-FEM model the element deletion due to failure causes non physical behaviour with material loss during cutting.

Generally, the 3D-FEM model generates a fragmented chip, which is formed by isolated fibre pieces with a few matrix elements attached to them. On the macro-scale it can be described as a powder-like chip. In contrast, the chip formed using the SPH method is

continuous for fibre angles θ=45° and θ=90°, as observed in the experiments. It is composed mainly of damaged particles, which can interact between each other after failure, deforming according to the constitutive model implemented in the VUMAT subroutine.

When machining at θ=90°, the chip sliding on the rake face tends to separate, forming a curling chip. This behaviour is comparable with the high-speed camera image. It is less visible for fibre orientation θ=45°.

Fibre angle θ=135° represents the most expensive numerical model. It is due to the large number of elements necessary to represent the composite material for that fibre orientation. For this reason, only the cutting length necessary to study and understand the chip formation mechanism was simulated. It is not enough to observe the formation of the periodic chip as for the other orientations. However, using the 3D-SPH model, fibres are able to withstand higher bending deformations. Even in this case, the 3D-FEM model generates a chip formed by separated short fibres. The SPH method seems more prone to show a deformation similar to the experimental image, where fibres deform in a bundle, remaining connected to each other.

5.4.3 Bouncing back

The bouncing back can be observed when using the SPH method; which is different from the FEM where the element deletion usually leads to a gap between the tool clearance face and the machined surface. Hence, the magnitude of the elastic recovery the material undergoes can be measured for the SPH method at each fibre orientation.

The cutting length represents an important factor that could affect the measurements.

In fact, after the tool has passed the material needs time to experience the elastic recovery. Hence, a long cutting length is required to move the tool far from the machined area, where the bouncing back is measured, allowing the material to reach the final configuration.

Except for fibre orientation θ=0°, material elastic recovery was not completed at the end of the analysis. In addition, chip formation was not completed during simulation at fibre angle θ=135°, due to the high computational cost. For this reason only the bouncing back at fibre orientation θ=0° has been measured. The bouncing back amount was estimated ∼5 μm, i.e. equal to the cutting edge radius of the tool, which represents the expected value based on the experimental observation of Wang and Zhang [24]. This result highlighted the ability of the SPH method to provide additional and important information when compared to the FEM. In fact, the bouncing back affects the actual depth of cut and the thrust force during cutting.

5.4.4 Validation of cutting force and thrust force

Cutting force and thrust force calculated in the 3D-SPH model were compared with results obtained by means of a 3D-FEM model and from experiments [25]. Cutting force prediction improves when using the 3D-SPH model, except for fibre orientation θ=135° (Figure 5.20). In particular, a good agreement can be observed for θ=0° and θ=90°. Cutting force at θ=45° remains underestimated with an error of ∼27 %. At fibre angle θ=135°, both the 3D-SPH model and the 3D-FEM model overestimate the cutting force, with the former showing a prediction which is double the experimental value. This could be attributed to the cutting length simulated, which is not sufficient to observe a periodic chip.

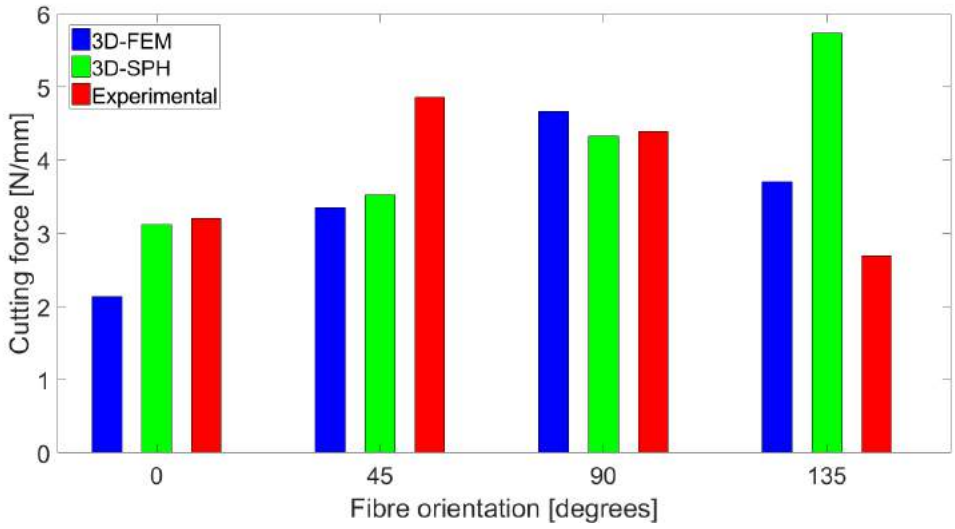

Figure 5.20: Cutting force comparison for the 3D-SPH model, 3D-FEM model, and experiments [25].

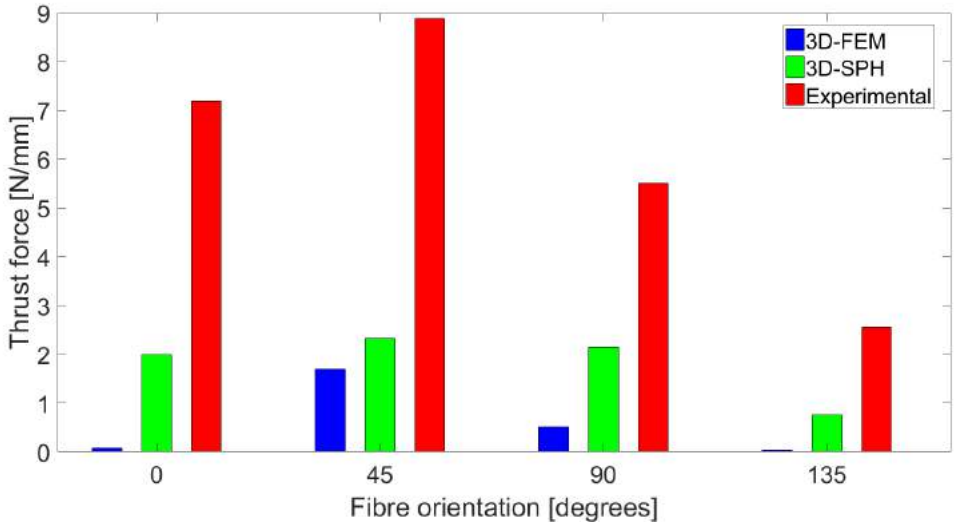

Figure 5.21: Thrust force comparison for the 3D-SPH model, 3D-FEM model, and experiments [25].

The SPH method shows a better agreement with the experimental results in terms of thrust force for all the fibre orientations considered (Figure 5.21). It is possible to observe a large increase in the force predicted compared to the 3D-FEM model, becoming closer to the experimental results. It is particularly evident for fibre angles θ=0°,90°,135°. However, thrust force is still underestimated for all fibre angles.

Since bouncing back and thrust force are connected, a longer analysis time could increase the thrust force due to an increase of the bouncing back, allowing the material to reach the final configuration after the tool has passed.

5.5 Summary

The smoothed particle hydrodynamics method has been employed to simulate the orthogonal cutting of UD-CFRP, using the micro-mechanical approach. Different fibre orientations have been considered and compared with the 3D-FEM model developed in the previous chapter, and with experimental results [25].

The chip formation mechanisms using the SPH method have been found to be more similar to the experiments, being also able to show the bouncing back. In particular, for fibre orientation θ=0° the cutting length simulated is enough to measure the final bouncing back amount, being equal to the cutting edge radius, as expected from the literature.

The chip formation mechanism differs when using the SPH or the FEM at fibre orientation of θ=0°, with the former being more similar to the experimentally observed mechanism. For fibre angles of θ=45°,90°,135° the chip formation mechanisms are similar for both methods.

For all fibre orientations, damage extension is larger when employing the SPH method. Also the matrix' plastic deformation in the machined workpiece results more extended.

In general, the chip morphology predicted by the SPH method seems to be more accurate when compared with high-speed camera images, being more prone to generate a continuous chip.

For θ=0° and θ=135°, it is possible to observe how the SPH method is able to predict behaviour similar to debonding at the fibre-matrix border.

The SPH method shows a better prediction in terms of cutting force for all fibre orientations, except for θ=135°. The high value presented for the latter can be associated with the cutting length simulated, which is not enough to obtain a periodic chip. Thrust force results improve using the SPH method for all fibre orientations. A longer cutting length could help increase the numerical results, and bring them closer to the experimental values.

Finally, the SPH method is able to improve the prediction of chip formation mechanisms and machining force during cutting compared with the generally used FEM. However, it is not able to provide any information on the fibre-matrix interface due to the absence of a cohesive model. Therefore, a hybrid model implementing a FEM to SPH conversion during the analysis, combining the advantages of both methods, will be presented in Chapter 7.

Chapter 6

Experimental investigation on the orthogonal cutting of UD-CFRP

6.1 Introduction

Experimental studies on the orthogonal cutting of UD-CFRP can be found in the literature. Generally, cutting force, thrust force, type of chip and chip formation mechanisms are the aspects investigated. The necessity to study different aspects in depth, including damage extension, surface roughness and bouncing back, and furthermore, to determine also the critical working parameters affecting each of them, led to the conducted in-house experiments. The direct observation of the process and the access to all data collected will be used to support the calibration of the model presented in the next chapter.

In the present chapter the experimental work on the orthogonal cutting of UD-CFRP composite is described. First, material properties are reported, followed by the

methodology employed with regards to the experimental set-up and the experimental plan. Afterwards, outcomes, in terms of types of chips and chip formation mechanisms, damage depth, surface quality and integrity, cutting force, thrust force and bouncing back are presented and discussed. Finally, an optimization for each fibre orientation is realised in order to improve the quality of the machined workpiece.

6.2 Material properties

Unidirectional samples of carbon fibre reinforced plastic with different fibre orientations were used to investigate the influence of the machining parameters on the orthogonal cutting process. The composite material is made of T800S carbon fibre and a very tough HexPly® M21 epoxy matrix (Table 6.1). The latter is used in primary aerospace structures exhibiting excellent damage tolerance, especially at high energy impacts [119].

Table 6.1: Properties of UD-CFRP [119, 120].

Material	Property	Value
Carbon fibre - T800S	Density	1.80 g/cm^3
	Tensile modulus	294 GPa
	Tensile strength	5.88 GPa
	Diameter	5 μm
	Volume percentage	56.6%
HexPly® M21	Tensile modulus	172 GPa
	Compression modulus	136 GPa
	In-plane shear modulus	5 GPa
	Tensile strength	3 GPa
	Compression strength	1.67 GPa
	In-plane shear strength	79 MPa

6.3 Methodology

6.3.1 Experimental set-up

In the literature, several works employed a milling machine with a locked tool spindle and the sample translating with the table [21, 29, 31]. The experiments were conducted using a similar set-up. In particular, a Cincinnati vertical milling machine was used with the tool held stationary, while the sample was subjected to a translational movement, being connected with the table of the machine, as shown in Figure 6.1.

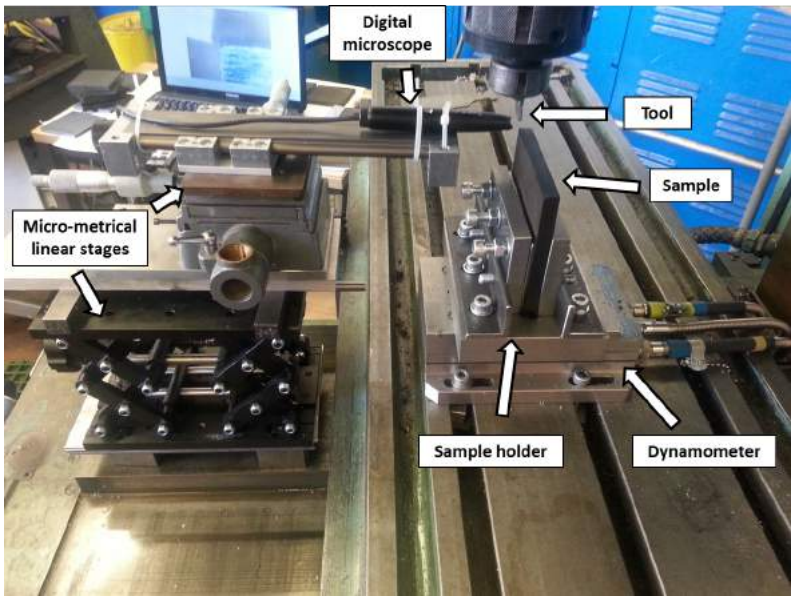

Figure 6.1: Experimental set-up.

Like previous investigations [23–26, 29–31], cutting force and thrust force were measured during cutting using a Kistler 9257A tri-axial dynamometer, which was connected to a data acquisition system and channel amplifier. In order to vertically position the workpiece on the dynamometer, a sample holder was appositely designed (Figure 6.1), similar to that used by Kahwash *et al.* [23]. A Supereyes® digital microscope was used to record the process

at 15 fps, and the videos obtained were used to analyse the chip types and chip formation mechanisms. It provided information for the lowest cutting speed in the range considered (12 mm/min) at different values of fibre orientation, rake angle and depth of cut. It was positioned on the side of the sample looking to the tool tip-workpiece contact area. The microscope was placed in the desired spot using three micro-metrical linear stages. It was provided with LED lights and connected to a laptop for the image acquisition.

Surface quality was assessed by means of surface roughness measurements using an Alicona Infinite Focus G5 optical scanner, as also employed by Kahwash *et al.* [23]. A scan along the centre line of the machined surfaces was performed using 2 μm vertical resolution and 4 μm lateral resolution at the interested depths of cut, as shown in Figure 6.2. In fact, a linear variation of the depth of cut was realised during cutting, as described later. The position along the sample at which the desired depth of cut is reached lies in an interval that takes into account the error to which the measurements are affected. The Alicona Infinite Focus G5 optical scanner was also used to obtain the machined surface profile, and calculate the bouncing back amount. The scanning electron microscope (SEM) was used to accurately measure the damage extension in the machined workpiece, as usually used in the

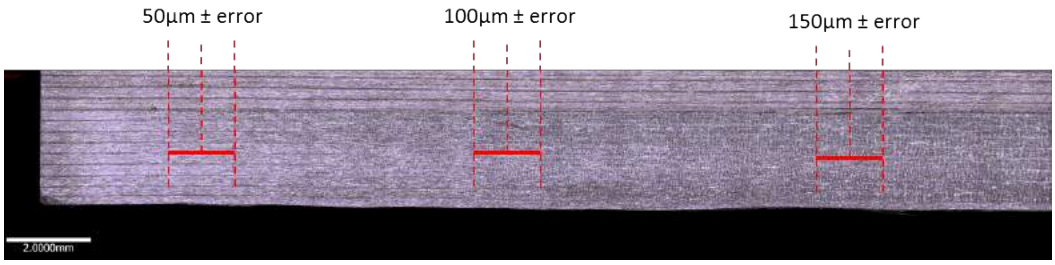

Figure 6.2: Location for surface roughness measurement on machined surface; error on depth of cut location not to scale.

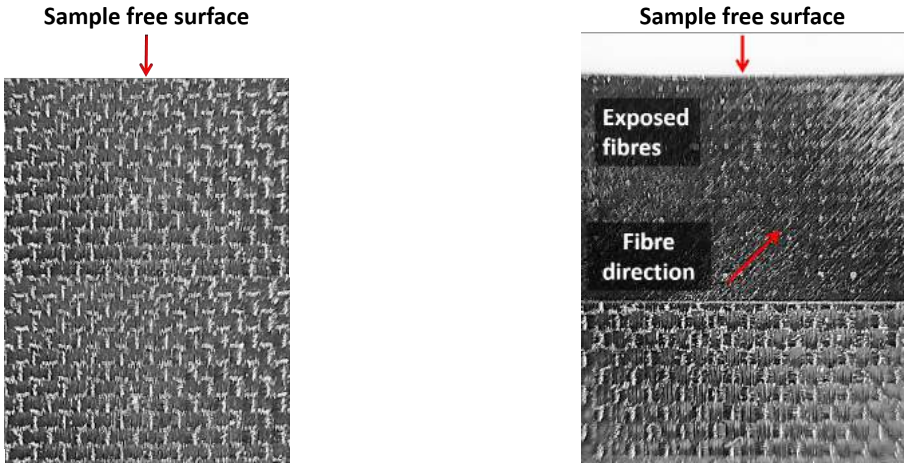

(a) *(b)*

Figure 6.3: Sample surface (a) before; and (b) after laser ablation.

literature [18, 20–22].

Before the experiments were conducted, the samples were subjected to laser ablation in order to expose the fibres (Figure 6.3); this allowed observation of the chip formation mechanism, and the damage formation and propagation during cutting.

Single point cutting tools with different rake angles were appositely modified by Cutter Grinders (B'ham) Ltd to meet dimensional requirements. They were measured using the Alicona Infinite Focus G5 optical scanner, showing an average value of the tool edge radius of about 20 μm, as shown in Figure 6.4.

The Cincinnati vertical milling machine is not a computer numerical control (CNC) machine, hence it makes it difficult to investigate the orthogonal cutting process for the depths of cut of interest (50-100-150 μm) because of their extremely small values and the very small difference between them (50 μm). In fact, it is challenging to address the desired depth of cut manually. Other than the error in the vertical positioning of the tool to

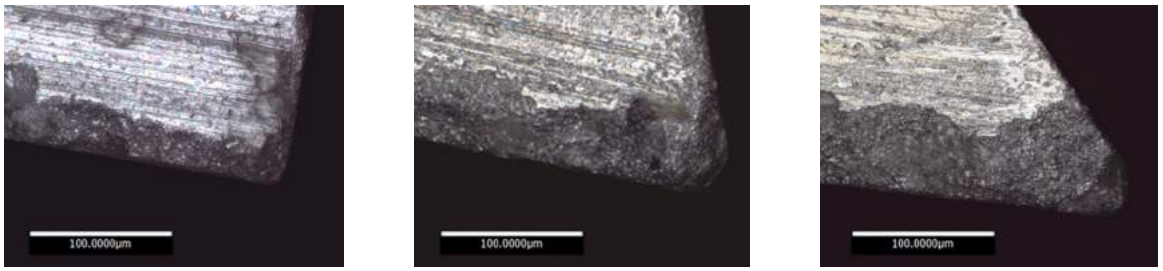

(a) (b) (c)

Figure 6.4: Cutting tools used for orthogonal cutting of UD-CFRP with rake angles (a) α=-10°; (b) α=10°; and (c) α=30°.

address the desired depth of cut, also a second contribution to the error has to be considered, which is due to the sample alignment to the horizontal direction. The latter error represents a challenge. In fact, even a very small error in the alignment to the horizontal direction produces an undesired variation in the depth of cut during machining. This can cause an undesired increase or decrease of the depth of cut, which could eventually lead to the absence of the cut after a certain cutting length. In addition, as the investigation involves three depths of cut close to each other, it can be compromised by this error. In order to reduce as much as possible the two contributions to the error described above, a linear variation of the depth of cut was achieved. It was developed during the experiments by providing a very small slope ($\beta \sim 0.44°$) to the sample, as shown in Figure 6.5. This was accurately realised using block gauges and double checked by means of a dial gauge having a resolution of 1 μm (Figure 6.5). Employing this methodology the digital microscope was used to align the tool tip with the sample corner at the start of the cutting in order to have a depth of cut equal to zero at the beginning. Calculating the angle β by means of the measurements obtained using the dial gauge, it is possible to know the depth of cut reached by the tool along the cutting path during machining.

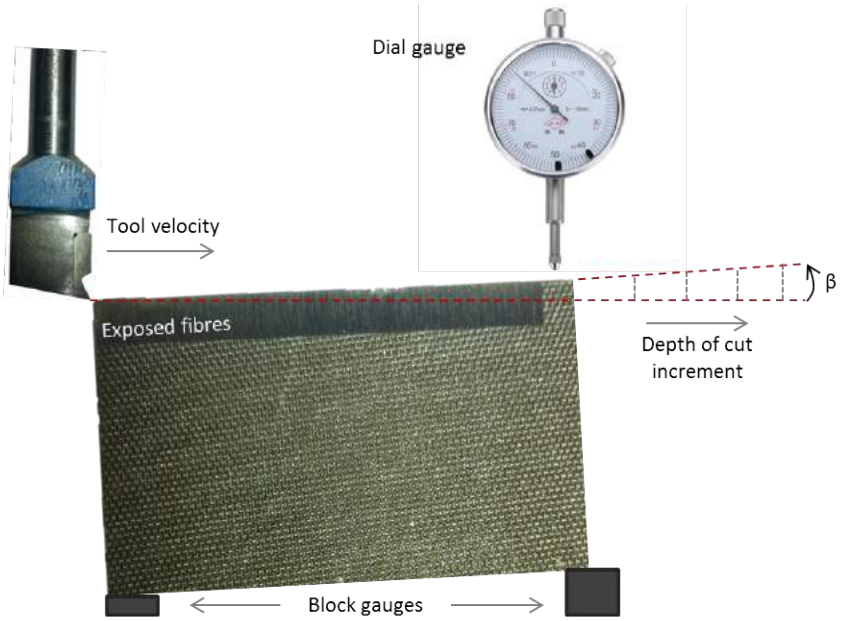

Figure 6.5: Schematic of the set-up for sample alignment; image not to scale.

6.3.2 The experimental plan

The machining parameters considered in the study involved: fibre orientation, cutting speed, depth of cut, and tool geometry in terms of rake angle. The values considered for each parameter are reported in Table 6.2.

Table 6.2: Machining parameters.

Factor	Symbol	Levels			
Fibre orientation	θ	0°	45°	90°	135°
Rake angle	α		-10°	10°	30°
Cutting speed (mm/min)	Vel		12	570	1100
Depth of cut (μm)	DOC		50	100	150

The effect of these factors on the cutting force, thrust force, chip formation mechanisms, type and morphology of the chip, surface quality and integrity, damage and bouncing back, was studied. Since a very small slope was imposed on the sample during cutting, all cutting

conditions, shown in Table 6.3, were carried out. These represent a total of 38 experiments.

Two experimental plans were considered. The first included testing the conditions reported in Table 6.3 to study the chip type and the chip formation mechanism. The second included a subset of Table 6.3 (reported in bold), which is based on the response surface methodology (RSM). It was used to carry out the analysis of variance (ANOVA) to identify the most critical process parameters, and to determine the optimal setting for these parameters. This approach has been widely used in the literature [23, 121–123].

The response surface method was employed using a face centred central composite design with three replications of the centre point (conditions 23/37/38). Three levels of each factor were considered and reported in Table 6.2. For the fibre orientations the three levels chosen were θ=45°, θ=90° and θ=135°. The response surface method and the ANOVA were carried out using the Design-Expert 7.0 software.

For each condition (N), types of chip, chip formation mechanisms and surface integrity were observed, and cutting force and thrust force were measured. The damage depth, surface roughness and bouncing back were obtained at the post-processing stage only for a subset composed of 27 out of 38 conditions reported in bold in Table 6.3.

Table 6.3: Experimental conditions carried out for orthogonal cutting of UD-CFRP.

Fibre orientation (degrees)	Rake angle (degrees)	Cutting speed (mm/min)	Depth of cut (μm)	N
		12	50/100/150	1
	-10°	570	50/100/150	2
		1100	50/100/150	3
		12	50/100/150	4
θ=0°	10°	570	50/100/150	5
		1100	50/100/150	6
		12	50/100/150	7
	30°	570	50/100/150	8
		1100	50/100/150	9
		12	**50**/100/**150**	10
	-10°	570	50/100/150	11
		1100	**50**/100/**150**	12
		12	50/100/150	13
θ=45°	10°	570	50/**100**/150	14
		1100	50/100/150	15
		12	**50**/100/**150**	16
	30°	570	50/100/150	17
		1100	**50**/100/**150**	18
		12	50/100/150	19
	-10°	570	50/**100**/150	20
		1100	50/100/150	21
		12	50/**100**/150	22
θ=90°	10°	570	**50**/**100**/**150**	23/37/38
		1100	50/**100**/150	24
		12	50/100/150	25
	30°	570	50/**100**/150	26
		1100	50/100/150	27
		12	**50**/100/**150**	28
	-10°	570	50/100/150	29
		1100	**50**/100/**150**	30
		12	50/100/150	31
θ=135°	10°	570	50/**100**/150	32
		1100	50/100/150	33
		12	**50**/100/**150**	34
	30°	570	50/100/150	35
		1100	**50**/100/**150**	36

6.4 Results and discussion

6.4.1 Types of chip

The image post-processing reveals a strong dependence on the type of chip on the fibre orientation and the rake angle, but less on the depth of cut. The type of chips are a consequence of the chip formation mechanisms.

For fibre orientation θ=0°, a powder-like chip occurs when using a negative rake angle for a depth of cut of 50 μm and 100 μm (Figure 6.6(a) and Figure 6.6(b)), and becomes coexistent with a discontinuous and very fragile chip at 150 μm (Figure 6.6). At a slightly positive tool rake angle (α=10°), a continuous curling chip was observed, whose thickness increased with the increase of the depth of cut (Figure 6.7). The different type of chips can be linked with the different chip formation mechanisms taking place during cutting and is discussed in section § 2.5.1. When machining with a negative rake angle the chip formation mechanism is represented by fibre failure due to buckling (Type II), which generates multi-fracture in the fibres ahead of the tool. For this reason the chip obtained tends to be a powder-like chip. Using positive rake angles, the tool advancement causes an opening in the material due to fibre-matrix interface failure, with consequent fibre bending. The chip slides on the rake face of the tool producing a continuous chip. At rake angle α=30° the chip slides on the tool rake face and similar to α=10° it is continuous with the thickness increasing with the depth of cut increase (Figure 6.8).

For fibre orientation θ=45°, a change in the chip type with the depth of cut was noticed for each rake angle (Figure 6.9). In fact, a transition from powder-like chip to continuous

chip with the increase of the depth of cut was observed. This is due to the independence of the chip formation mechanism from the rake angle when machining at θ=45°.

For fibre orientation θ=90° and negative or slightly positive rake angle (Figure 6.10), a powder-like chip was observed for a depth of cut of 50 μm and 100 μm. Differently from previous fibre orientations, where an increase of the depth of cut usually leads to a continuous chip, an almost absence of cut is experienced at 150 μm. Only a few small splinters flying off the workpiece were observed. The chip observed is due to the round cutting edge used, which is not able to cut the fibre at the contact point. Instead, it causes fibre bending as also observed by Pwu and Hocheng [27]. After the tool has passed, the fibres undergo elastic recovery coming back to the original position. Increasing the rake angle (Figure 6.11), the chip type changes. An irregular curling chip takes place with the thickness increase function of the depth of cut. This change could be attributed to the reduction of the contact area between the cutting tool and the workpiece, due to the increase of the rake angle. This makes the tool able to cut the fibre near the contact point. The chip type observed at positive rake angles corresponds to studies in the literature; indeed, Figure 6.11(b) and Figure 6.10(c) are comparable to Figure 2.11(a) and Figure 2.11(b) [26], respectively.

Unlike what was reported by Li *et al.* [26] where a similar chip type takes place over a wide range of fibre orientations (75°<θ≤180°), a change was observed in the experiments moving from θ =90° to θ=135°. Machining with a negative rake angle (Figure 6.12) produces a brittle discontinuous chip mixed with powder, whose thickness increases with the depth of cut. A slightly positive rake angle (Figure 6.13) leads to a continuous curling chip with greater thickness in correspondence to the highest depth of cut. For rake angle α=30° (Figure

6.14) a large amount of deformation takes place, so that deformed material completely covers the cutting tool. In order to analyse the chip type at a higher depth of cut, a photo was taken at the end of the cut showing a thick chip (Figure 6.14(c)). Differently from positive rake angles, when machining using a negative rake angle the larger amount of deformation the material undergoes during cutting favours a discontinuous chip.

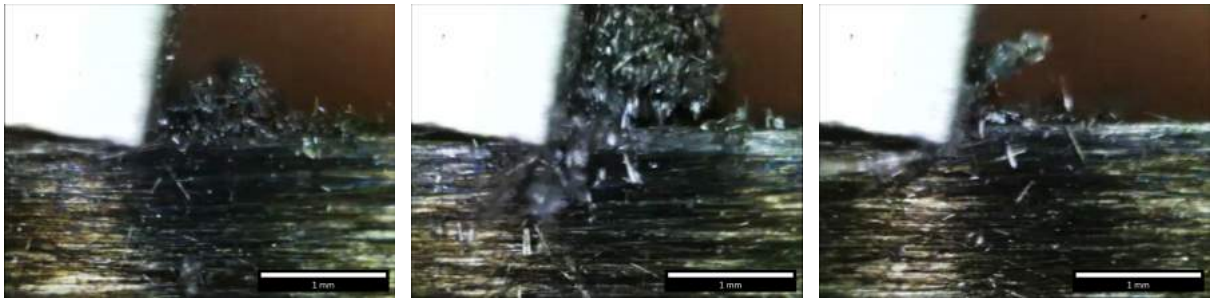

(a) *(b)* *(c)*

Figure 6.6: Chip formation during orthogonal cutting of UD-CFRP for condition 1 (θ=0°, α=-10°), and depth of cut (a) 50μm, (b) 100μm and (c) 150μm.

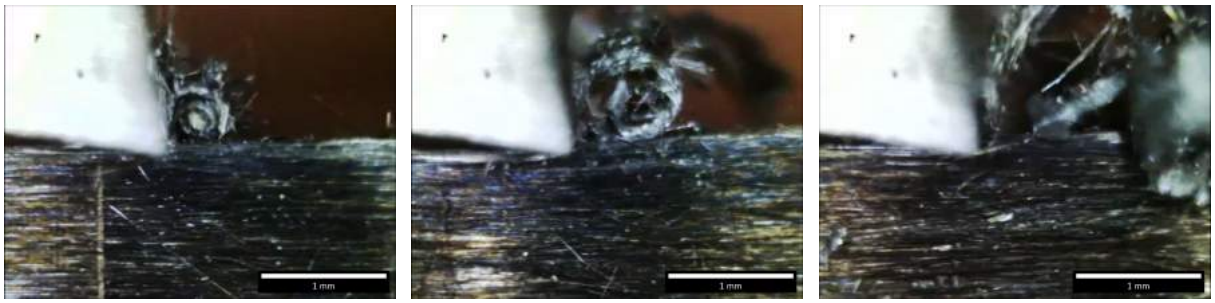

(a) *(b)* *(c)*

Figure 6.7: Chip formation during orthogonal cutting of UD-CFRP for condition 4 (θ=0°, α=10°), and depth of cut (a) 50μm, (b) 100μm and (c) 150μm.

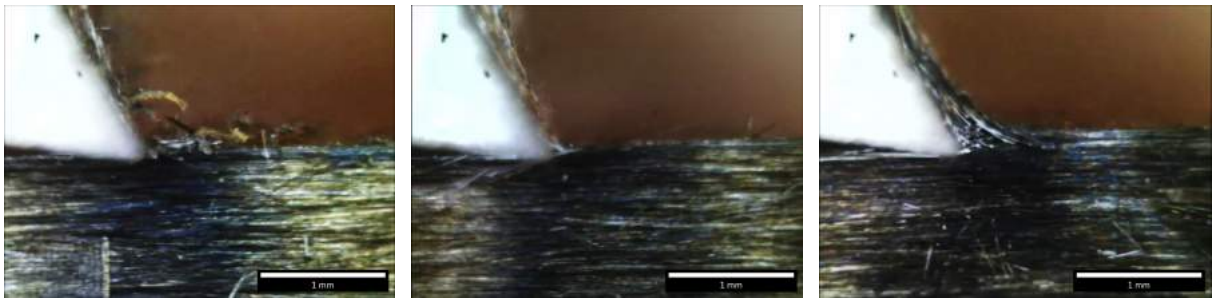

(a) (b) (c)

Figure 6.8: Chip formation during orthogonal cutting of UD-CFRP for condition 7 (θ=0°, α=30°), and depth of cut (a) 50µm, (b) 100µm and (c) 150µm.

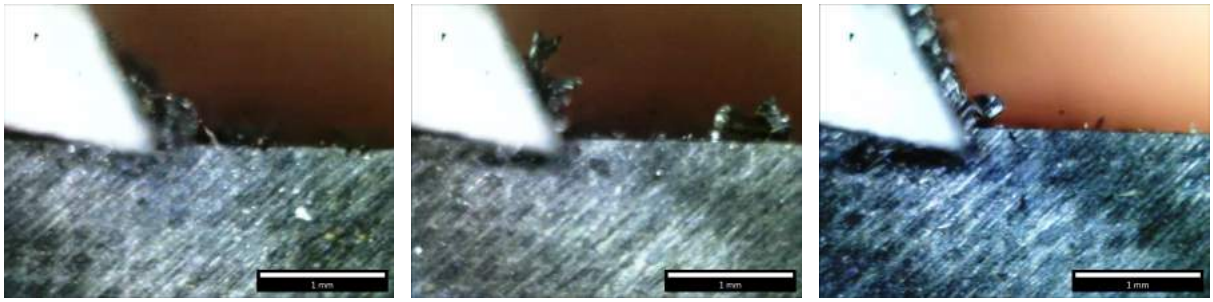

(a) (b) (c)

Figure 6.9: Chip formation during orthogonal cutting of UD-CFRP for condition 16 (θ=45°, α=30°), and depth of cut (a) 50µm, (b) 100µm and (c) 150µm.

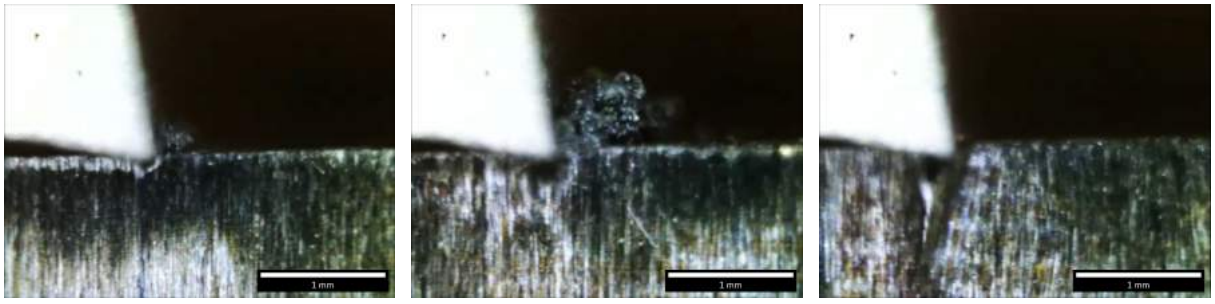

(a) (b) (c)

Figure 6.10: Chip formation during orthogonal cutting of UD-CFRP for condition 22 (θ=90°, α=10°), and depth of cut (a) 50µm, (b) 100µm and (c) 150µm.

(a) (b) (c)

Figure 6.11: Chip formation during orthogonal cutting of UD-CFRP for condition 25 (θ=90°, α=30°), and depth of cut (a) 50μm, (b) 100μm and (c) 150μm.

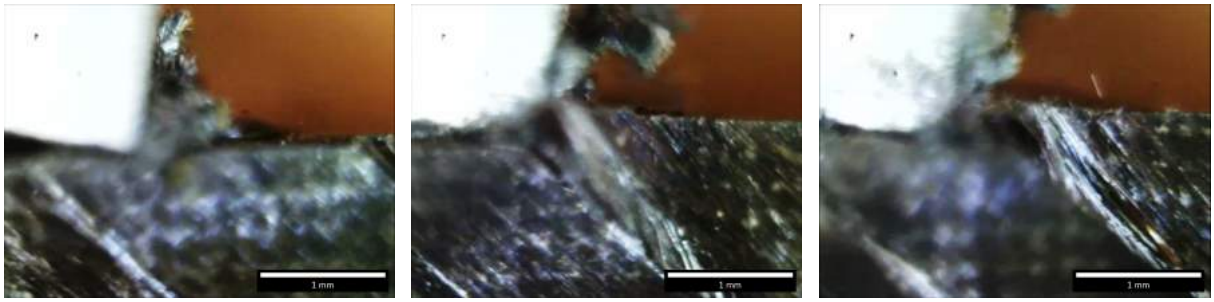

(a) (b) (c)

Figure 6.12: Chip formation during orthogonal cutting of UD-CFRP for condition 28 (θ=135°, α=-10°), and depth of cut (a) 50μm, (b) 100μm and (c) 150μm.

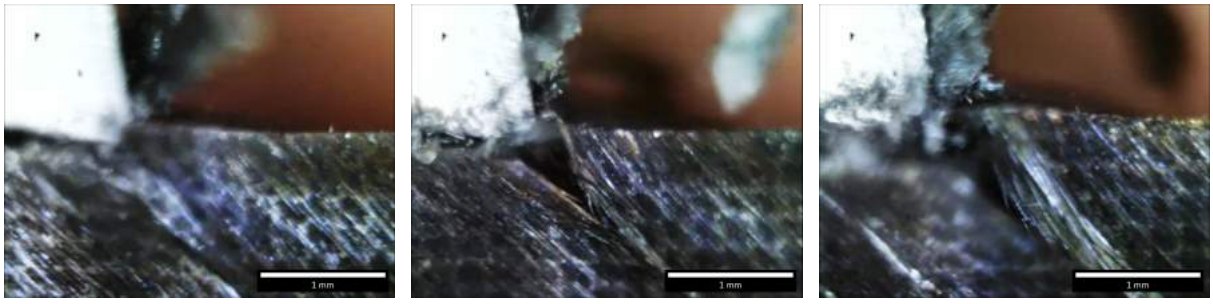

(a) (b) (c)

Figure 6.13: Chip formation during orthogonal cutting of UD-CFRP for condition 31 (θ=135°, α=10°), and depth of cut (a) 50μm, (b) 100μm and (c) 150μm.

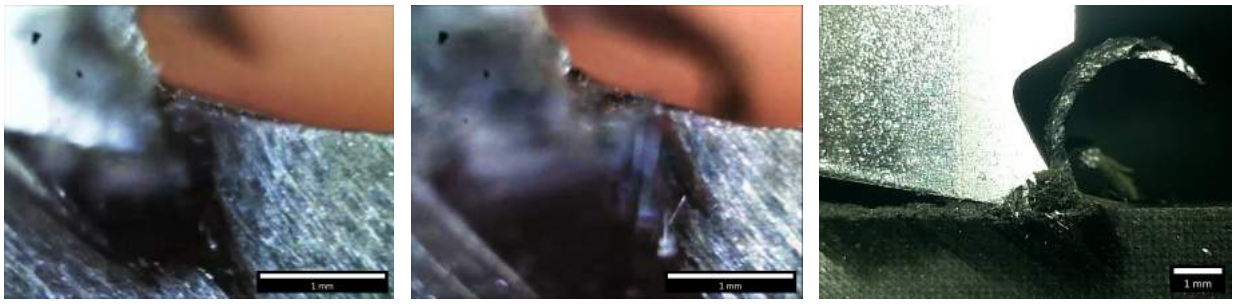

(a) (b) (c)

Figure 6.14: Chip formation during orthogonal cutting of UD-CFRP for condition 34 (θ=135°, α=30°), and depth of cut (a) 50μm, (b) 100μm and (c) at the end of cutting.

6.4.2 Chip formation mechanisms

Visual aids are fundamental to analysing the chip formation mechanisms, which were found to be highly dependent on fibre orientation and rake angle. In particular, images obtained by the digital microscope during cutting were used to develop a schematic of material removal for each condition. In addition, pictures from SEM were used to support and better understand the described behaviour. Even if these SEM images were obtained after machining, hence they were affected by tool deceleration till stopping, they could still provide useful information on the chip formation mechanism. However, the analysed samples were those machined with the lowest speed in order to reduce the deceleration effect as much as possible.

As observed in the literature (§ 2.5.1) for the Type II chip formation mechanism, at fibre orientation θ=0° and negative rake angle (Figure 6.15), fibre buckling represents the predominant failure mechanism at the tool tip. However, close observation of the data collected highlighted a more complex mechanism due to the round cutting edge of the tool, whose schematic is shown in Figure 6.15(a). Indeed, during tool advancement, damaged material in the form of powder and short fibres pieces, accumulates at the tool tip, dividing

the material flow into two parts ahead of the tool. The upper part generates a powder-like chip, while the lower part streams below the cutting tool, with fibres located below the cutting path pushed down. This behaviour is visible in Figure 6.15(b) and Figure 6.15(c), where powder-like material is accumulated, showing the shape of the cutting edge impressed on it at the end of the cut. In fact, looking at the pictures it is easy to imagine the tool position and shape. During cutting, the fractured material is pushed forward by the tool. It tends to lift the above material, located ahead of the tool, in which fibres experience bending deformation until failure near the tool tip (Figure 6.15(c)). Short fibre pieces formed and matrix parts contribute to generate a powder-like chip. Fibre failure is due to cracks, which propagate orthogonally to their axis (Figure 6.15(e)). Debonding and matrix fracture taking place between two consecutive fibres are also visible in Figure 6.15(d). Material forced to flow below the tool shows multi-cracks in the fibres due to the downward force exerted by the tool, as visible in Figure 6.15(f) and also observed by Wang and Zhang [24].

For positive rake angles, the continuous chip is due to a change in the material removal mechanism, whose schematics are reported in Figure 6.16(a) and Figure 6.17(a). As in the previous case, the tool divides the material into two parts, as shown in Figure 6.16(b), where areas with deformed fibres pointing downwards and upwards are clearly visible. Since the tool cutting edge is round, a zone where buckling takes place is always present, but reduced. The print left by the tool in the workpiece is visible in Figure 6.16(c). Due to the elastic recovery the chip returns to the horizontal position after the tool is removed. Bending failure of fibres was observed with cracks propagating orthogonal to their axis (Figure 6.16(d)), which is typical of a Type I mechanism. Fibre deformation, due to the downward force exerted by

the tool, causes cracks propagating across the fibre allowing the material to deviate (Figure 6.16(e)). A view of the machined surface from the top in Figure 6.16(f) shows fibres presenting multi-cracks due to the behaviour previously described. Independently from the depth of cut, fibre failure takes place very close to the tool tip for α=10°. This is due to the small value of the rake angle, which causes fibres to suddenly undergo large bending deformation.

In contrast, for a higher rake angle the upper material flow forming the chip comes from two distinct areas ahead of the tool (Figure 6.17). This behaviour was also observed by Li *et al.* [26] as reported in Figure 2.9. Similarly to a slightly positive rake angle, the material is divided at the tool tip, but shows a more gradual bending of fibres. In addition to this, a second flow of material is formed far from the tool tip. It is due to material peeling, and in agreement with Zitoune *et al.* [21] it becomes more significant with a depth of cut increase, moving farther ahead of the tool. Material opening in front of the tool is due both to fibre-matrix debonding and to matrix cracking, as shown in Figure 6.17(c). Even in this case, cracks due to bending propagate perpendicularly to the fibre axis (Figure 6.17(d)). The red line in Figure 6.17(b) indicates the extension of the chip that experienced elastic recovery after removing the tool. It was positioned on the tool rake face during cutting. The top view of the machined surface shows multi-fractured fibres as for the previous conditions (Figure 6.17(e)).

For fibre orientation θ=45° a similar chip formation mechanism was detected for all rake angles. Tool advancement causes multi-fracture in the fibres orthogonal to the fibre axis ahead of the tool (Figure 6.18). The first fracture takes place close to the trim plane. The upper part of the fibre forms the chip and the lower part flows below the cutting tool along with the

other pieces of damaged material due to deeper fractures. High magnification images (SEM) confirm the crack propagation orthogonally to the fibre axis and some subsurface damage. The fibre direction highlighted in the chip shows that the material undergoes shear along the fibre axis near to the tool tip. The shear magnitude increases with the rake angle reduction. The described mechanism is representative of Type III, where insignificant discrepancies can be observed for negative or positive rake angles, as reported in the literature (§ 2.5.1).

For fibre orientation θ=90° similar behaviour was observed at rake angles $\alpha = -10°$ and α=10° (Figure 6.19). The chip formation mechanism observed differs from that reported in Figure 2.6 (§ 2.5.1), which refers to a sharp cutting edge. Instead, it is similar to that described by Pwu and Hocheng [27] where a round cutting edge was used. Indeed, during advancement, the tool pushes the material ahead of it with fibres undergoing large bending deformation. It leads to deep damage due to separation of deformed material from the already machined zone. At the same time fibre compression failure near the tool tip takes place with the release of a powder-like chip. Once the tool has passed, the elastic recovery takes place, bringing the fibres back in position. In the meantime, the tool pushes forward the next area of material. The double action, due to elastic recovery and tool pushing, causes an increase in the depth of material separation. Fibre bundles observed in the SEM images, which are contained between two consecutive vertical cracks due to material separation (red arrows), confirm the described behaviour. For rake angle α=30°, the chip formation mechanism is different, leading to a continuous chip. Similarly, the tool pushes forwards causing the fibre to experience bending deformation. Due to a higher rake angle, the tool is sharper with a reduction of the contact area with the workpiece. During advancement, a crack propagates

from the tool tip horizontally ahead of the tool. The upper part slides on the rake face, forming the chip. Similarly to θ=45°, shear is experienced by the material in the plane parallel to the fibre orientation. The material below the crack undergoes elastic recovery, brushing against the clearance face. Independently from the rake angle, fibre failure due to bending was also observed below the cutting plane (Figure 6.19(b)), with cracks propagating orthogonal to the fibres' axis.

For fibre orientation θ=135° similar behaviour was observed for all rake angles (Figure 6.20). The cutting tool engages fibres during advancement, lifting the material and exerting a peeling action. Similarly to the Type V mechanism, fibres undergo large bending deformations leading to bending failure. The formed crack propagates through the fibres orthogonal to their axis towards the free surface of the sample, as shown in Figure 6.20(f). Even in this case the material is divided into two parts. The upper part forms the chip, while the lower undergoes elastic recovery. As already pointed out for fibre orientation θ=90°, the combined effect of the tool pushing and elastic recovery increases the damage depth due to material separation. An example of the deformation carbon fibres can undergo is shown in Figure 6.20(d), which is useful in order to understand the nature of material separation due to fibre peeling. In particular, a magnification of the area of interest is reported in Figure 6.20(e). It is possible to observe that the material separation is due to a combination of fibre-matrix debonding and matrix fracture between two consecutive fibres.

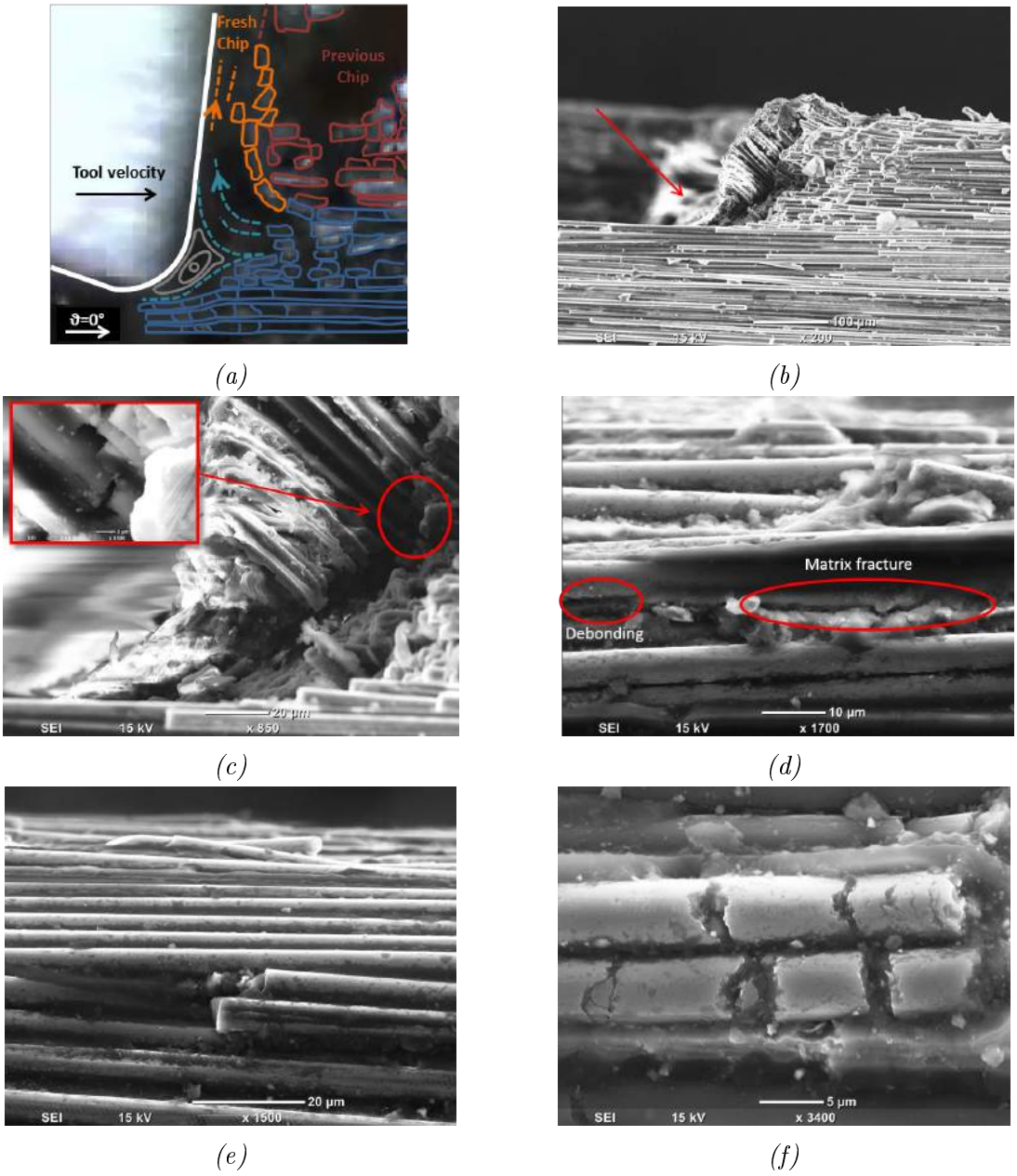

Figure 6.15: Chip formation mechanism at fibre orientation θ=0° and tool rake angle α=-10°: (a) schematic on digital microscope image captured during cutting; (b) chip root (SEM); (c) zoom of the chip root (SEM); (d) matrix damage on side view (SEM); (e) fibre damage on side view (SEM); (f) top view of machined surface.

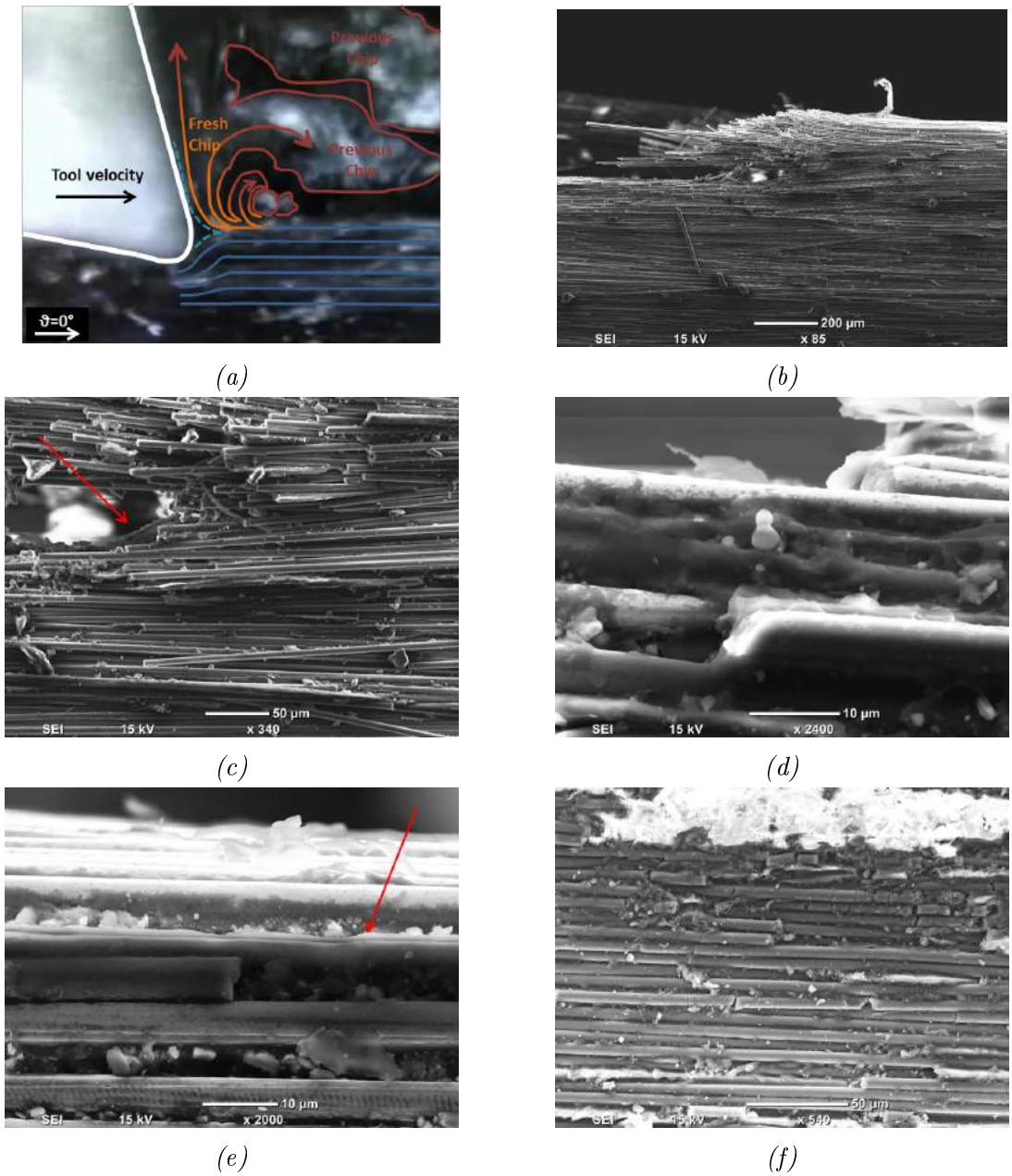

(a) *(b)*

(c) *(d)*

(e) *(f)*

Figure 6.16: Chip formation mechanism at fibre orientation θ=0° and tool rake angle α=10°: (a) schematic on digital microscope image captured during cutting; (b) chip root (SEM); (c) zoom of the chip root (SEM); (d) fibre failure on side view (SEM); (e) fibre crack on side view (SEM); (f) top view of machined surface.

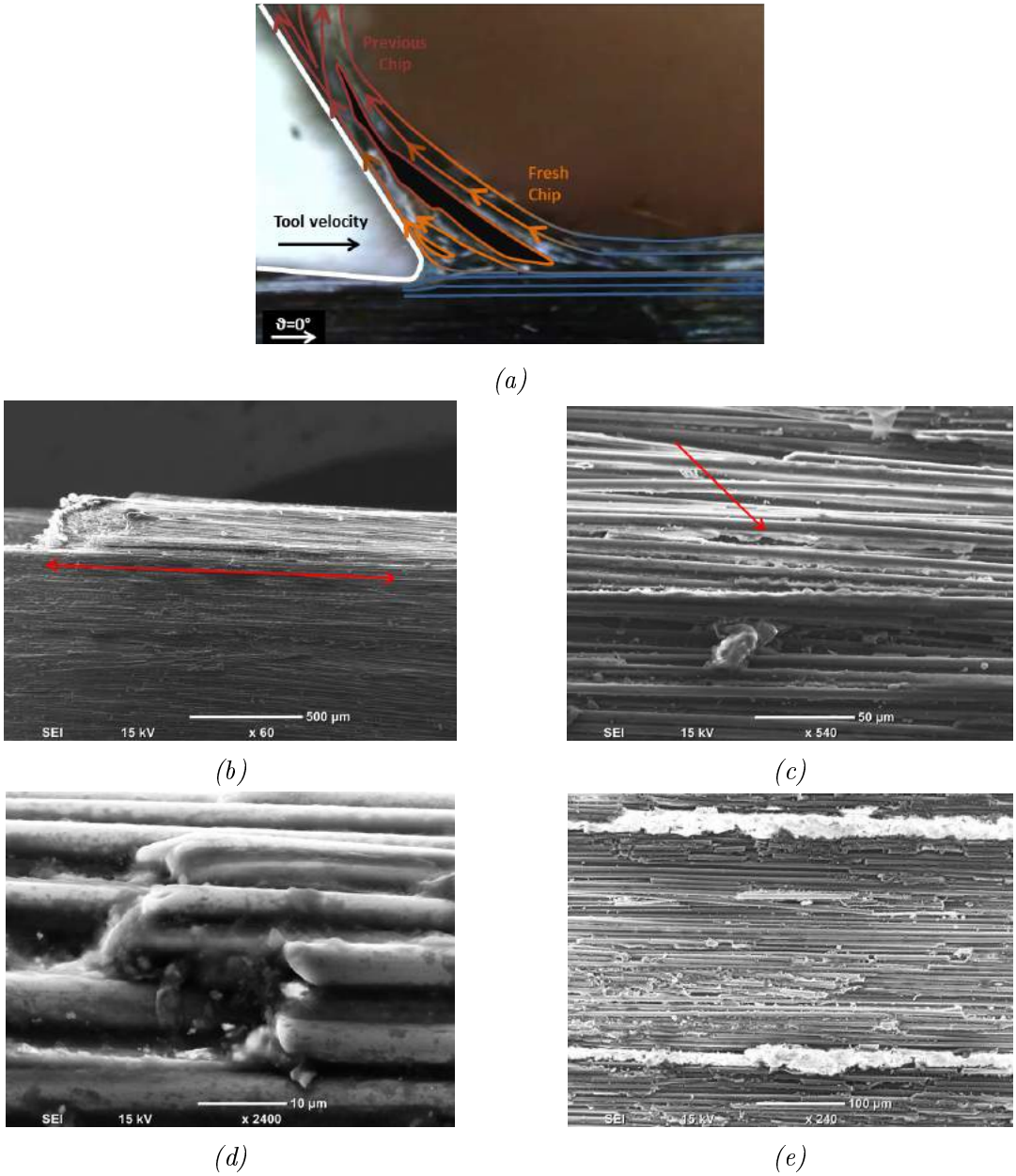

Figure 6.17: Chip formation mechanism at fibre orientation θ=0° and tool rake angle α=30°: (a) schematic on digital microscope image captured during cutting; (b) chip root (SEM); (c) matrix damage on side view (SEM); (d) fibre failure on side view (SEM); (e) top view of machined surface.

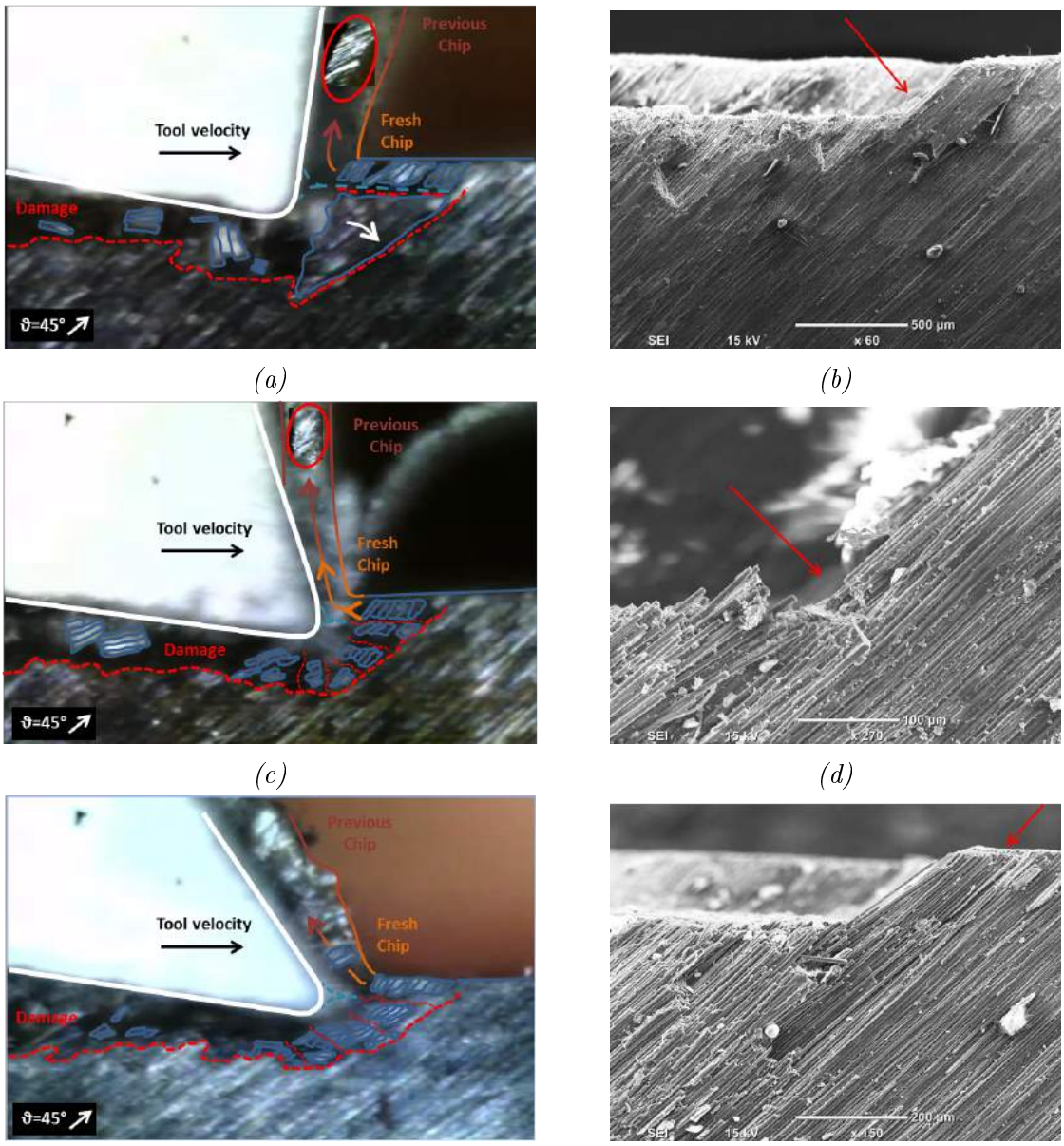

Figure 6.18: Chip formation mechanism at fibre orientation θ=45° and tool rake angle (a-b) α=-10°; (c-d) α=10°; (e-f) α=30°.

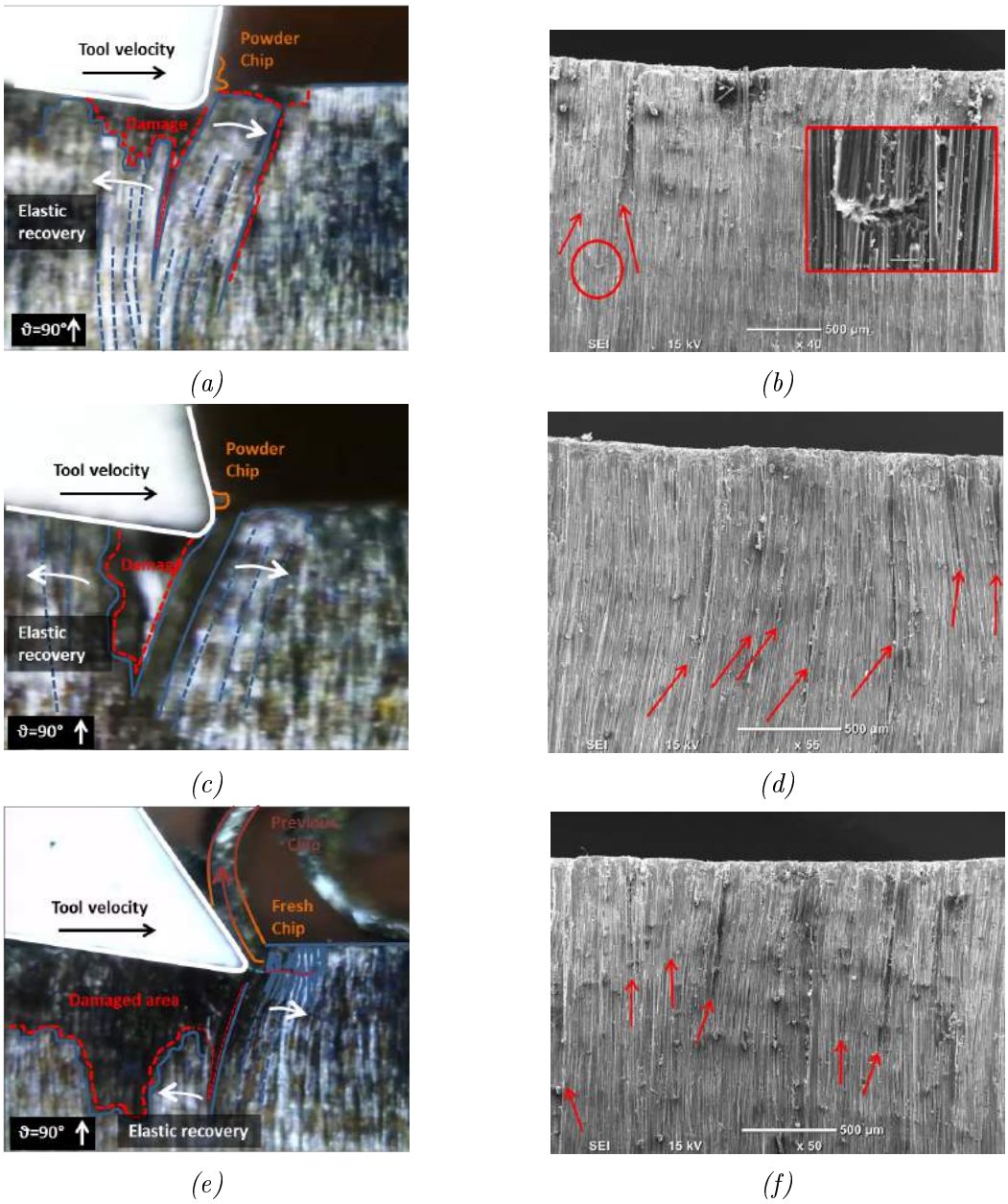

Figure 6.19: Chip formation mechanism at fibre orientation θ=90° and tool rake angle (a-b) α=-10°; (c-d) α=10°; (e-f) α=30°.

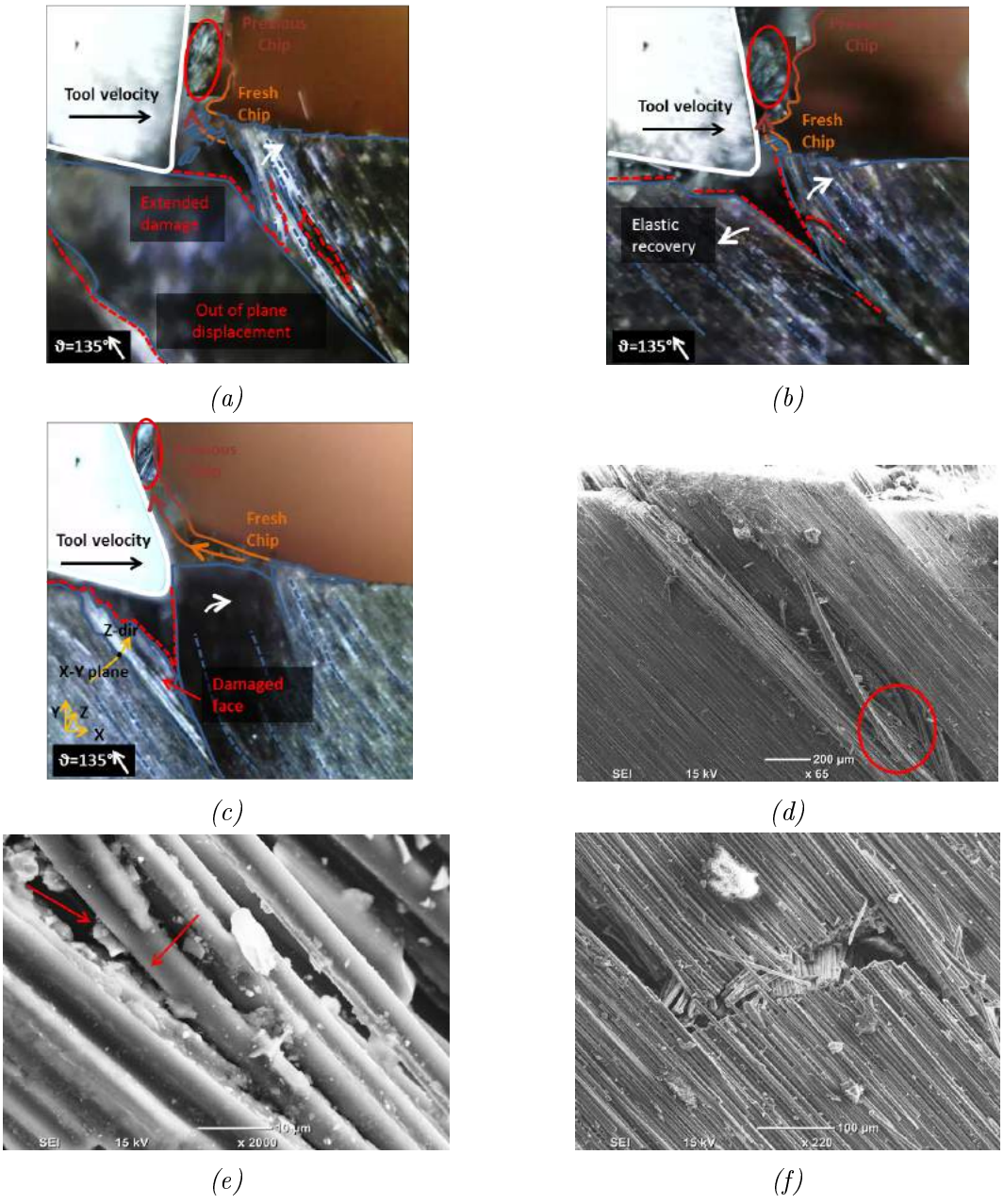

Figure 6.20: Schematic of chip formation mechanism at fibre orientation θ=135° and tool rake angle (a) α=-10°; (b) α=10°; (c) α=30°; and (d-f) workpiece damage on side view.

6.4.3 Analysis of response surface of DOE

The results for the experimental conditions reported in the DOE are shown in Table 6.4. Examples of the trends for the cutting force and the thrust force during cutting are shown in Figure 6.21. The values of the cutting force and thrust force, reported in Table 6.4, were obtained at the desired depth of cut as the average in the interval, whose limits take into account the error on the position of the depth of cut along the sample (Figure 6.2).

The analysis of variance (ANOVA) was carried out to identify the most critical working parameters affecting each output variable. The p-value represents the probability that the parameter x_i has an effect on the output variable. In this work, a 95% confidence level was assumed. This means parameters with p-value less than 0.05 are important. In Table 6.5 p-values for each parameter x_i and their combined effect $x_i x_j$ are reported.

The R-square represents a measure of the model fit. Results obtained for the R-square, reported in Table 6.6, suggest that the 2-factorial interaction (2FI) model can be used to achieve good predictions of cutting force, thrust force and damage depth. In addition, a quadratic model is able to provide good results for surface roughness and bouncing back. In fact, the R-square values are around 90% and above.

Equations for prediction of the output variables (var), as a function of process parameters, can be expressed in the following general form:

$$\begin{aligned} var = a + bx_1 + cx_2 + dx_3 + ex_4 + fx_1x_2 + gx_1x_3 + hx_1x_4 + ix_2x_3 \\ + mx_2x_4 + nx_3x_4 + px_1^2 + qx_2^2 + rx_3^2 + sx_4^2 \end{aligned} \tag{6.1}$$

where x_1, x_2, x_3 and x_4 represent fibre orientation, rake angle, cutting velocity and depth of cut, respectively. Equations' coefficients obtained by the software Design-expert 7.0 are reported in Table 6.7.

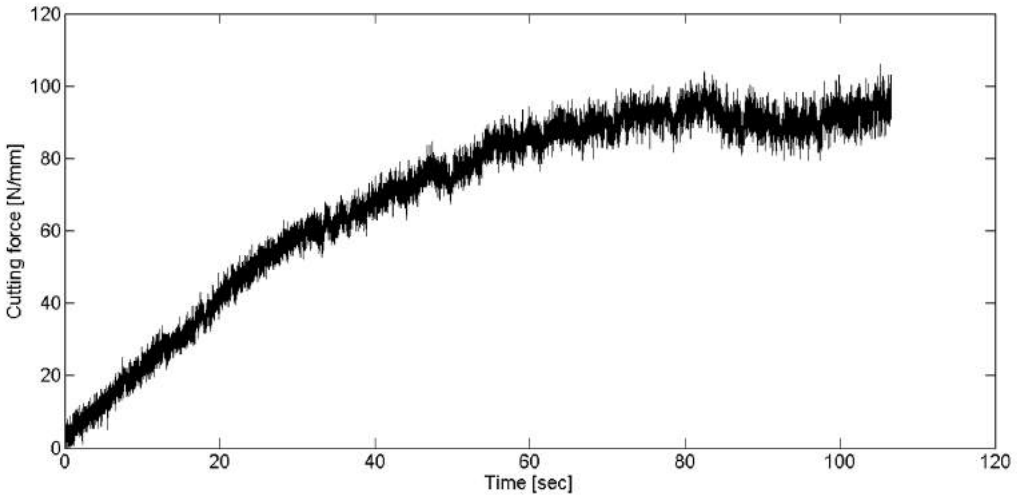

(a)

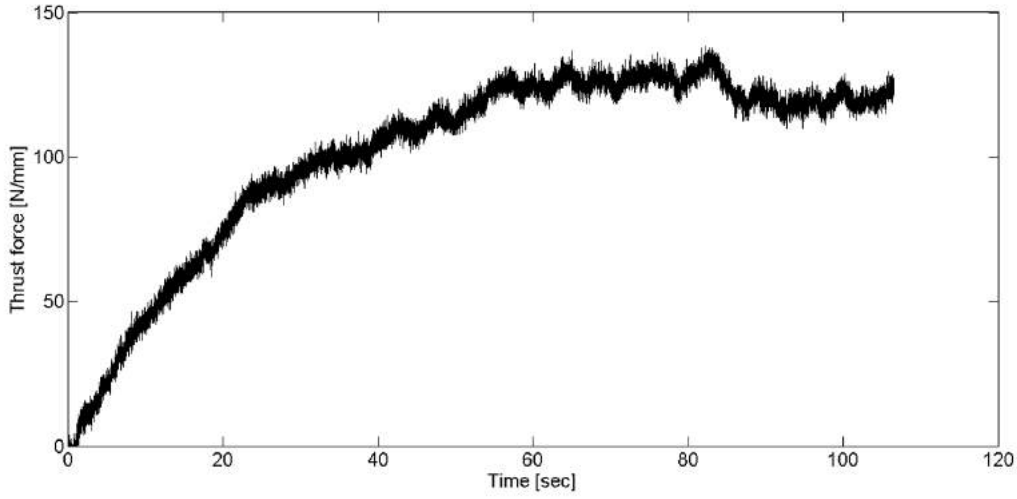

(b)

Figure 6.21: (a) Cutting force and (b) thrust force during cutting for Condition 16.

Table 6.4: Experimental results.

Fibre orientation (degrees)	Rake angle (degrees)	Cutting speed (mm/min)	Depth of cut (mm)	Cutting force (N/mm)	Thrust force (N/mm)	Surface roughness (Ra) (μm)	Damage depth (μm)	Bouncing back (μm)	N
		12	50	38.3	52.9	0.56	117.2	24	10
	-10°	12	150	113.4	81.7	0.62	292	24	10
		1100	50	25.5	50.5	0.3	117	23.9	12
		1100	150	78.4	80.44	0.47	182.5	30	12
θ=45°	10°	570	100	60.2	82.9	1.02	328.5	16.1	14
		12	50	62.4	115	0.45	162.3	31.6	16
	30°	12	150	102	122.7	1.37	328.5	36.4	16
		1100	50	61.63	117	0.54	122.55	20.7	18
		1100	150	90.14	124.7	1.11	255.47	23.59	18
	-10°	570	100	93.64	66.27	1.06	588.235	34.7	20
		12	100	103.1	66.26	0.85	760.24	23.43	22
		570	50	78.5	60.2	0.52	245.098	8.4	23
		570	100	131.9	44.6	2.31	2043.8	19.54	23
θ=90°	10°	570	100	157.4	35.72	2.73	2549.02	28.18	37
		570	100	140.6	56.67	1.73	980.392	7.49	38
		570	150	202.7	53.17	2.81	2549.02	12.61	23
		1100	100	147.3	54.18	1.96	985.4	15.14	24
	30°	570	100	129.6	55.29	3.2	1240.88	29.25	26
		12	50	124	42.1	18.5	1372.55	194.159	28
	-10°	12	150	211.7	72.46	29.16	4901.96	413.12	28
		1100	50	165	49.5	17.72	2745.1	159.98	30
		1100	150	200.5	72.87	43.29	4411.76	295.304	30
θ=135°	10°	570	100	214.2	27.88	19.02	2352.94	55.14	32
		12	50	189	-24	5.83	1960.78	0	34
	30°	12	150	220.5	-37.2	14.7	3000	0	34
		1100	50	147	-20	6.11	1431.37	0	36
		1100	150	185.1	-29.9	14.74	2549.02	0	36

Table 6.5: Influence of process parameters on output variables: p-value.

Process parameters	Cutting force	Thrust force	Damage depth	Surface roughness	Bouncing back
Fibre orientation (x_1)	**<0.0001**	**<0.0001**	**<0.0001**	**<0.0001**	**0.0004**
Rake angle (x_2)	0.1930	**0.0012**	0.1799	**0.0008**	**<0.0001**
Cutting velocity (x_3)	0.5353	0.8442	0.9714	0.3409	0.3438
Depth of cut (x_4)	**0.0001**	**0.0174**	**0.0013**	**0.0017**	0.0616
x_1x_2	0.8344	**<0.0001**	0.0783	**0.0003**	**<0.0001**
x_1x_3	0.8941	0.5964	0.9605	0.3111	0.4457
x_1x_4	0.9728	0.2285	**0.0141**	**0.0023**	0.0687
x_2x_3	0.4595	0.7523	0.4614	0.3628	0.4858
x_2x_4	0.2498	**0.0032**	0.2455	0.2198	0.0606
x_3x_4	0.4185	0.9422	0.4471	0.3058	0.6491
x_1^2				**0.0022**	0.3061
x_2^2				0.9083	0.3703
x_3^2				0.8241	0.6588
x_4^2				0.9205	0.9049

Table 6.6: Models' summary statistics.

Output variable	Model fit	R-Squared
Cutting force	2FI	0.89
Thrust force	2FI	0.98
Damage depth	2FI	0.87
Surface roughness	Quadratic	0.95
Bouncing back	Quadratic	0.91

Table 6.7: Model coefficients for each output variable.

Coeff.	Cutting force	Thrust force	Damage depth	Surface roughness	Bouncing back
a	-62.34078	71.16719	-1195.60251	20.61315	28.33589
b	1.27039	-0.34785	12.29852	0.63961	-1.43711
c	1.44578	3.82401	43.43755	0.39097	4.34509
d	0.012795	-3.61647e-3	0.51158	-2.61787e-3	-0.021271
e	0.75006	0.29579	-1.38042	-0.056215	-0.37485
f	-1.40208e-3	-0.039019	-0.32295	-4.77887e-3	-0.074506
g	3.28074e-5	4.79473e-5	3.17758e-4	3.64457e-5	-3.42804e-4
h	-9.13889e-5	-1.20889e-3	0.18927	1.44424e-3	9.45784e-3
i	-4.13660e-4	6.41085e-5	-0.010718	-7.33613e-5	7.03574e-4
m	-7.09187e-3	-7.51125e-3	-0.18628	-1.09216e-3	-0.022043
n	-1.81319e-4	-5.88235e-6	-4.42734e-3	3.31766e-5	-1.82604e-4
p	0	0	0	4.01949e-3	0.014014
q	0	0	0	6.19128e-4	0.061777
r	0	0	0	-1.61521e-6	4.06196e-5
s	0	0	0	-8.57595e-5	1.29633e-3

6.4.4 Induced damage and surface integrity

The significant parameters influencing the damage depth can be obtained by observing the p-value reported in Table 6.5. Results show that damage depth is significantly influenced by fibre orientation and by depth of cut, which is in agreement with the literature [24]. A better understanding of the effect of these parameters on damage depth is provided through the observation of the model graph reported in Figure 6.22.

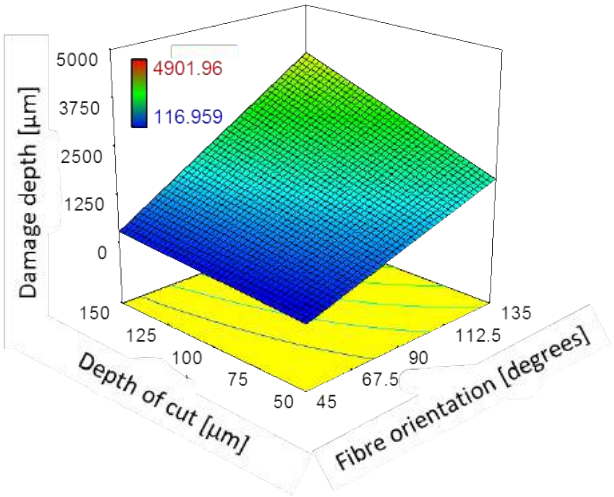

Figure 6.22: Combined effect of fibre orientation and depth of cut on damage depth for α: 10°and Vel: 570mm/min.

In the graph, variables not reported on the axis are considered constant and fixed to the middle level reported in Table 6.2. Damage depth increases with the increase of fibre orientation and depth of cut, as supported by the literature [15, 16, 24, 35]; leading to very high levels of damage when both effects are combined. In particular, the effect of the depth of cut is more visible when increasing the fibre orientation.

Damage variation with fibre orientation is shown in Figure 6.23, obtained using SEM. It is clear that the damage depth rises with the fibre angle increase. As expected from

(a) Condition 5

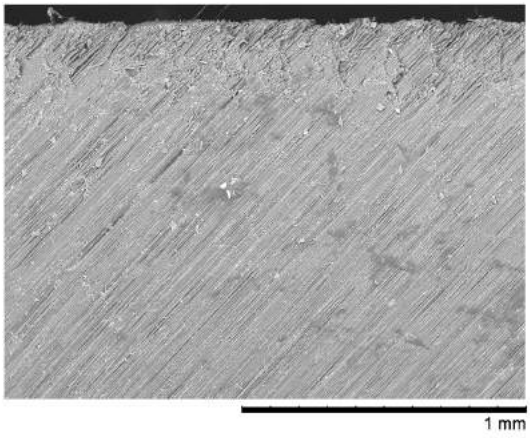

(b) Condition 14

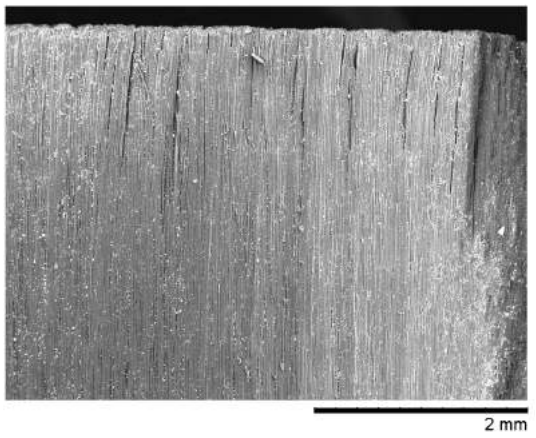

(c) Condition 23

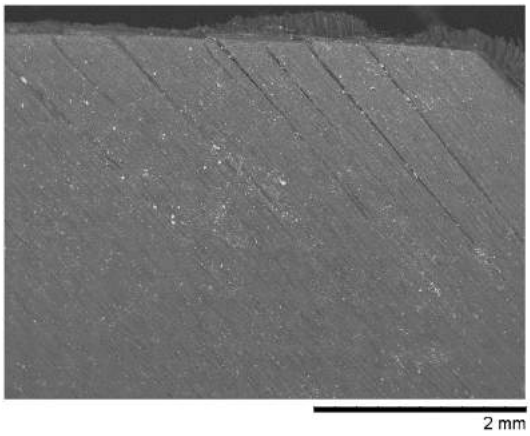

(d) Condition 32

Figure 6.23: Damage in machined workpiece for different fibre orientation and depth of cut 50 μm.

the ANOVA results, the minimum amount of damage was experimentally detected for fibre orientation θ=0°, where the damage is contained close to the trim plane, as observed also in the literature [16, 20].

Images obtained by digital microscope can also provide some useful information about damage evolution during cutting; while the Alicona Infinite Focus G5 optical scanner and

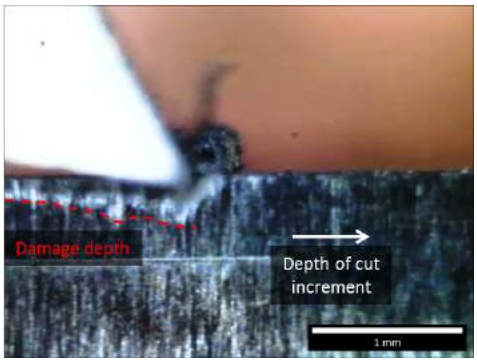

(a) Condition 25

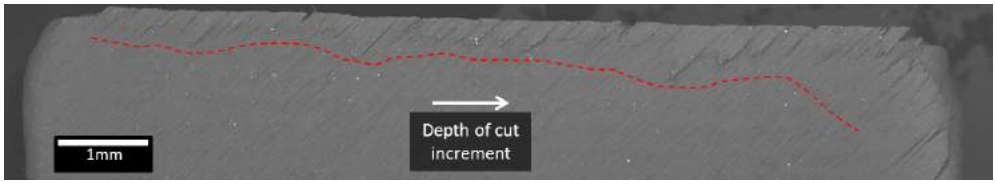

(b) Condition 10

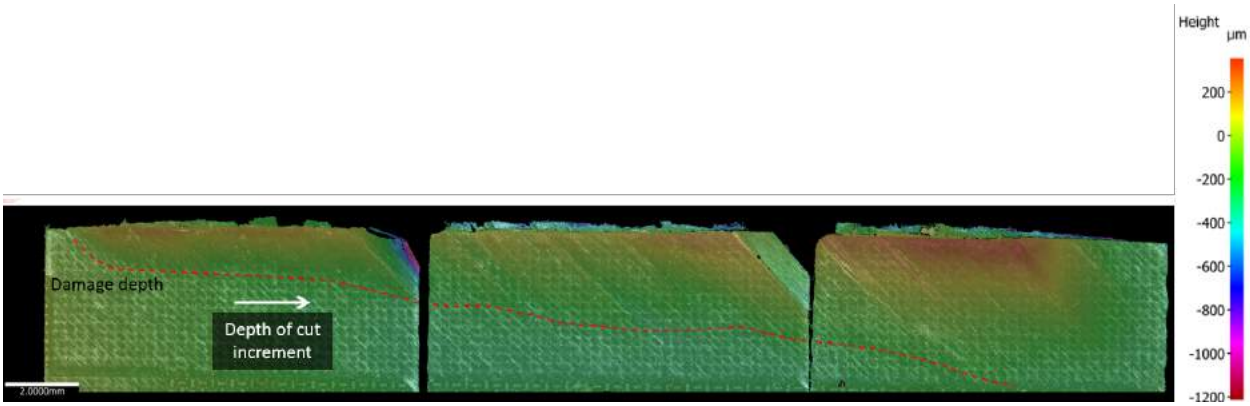

(c) Condition 36

Figure 6.24: Analysis of damage depth using (a) digital microscope, (b) SEM, and (c) Alicona Infinite Focus G5 optical scanner.

SEM can be used in the post-processing phase, as shown in Figure 6.24. The SEM was used to obtain very accurate measurements up to fibre diameter scale. In particular, it is clear how the damage depth increases with the depth of cut increase.

The Alicona Infinite Focus G5 optical scanner was used to scan the machined surfaces of the samples obtaining more detailed information about the depth of cut, reported in terms of a colour map. This is shown in Figure 6.25 and Figure 6.26, which are relative to the lowest

cutting velocity used in the experiments. In addition, profiles of the machined surfaces at the centre of the cut were obtained.

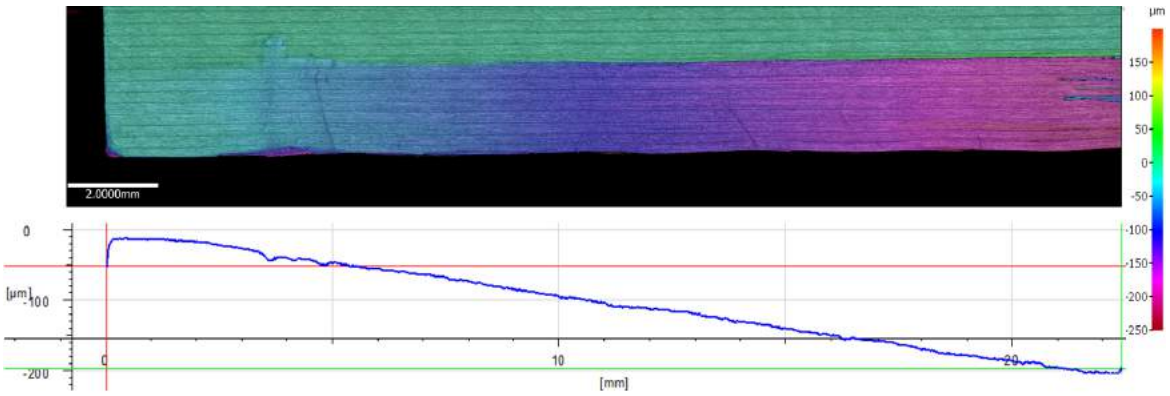

(a) Condition 7

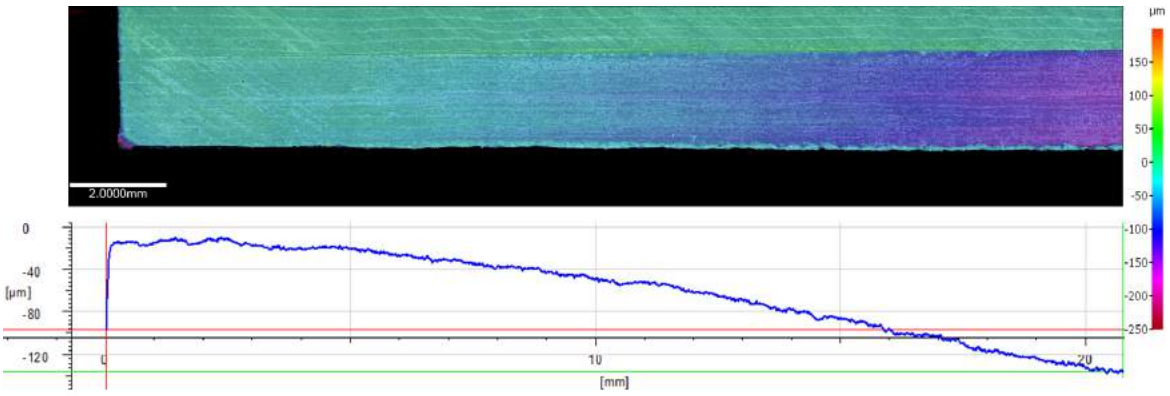

(b) Condition 16

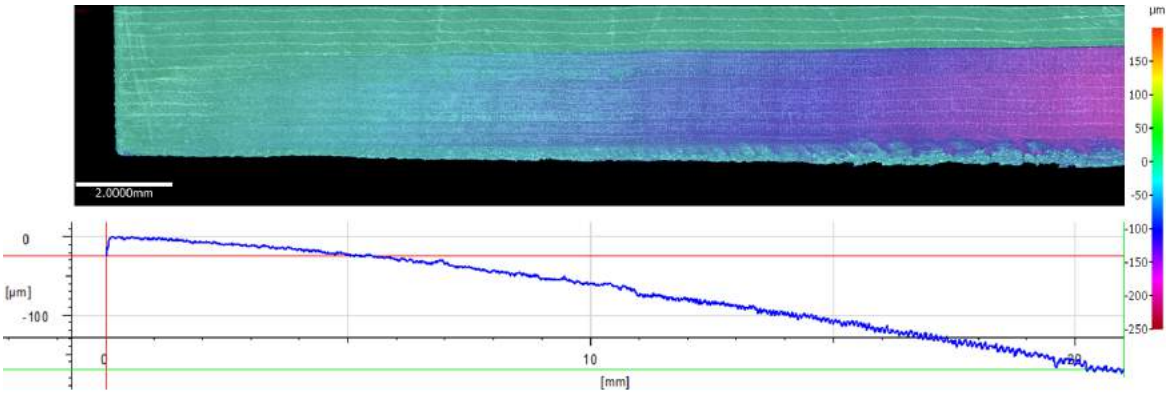

(c) Condition 22

Figure 6.25: Depth of cut evolution along the cutting path for: (a) Condition 7 (θ=0˚α=30˚); (b) Condition 16 (θ=45˚, α=30˚); and (c) Condition 22 (θ=90˚, α=10˚).

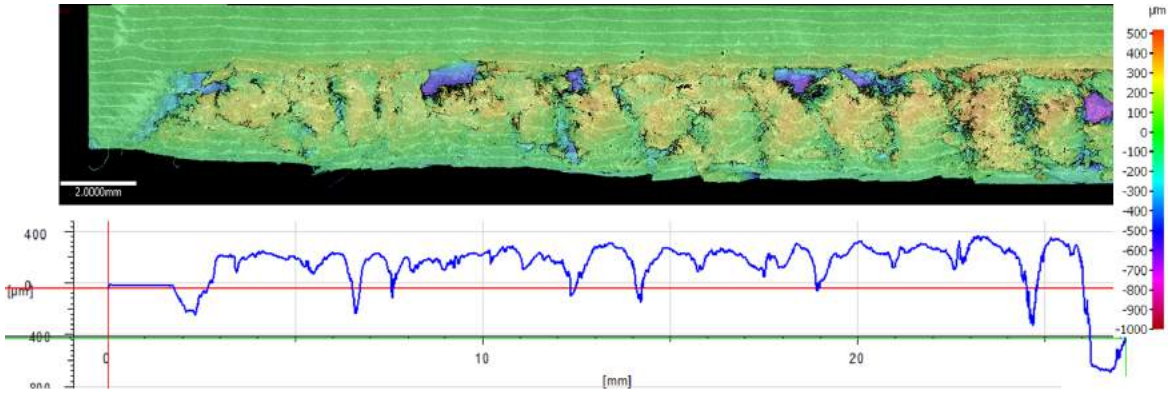

(a) Condition 28

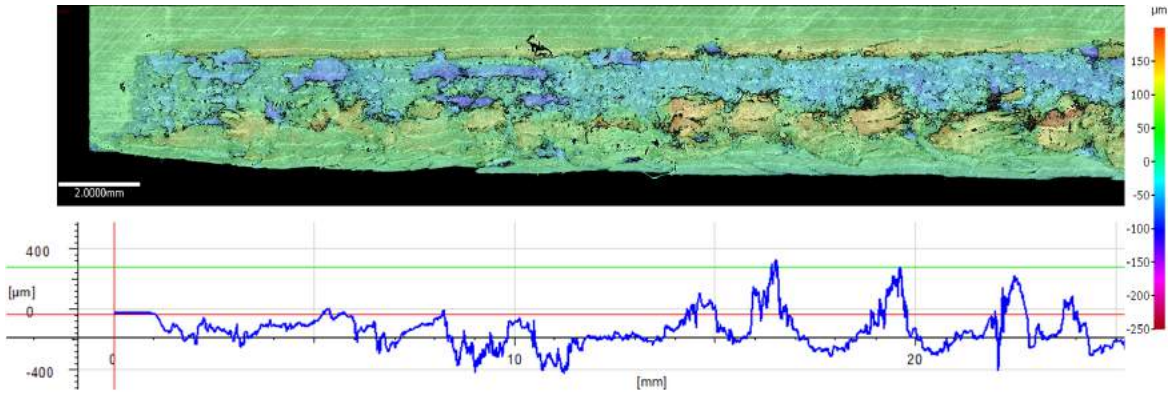

(b) Condition 31

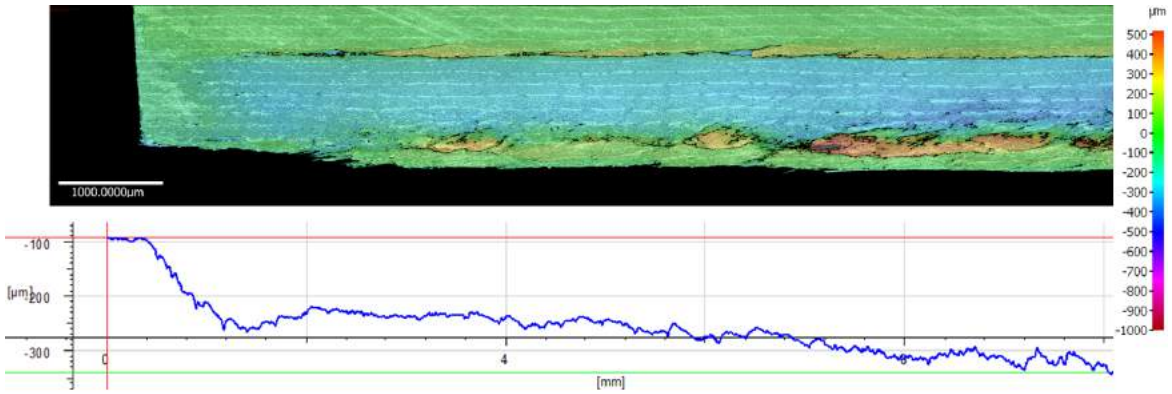

(c) Condition 34

Figure 6.26: Depth of cut evolution along the cutting path for fibre orientation θ=135° and cutting speed 12 mm/m at different rake angles: (a) α=-10°; (b) α=10°; and (c) α=30°.

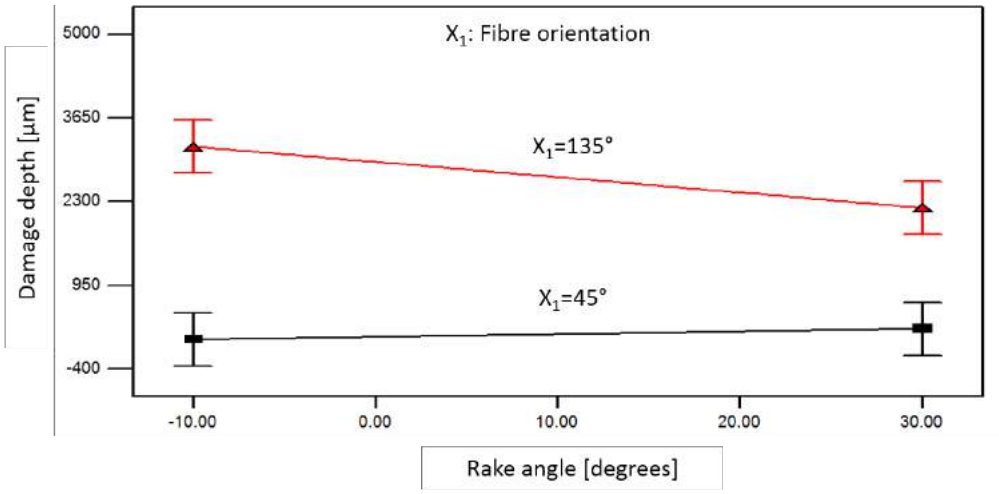

Figure 6.27: Combined effect of fibre orientation and rake angle on damage depth for α: 10° and Vel: 570 mm/min.

The p-value reported in Table 6.5 for the effect of the interaction between fibre orientation and the rake angle on the damage depth is slightly higher than 0.05, making it worthy of study. This effect on the damage depth is shown in Figure 6.27. It is possible to observe how, at high fibre orientation (θ=135°), damage depth strongly depends on the rake angle. In fact, when using negative or a slightly positive rake angle, even if the material experiences failure, it undergoes large deformation rather than being cut. It leads to a depth of cut much lower than the set nominal depth; to formation of protruded material, which sticks out from the machined surface; and to a deep depth of damage. Conversely, when a high positive rake angle is used (α=30°), a cleaner machined surface is obtained, showing a depth of cut higher than the set nominal depth, leading to a very thick chip and a shallower depth of damage compared with previous rake angles.

Images obtained also allow observation of the out-of-plane displacement, which increases with the depth of cut and fibre orientation increase. The effect of fibre orientation is

particularly visible when machining at θ=135°, which leads to a very large out-of-plane displacement during cutting (Figure 6.26). A scan of the lateral surface of the sample using the Alicona Infinite Focus G5 optical scanner also provides useful information on the out-of-plane displacement, as shown in Figure 6.24(c). The experimental condition displayed is for fibre orientation θ=135° and rake angle α=30°, showing an increase of the out-of-plane displacement with the depth of cut increase.

It is worth noticing that the large amount of elastic recovery, taking place when machining at fibre orientation θ=90° (Figure 6.19) and θ=135° (Figure 6.20), makes it very difficult to evaluate damage depth due to re-closing of damaged areas.

Surface integrity was also studied by means of SEM. For fibre angle of θ=0°, the machined surface appears similar for all rake angles used. It presents exposed fibres with some matrix pieces still attached to them (Figure 6.28(a)). Borders between consecutive layers are clearly visible, and indicated with red arrows. Damages arise in the material during cutting in terms of fibre fracture and matrix crushing below the trim plane (Figure 6.28(b)). It is due to the force exerted by the tool pushing down the material in the pressing area.

For fibre orientation of θ=45° (Figure 6.28(c)), and θ=90° (Figure 6.28(d)), the machined surfaces look similar to each other. Differently from fibre orientation of θ=0°, matrix redistribution takes place. In fact, some areas, completely covered by matrix material can be observed. Fibres fracture is visible, with pieces of cracked fibres still lying on the machined surface. Similar observations were reported in the literature for fibre angles θ=0° [16, 24] and θ=90° [16, 18, 24]. In particular, it is possible to observe how images obtained by Wang and Zhang [24] for θ=0° and θ=90°, and reported respectively in

Figure 2.21 and Figure 2.22, are similar to those obtained and shown in Figure 6.28.

For fibre orientation of θ=135° (Figure 6.29), machined surfaces show exposed fibres with some fractured parts of the matrix still attached to them. Out-of-plane displacements are clearly visible in Figure 6.29(b), showing the lines indicating the borders between consecutive layers. They are completely deformed after machining and no longer straight. A large amount of damage is also visible at the end of the cutting width.

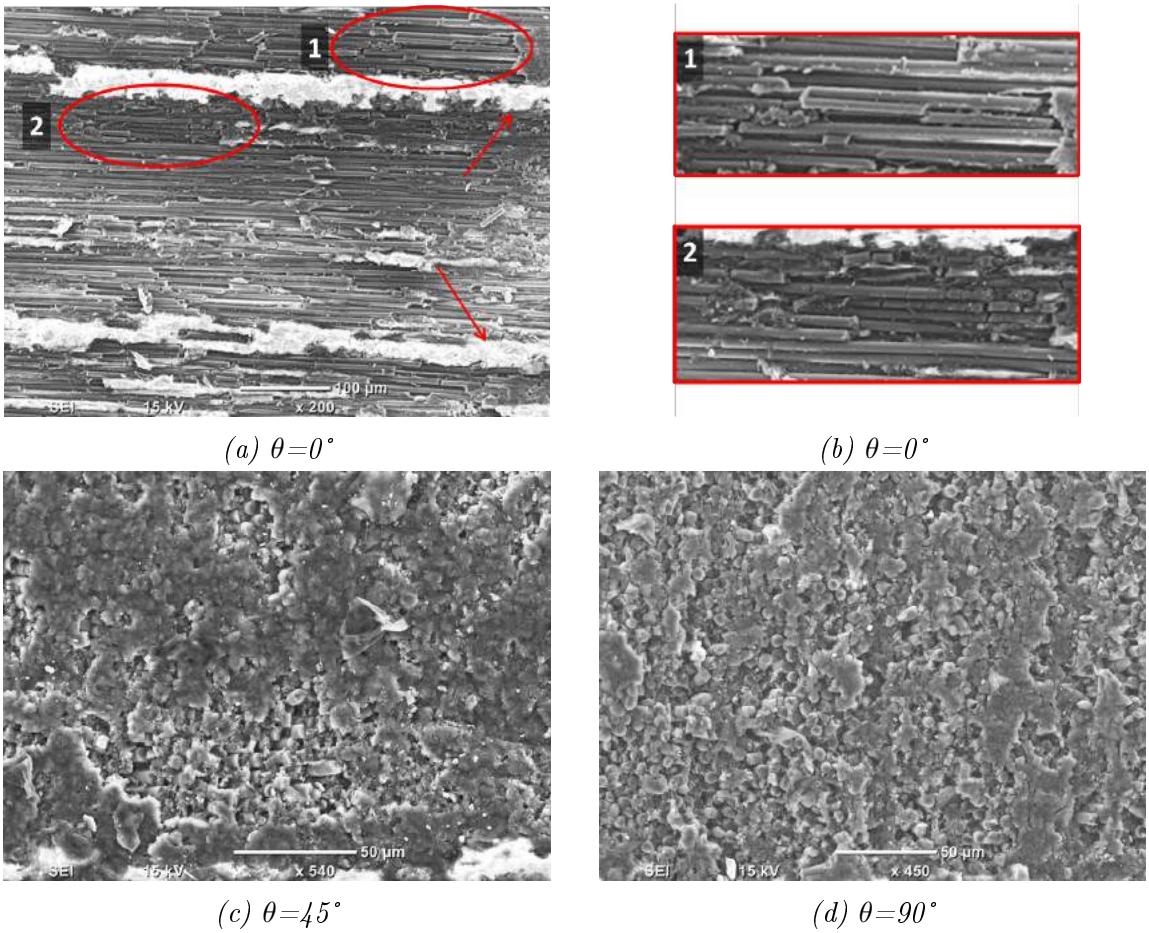

(a) θ=0° *(b) θ=0°*

(c) θ=45° *(d) θ=90°*

Figure 6.28: Machined surface images captured by SEM for (a) Condition 4; (b) magnification for Condition 4; (c) Condition 13; and (d) Condition 22. Machining direction is left to right.

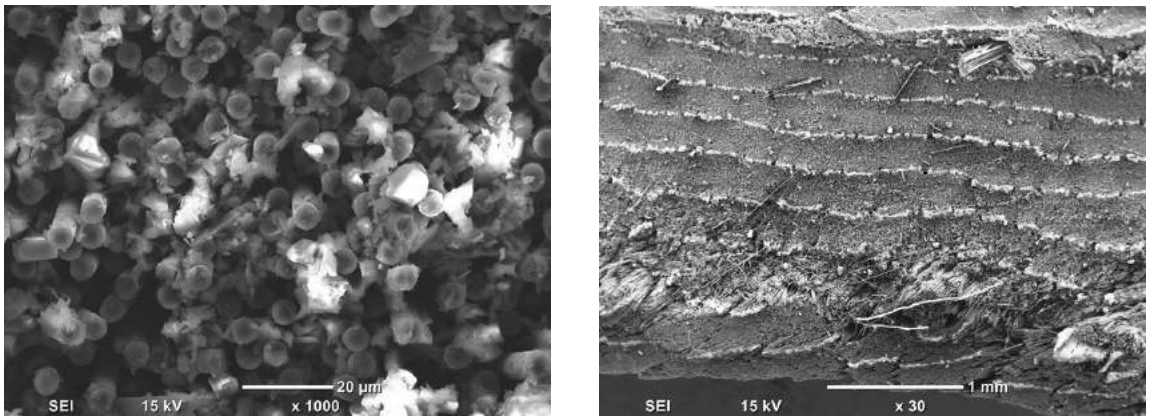

(a) *(b)*

Figure 6.29: Machined surface images captured by SEM for (a) Condition 31; and (b) Condition 34. Machining direction is left to right.

6.4.5 Surface quality

The significant parameters influencing the surface quality can be obtained by observing the p-value reported in Table 6.5. It is possible to see how surface roughness is significantly influenced by fibre orientation, rake angle and depth of cut. A better understanding of the effect of these process parameters on surface roughness is provided through the examination of the model graphs, reported in Figure 6.30. Generally, the rising of fibre orientation causes an increase of surface roughness. The effect of the fibre orientation is due to the change in the chip formation mechanisms as noticed by Wang and Zhang [24]. The effect of the depth of cut is particularly visible at fibre orientation θ=135°, where its increase causes an increase of the surface roughness. It is due to the larger amount of material involved during cutting, which is bent and pressed by the tool, and so also to the greater amount of damage the material undergoes. The effect of the rake angle is completely opposite; producing a better surface quality when high positive values are used; and it is particularly visible at

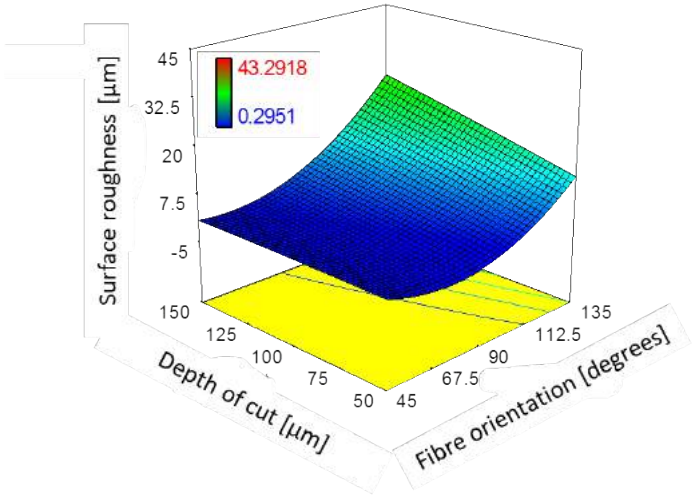

(a) α:10°; Vel:57 mm/min

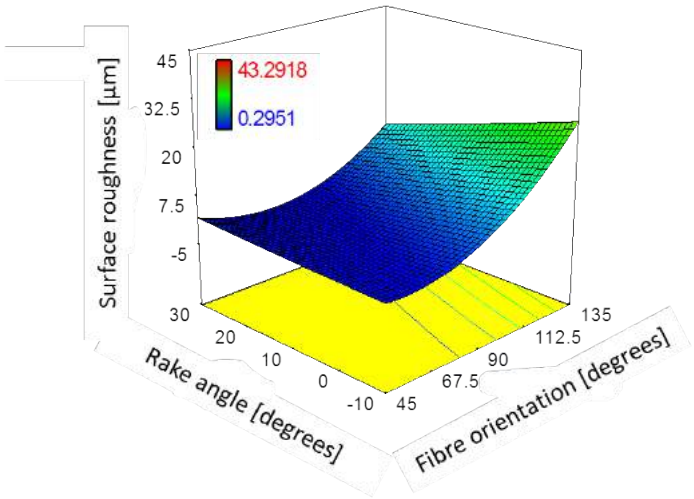

(b) DOC: 100µm; Vel: 570mm/min

Figure 6.30: Combined effect of (a) fibre orientation and depth of cut; and (b) fibre orientation and rake angle, on surface roughness (Ra).

fibre orientation θ=135°. This effect is due to the reduction of the amount of deformation and damage experienced by the material when reducing the rake angle.

Surface roughness is plotted against fibre orientation for different tool rake angles at depths of cut 50 μm and 150 μm in Figure 6.31. The trend of surface roughness is similar in both graphs. In fact, its value is very low for fibre orientation up to θ=90° showing small

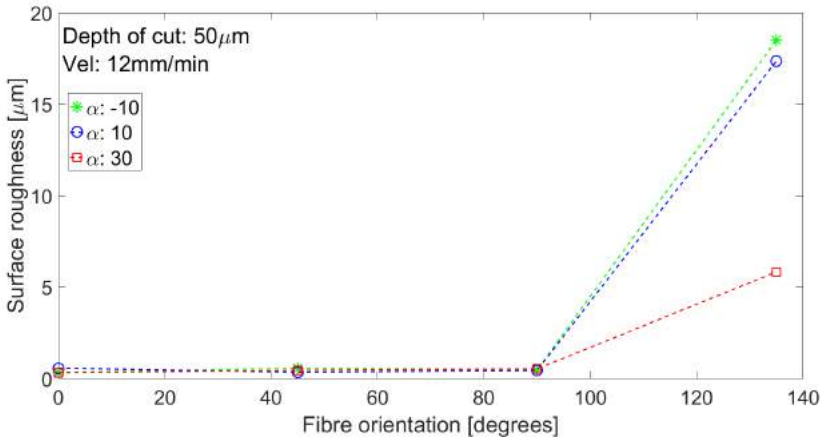

(a)

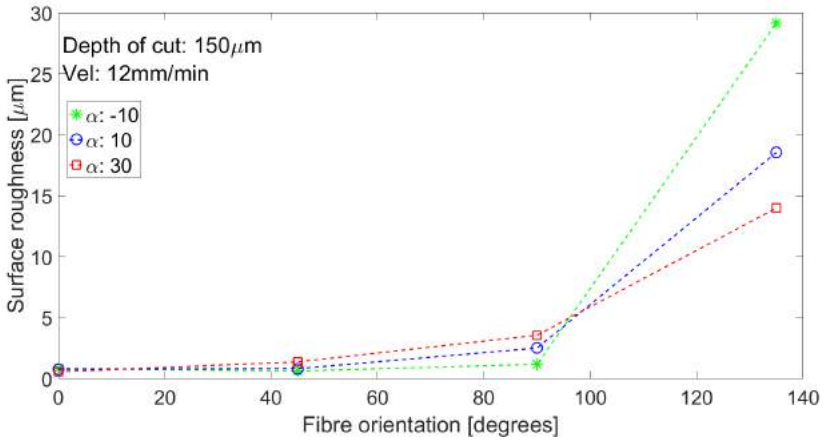

(b)

Figure 6.31: Surface roughness as function of fibre orientation for different values of the rake angle at depth of cut (a) 50 μm, and (b) 150 μm.

fluctuations, independently from the rake angle. This trend is comparable to that reported in Figure 2.12(b) (§ 2.5.3), obtained by Wang and Zhang [24]. However, at a depth of cut of 150 μm a small increase can be observed moving from θ=45° to θ=90°. For a further increase of the fibre angle an abrupt increase can be observed at θ=135° for both depths of cut, whose slope rises with the depth of cut increase, leading to higher values of surface roughness for a depth of cut 150 μm. At fibre orientation θ=135° a completely different surface is obtained,

depending on the rake angle used. An increase in the rake angle causes a reduction of the surface roughness. It is possible to observe the benefit of using a large positive rake angle in Figure 6.26(c), where a higher surface quality can be observed for α=30°. In contrast, machining with negative or slightly positive rake angles leads to poor surface quality, with the material undergoing very large deformation and damages, as shown in Figure 6.26(a-b).

6.4.6 Bouncing back

The bouncing back was analysed knowing the nominal depth of cut and the machined surface profile (actual depth of cut reported in Figure 6.25 and Figure 6.26).

The typical curve describing the bouncing back variation with the increase of the nominal depth of cut is reported in Figure 6.32, which follows the same trend observed by Wang and Zhang [24] and reported in Figure 2.8. For small values of the nominal depth of cut, the material exhibits deformations and no cut takes place. In particular, when increasing the depth of cut, the actual depth of cut remains at zero, while the bouncing back value rises.

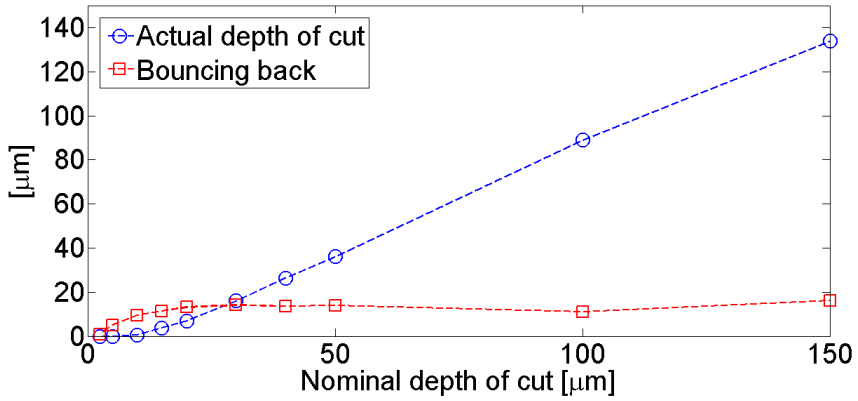

Figure 6.32: Bouncing back and actual depth of cut for fibre orientation θ=0°, rake angle α=-10° and cutting speed 12 mm/min (condition 1).

This behaviour can be observed for values of the set depth of cut until about half of the cutting edge radius for the machining conditions considered. A further increase of the depth of cut leads to an actual depth of cut different from zero, which increases with the nominal depth of cut increase. At the same time the bouncing back amount continues to increase but with a lower slope. A value of the nominal depth of cut, after which the bouncing back remains constant, exists and the increase of the depth of cut leads only to an increase of the actual depth of cut.

The significant parameters influencing the bouncing back can be obtained by looking at the p-value reported in Table 6.5. The bouncing back is affected by the rake angle and fibre orientation. However, the p-value representing the effect of the depth of cut and the effect of the interaction between the depth of cut and fibre orientation, and the depth of cut and rake angle on the bouncing back are slightly higher than 0.05, making them worthy of study. The effect of these machining parameters on the bouncing back can be better analysed considering the graphs reported in Figure 6.33.

An increase in the fibre orientation leads generally to increased bouncing back. Indeed, Wang and Zhang [24] observed that the amount of bouncing back for $\theta<90°$ is about the tool radius size; while it can reach up to double this size for higher fibre orientations. This effect is more evident with the increase of the depth of cut and with the decrease of rake angle. An increase in the rake angle generally reduces the bouncing back; while an increase in the depth of cut tends to increase it. This effect is more visible with the increase of the fibre orientation.

The combined effect of rake and fibre angles on bouncing back can be observed in Figure

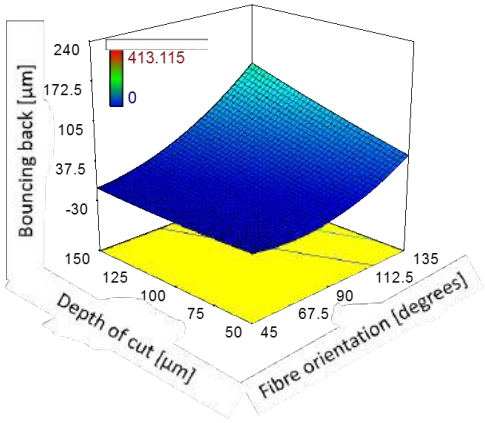

(a) α: 10°; Vel: 570 mm/min

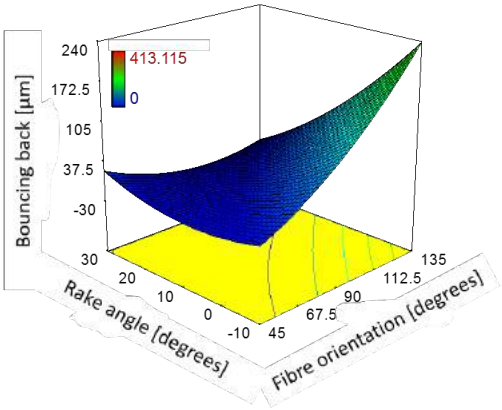

(b) DOC: 100 µm; Vel: 570 mm/min

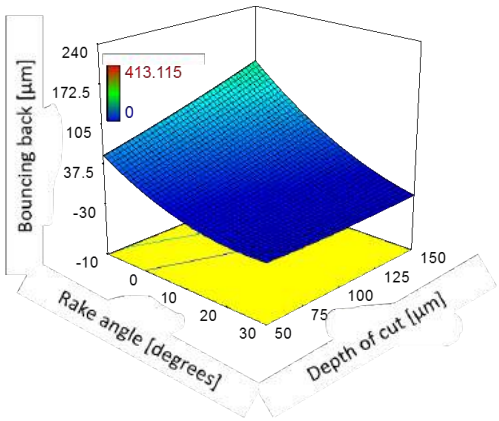

(c) θ: 90°; Vel: 570 mm/min

Figure 6.33: Combined effect of (a) fibre orientation and depth of cut; (b) fibre orientation and rake angle; (c) rake angle and depth of cut, on bouncing back.

6.33(b), and better analysed considering also Figure 6.26. In fact, two extreme cases can be recognised, which are associated with the maximum and minimum amount of bouncing back observed during the experiments. When using slightly positive or negative rake angles and high fibre orientation (θ=135°), high levels of deformation take place in the workpiece rather than cutting. A high amount of material is bent and pressed under the tool. It leads to a very high amount of bouncing back after the tool has passed. Conversely, no bouncing back was detected when machining with high rake and fibre angles (α=30° and θ=135°). In fact, the actual depth of cut measured was found to be higher than the set nominal depth of cut.

6.4.7 Cutting force and thrust force

Machining force acting on the tool can be decomposed in cutting force and thrust force, along the cutting direction and orthogonally to it, respectively (Figure 6.34).

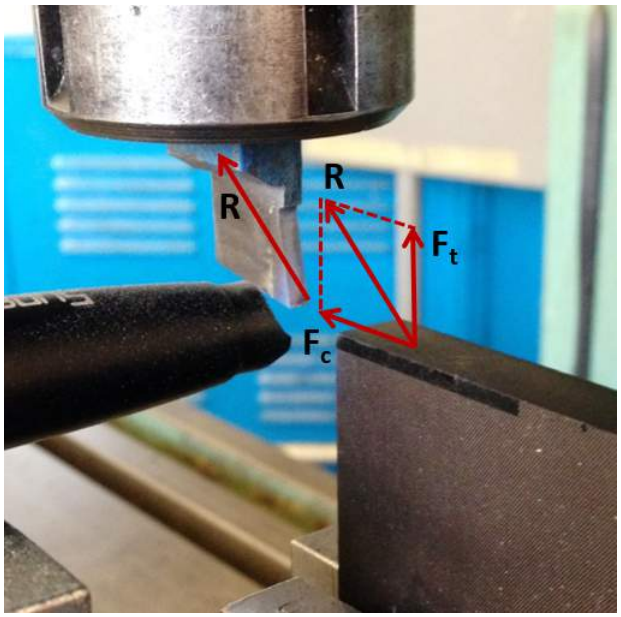

Figure 6.34: Schematic of resultant machining force decomposition, with components considered positive in the shown direction.

In order to study the effect of machining parameters on cutting force and thrust force, values for depths of cut of 200 μm and 250 μm were also considered. These values were obtained using the equation provided by the ANOVA (Equation (6.1)), whose coefficients are reported in Table 6.7.

6.4.7.1 Cutting force

The significant parameters influencing the cutting force can be obtained observing the p-value reported in Table 6.5. They are fibre orientation and depth of cut, and their effect on the cutting force is shown in Figure 6.35.

An increase of the fibre orientation and of the depth of cut causes an increase of the cutting force. It is possible to notice that the effect of the interaction between the two variables on the cutting force is not significant, as also shown in Table 6.5 where the relative

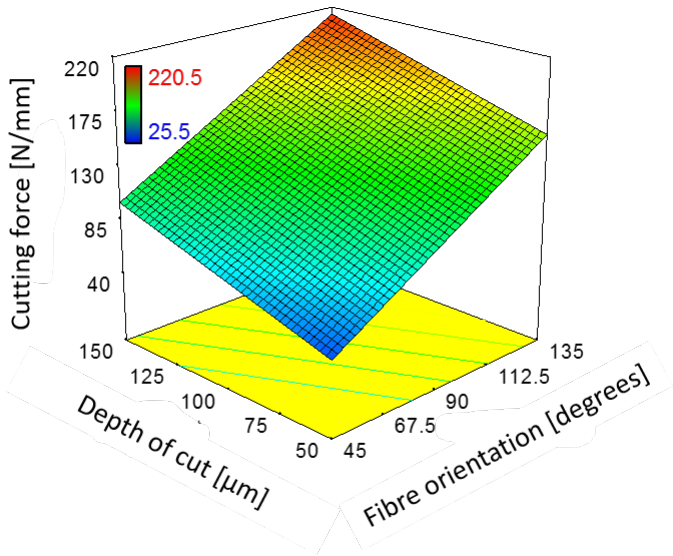

Figure 6.35: Effect of fibre orientation and depth of cut on the cutting force when machining at α: 10°, and Vel: 570 mm/min.

p-value is equal to 0.9728.

Variation of cutting force with fibre orientation at different depths of cut is reported in Figure 6.36, where also fibre orientation θ=0° is included. The trend of the cutting force is reported for rake angle α=10° and cutting speed 570 mm/min, and it represents the general trend observed in the experiments.

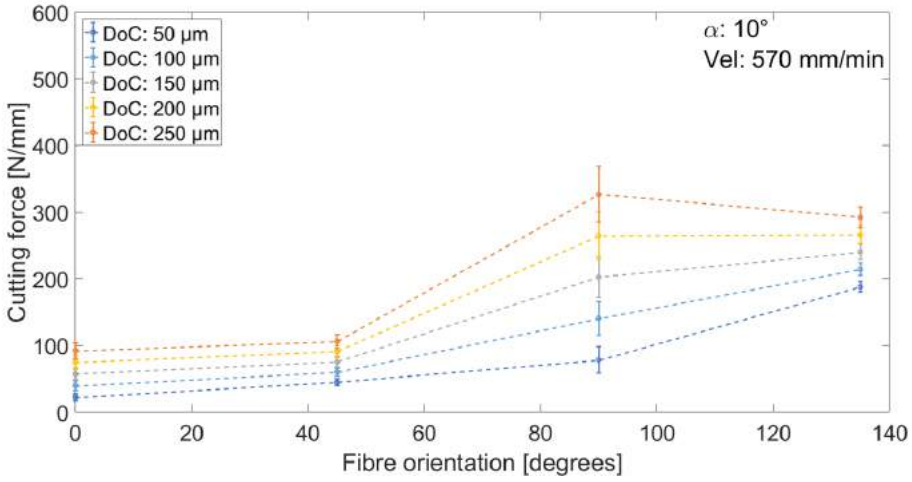

Figure 6.36: Experimental cutting force for various fibre orientations and depths of cut when machining at α: 10°, and Vel: 570 mm/min.

Figure 6.36 shows that cutting force rises slightly from fibre orientation θ=0° to θ=45°, as also confirmed by the literature and reported in Figure 2.24(a). An increase in the depth of cut usually causes a change in the curvature for 45°≤θ≤135°, and it varies from positive to negative. An increase in the depth of cut leads always to an increase of the cutting force, as found in the literature and reported in Figure 2.25 [26]. This is due to the increase of the amount of material involved during cutting pressing against the rake face of the tool. The effect of the depth of cut is maximum at θ=90°, where a large variation can be observed in the cutting force.

For all conditions analysed, the cutting force generally shows a minimum point at fibre orientation θ=0°.

6.4.7.2 Thrust force

The significant parameters influencing the thrust force can be obtained by examining the p-value reported in Table 6.5. They are fibre orientation, rake angle and depth of cut, and their effect on the thrust force is reported in Figure 6.37 and Figure 6.38.

Figure 6.37(a) shows that the effect of the fibre orientation increases with the increase of the rake angle. In particular, an increase of the fibre orientation causes a decrease of the thrust force. The effect of the rake angle is dependent on the fibre orientation. In fact, Figure 6.37(b) shows that at fibre orientation of θ=45° an increase of the rake angle leads to an increase of the thrust force; while for fibre orientation θ=135°, it leads to a decrease. The effect of the rake angle is also dependent on the depth of cut and it increases with the depth of cut increase. Figure 6.38 shows that an increase of the rake angle leads to a decrease of the thrust force. Differently, the effect of the depth of cut increases with the decrease of the rake angle. An increase of the depth of cut leads to an increase of the thrust force.

The experimental trends of the thrust force with fibre angle, rake angle and depth of cut are reported in Figure 6.39, where fibre orientation of θ=0° is also considered.

For a negative rake angle (Figure 6.39(a)) a small variation (∼20 N/mm) of the thrust force can be observed with fibre orientation. In addition, a depth of cut increase leads to an increase of the thrust force, as also observed by Li *et al.* [26] and shown in Figure 2.25.

A more complex trend is shown for positive values of rake angles. For α=10° (Figure

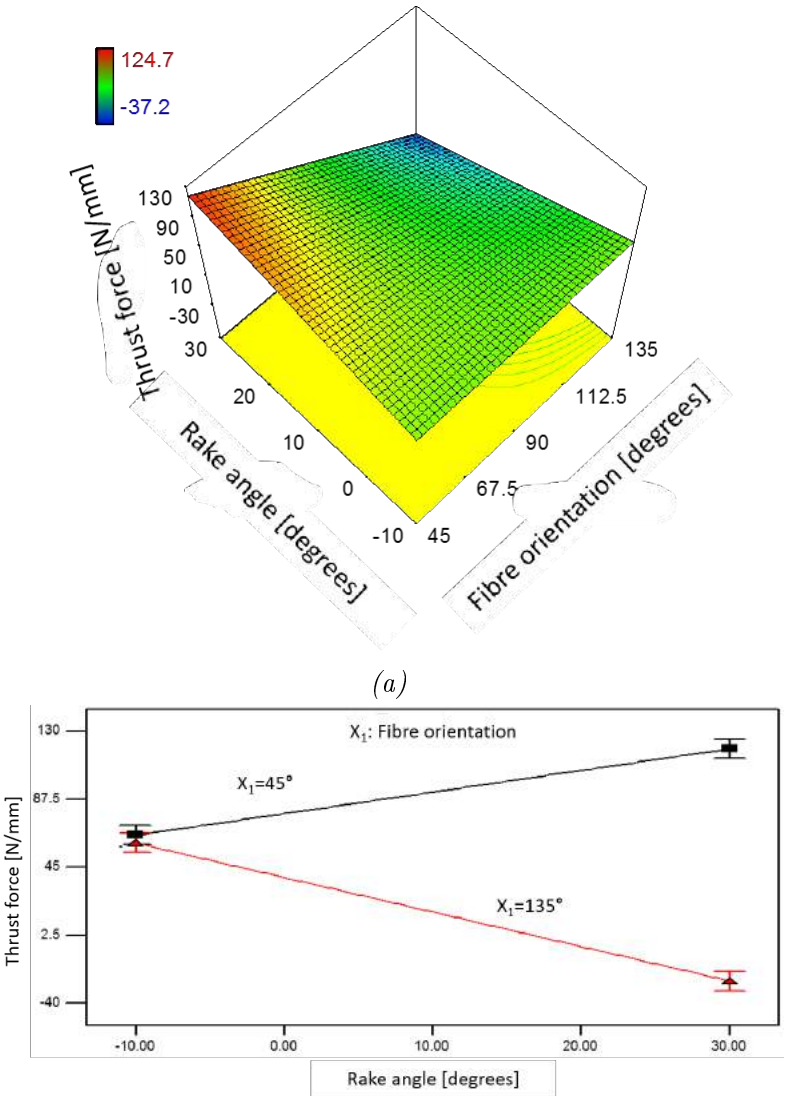

Figure 6.37: Combined effect on the thrust force of fibre orientation and rake angle when machining at depth of cut 100 μm and cutting speed 570 mm/min: (a) 3D view, and (b) trend for fibre orientations of θ=45° and θ=135°.

6.39(b)), the depth of cut effect becomes negligible at θ=45°. For lower fibre angles an increase of the depth of cut leads to an increase of the thrust force; while for higher values of the fibre orientation it leads to a decrease. At θ ∼120° a change in the depth of cut effect can be noticed again. In fact, at θ=135° a higher depth of cut causes a rising of the thrust

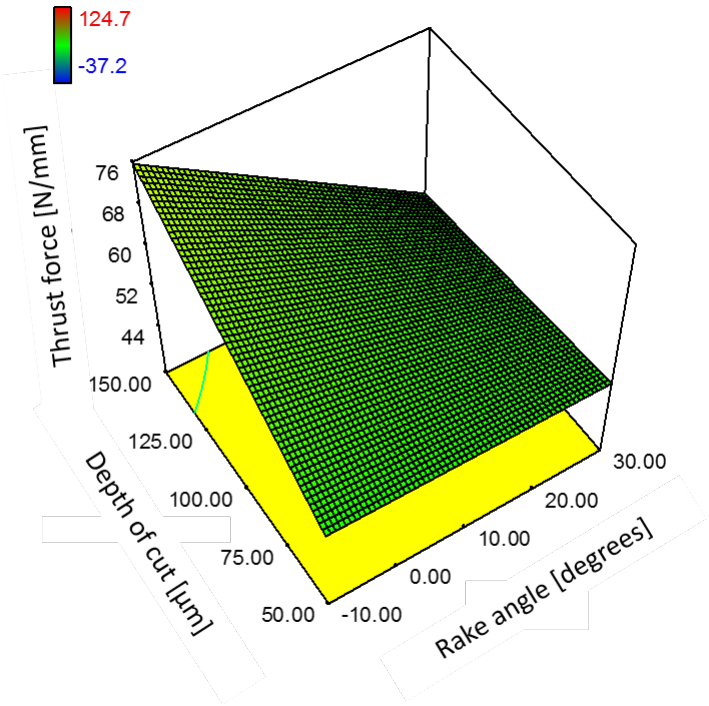

Figure 6.38: Combined effect on the thrust force of depth of cut and rake angle when machining at fibre orientation θ=90° and cutting speed 570 mm/min.

force.

For α=30° (Figure 6.39(c)), the depth of cut influence is negligible at θ=0° and is very small (∼20 N/mm) for θ=45°. An inversion in the effect of the depth of cut can be observed after θ=45°, where its increase causes a decrease of the thrust force. Differently from other rake angles, a change in the thrust force sign can be observed at high fibre orientations. This change in sign was also detected by Wang and Zhang [24] and shown in Figure 2.26(b). It could be explained considering Figure 6.40. The force exerted by a fibre during cutting can be decomposed along the cutting direction and orthogonally to it, obtaining the contributions to the cutting force and thrust force, respectively. These have to be summed to the forces exerted by the surrounding material, e.g. contribute to the thrust force due to the spring

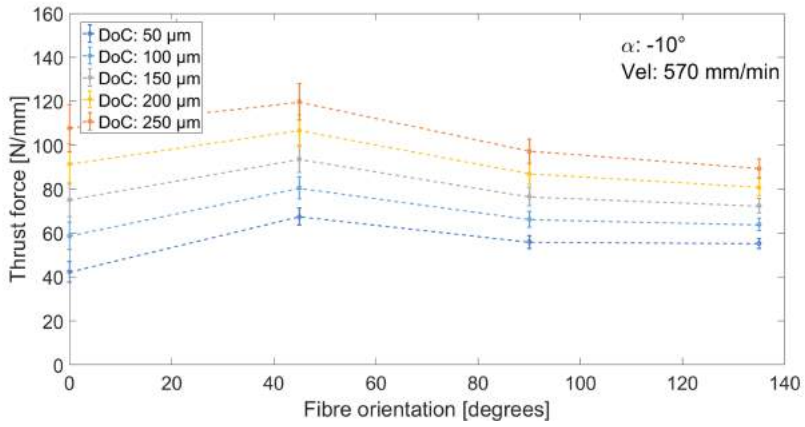

(a) α: -10°

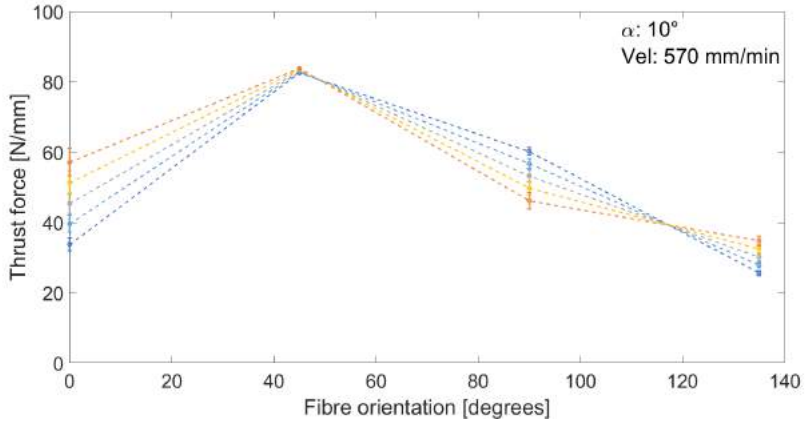

(b) α: 10°

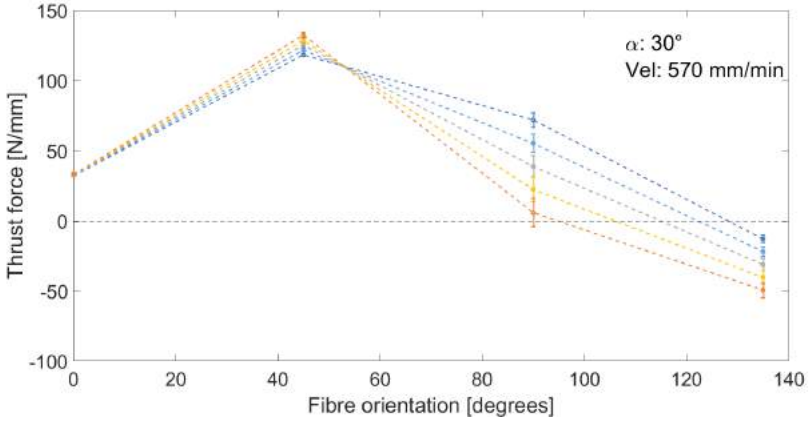

(c) α: 30°

Figure 6.39: Thrust force trend with fibre orientation at different depths of cut when machining at cutting speed 570 mm/min.

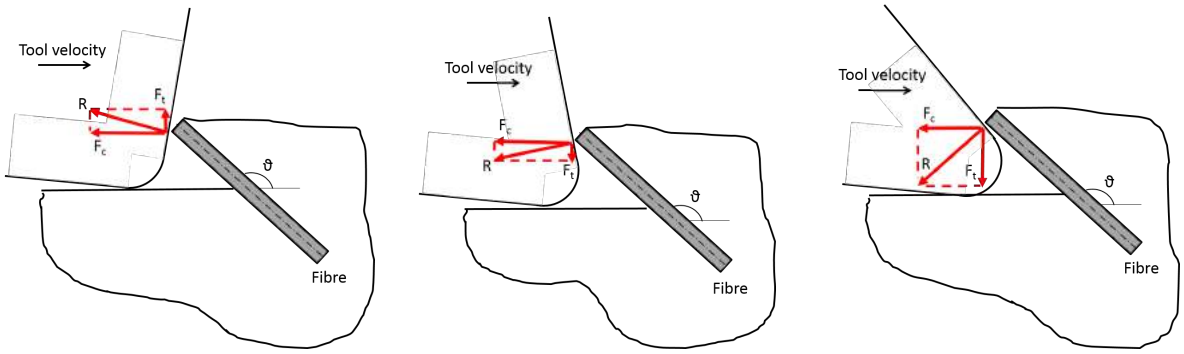

(a) Negative *(b) Slightly positive* *(c) Highly positive*

Figure 6.40: Effect of the rake angle on the thrust force.

back of the machined material pushing on the clearance face, to obtain the total cutting force and thrust force.

For a negative rake angle (Figure 6.40(a)), the force exerted by the fibre on the rake face provides a positive contribution to the thrust force, pushing up the tool. Moving from negative to high positive rake angles (Figure 6.40(c)), the force exerted R rotates anticlockwise providing a negative thrust force. It is due to the tool geometry that for a negative rake angle tends to push down the fibres; while for positive rake angles tends to lift them. For high rake angles the negative contribution to the thrust force increases so much that the total thrust force changes sign becoming negative, opposing to the tool, which tends to lift the fibres.

The thrust force trend with the rake angle is reported in Figure 6.41. The effect of the rake angle depends on the fibre orientation. In fact, for θ=0° and θ=90° a positive rake angle is suggested to be used, as the thrust force reduces with the increase in the rake angle. For θ=45°, both negative or slightly positive rake angles can be used leading to similar thrust force. For θ=135°, rake angles of α=10° and α=30° can be used, leading to a similar

magnitude of the thrust force (∼25 N/mm), but with a different sign.

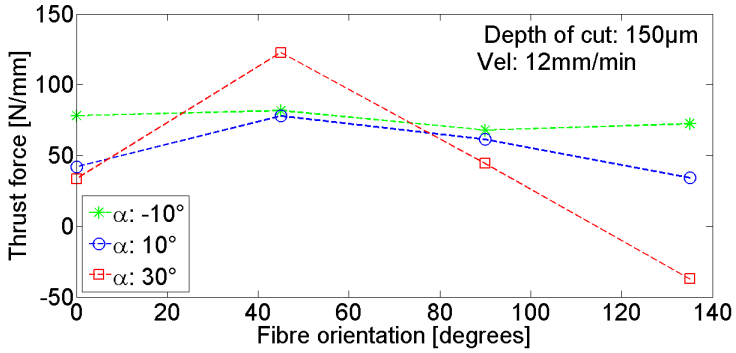

Figure 6.41: Thrust force trend with fibre orientation for different rake angles at a cutting speed of 12 mm/min and depth of cut of 150 µm.

6.4.8 Optimization of process parameters

The optimization tool of Design-expert 7.0 was used to identify the set of machining parameters in order to optimize the output variables. In particular, for each fibre orientation a depth of cut of 100 μm was considered for the analysis, while no constraints were set for rake angle and cutting velocity. In terms of output variables, minimization of cutting force and thrust force, surface roughness and damage depth was set as the goal. In addition, different levels of importance were set for the output variables, giving more importance to the final quality of the workpiece rather than to the machining forces' magnitude. Hence, the levels of importance of surface roughness and damage depth were set at the maximum; while the levels of the machining forces, at the minimum. The results obtained are reported in Table 6.8.

It is likely that it is possible that there is not a unique solution for each fibre orientation. This is due to the fact that the effect of machining parameters could not be the same on

Table 6.8: Rake angle and cutting velocity optimizing the surface quality and the damage depth for each fibre orientation and depth of cut of 100 μm.

θ	α	Cutting speed (mm/min)	F_c (N/mm)	F_t (N/mm)	Surface roughness (μm)	Damage depth (μm)
45°	-10°	366.82	62.78	65.49	0.3	38.53
90°	30°	1100	128.22	47.63	0.3	1102
135°	30°	1100	184.70	-23.76	12	2087

each output variable. Hence, some solutions could present closer values to those desired for some output variables and not for others; while other solutions could behave differently. In this case, the solution selected by the software, which has the highest level of desirability, was chosen.

For fibre angle of θ=45° a negative rake angle together with a moderately low cutting velocity are suggested. Differently, for fibre orientations of θ=90° and θ=135° a high positive rake angle has to be used and combined with a high cutting speed.

6.5 Summary

Experiments on the orthogonal cutting of unidirectional carbon fibre plastic composite have been carried out in order to study the chip type and the chip formation mechanism; and to understand the influence of machining parameters on the output variables. To this end, the response surface method and the ANOVA technique have been employed. Moreover, equations for prediction of the output variables have been obtained.

The type of chip has been found to be strongly influenced by fibre orientation and rake angle, but less by the depth of cut. An increase in the tool rake angle favours a continuous

chip. A strong dependence on the fibre angle can be observed moving to θ=90°, where, differently from all other fibre orientations, an almost complete absence of cut has been observed for α=-10° and α=10°, with the chip formed by powder or small splinters. Finally, an increase in the depth of cut favours the formation of a continuous chip and an increase in the chip's thickness.

As for the chip type, also the chip formation mechanism has been found to be strongly influenced by the fibre orientation and rake angle. Indeed, the influence of the rake angle is particularly evident when machining at θ=0°. The material removal mechanism is mainly due to fibre buckling for a negative rake angle, accompanied by fibre failure due to bending in the vicinity of the cutting edge. For a slightly positive rake angle, bending failure in the fibres becomes predominant. It takes place very close to the cutting edge, producing a continuous chip. For high positive rake angles a second cutting zone ahead of the tool has been observed, where the chip formation is due to a peeling action exerted by the tool. Differently, the influence of the rake angle has been found negligible at θ=45°, where cracks propagate from the tool tip through fibres orthogonal to their axis and shear at the fibre-matrix interface takes place. Similar behaviour has been observed for θ=90° and high positive rake angles. At θ=135° no difference in the chip formation mechanism with the rake angle has been observed from microscope and SEM images. The chip formation seems due to fibre peeling followed by fibre bending fracture propagating towards the free surface of the sample. In addition, a large amount of deformation in the workpiece, involving high out-of-plane displacement, has been noticed. However, the machined surface profile obtained using the Alicona G5 infinite focus highlighted a difference when using rake angle α=-10° (or α=10°) and α=30°. While

high deformation prevails on cutting for α=-10° and α=10°, cutting takes place for α=30° leading to an actual depth of cut higher than the nominal depth of cut.

In addition, the effect of a round cutting edge on the chip formation mechanisms for fibre angles θ=0° and θ=90° has been highlighted.

Results obtained by ANOVA pointed out that the cutting speed is not a significant parameter. In contrast, fibre orientation represents the most significant parameter affecting the output variables of the process.

Damage depth rises with the increase of fibre angle and depth of cut; while the rake angle increase generally leads to a reduction of damages. The minimum amount of subsurface damages has been found when machining at fibre angle θ=0°. Surface roughness has been found to be independent from the rake angle for fibre orientation 0°≤θ≤90°, especially at a low depth of cut. Differently, high fibre angles lead to a reduction of the surface quality, where a high positive rake angle is suggested to be used. The bouncing back has been also studied, which generally rises with fibre orientation increase and rake angle reduction. The most significant parameter affecting the cutting force and thrust force is represented by the fibre orientation. An increase in the depth of cut always leads to an increase in the cutting force. The same effect has been observed for the thrust force when machining with a negative rake angle; while a more complex trend takes place for positive rake angles. Moreover, a change in the sign of the thrust force has been observed when machining at high fibre and rake angles.

The optimization problem has also been solved, determining the optimal machining parameters to improve the workpiece quality. For fibre angle θ=45°, a negative rake angle and moderately low cutting velocity have to be used. Conversely, for θ=90° and θ=135° a

high positive rake angle and high cutting speed are required.

Finally, the results obtained are in agreement with trends reported in the literature, showing that the linear variation of the depth of cut during machining does not affect the results.

Chapter 7

Development of a hybrid FEM-SPH model

7.1 Introduction

The SPH approach, developed in Chapter 5, showed it was better in predicting the cutting force and thrust force compared to the FEM. This was mainly due to material degradation after failure instead of element deletion. The chip formation mechanism was also found to be more realistic using the SPH model; leading to mesh-free methods to be considered very attractive for simulating machining processes. Despite the encouraging results obtained, the absence of a cohesive model for fibre-matrix interface simulation still makes the FEM approach fundamental to study and evaluate the debonding defect.

In order to take advantage of the potential of both methods, a hybrid model, where FEM and SPH coexist, could be used. A few examples of the implementation of a such

technique can be found in the literature, mainly for impact problems and generally where large deformations are involved [124–129].

In the present chapter a hybrid approach is developed to simulate the orthogonal cutting of UD-CFRP. A conversion from FEM to SPH takes place for each element experiencing failure and belonging to the fibre or matrix phase. This method allows the implementation of the cohesive model between the finite elements of the fibre and matrix at the beginning of the analysis and avoids material loss during cutting caused by the elements' deletion. In addition, a three-dimensional FEM model is developed and compared with the hybrid approach, in order to assess the potential of the latter; and both are validated with experiments carried out in the previous chapter.

7.2 Development of the hybrid model

A three-dimensional model was developed by implementing the hybrid approach. Two fibre orientations were analysed (θ=0° and θ=90°), relative to experimental conditions 9 and 24 (see Table 6.3), respectively. As for models developed previously, a meso-scale technique for simulating the composite material was employed, assuming the symmetry (half of the fibres' geometry) to reduce the computational time. A schematic of the hybrid model is shown in Figure 7.1.

The cutting edge radius was measured in the previous chapter resulting ∼20 μm. It is bigger than that provided by the published experiments [25] (5 μm), based on which previous models were developed. A larger cutting edge radius causes a bigger amount of

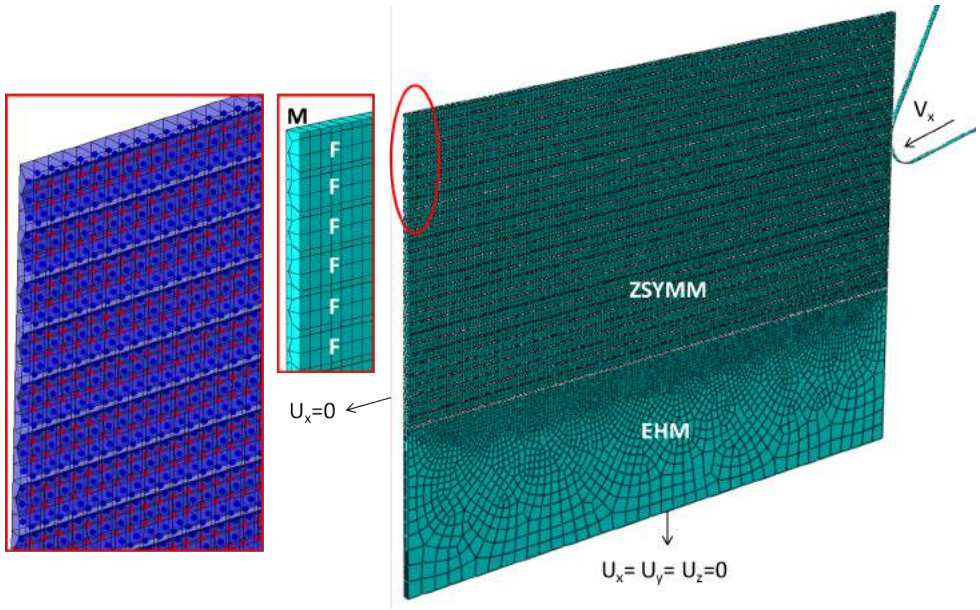

Figure 7.1: Schematic of the three-dimensional hybrid model with boundary conditions applied in the case of fibre orientation θ=0°.

material involved during cutting and also a higher depth of cut, leading to the necessity to simulate a wider area of the composite material. If three fibres were sufficient to simulate the orthogonal cutting at fibre orientation θ=0° when a cutting edge radius of 5 μm and a depth of cut 15 μm were implemented, at least 30 fibres have to be considered for a cutting edge radius of 20 μm and a depth of cut 100 μm. The computational cost, which was already high for previous models, increases considerably. In order to contain it, an increase in the mesh size was made, reducing the total number of elements in the model. Hence a compromise between computational cost and accuracy had to be made. A mesh seed of two micrometres was implemented along the fibre direction; while in the plane orthogonal to the fibre axis the elements' size changed according to the parts' geometry. In particular, the fibres were represented by two elements.

Particles representing the SPH were positioned at the centre of each finite element, as

shown in Figure 7.1. A tie constraint between the SPH particles and the finite elements was imposed to make the former follow the latter before material failure took place. After a finite element was deleted from the analysis due to failure, the corresponding particle was free to move according to the constitutive model used. Tie constraints were also used to link cohesive elements to the matrix and fibres in the FEM model, as well as the matrix to the EHM phase.

Boundary conditions applied during the explicit analysis were the same as applied in previous models for both FEM and SPH approaches. In addition, lateral surfaces were implemented in order to avoid the SPH particles moving in the z direction out from the simulated strip. Contact with no friction was implemented between particles and rigid surfaces. A Coulomb friction model with a friction coefficient of 0.3 was implemented in the model among finite elements, particles and the tool.

The cutting speed was set to the maximum value used in the experiments, i.e. 1100 mm/min. That choice helped in reducing the computational cost of the analysis. In fact, by fixing the cutting length a shorter cutting time needs to be analysed when considering a higher cutting speed.

In addition, a tool rake angle α=30° was chosen for simulating the fibre angle of θ=0°. A depth of cut of 100 μm was fixed in the model, and a cutting length of 200 μm was simulated. In contrast, a tool rake angle α=10° was chosen for θ=90°and a depth of cut equal to 50 μm was modelled.

The hybrid model features the coexistence of FEM elements and SPH particles, with the latter implemented for the fibre and matrix phases. In particular, the composite material at

the beginning of the analysis is entirely represented using the classic finite element approach. At that stage, the novel cohesive model, developed in Chapter 3, was implemented between the fibre and matrix to simulate the fibre-matrix interface behaviour. When the failure criterion is satisfied during cutting, the fibre or matrix finite element is converted to a SPH particle. At the same time, the linked cohesive element is considered as failed if still active in the model, as described in the novel approach previously developed.

Finite elements and particles coexist through the duration of the analysis. This implies that a change in the material properties has to be realised in the particle when the correspondent finite element fails and is deleted from the analysis. In particular, they have to switch from a dormant state, where they do not affect the simulation, to an active state, where they represent the fractured material. To this end a subroutine was developed to simultaneously take into account the constitutive behaviour implemented in the finite elements, SPH particles and the novel cohesive model elements, as described in detail below.

7.2.1 Implementation of the user subroutine for the hybrid model

The subroutine developed for the hybrid model is composed of different parts. The first section calculates the coordinates of the centre of each finite element in the model. Then the SPH particles created are translated to these points ensuring that for each finite element there is a particle positioned at its centre.

The second section includes the material's constitutive behaviour for the matrix and fibres, which is obtained by coupling the FEM and SPH material models. In fact, the

FEM represents the composite material from the beginning of the analysis until failure; while the SPH represents the post-failure behaviour. To this end, both VUSDFLD and a VUMAT subroutines were used. The former calculates the connectivity matrices containing information on the fibre-cohesive and matrix-cohesive elements' connectivity. In addition it implements the failure conditions for the FEM fibre and matrix phases, whose material models were implemented by means of Abaqus/CAE. When the condition is satisfied, the VUSDFLD looks for the connected cohesive element, deleting it from the analysis if still active.

Information regarding the finite element failure is passed to the VUMAT subroutine, where constitutive models for fibre and matrix, represented in terms of SPH particles, are reported. When the finite element fails, the particle switches from a dormant to an active state. The former is characterised by unreal and very low values of the material stiffness properties (1e-6), so that it does not affect the analysis while the corresponding finite element is still active. In the latter state, the real material properties are attributed to the particle, but material stiffness degradation is carried out to simulate the damaged material, as realised for the 3D-SPH model in Chapter 5.

The matrix constitutive behaviour implemented is shown in Figure 7.2. Differently from models based on the literature, where the cutting speed was 8.33 mm/s, the cutting speed implemented in the hybrid model is 18.33 mm/s. An increase in the cutting speed causes an increase in the strain rate, affecting the epoxy matrix stress-strain curve. This effect was studied by Gilat *et al.* [130]. In the tensile test a transition from ductile to brittle response was observed with the strain rate increase. For this reason the matrix was simulated as perfectly

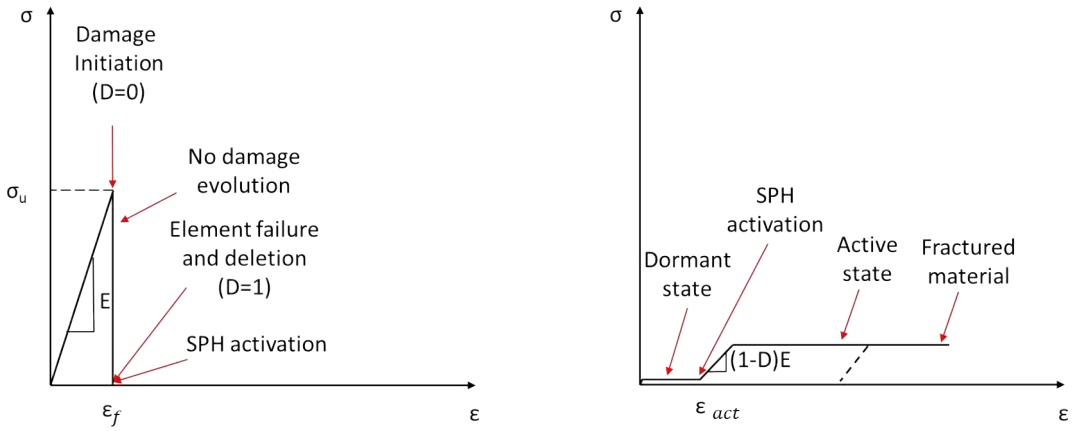

(a) Matrix - FEM *(b) Matrix - SPH*

Figure 7.2: Matrix material model implemented in the subroutine for (a) finite elements and (b) SPH particles.

elastic until failure, as shown in Figure 7.2(a). When the failure condition is satisfied the finite element is deleted from the analysis. The corresponding particle that was in a dormant state is activated and its constitutive behaviour, implemented in the VUMAT subroutine, is shown in Figure 7.2(b). The material property degradation was implemented to simulate the fractured material.

Differently from the epoxy matrix, carbon fibres are not affected by the strain rate [15, 89, 90]. They were simulated implementing a diverse behaviour under tension and compression, as reported in Figure 7.3.

Fibre behaviour was simulated as transversely isotropic and perfectly elastic until failure under tension. The failure condition was represented by the maximum principal stress criterion, as for models developed in previous chapters.

Longitudinal compression tests were carried out on a single carbon fibre T800S by Ueda *et al.* [93]. Results highlighted how the typical compressive stress-strain curve presents an

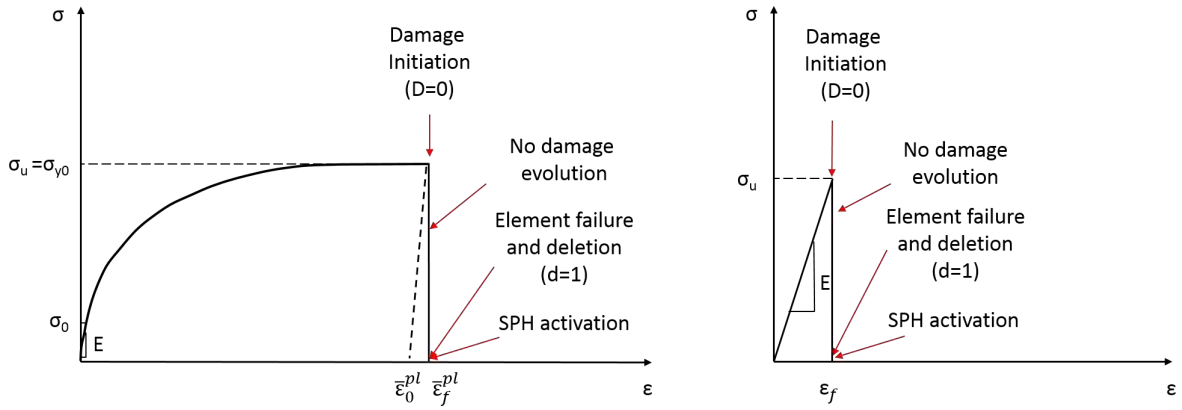

(a) Tension *(b) Compression*

Figure 7.3: Fibre material model implemented in the subroutine for finite elements.

elasto-plastic behaviour. The failure strain under compression was found to be bigger than 10%, which is higher than the tensile failure strain (2% typical of a brittle failure). The ratio between the compressive and tensile strengths was found to be ∼0.5, denoting a much lower failure stress under compression. The variability of the tensile and compression strength were evaluated by means of a Weibull analysis. This showed a bigger variability of the compressive strength compared to the tensile strength. Data collected by Ueda *et al.* [93] were used to obtain as reliable/accurate as possible fibre behaviour under compression to be implemented in the hybrid model. In particular, the failure strength under compression was calculated as a function of the failure strength under tension. The latter was fixed to the value reported on the TORAYCA data sheet [120]. Elasto-plastic behaviour was considered until failure. Since the fibre is transversely isotropic, the described behaviour was implemented in Abaqus/CAE by means of the Hill criterion.

When the failure condition under tension or compression is satisfied, the finite element is deleted from the analysis and the corresponding SPH particle is activated. The SPH material

model is identical to that implemented in Chapter 5 for the 3D-SPH model.

In order to assess the influence of the damage variable on the results, two simulations implementing different values for the damage variable in the matrix material (D=0.8 and D=0.1) were considered. The damage variable for the fibres' particles was set to $d_1 = d_2 = d_3 = 0.8$ for both simulations. The reason for this choice is due to the elasto-plastic behaviour under compression of the fibre and the brittle failure of the matrix material. In fact, few finite elements of the fibres are deleted during the analysis and converted to particles, while a large amount of damage in the matrix takes place leading to a very high number of particles being activated. For this reason, a change in the damage variables for particles belonging to the fibres should not affect the results, differently from a change in the damage variable for the matrix particles.

Material properties for the fibre and matrix used in the hybrid model are summarised in Table 7.1.

Table 7.1: Properties of carbon fibre and epoxy matrix implemented in the hybrid model [25, 62, 84, 93, 98, 120].

Material	Property	Value
Carbon fibre	Elastic constants	E_1=294 GPa, E_2=E_3=14 GPa
		$\nu_{12} = \nu_{13}$=0.2, ν_{23}=0.25
		G_{12}=G_{13}=28 GPa, G_{23}=5.5 GPa
	Longitudinal strength	X_t=5.88 GPa, X_c=3.288 GPa
	Compressive failure strain	0.155
	Compressive yield strength	594.5 MPa
Epoxy matrix	Elastic constants	E=2.96 GPa, ν=0.4
	Failure strength	σ_u=74.7 MPa
Interface	Normal strength	σ_{max}=167.5 MPa
	Shear strength	τ_{max}=25 MPa
	Fracture energy	G^c=0.05 N/mm^2

It is worth noting that Abaqus/CAE allows the automatic FEM-SPH conversion when specified in the element control section. However, after conversion the contact between matrix and fibre particles needs to be realised. As for the 3D-SPH model previously developed, the contact is possible only when using the same material card. To this end the VUMAT subroutine, similar to that developed in Chapter 5, was used for the post-failure behaviour.

7.2.2 Dimension of the SPH particles

When the SPH approach is employed, it is necessary to assign the radius value to the particles. A unique value has to be defined and it is automatically used for all particles. Using the micro-mechanical approach with cylindrical fibres, the geometry of the parts is formed by specific features. For example, the matrix becomes very tiny in the narrow space between two consecutive fibres, so a particle in that location should be represented by a very small radius. This choice leads to a high computational cost since the SPH particles for the whole model are consequently very small.

A further difficulty in choosing the particles' radius is due to the deformation that the finite elements undergo during cutting, especially for areas subjected to compression. In fact, particles are forced by the tie constraint to follow the finite elements. When two consecutive finite elements undergo compression, they deform accordingly, causing a reduction of distance between the corresponding particles. It is possible to imagine two cubic finite elements. If the particle diameter is chosen at the beginning of the analysis equal to the edge of the cube, the particles are in contact at this time. Due to the finite elements' deformation, the particles would tend to overlap. This usually leads to a numerical error in the contact during

the analysis when the overlap becomes significant. Hence, ideally the particles' diameter has to be smaller than the smallest finite element in the model. This choice leads to two different limitations. Firstly, the amount of material deleted during the analysis due to the finite element failure is not replaced by the same amount when the SPH particle is activated: it is lower. Secondly, thrust force prediction is affected. In fact, if two finite elements are deleted below the cutting tool, the two SPH particles activated are not usually in contact, as shown in Figure 7.4. Further compression of the particles is necessary in order to obtain a compacted fractured material below the tool. This causes a reduction of the thrust force compared with the pure SPH model. Finally, a value of the particles' radius equal to 0.7 μm was used.

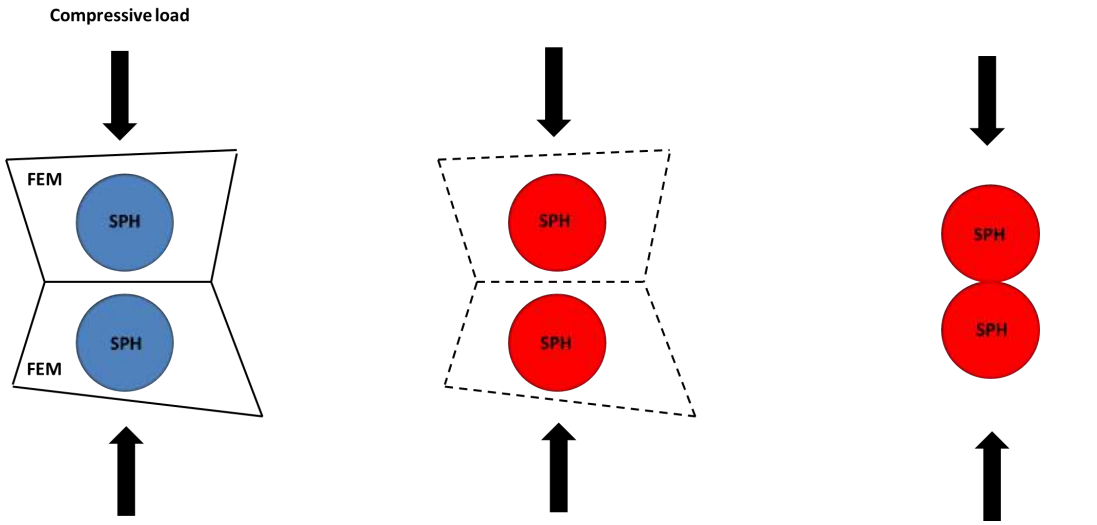

(a) Tension *(b) Compression* *(c) Compression*

Figure 7.4: Schematic of the particles' position under compression: (a) dormant particles, (b) activated particles, and (c) particle deformation due to compressive load.

7.3 Results and discussion

The hybrid model described above and a finite element model were developed for fibre angles θ=0° and θ=90°and compared with the experimental results described in the previous chapter. This allows assessment of the potentiality of the former approach when compared with the latter, which is generally used for simulating machining processes.

7.3.1 Chip formation mechanisms and damage at various fibre orientations

7.3.1.1 Finite Element Model for fibre orientation θ=0°

The configuration of the finite element model, at time 5.77e-4 seconds after the starting of the cut, is reported in Figure 7.5. Tool advancement causes fibre compression at the tool tip. The central fibre undergoes axial load, which leads to buckling failure. The model shows also how the tool exerts an opening action on the material. In particular, fibres located next to the central fibre undergo bending, being deflected upwards on the rake face and downwards. Stress propagates far ahead of the cutting tool. A brittle failure of the matrix takes place around the cutting tool and propagates along the fibre direction. In fact, the large deformation due to compression that fibres can undergo causes matrix deformation and failure very far ahead of the cutting area. This effect is particularly visible for the central fibre subjected to buckling.

Further advancement of the tool causes a fibre failure due to bending in the fibres near the tool tip deforming upwards, with crack propagation orthogonal to the fibres' axis (Figure 7.6).

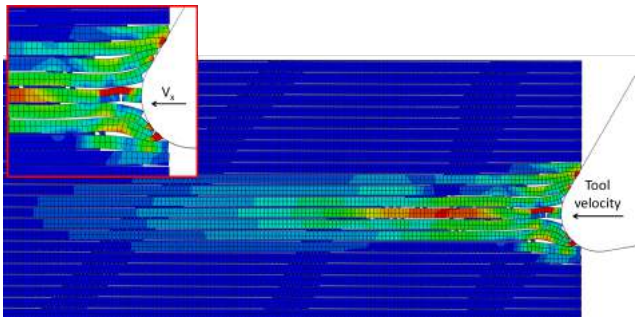

(a) Fibre side

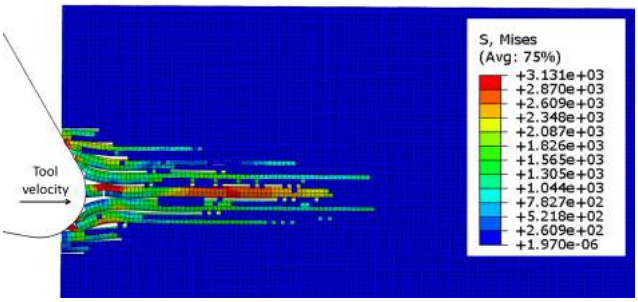

(b) Matrix side

Figure 7.5: Finite element model configuration at time 5.77e-4 seconds for fibre orientation θ=0°.

The bending deformation reduces when moving towards the fibre located at the free surface of the sample. After buckling, the fragments of the central fibres crush under compression load, being entrapped between the workpiece and the tool. In general, instability due to axial load can be observed in the area ahead of the cutting edge that could lead to buckling failure. Fibres deflected downwards are compressed by the tool. In particular, the fibre in contact with the tool presents a fracture in the upper part. Due to high fibre deformation, cohesive elements struggle to keep the matrix and fibre together, undergoing large deformations. Matrix failure seems to propagate radially from the cutting tool, in particular ahead of it along the fibre direction, reaching almost the border of the model.

The configuration of the model at time 2.845e-3 seconds is reported in Figure 7.7. Bending deformation becomes more significant for fibres located above the cutting edge, with crack

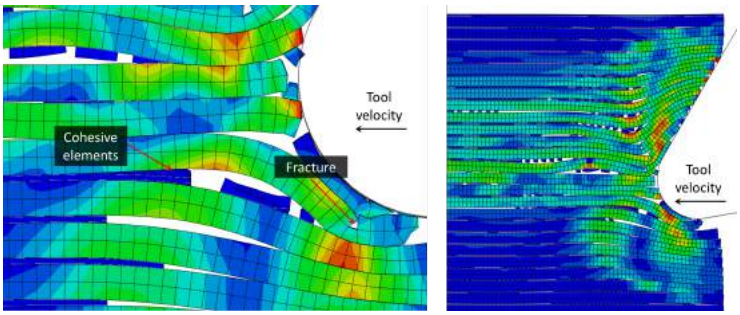

(a) Fibre side

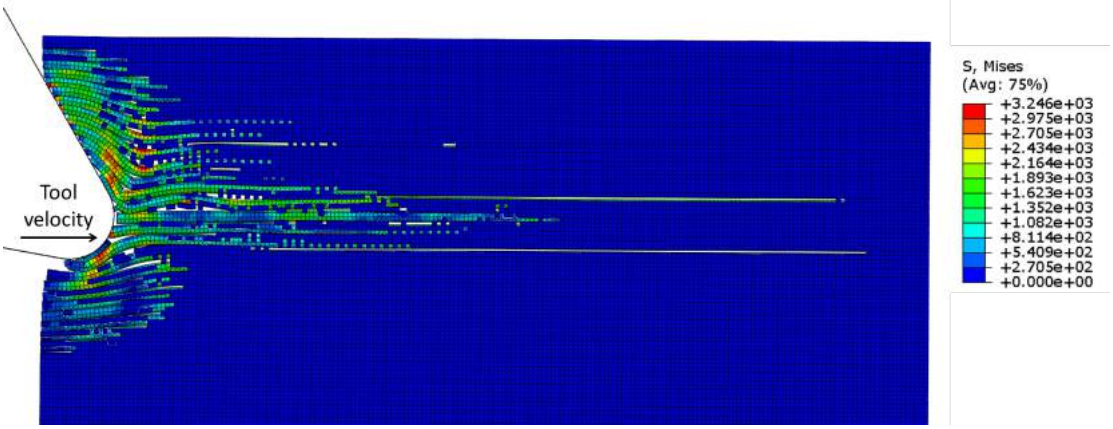

(b) Matrix side

Figure 7.6: Finite element model configuration at time 1.79e-3 seconds for fibre orientation θ=0°.

propagation towards the free surface of the sample through adjacent fibres. Deflection due to axial load increases ahead of the tool, as well as the damage in the fibre below the cutting plane, where some cracks, due to compression, are visible. Also matrix fracture increases. In particular, in the vicinity of the tool the majority of the finite elements, representing the matrix phase, are deleted from the analysis due to failure.

Further tool advancement causes buckling instability and failure ahead of the tool leading to multi-fractured fibres (Figure 7.8). The area interested by the cut increases, and the material bends and slides on the rake face of the tool. Also the zone affected by compression below the tool extends, with the matrix fracture reaching the EHM phase. A larger model

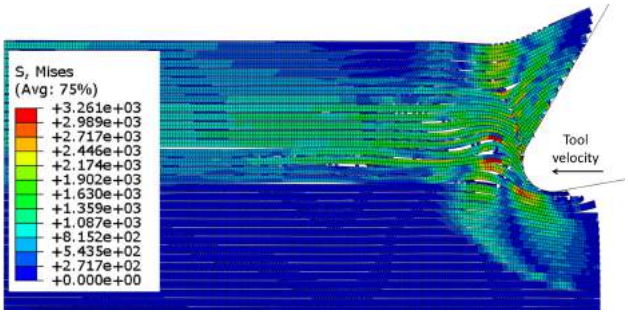

(a) Fibre side

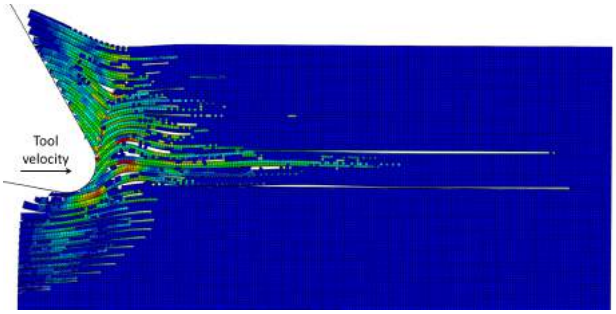

(b) Matrix side

Figure 7.7: Finite element model configuration at time 2.845e-3 seconds for fibre orientation θ=0°.

would be necessary in order to visualize the matrix failure deeper in the workpiece. The sample seems to be divided into four different horizontal strips depending on the material deformation. In fact, strips one and four can be associated with fibre bending. In strips two and three the fibre behaviour is mainly due to buckling, which tends to change to bending when moving towards strips one and four, respectively.

Configuration of the model at the end of the analysis is shown in Figure 7.9. Four strips can still be distinguished. The fibres contained in strips two and three fail mainly under buckling. With tool advancement, fractured pieces accumulate ahead of the tool, forming an agglomeration. The opening action is exerted by the tool to the material through this agglomeration. In particular, material belonging to strip one bends ahead of the cutting tool deforming on that agglomeration. In the same way, also the downward deformation of the

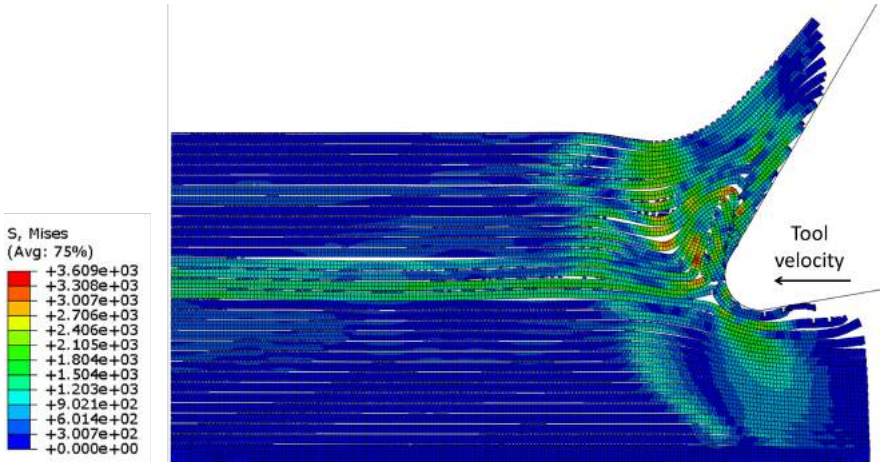

(a) Fibre side

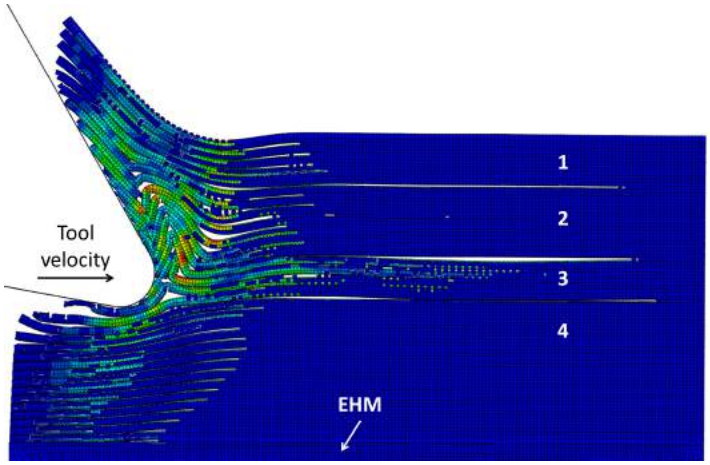

(b) Matrix side

Figure 7.8: Finite element model configuration at time 4.527e-3 seconds for fibre orientation θ=0°.

fibres in strip four starts ahead of the tool. Matrix damage is wide and it is possible to imagine it extending far below the cutting plane. A continuous chip takes place and slides onto the rake face of the tool. It is important to notice how almost no contact between the clearance face and the workpiece takes place, because of the elements' deletion due to failure, as visible in Figure 7.10.

The cohesive elements' configuration at the end of the analysis is shown in Figure 7.11, where the QUADSCRT variable, indicating the damage initiation condition, is reported.

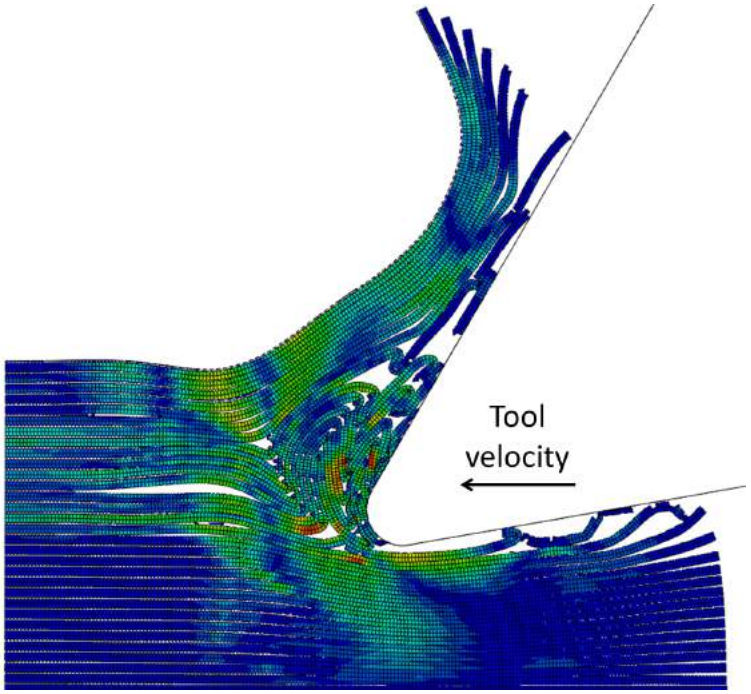

(a) Fibre side

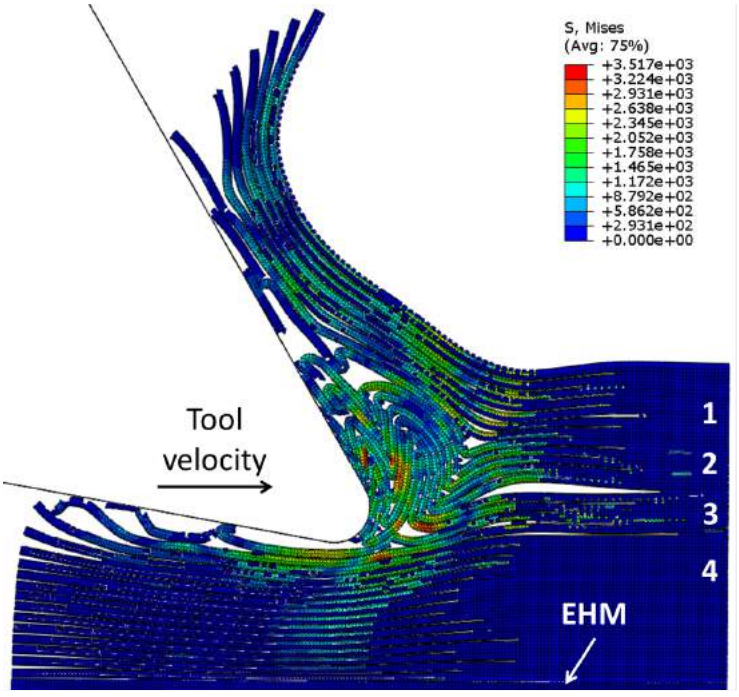

(b) Matrix side

Figure 7.9: Finite element model configuration at time 1.09e-2 seconds corresponding to the end of the analysis for fibre orientation θ=0°.

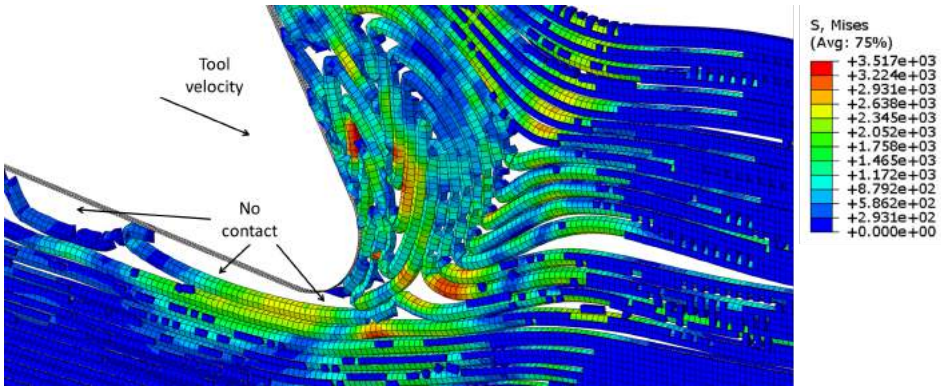

Figure 7.10: Tool tip-workpiece interaction at time 1.09e-2 seconds in the finite element model for fibre orientation θ=0°.

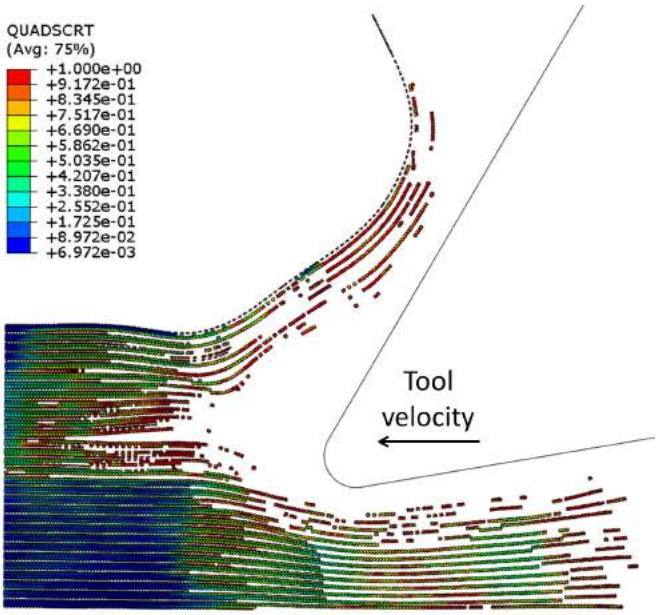

Figure 7.11: Cohesive elements' configuration at the end of the analysis in the finite element model for fibre orientation θ=0°.

Values equal to the represent cohesive elements that have been damaged, but have not yet failed. All cohesive elements fail ahead of the tool, where the agglomeration of fibres is located. The failure is due to two reasons. Firstly it is caused by the matrix failure, which leads to the linked cohesive element deletion. Secondly, the large amount of deformation the fibres undergo causes stretching of cohesive elements until failure, i.e. debonding between

fibre and matrix. Cohesive elements located in the vicinity of the fibre agglomeration are generally damaged and prone to failure with further advancement of the tool. Cohesive elements' failure below the cutting plane in the region under compression is connected to matrix failure.

7.3.1.2 Hybrid model for fibre orientation θ=0°

Damage variable for SPH matrix set to D=0.8. The results obtained by implementing the hybrid model were analysed at the same time-steps considered for the finite element model for comparison purposes. The configuration of the model at time 5.77e-4 seconds is shown in Figure 7.12. The behaviour of the finite elements in the hybrid model is similar to that observed in the FEM model, with the fibre at the centre undergoing buckling and the others bending due to the opening action exerted by the tool. Differently, finite elements deleted are converted to particles. This is particularly visible for the matrix due to its brittle behaviour.

At time 1.79e-3 seconds (Figure 7.13) an increase of the bending can be observed for

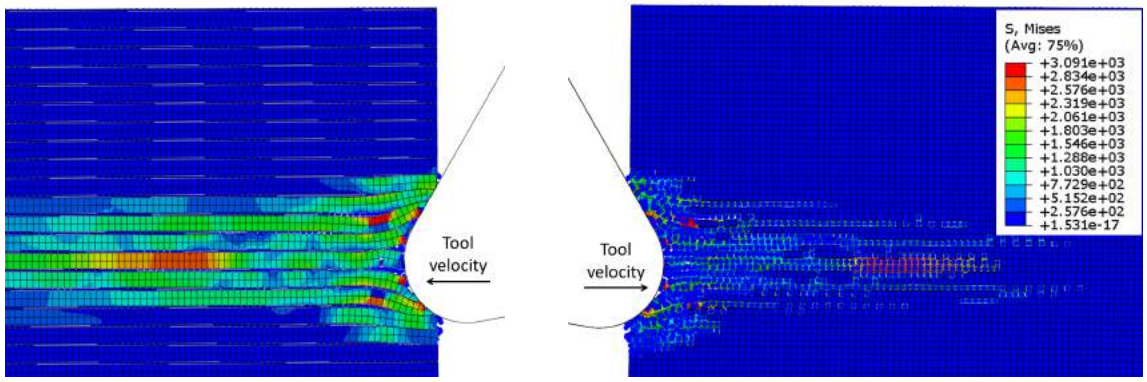

(a) Fibre side *(b) Matrix side*

Figure 7.12: Hybrid model configuration at time 5.77e-4 seconds for fibre orientation θ=0° when implementing a matrix damage variable for the SPH D=0.8.

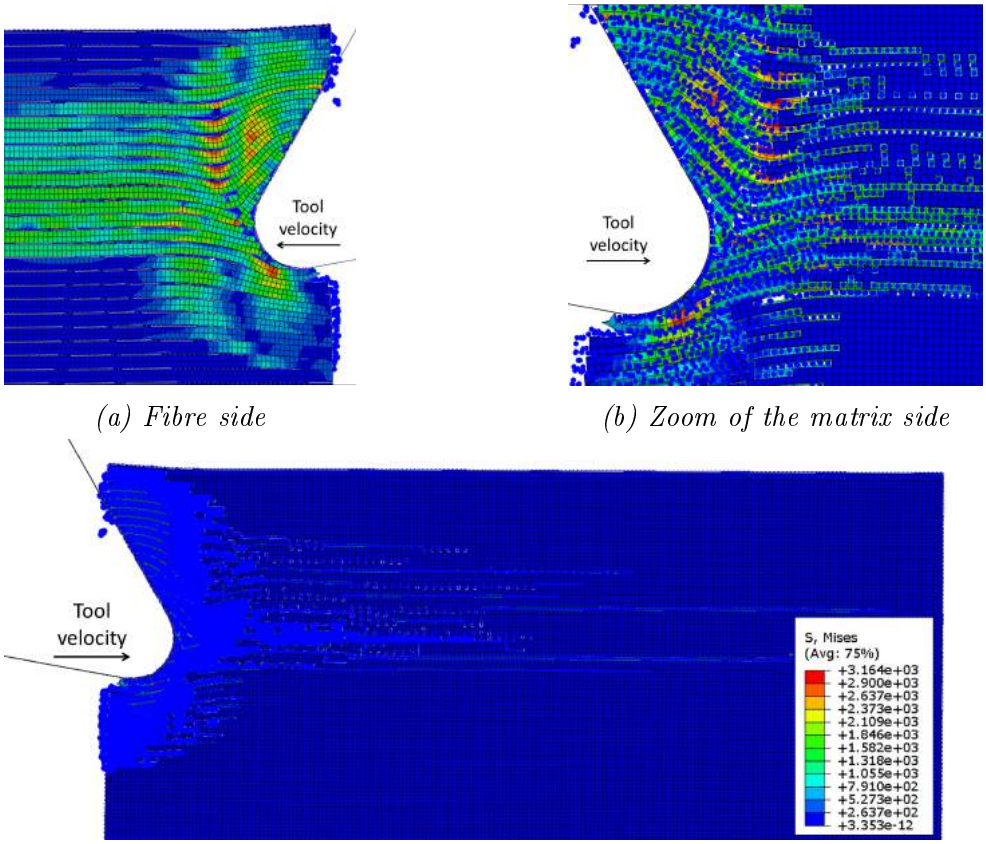

(a) Fibre side *(b) Zoom of the matrix side*

(c) Matrix side

Figure 7.13: Hybrid model configuration at time 1.79e-3 seconds for fibre orientation θ=0° when implementing a matrix damage variable for the SPH D=0.8.

fibres above the cutting edge, which leads to bending failure. Fibres below the cutting plane are bent downwards with a consequent arising of cracks. At this time-step it is already possible to appreciate the difference between the hybrid and the FEM model. Firstly, it is possible to notice how particles accumulate around the cutting edge of the tool. Secondly, the presence of damaged material in the model increases the volume of material affected by the cut. The stress propagates farther from the cutting area compared with the FEM model. This is particularly visible on the upper corner of the sample. At the time-step considered, it experiences an upward bending deformation; while in the FEM model the fibre located

on the free edge was still in the original configuration (Figure 7.6). Also, the matrix finite elements failed corresponding to the corner, which is different from the FEM model. Hence, the tool exerts the opening action through the damaged material involving material located far from it.

As for the FEM model, cohesive elements are stretched due to the high amount of deformation that fibres undergo during compression, leading to debonding ahead of the tool (Figure 7.14). However, a large number of cohesive elements are deleted because of matrix failure.

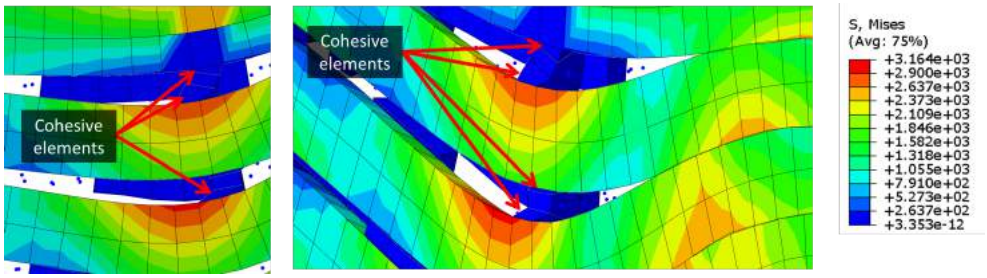

Figure 7.14: Cohesive elements behaviour at time 1.79e-3 seconds in the hybrid model for fibre orientation θ=0° when implementing a matrix damage variable for the SPH D=0.8.

At time-step 2.845e-3 seconds (Figure 7.15) the material configuration is similar for the two approaches. A crack propagates from the cutting edge towards the free surface of the sample orthogonally to the fibres' axis. Along its path, crack formation seems to be caused by different failure mechanisms. It starts ahead of the cutting edge due to buckling instability, and propagates far from it due to bending failure.

The compression exerted by the tool on the material below it is visible, showing the deformations of the particles located on the vertical free edge of the sample, which tends to come out.

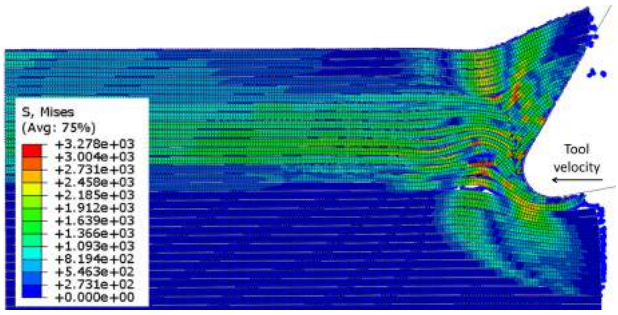

Figure 7.15: Hybrid model configuration at time 2.845e-3 seconds for fibre orientation θ=0°when implementing a matrix damage variable for the SPH D=0.8.

At time-step 4.527e-3 seconds (Figure 7.16) the fractured fibres and matrix in front of the tool, composed by the FEM and SPH elements, contribute to form an agglomeration, as was observed for the FEM approach. Differently from the latter method, the agglomeration is formed also by failed matrix elements. The material ahead of the tool can be divided into four strips, with number one and four containing fibres undergoing bending and number two and three composed of fibres experiencing mainly buckling. With tool advancement, SPH particles tend to accumulate in the vicinity of the cutting edge.

The difference between the hybrid and the finite element model can be even more appreciated at time-step 1.09e-2 seconds (Figure 7.17).

In both approaches a continuous chip is formed, but the angle formed by the free surface of the chip in the hybrid model is higher than that in the FEM due to a higher amount of material in the former approach, which includes the damaged material. It is possible to observe how the material surrounds the tool, and in particular the cutting edge. No loss of contact takes place between the clearance face and the machined surface. The pressure applied by the material on the clearance face contributes to the thrust force.

In addition, the hybrid model is able to simulate and predict the bouncing back. In

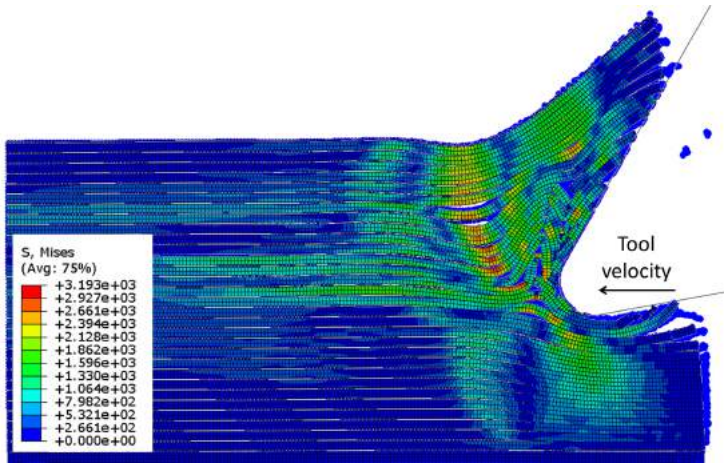

(a) Fibre side

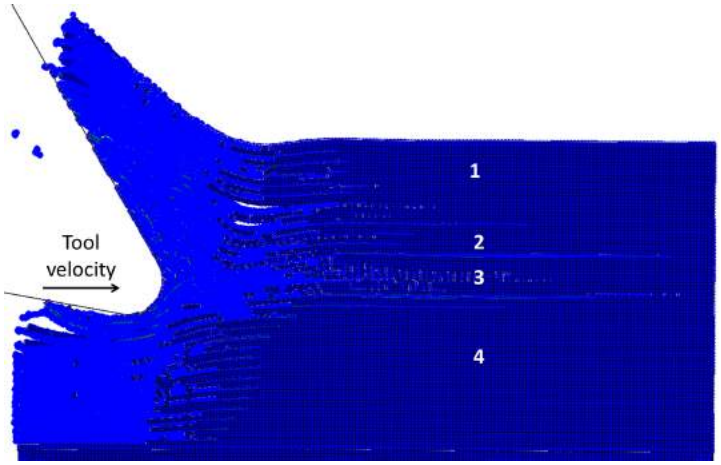

(b) Matrix side

Figure 7.16: Hybrid model configuration at time 4.527e-3 seconds for fibre orientation θ=0° when implementing a matrix damage variable for the SPH D=0.8.

fact, each particle representing the damaged material can weakly interact with other SPH particles according to the constitutive model assigned. Hence, the activated particles are able to simulate a material full of cracks that can experience an elastic recovery.

When compared with the finite element model (Figure 7.11), the extension of the cohesive element failure is wider for the hybrid model (Figure 7.18). It is possible to observe that almost the totality of the cohesive elements failed below the tool. This is mainly due to the

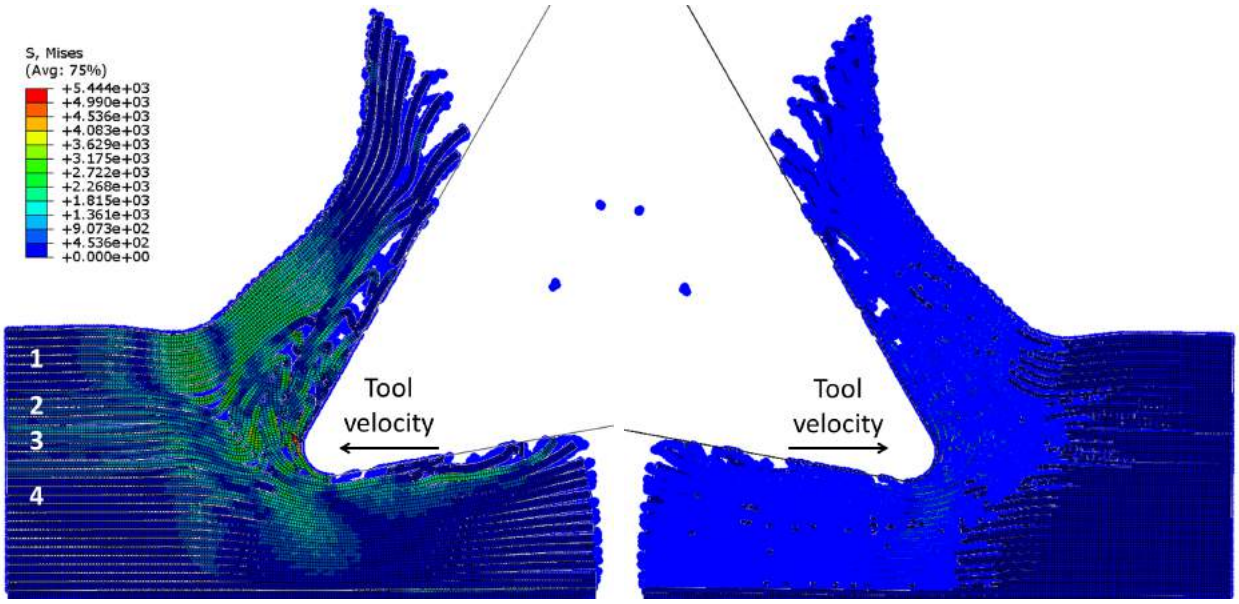

(a) Fibre side *(b) Matrix side*

Figure 7.17: Hybrid model configuration at time 1.09e-2 seconds for fibre orientation θ=0° when implementing a matrix damage variable for the SPH D=0.8.

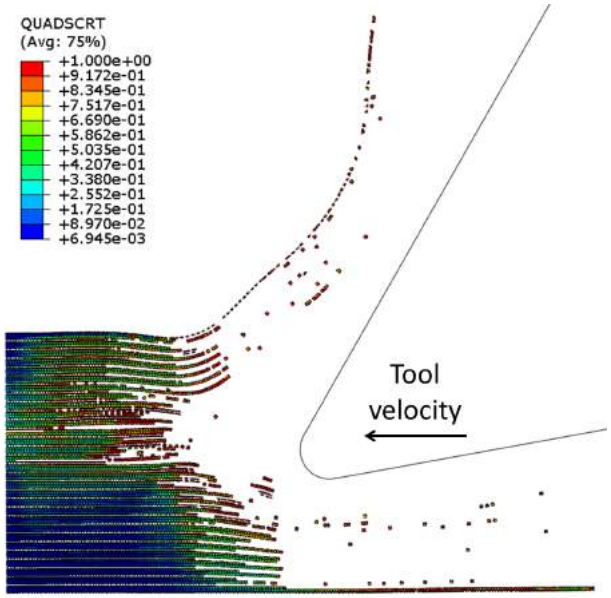

Figure 7.18: Cohesive elements' configuration at the end of the analysis in the hybrid model for fibre orientation θ=0° when implementing a matrix damage variable for the SPH D=0.8.

matrix finite elements' failure. In fact, the damage in the matrix phase is also more extended in the hybrid model. As it was previously observed, the presence of damaged material in the

model, due to the conversion, causes a larger volume of material involved during cutting in all directions.

Damage variable for SPH matrix set to D=0.1. A simulation using the hybrid model employing variable damage for the matrix phase D=0.1 is presented in the following.

A small change in the results can be appreciated already at time-step 5.77e-4 seconds (Figure 7.19). In fact, the finite elements of the central fibre fail in the vicinity of the tool. During tool advancement, fibre deformation under compressive axial load takes place. Unlike with previous models, the presence of a stiffer fractured material ahead of the tool causes a local failure due to compression, which anticipates the failure due to buckling instability.

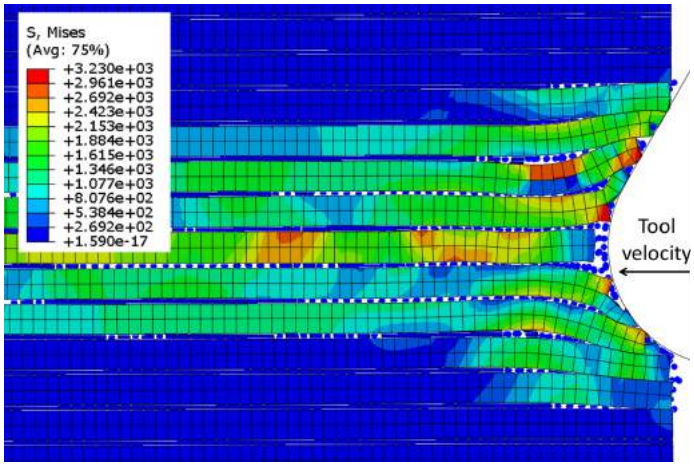

Figure 7.19: Hybrid model configuration at time 5.77e-4 seconds for fibre orientation θ=0° when implementing a matrix damage variable for the SPH D=0.1.

This behaviour is more evident at time-step 1.79e-3 (Figure 7.20). During cutting, the matrix finite elements around the fibres fail. When a stiffer fracture material is implemented for the matrix, it could cause a reduction of the fibre deformation due to axial loads, favouring a local failure under compression. In this case it is also possible to observe the opening action

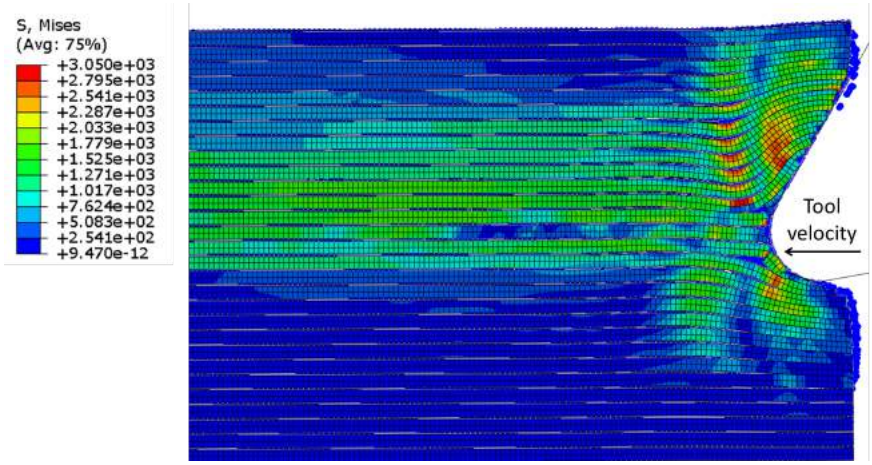

(a) Fibre side

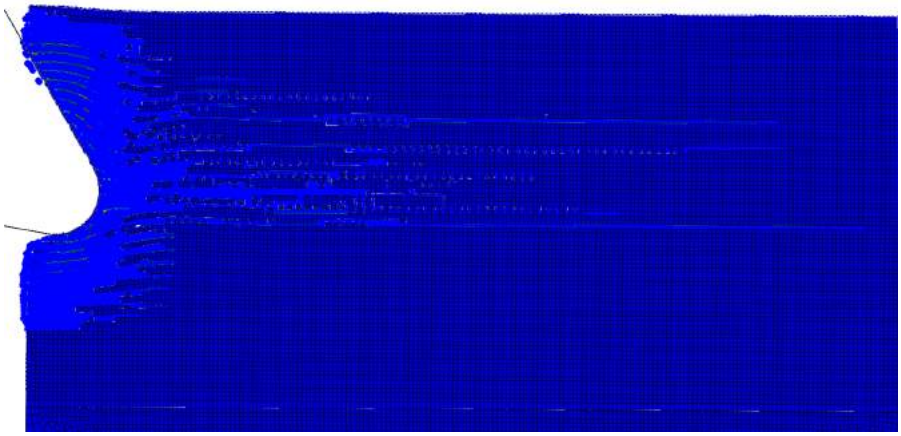

(b) Matrix side

Figure 7.20: Hybrid model configuration at time 1.79e-3 seconds for fibre orientation θ=0° when implementing a matrix damage variable for the SPH D=0.1.

exerted by the tool on the workpiece with the fibre bending upwards and downwards above and below the cutting edge, respectively. The latter undergoes fracture and crack formation due to the pushing down action of the tool.

During tool advancement, deformations due to axial load start to rise in the fibres ahead of the cutting area (Figure 7.21). These are smaller when compared with previous models. Also a crack, propagating towards the free edge of the sample through adjacent fibres can be

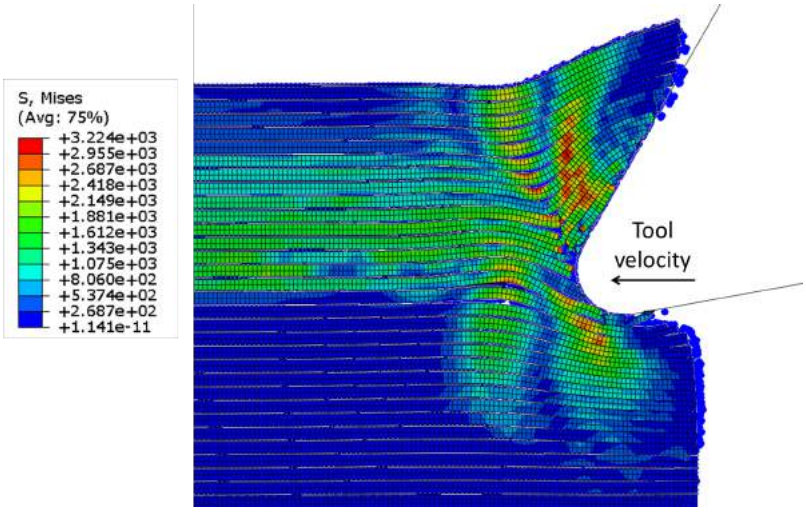

Figure 7.21: Hybrid model configuration at time 2.845e-3 seconds for fibre orientation θ=0° when implementing a matrix damage variable for the SPH D=0.1.

observed, whose extension is smaller than in the previous models.

Axial load deformations in the fibres increase during tool advancement causing buckling instability and failure.

A significant difference to previous models can be observed in Figure 7.22. A smaller number of fibres undergo buckling failure ahead of the tool, with the majority experiencing bending deformation. Consequently, the agglomeration formed has a smaller dimension, and it is contained near the tool tip. Results suggest that higher stiffness properties of fractured material allow an increase of the amount of bouncing back. In fact, a bigger amount of material is in contact with the clearance face of the tool.

Cohesive elements in the final configuration are reported in Figure 7.23. As observed for the previous hybrid model, a larger area with failed cohesive elements can be observed when compared with the FEM model (Figure 7.11). A few damaged cohesive elements are still present in the chip, while they have almost all totally failed below the cutting plane. In the

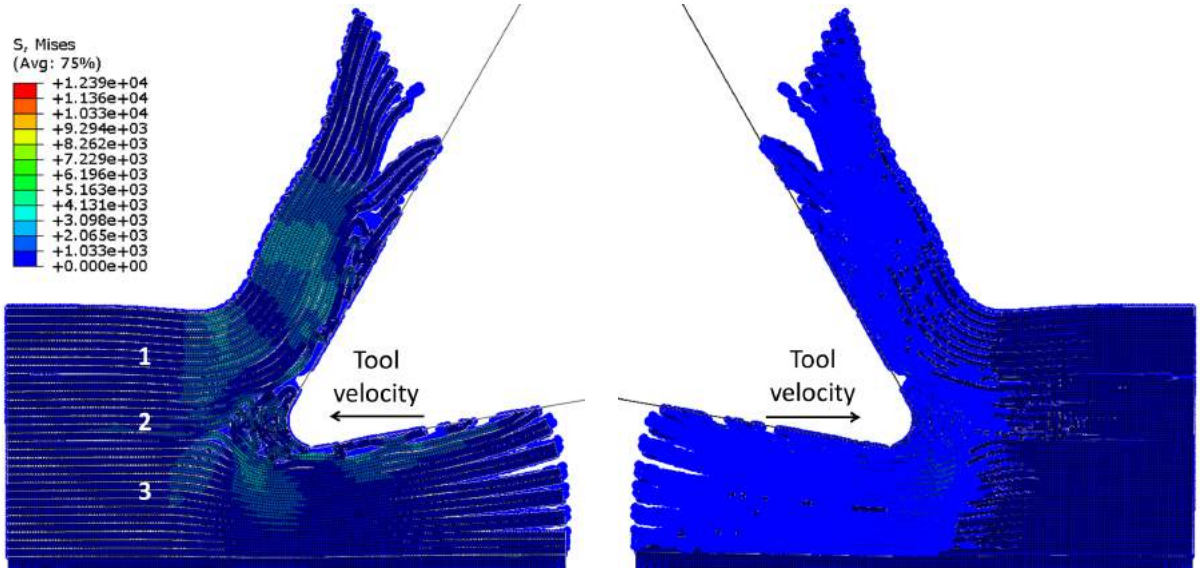

(a) Fibre side *(b) Matrix side*

Figure 7.22: Hybrid model configuration at time 1.09e-2 seconds for fibre orientation θ=0°when implementing a matrix damage variable for the SPH D=0.1.

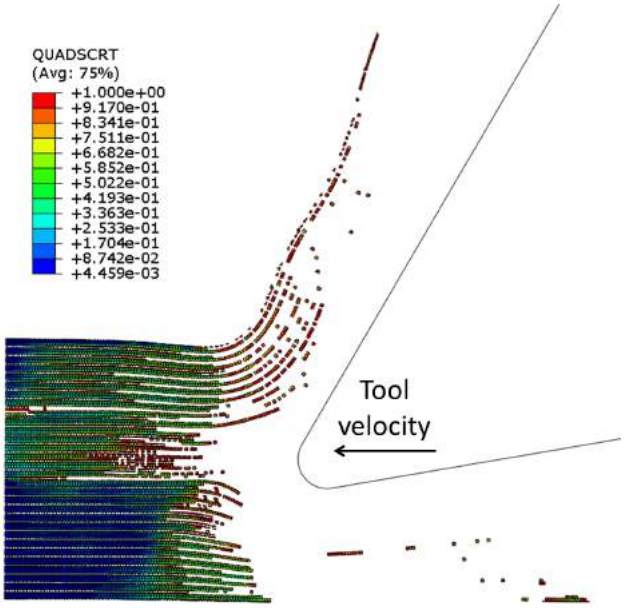

Figure 7.23: Cohesive elements' configuration at the end of the analysis in the hybrid model for fibre orientation θ=0° when implementing a matrix damage variable for the SPH D=0.1.

.

latter zone, the cohesive element deletion is mainly due to the matrix finite elements' failure.

It is possible to imagine how the matrix and cohesive elements' damage extends far below

the micro-mechanical model area. A bigger number of fibres should be implemented in the model in order to be able to evaluate the damage extension.

7.3.1.3 Finite Element Model for fibre orientation θ=90°

For fibre orientation θ=90°, the chip formation mechanism changes compared to that observed for θ=0°. At the beginning of the analysis, the tool comes into contact with the workpiece (Figure 7.24). Tool advancement causes matrix fracture, which extends ahead of

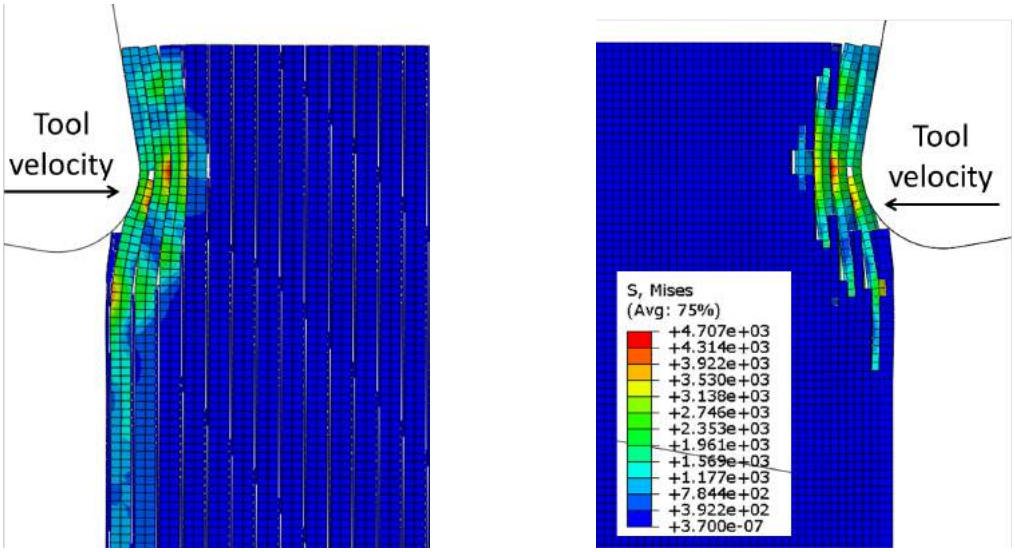

(a) Fibre side *(b) Matrix side*

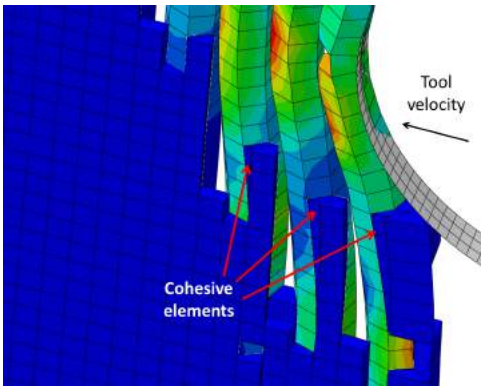

(c) Cohesive elements behaviour - Matrix side

Figure 7.24: Finite element model configuration at time 4.2e-4 seconds for fibre orientation θ=90°.

the cutting zone and below the cutting plane. The latter is due to the high amount of bending the fibres undergo, being pushed by the tool. The high level of deformation arising in all phases of the material can be noticed on observing the cohesive elements' behaviour, which is shown in Figure 7.24(c). They are highly deformed trying to keep matrix and fibres together. Debonding and cohesive element delation due to matrix failure can be observed during cutting. Fibre fracture takes place in the first fibre in contact with the tool. It is possible to assume that a crack starts propagating across the fibre along points where the maximum principal stress criterion is satisfied. The fibre is not totally cut at this stage.

Tool advancement causes a large amount of failure of the matrix elements far ahead of the tool and below the cutting path (Figure 7.25). Due to the matrix elements' deletion, consecutive fibres come into contact. The tool action is transmitted between two adjacent fibres. A large amount of bending takes place in the fibres. The fibre in contact with the

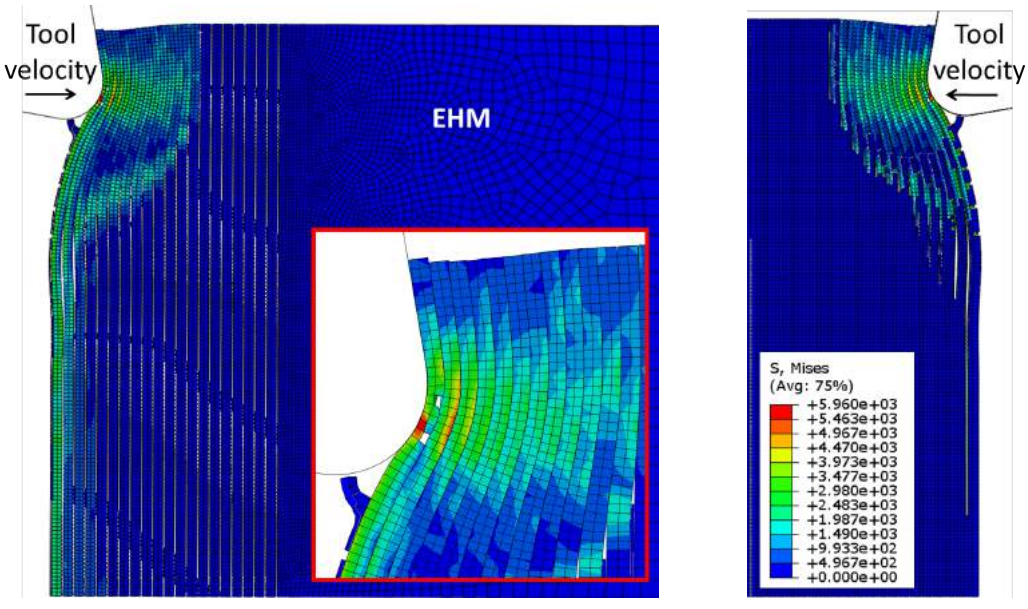

(a) Fibre side *(b) Matrix side*

Figure 7.25: Finite element model configuration at time 1.46e-3 seconds for fibre orientation θ=90°.

cutting edge is compressed in the cutting direction. A second crack arises below that which was previously formed. The matrix fracture propagates along the first fibre to almost the border of the model, deep in the workpiece.

Fibre bending continues to increase with tool advancement, involving a growing number of fibres (Figure 7.26). Cracks formed in the first fibre propagate dividing it into two parts. The upper part forms the chip, sliding slowly on the rake face of the tool, while the lower slides on the cutting edge towards the clearance face. In addition, a crack formation in the second fibre can be observed. The extension of the matrix failure increases with the fibre bending, moving far ahead of the tool and deep into the workpiece.

The cohesive elements' failure extends far ahead of the cutting tool and below the cutting path. Comparing Figure 7.27 and Figure 7.26(b), it is possible to observe that the cohesive

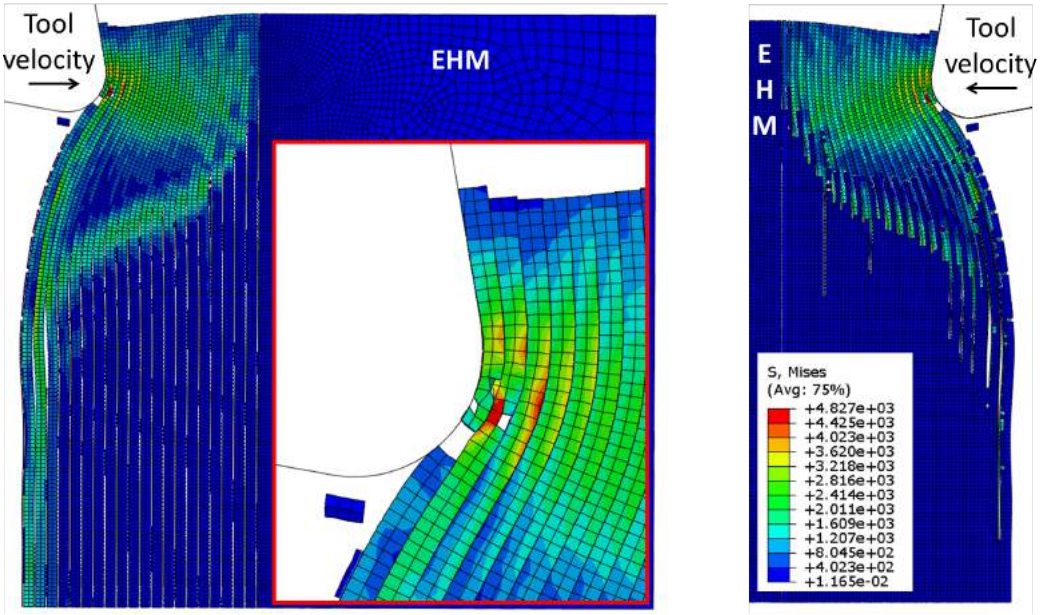

(a) Fibre side *(b) Matrix side*

Figure 7.26: Finite element model configuration at time 2.26e-3 seconds for fibre orientation θ=90°.

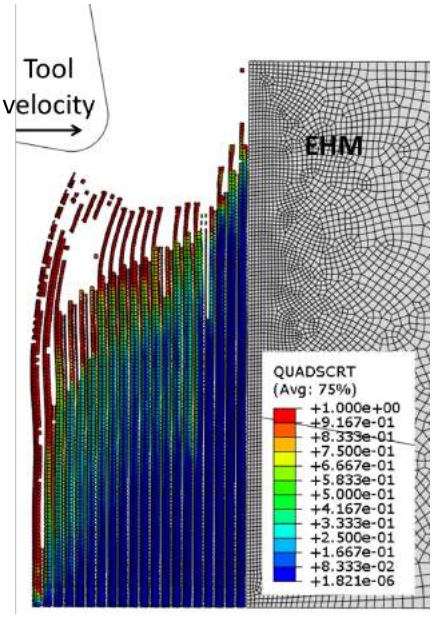

Figure 7.27: Cohesive elements' configuration at time 2.26e-3 seconds in the finite element model for fibre orientation θ=90°.

element failure is mainly associated with the matrix elements' deletion.

A longer analysis could reveal the elastic recovery that the first fibre undergoes after the tool has passed, bending in the opposite direction. It could also reveal if the fibres far ahead of the cutting tool, and so not in direct contact with it, could bend without experiencing damage and return to the original position after the tool has passed. However, fibre failure near the cutting edge takes place above the cutting plane.

7.3.1.4 Hybrid Model for fibre orientation θ=90°

Simulation using the hybrid model was carried out considering the value of the damage variable for the SPH matrix D=0.1. A difference between hybrid and FEM models can be already observed at the beginning of the analysis (Figure 7.28). Tool advancement causes fibre bending with associated matrix and cohesive elements' failure, as previously observed.

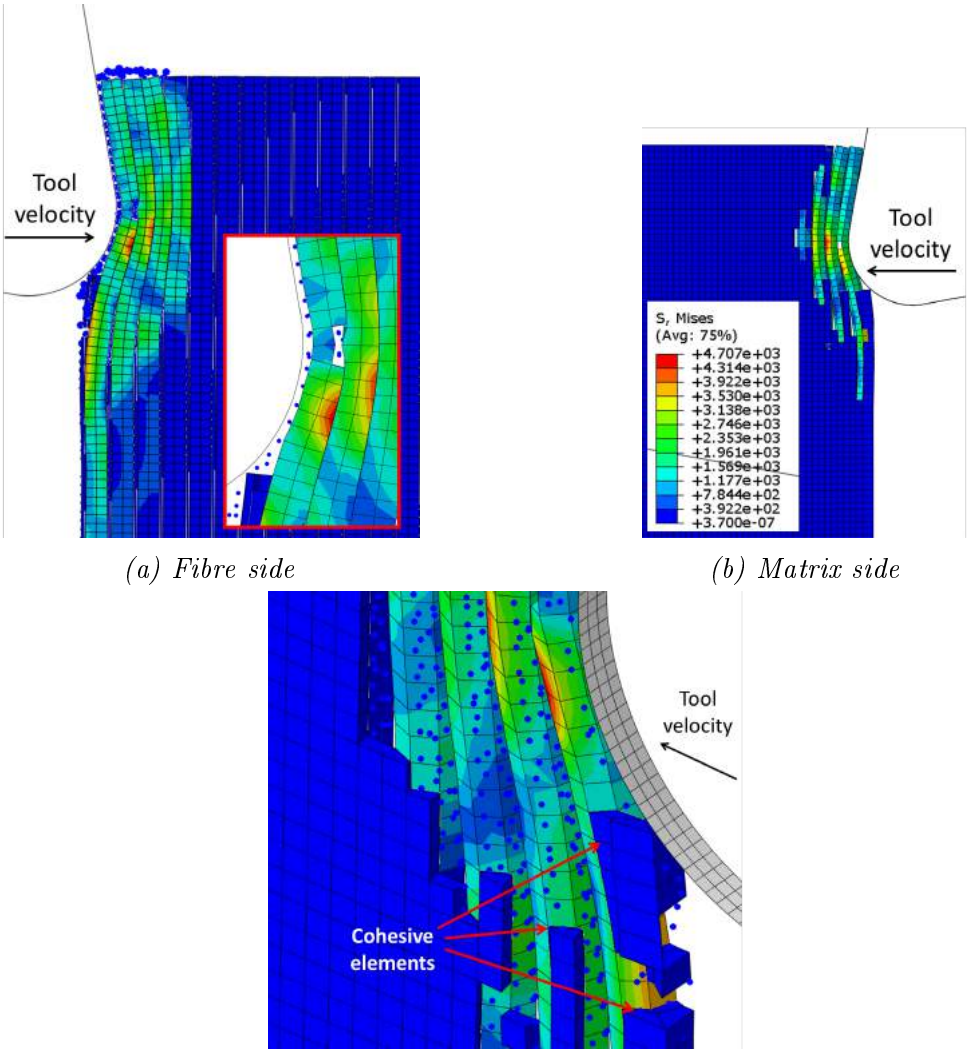

(a) Fibre side *(b) Matrix side*

(c) Cohesive elements behaviour - Matrix side

Figure 7.28: Hybrid model configuration at time 4.2e-4 seconds for fibre orientation θ=90° when implementing a matrix damage variable for the SPH D=0.1.

However, in the hybrid approach the extension of the crack formed in the first fibre is larger. Furthermore the number of fibres experiencing bending ahead of the tool is higher when compared with the FEM model. In fact, it is possible to observe the higher magnitude of the Von Mises stress in the fourth fibre (2.35e3 MPa instead of 1.17e3 MPa), which already starts to bend. Consequently, the amount of matrix and cohesive elements

which have failed is also higher, involving a larger area. As for fibre orientation θ=0°, the difference in behaviour between the two models is due the presence of fractured material represented by the SPH particles. Therefore, while in the FEM model elements' deletion usually causes a reduction of the stresses due to a loss of material, when FEM to SPH conversion is applied, the fractured material compacts under the tool forces, transferring the tool action to the undamaged material. As for the finite element model, cohesive elements undergo large deformations trying to keep together the matrix and fibre phases.

With tool movement fibres bending increases. Meanwhile, a large number of matrix elements are converted to particles (Figure 7.29). The conversion from FEM to SPH allows the simulating of the powder chip formation. In fact, it can be observed how particles tend to fly away from the cutting zone, in a form that it is possible to consider as representative of powder.

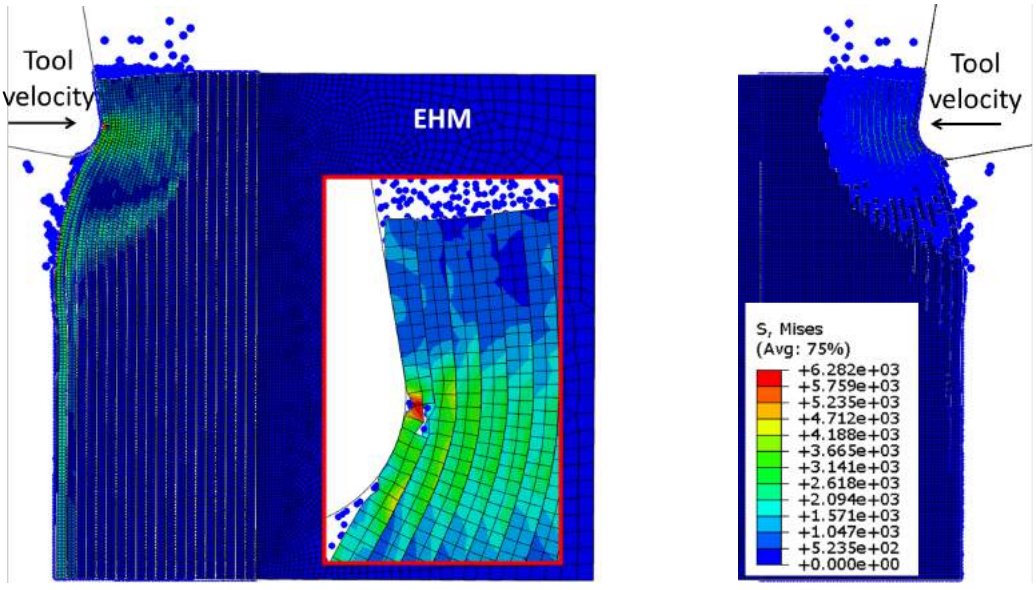

(a) Fibre side *(b) Matrix side*

Figure 7.29: Hybrid model configuration at time 1.46e-3 seconds for fibre orientation θ=90° when implementing a matrix damage variable for the SPH D=0.1.

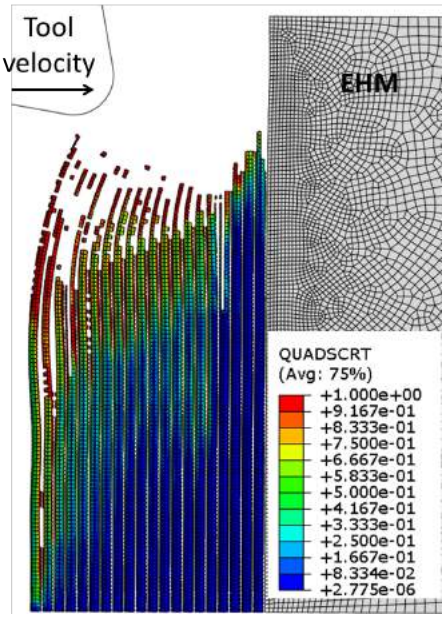

Figure 7.30: Cohesive elements' configuration at time 1.46e-3 seconds in the hybrid model for fibre orientation θ=90° when implementing a matrix damage variable for the SPH D=0.1

The cohesive elements' failure is mainly due to the matrix finite elements' deletion (Figure 7.30). The damage extension in the cohesive elements, still active in the model, extends far below the cutting plane (red areas), and a large number of them are near to experiencing damage initiation.

Fibre failure was analysed at the end of the simulation to observe the possible path that the formed crack could follow (Figure 7.31). As in the FEM model, the first fibre is divided into two parts, with the upper sliding slowly on the rake face. The second fibre experiences multi-fractures, but it is still composed of one part. Also in this case, the fibre failure takes place above the cutting plane.

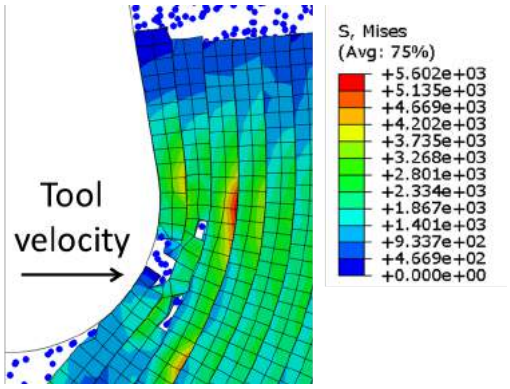

Figure 7.31: Hybrid model configuration at time 2.72e-3 seconds for fibre orientation θ=90° when implementing a matrix damage variable for the SPH D=0.1.

7.3.2 Comparison with experimental results

Results obtained for fibre orientations of θ=0° and θ=90° by means of the finite element model and the hybrid model were compared with the experiments reported in the previous chapter. Machining force and the chip formation mechanism have been considered for the comparison.

7.3.2.1 Validation of cutting force and thrust force

Cutting forces obtained when employing the hybrid and the FEM models are compared with experimental values shown in the previous chapter and reported in Figure 7.32. For fibre orientation θ=0°, the FEM model and the hybrid models show similar cutting force predictions. However the FEM model is closer to the experimental value. Between the hybrid models, a decrease in the matrix damage variable causes a slight increase of the cutting force, from 32.17 N/mm to 35.05 N/mm. The higher value obtained in the hybrid models is due to the element conversion. Damaged material remains in the model, helping in transferring the tool action to the undamaged material. In addition, the damaged material is compressed by

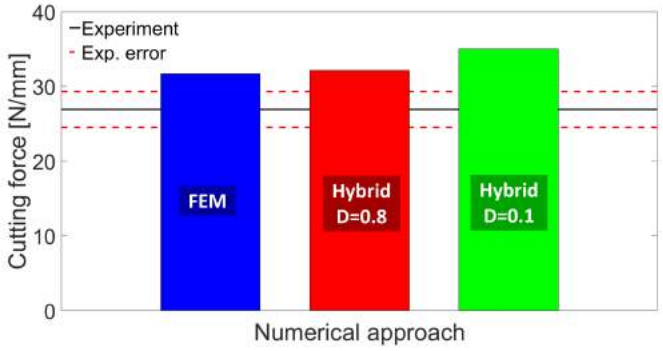

(a) θ=0°

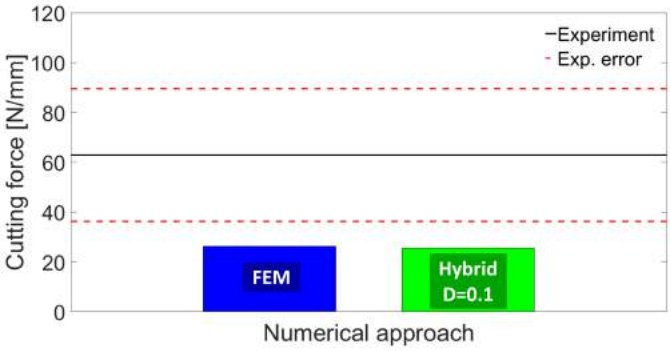

(b) θ=90°

Figure 7.32: Cutting force comparison between the hybrid model, the FEM model and the experimental results for fibre orientation (a) θ=0° and (b) θ=90°.

the tool, surrounding it. The smaller the damage variable is set for the particles, the stiffer the damaged material results, causing an increase in the cutting force.

As for the previous fibre angle, for fibre orientation θ=90° the cutting force predicted is similar for both approaches. It underestimates the experimental value. However, at the end of the simulation the chip formation mechanism was not simulated completely; this was due to the high computational cost necessary to create a model able to accommodate the chip formation and observe its repetition during cutting. In the simulations, an increasing number of fibres were involved and bent during tool advancement. This could lead to an increase of the cutting force in the case of a longer cutting length simulation.

Table 7.2: Comparison of the thrust force [N/mm] between the hybrid model, the FEM model and the experimental results.

	θ=0°	θ=90°
Experiment	35.68	59.29
FEM	-3.03	-4.28
Hybrid (D=0.8)	-1.42	N/A
Hybrid (D=0.1)	1.61	-2.49

The thrust force obtained from numerical simulations is reported in Table 7.2 and compared with the experimental results. It is possible to notice the thrust force is underestimated for both numerical approaches and fibre orientations. As observed for the cutting force, the models' prediction at fibre orientation θ=90° is affected by an incomplete simulation of the chip formation mechanism. In fact, at the end of the simulations the fibres are bent ahead of the cutting tool, with contact between the tool and the workpiece on the rake face and on the cutting edge. In addition, the tool displacement is not sufficient to penetrate the material allowing for possible contact between the machined surface and the clearance face.

Even if the thrust force is still underestimated, the hybrid model slightly improves its prediction compared with the FEM model for both fibre orientations. This is particularly visible at fibre angle θ=0°. The value predicted by the FEM model is negative, showing a downward force applied from the material on the tool. This thrust force direction is opposite to that observed experimentally. It is due to the chip formation mechanism, and can be explained considering Figure 7.9. In fact, an agglomeration of fractured fibres accumulates ahead of the tool above the cutting plane and in contact with the rake face. This exerts a force on the rake face pushing the tool downwards. At the same time, the element failure

and deletion causes the presence of a void below the cutting tool with absence of contact between the machined surface and the clearance face. Hence, there is no force that could contrast the downward action.

Differently, when the hybrid model is employed, the element conversion seems to provide more realistic behaviour during cutting. When a damage variable D=0.8 is used for the SPH matrix, the chip formation mechanism remains similar to that observed for the FEM model (Figure 7.17). However, the presence of particles after conversion allows simulation of the damaged material, which accumulates around the tool coming also in contact with the clearance face. The force exerted by machined material on the clearance face and on the lower part of the cutting edge acts upwards, opposing the downward force due to the material action on the rake face. The thrust force obtained still acts in the opposite direction to that experimentally observed, but its magnitude reduces, getting closer to a change of sign.

When a stiffer damaged material is considered (D=0.1), a smaller agglomeration forms ahead of the tool and around the cutting edge, through which the tool exerts the opening action (Figure 7.22). At the same time, more particles come into contact with the clearance face due to a larger elastic recovery experienced by the material after cutting. Differently from previous models, a weaker downward force is exerted by the already bent fibres on the rake face. Hence, the thrust force changes sign becoming positive. The material exerts an upward force on the tool in agreement with the experimental results.

7.3.2.2 Chip formation mechanisms and types of chip

The chip formation mechanisms observed during the experiments using the digital microscope are compared with the numerical results in Figure 7.33 and Figure 7.34. Since only images for the lowest cutting speed are available, these were used for a qualitative validation.

For fibre orientation θ=0°, both hybrid and FEM models show a continuous chip, as experimentally observed. In the FEM model, the chip tends to be a curling chip. Differently, the free surface of the chip in the hybrid model remains almost parallel to the rake face of the tool. This behaviour is closer to that observed in the experiments. The different shape of the chip is due to the presence of fractured material in the hybrid model that contributes, albeit weakly, to keep the fibres together.

Both models show a material opening similar to that experimentally observed, with the upper part bending upwards forming the chip and sliding on the rake face, and the lower bending downward below the cutting tool. A small amount of material seems to be accumulated ahead of the cutting edge in the digital microscope image (Figure 7.33(c)). The position of this agglomeration seems to be more similar to that observed in the hybrid model, i.e. all around the cutting edge instead of above it on the rake face (FEM).

In both models, fibres bending below the tool undergo multi-fracture, as observed experimentally on the machined surface by SEM (Figure 6.17(e)). However, after machining separated fractured and curled fibres can be observed on the machined surface in the FEM model. In contrast, as noticed for the chip, the damaged material in the hybrid model seems to help in keeping the fibres together. Furthermore, the machined surface is

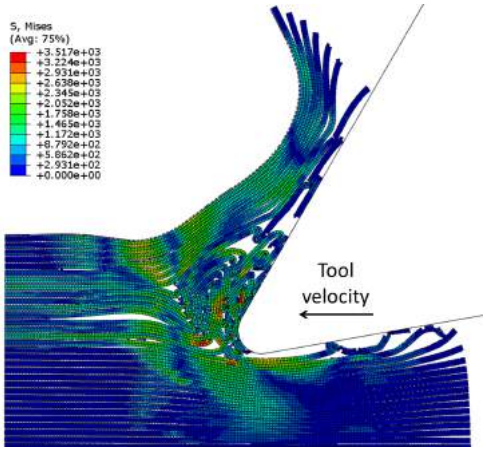

(a) FEM model

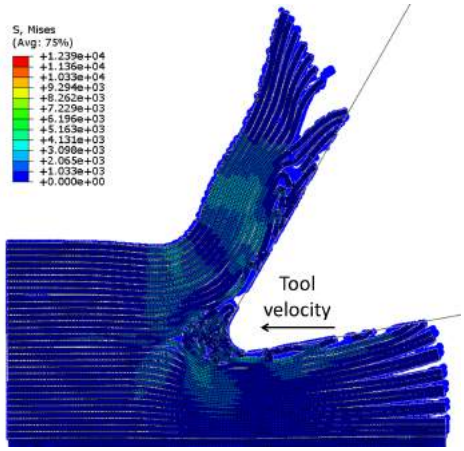

(b) Hybrid model D=0.1

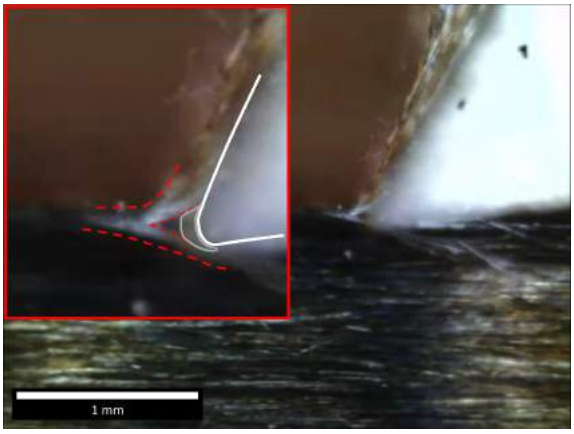

(c) Digital microscope image

Figure 7.33: Chip formed at the end of the analysis for (a) hybrid model; (b) FEM model; and (c) during the experiment, for fibre orientation θ=0°.

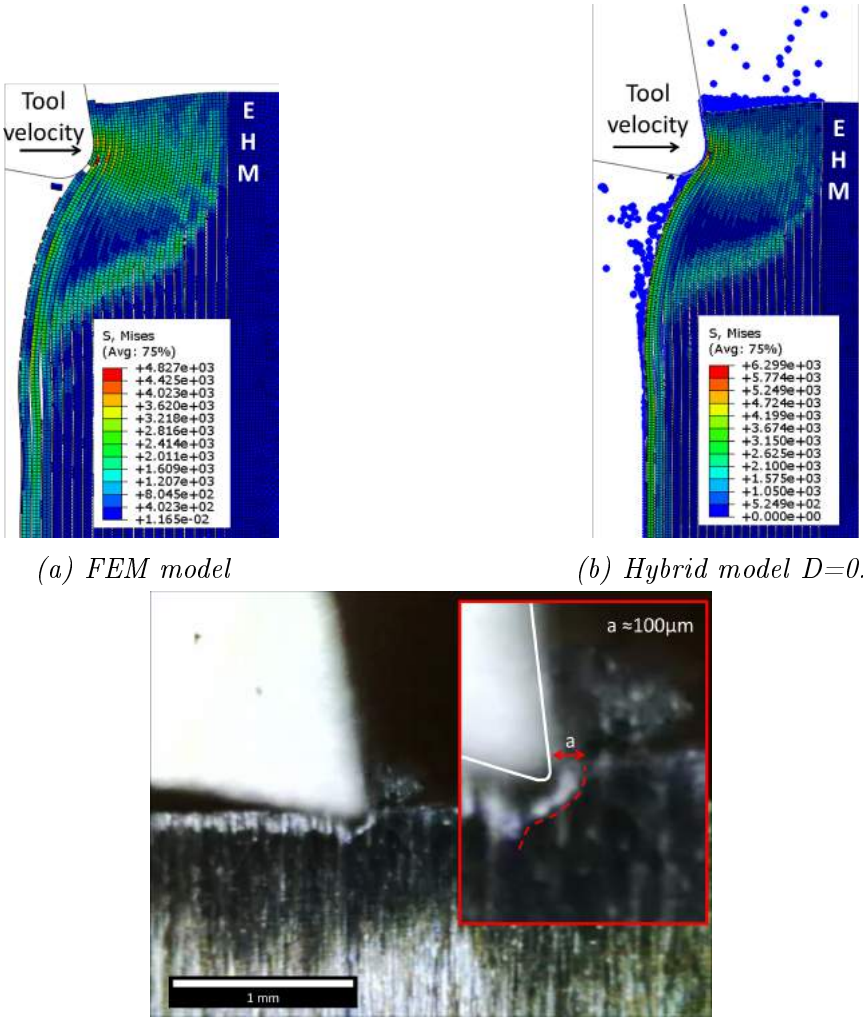

(a) FEM model *(b) Hybrid model D=0.1*

(c) Digital microscope image

Figure 7.34: Chip formed at the end of the analysis for (a) hybrid model; (b) FEM model; and (c) during the experiment, for fibre orientation θ=90°.

composed of fractured fibres embedded in the damaged material, which seems more similar to what was experimentally observed (Figure 6.17(e)).

Experimentally, no loss of contact seems to be experienced by the tool on the clearance face in the vicinity of the cutting edge. This condition is well represented by the hybrid model.

As for fibre orientation of θ=0°and also at θ=90° both models show a deformation

during cutting similar to that observed experimentally (Figure 7.34). The tool pushes the material ahead of it causing severe fibre bending. The material deformation during cutting is highlighted with a red line in the digital microscope image. This is very similar to that obtained numerically. From the experiments, the deformation extension in the material ahead of the tool was estimated to be at least 100 μm. It is clear that only a very large model would be able to capture the entire material removal mechanism.

Both models show fibre failure above the cutting plane with fibre sliding on the rake face. At the same time, a huge amount of matrix damage was observed. Hence, a powder-like chip is likely to form.

Due to the element conversion, the hybrid model shows the matrix particles flying away from the cutting area, confirming it to be a more realistic approach.

Finally, it is possible to observe the difference in the cutting mechanism between models developed in this chapter, implementing a round cutting edge (r=20 μm), and models based on the literature (developed in Chapter 4 and Chapter 5), where the cutting edge can be considered sharp (r=5 μm). This is particularly visible at fibre orientation θ=90°, where significant fibre bending was observed when machining with a round cutting edge; instead of local failure due to the compression exerted by the tool at the contact point, which produces a clear cut.

7.4 Summary

In order to overcome the drawbacks shown by the FEM approach, usually used for simulating machining processes, a hybrid model implementing finite element conversion to SPH particles has been developed. Results obtained using the classic FEM approach and the new hybrid approach have been compared with experimental findings reported in the previous chapter.

For fibre orientation θ=0° both approaches show similar prediction in terms of the cutting force, agreeing well with the experimental results. Even if the thrust force is underestimated for both models, the hybrid approach shows a slight improvement in the prediction. In addition, a change in thrust force direction has been detected between the FEM and the hybrid model (D=0.1), with the latter in agreement with experimental results. This has been linked to the chip formation mechanism observed during the analysis. In particular, the better agreement of the hybrid model is due to: conversion of failed elements that, experiencing spring back after machining, exert an upward force on the clearance face; and to a smaller agglomeration composed of deformed and damaged material located around the cutting edge and not on the rake face, as observed for the FEM model. The material removal mechanism in the hybrid model seems also more similar to the images captured using the digital microscope during cutting.

For fibre orientation θ=90° both approaches show a similar chip formation mechanism, which agrees well with images captured during machining. A significant fibre bending has been detected with fibre failure above the cutting plane. Cutting force and thrust force are underestimated for both approaches. However, the hybrid model shows a slightly better

thrust force prediction.

The hybrid model developed is able to make the most of the FEM approach, implementing cohesive elements for the fibre-matrix interface simulation, and to improve the thrust force prediction due to the FEM to SPH element conversion after failure.

The difference between the hybrid model and the FEM model is more evident with the increase of the number of finite elements failed during the analysis, and so with the increase of elements converted. The particles' dimension set in the analysis plays an important role. Problems in the contact between dormant particles due to finite elements' deformation lead to setting a smaller radius for the SPH particles. This negatively affects the thrust force prediction; since the damaged material can undergo larger deformation before it is compacted by the tool action. Better results have been obtained using a lower damage variable for the matrix particle. In fact, higher stiffness properties in the damaged material could compensate for the smaller radius of the particles.

Models developed in this chapter have also been able to capture the change in the chip formation mechanism when using a round cutting edge (r=20 μm). This can be observed when comparing results obtained with those reported in Chapter 4 and Chapter 5, where a sharp cutting edge was used (r=5 μm).

Chapter 8

Conclusions and future works

8.1 Conclusions

This thesis deals with the numerical simulation of the orthogonal cutting of unidirectional carbon fibre reinforced plastic composite. A comprehensive review of models developed highlighted a paucity of the description of the cohesive models' behaviour during simulation of machining operations; an excessive distortion that zero thickness cohesive elements based on the traction-separation law usually undergo during the analysis; and the poor thrust force prediction when using the commonly implemented FEM. In this thesis, new methodologies were suggested and tested to improve the capability of current numerical models to predict the machining force and the material response during orthogonal cutting, using the micro-mechanical approach. In particular, a new cohesive model able to avoid excessive distortion, linking cohesive element failure to that of surrounding elements, was developed. A comparison between the new model and previously used models was carried

out. The smoothed particle hydrodynamics (SPH) method was implemented to improve thrust force prediction, preventing element deletion during the analysis. However, the absence of a cohesive model does not allow the study of the fibre-matrix interface. Hence, a hybrid model, based on the FEM to SPH conversion and able to combine the advantages of both models, was developed. In-house experiments were conducted to support and validate the hybrid model; and furthermore to investigate the influence of machining parameters on the machining force and on the quality of the final component, combining the response surface method (RSM) and the analysis of variance (ANOVA).

The principal conclusions of this work can be summarised as follows:

- the novel interface model presented overcomes excessive deformation usually experienced by zero thickness cohesive elements based on the traction-separation law, providing more realistic behaviour and facilitating the fibre-matrix interface analysis, when compared with the surface-based cohesive behaviour.

- The comparison between a 2D-extruded model and a three-dimensional model implementing cylindrical fibres (3D-FEM model) showed a change in the cutting mechanism for fibre orientation θ=0° and θ=90°. While for fibre angle θ=0° a non realistic fibre failure due to compression was observed, for θ=90° a cleaner cut, due to compression induced fracture perpendicularly to the fibre axis, took place in the 3D-FEM model, as expected when machining with a sharp cutting edge. In the case of cylindrical fibres more compact behaviour of the composite material was detected, causing a slight increase and better prediction of the cutting force for fibre orientation

θ=0° and θ=90°. Independently from the assumption on the geometry, the thrust force is always underestimated.

- The smoothed particle hydrodynamics (SPH) method showed a better capability in simulating the process when compared with the 3D-FEM model. In fact, the chip type observed is close to that obtained from high-speed camera images. The SPH method is able to improve the chip formation mechanisms, in particular at fibre orientation θ=0°.

- The SPH method allows the studying and measuring of the bouncing back, providing a significant improvement in the prediction of the thrust force. The presence of damaged material in the model causes more material involved during cutting, which increases the damaged area when compared with the 3D-FEM model. Despite the advantages listed above, the absence of a cohesive model in the SPH method means information on the fibre-matrix interface is not obtained.

- In-house experiments revealed that the type of chip and the chip formation mechanism depend strongly on the fibre orientation and the rake angle.

- The effect of a round cutting edge was observed when machining at θ=0° and θ=90°, which promotes fibre buckling at the tool tip for the former and a predominance of fibre bending for the latter.

- The depth of damage is strongly affected by the fibre orientation and the depth of cut. An increase of fibre orientation and depth of cut leads to an increase in the damage depth.

- A good surface quality can be generally obtained for fibre angles θ<90° with negligible influence from the rake angle. An abrupt increase of the surface roughness takes place for fibre angles θ>90°, suggesting the use of a high positive rake angle to improve the quality of the machined surface.

- The bouncing back amount rises when machining with large fibre orientations, a deep depth of cut and a small rake angle.

- The most significant working parameters that affect the cutting force and thrust force are the fibre orientation and the depth of cut. However, the thrust force is also affected by the rake angle. An increase of the depth of cut always leads to an increase of the cutting force. The same effect was observed for the thrust force when machining with a negative rake angle; while more complex behaviour takes place for positive rake angles. Moreover, a negative thrust force was observed when machining at large fibre orientation and rake angles.

- The optimum setting of working parameters to minimise the surface roughness and the damage depth was determined for different fibre orientations. For θ=45°, rake angle α=-10° and moderate cutting speed Vel=366.82 mm/min are suggested; while for θ=90° and θ=135° a high positive rake angle α=30° and high cutting speed Vel=1100 mm/min should be used.

- A novel hybrid model able to combine the advantages of finite element and smoothed particle hydrodynamics methods was developed. It showed an improvement in the prediction of thrust force, when compared to the commonly used finite element method.

The hybrid model is also able to provide information about the bouncing back as well as about the fibre-matrix interface, due to the implementation of the novel cohesive model. It is able to take into account the effect of the round cutting edge on the chip formation mechanism for θ=0° and θ=90°, showing a closer behaviour than the FEM to that observed in the experiments for fibre orientation θ=0°. However, the computational cost of the hybrid model is higher than the generally used finite element model.

In conclusion, by the work undertaken it has been found out that the SPH method is the best to simulate the orthogonal cutting process. However, a future improvement in the hybrid method could lead to a more accurate simulation of the process, since it includes also the capability to simulate the interface between the fibre and matrix.

8.2 Future works

This thesis has suggested new approaches to fill some of the gaps reported in the literature review (Chapter 2). The hybrid model developed in Chapter 7 is able to implement the novel cohesive model presented in Chapter 3 and to improve the thrust force prediction, compared with the commonly used finite element method, thanks to the FEM to SPH conversion. A large amount of data was obtained from the in-house experiments. The type of chip, chip formation mechanism, cutting force, thrust force at fibre orientations θ=0° and θ=90° were all used to validate the model. Therefore, the following work could be carried out in the future to further improve the model:

- test the hybrid model for fibre orientation θ=45° and θ=135°;
- extend the model size to capture the periodicity of the chip formation mechanism for each fibre orientation as well as the damage far ahead of the cutting tool and below the cutting plane;
- validate the numerical models in terms of the amount of damage arising in each phase of the composite material;
- use SPH particles with a diameter equal to the length of the finite element with an aspect ratio equal to 1; this would improve the prediction of the thrust force;
- implement more than one particle for each finite element. This would improve the contact between particles and finite elements' faces in the model.

Further improvements based on the material data and material models need to be considered. In fact, availability of the material data for each phase is still limited in the literature. It will be necessary to develop more realistic material models for the fibres and matrix. For example, the matrix is strongly dependent on strain rate, loading conditions and temperature. However, existing models are usually simplified to a static elasto-plastic curve at room temperature. Therefore adequate material models that take into account the complex behaviour of each phase during the cutting process need to be developed.

Finally, the orthogonal cutting represents a fundamental step towards understanding the machining of composite materials. However, more complex machining operations, such as drilling and milling, which are more relevant to industrial applications, need to be investigated

using the developed numerical models.

Bibliography

[1] URL https://calfeedesign.com/tech-papers/technical-white-paper/.

[2] URL https://www.nap.edu/read/11424/chapter/3.

[3] . URL http://www.adhesivesmag.com/articles/94350-market-trends-lightening-up-with-carbon-fiber-reinforced-plastics.

[4] . URL http://blog.luxresearchinc.com/blog/2014/10/the-carbon-fiber-composite-market-will-reach-35-billion-in-2020-but-still-with-unmet-needs-for-developers-to-target/.

[5] . URL http://robbreport.com/aviation/slideshow/20-jaw-dropping-private-aircraft-interiors/ed-se-doret-boeing-787-dreamliner-vip.

[6] . URL http://www.modernairliners.com/boeing-787-dreamliner/boeing-787-dreamliner-specs/.

[7] . URL https://www.aircraftcompare.com/helicopter-airplane/Airbus-A350-XWB/71.

[8] . URL http://www.hkengineer.org.hk/program/articlephoto/paper_jun15_1.jpg.

[9] URL `https://en.wikipedia.org/wiki/Composite_material`.

[10] URL `http://netcomposites.com/guide-tools/guide/`.

[11] Jamal Y. Sheikh-Ahmad. *Machining of polymer composites*. Springer Science+Business Media, 2009.

[12] URL `https://en.wikipedia.org/wiki/Metal_matrix_composite`.

[13] URL `https://en.wikipedia.org/wiki/Ceramic_matrix_composite`.

[14] URL `http://www.modorplastics.com/thermoset-vs-thermoplastics`.

[15] C.R. Dandekar and Y.C. Shin. Multiphase finite element modeling of machining unidirectional composites: prediction of debonding and fiber damage. *J Manuf Sci E*, 130:1–12, 2008.

[16] A. Koplev, A. Lystrup, and T. Vorm. The cutting process, chip, and cutting forces in machining CFRP. *Composites*, 14(4):371–376, 1983.

[17] D. Arola, M. Ramulu, and D.H. Wang. Chip formation in the orthogonal trimming of graphite/epoxy composite. *Composites Part A*, 27A:121–133, 1996.

[18] D.H. Wang, M. Ramulu, and D. Arola. Orthogonal cutting mechanisms of graphite/epoxy composite. Part I: Unidirectional laminate. *Int J Mach Tools Manufact*, 35(12):1623–1638, 1995.

[19] D. Nayak, N. Bhatnagar, and N. Mahajan. Machining studies of uni-directional

glass fibre reinforced plastic (UD-GFRP) composites part 1: effect of geometrical and processparameters. *Mch Sci Technol*, 9:481–501, 2005.

[20] R. Voß, M. Henerichs, F. Kuster, and K. Wegener. Chip root analysis after machining carbon fiber reinforced plastics (CFRP) at different fiber orientations. *Procedia CIRP*, 14:217–222, 2014.

[21] R. Zitoune, F. Collombet, F. Lachaud, R. Piquet, and P. Pasquet. Experiment - calculation comparison of the cutting conditions representative of the long fiber composite drilling phase. *Compos Sci Technol*, 65:455–466, 2005.

[22] G. Santhanakrishnan, R. Krishnamurthy, and S.K. Malhotra. Investigation into the machining of carbon-fibre-reinforced plastics with cemented carbides. *J Mater Process Tech*, 30:263–275, 1992.

[23] F. Kahwash, I. Shyha, and A. Maheri. Machining unidirectional composites using single-point tools: analysis of cutting forces, chip formation and surface integrity. *Procedia Eng*, 132:569–576, 2015.

[24] X.M. Wang and L.C. Zhang. An experiemental investigation into the orthogonal cutting of unidirectional fibre reinforced plastics. *Int J Mach Tools Manufact*, 43:1015–1022, 2003.

[25] K. A Calzada, S. G Kapoor, R. E De Vor, J. Samuel, and A. K Srivastava. Modeling and interpretation of fiber orientation-based failure mechanisms in machining of carbon fiber-reinforced composites. *J Manuf Proces*, 14:141–149, 2012.

[26] H. Li, X. Qin, G. He, Y. Gin, D. Sun, and M. Prince. Investigation of chip formation and fracture toughness in orthogonal cutting of UD-CFRP. *Int Adv Manuf Technol*, 82:1079–1088, 2016.

[27] H.Y. Pwu and H. Hocheng. Chip formation model of cutting fiber-reinforced plastics perpendicular to fiber axis. *J Manuf Sci E*, 120:192–196, 1998.

[28] D. Arola and M. Ramulu. Orthogonal cutting of fibre-reinforced composites: a finite element analysis. *Int J Mech Sci*, 39(5):597–613, 1997.

[29] N. Bhatnagar, N. Ramakrishnan, N.K. Naik, and R. Komanduri. On the machining of fiber reinforced plastic (FRP) composite laminates. *Int J Mach Tools Manufact*, 35(5): 701–716, 1995.

[30] Y. Wei, Q. An, X. Cai, M. Chen, and W. Ming. Influence of fibre orientation on single-point cutting fracture behavior of carbon-fibre/epoxy prepreg sheets. *Materials*, 8:6738–6751, 2015.

[31] G. Venu Gopala Rao, P. Mahajan, and N. Bhatnagar. Three-dimensional macro-mechanical finite element model for machining of unidirectional-fiber reinforced polymer composites. *Mat Sci Eng A*, 498:142–149, 2008.

[32] M. Ramulu. Machining and surface integrity of fibre-reinforced plastic composites. *SADHANA-ACAD P ENG S*, 22:449–472, 1997.

[33] D. Iliescu, D. Gehin, I. Iordanoff, F. Girot, and M.E. Guetiérrez. A discrete element method for the simulation of CFRP cutting. *Compos Sci Technol*, 70:73–80, 2010.

[34] G. Venu Gopala Rao, P. Mahajan, and N. Bhatnagar. Machining of UD-CFRP composites: experiment and finite element modeling.

[35] N. Bhatnagar, D. Nayak, I. Singh, H. Chouhan, and P. Mahajan. Determination of machining-induced damage characteristic of fiber reinforced plastic composite laminates. *Mater Manuf Process*, 19(6):1009–1023, 2004.

[36] T. Kaneeda. CFRP cutting mechanism. *Transaction of North American Manufacturing Research Institute of SME*, 19:216–221, 1991.

[37] D. Che, I. Saxena, P. Han, P. Guo, and K. F. Ehmann. Machining of carbon fiber reinforced plastics/polymers: a literature review. *J Manuf Sci Eng*, 136:1–5, 2014.

[38] H. Takeyama and N. Iijima. Machinability of glass-fiber reinforced plastics and application of ultrasonic machining. *CIRP Ann*, 37:93–96, 1988.

[39] L.C. Zhang, H.J. Zhang, and X.M. Wang. A force prediction model for cutting unidirectional fibre-reinforced plastics. *Mach Sci Technol*, 5:293–305, 2006.

[40] A.S. Jahromi and B. Bhar. An anlyttical method for predicting cutting forces in orthogonal machining of unidirectional composites. *Compos Sci Technol*, 70:2290–2297, 2010.

[41] G.C. Everstine and T.G. Rogers. Aplastics machining of fiber-reinforced materials. *J Compos Mater*, 5:94–106, 1971.

[42] A. Langella, L. Nele, and A. Maio. A torque and thrust prediction model for drilling of composite materials. *Composites Part A*, 36:83–93, 2005.

[43] J. Sheikh-Ahmad, J. Twomey, D. Kalla, and P. Lodhia. Multiple regression and committee neural network force prediction model in milling FRP. *Mach Sci Technol*, 11:391–412, 2007.

[44] D. Kalla, J. Sheikh-Ahmad, and J. Twomey. Prediction of cutting forces in helical and milling fiber reinforced polymers. *Int J Mach Tool Manu*, 50:882–891, 2010.

[45] Y. Karpat, O. Bahtiyar, and B. Deger. Mechanistic force modeling for milling of unidirectional carbon fiber reinforced polymer laminates. *Int J Mach Tool Manu*, 56: 79–93, 2012.

[46] Y. Karpat, O. Bahtiyar, and B. Deger. Milling force model of multidirectional carbon fiber reinforced polymer laminates. *Procedia CIRP*, pages 460–465, 2012.

[47] V. Chandrasekharan, S.G. Kapoor, and R.E. DeVor. A mechanistic approach to predicting the cutting forces in drilling: with application to fiber-reinforced composite materials. *ASME J Eng Ind*, 117:559–570, 1995.

[48] K.F. Ehmann, S.G. Kapoor, R.E. DeVor, and I. Lazoglu. Machining process modeling: a review. *J Manuf Sci E-T ASME*, 119:655–663, 1997.

[49] M. Vaz, D.R.J. Owen, V. Kalhori, M. Lundblad, and L.E. Lindgren. Modelling and simulation of machining prprocess. *Arch Comput Methods Eng*, 14:173–204, 2007.

[50] S.L. Soo and D.K. Aspinwall. Developments in modelling of metal cutting processes. *Proc IMechE Vol. 221 Part L: J Materials: Design and Applications*, 221:197–211, 2007.

[51] P.J. Arrazola, T. Özel, D. Umbrello, M.Davies, and I.S. Jawahir. Recent advances in modelling of metal machining processes. *CIRP Ann*, 62:695–718, 2013.

[52] C.E. Fisher, W.T. Wu, P. Chigurupati, and J.T. Jinn. Application of three dimensional finite element modeling for the simulation of machining processes. *AIP Conf Proc*, 712: 1353–1358, 2004.

[53] C.R. Dandekar and Y.C. Shin. Modeling of machining of composite materials: a review. *Int J Mach Tool Manu*, 57:102–121, 2012.

[54] K.K. Chawla. *Composite material:science and engineering*. Springer Science+Business Media, 2012.

[55] J. L Cantero, C. Santiuste, N. Marín, X. Soldani, and H. Miguélez. 2D and 3D approaches to simulation of metal and composite cutting. In *AIP Conference Proceedings*, volume 1431, pages 651–659. AIP Publishing, 2012.

[56] C. Santiuste, A. Olmedo, X. Soldani, and H. Miguélez. Delamination prediction in orthogonal machining of carbon long fiber-reinforced polymer composites. *J Reinf Plast Compos*, 31:875–885, 2012.

[57] C. Santiuste, X. Soldani, and M.H. Miguélez. Machining FEM model of long fiber composites for aeronautical components. *Compos Struct*, 92:691–698, 2010.

[58] D. Nayak, I. Singh, N. Bhatnagar, and P. Mahajan. An analysis of machining induced ddamage in FRP composites - a micromechanics finite element approach. *AIP Conf Proc*, 712:327–331, 2004.

[59] V. Palani. Finite element simulation of 3D drilling in unidirectional CFRP composite. Master's thesis, Wichita State University, 2006.

[60] O. Isbilir and E. Ghassemieh. Numerical investigation of the effects of drill geometry on drilling induced delamination of carbon fiber reinforced composites. *Compos Struct*, 105:126–133, 2013.

[61] V.A. Phadnis, A. Roy, and V.V. Silberschmidt. A finite element model of ultrasonically assisted drilling in carbon/epoxy composites. *Procedia CIRP*, 8:141–146, 2013.

[62] G. Venu Gopala Rao, P. Mahajan, and N. Bhatnagar. Micro-mechanical modeling of machining of FRP composites - cutting force analysis. *Compos Sci Technol*, 67:579–593, 2007.

[63] G. Venu Gopala Rao, P. Mahajan, and N. Bhatnagar. Machining of UD-GFRP composites chip formation mechanism. *Compos Sci Technol*, 67:2271–2281, 2007.

[64] R. Rentsch, O. Pecat, and E. Brinksmeier. Macro and micro process modeling of the cutting of carbon fiber reinforced plastics using FEM. *Procedia Eng*, 10:1823–1828, 2011.

[65] A.C. Orifici, I. Herszberg, and R.S. Thomson. Review of methodomethod for composite material modelling incorporating failure. *Compos Struct*, 86:194–210, 2008.

[66] R.S. Sandhu. A survey of failure theories of isotropic and anisotropic materials. Technical report, Air force flight dynamics laboratory, Wright-Patterson air force base, Ohio, 1973.

[67] M.J. Hinton, A.S. Kaddour, and P.D. Soden, editors. *Failure criteria in fibre-reinforced-polymer composites.*

[68] A.J. Kinloch and R.J. Young. *Fracture behaviour of polymers.* London : Applied Science, 1983.

[69] H. Altenbach amd K. Tushtev. A new static failure criterion for isotropic polymers. *Mech Compos Mater*, 37:475–482, 2001.

[70] Z. Xia, Y. Hu, and F. Ellyin. Deformation behavior of an epoxy resin subject to multiaxial loadload. Part II: constitutive modeling and predictions. *Polym Eng Sci*, 43: 734–748, 2003.

[71] D. Arola, M.B. Sultan, and M. Ramulu. Finite element modeling of edge trimming fiber reinforced plastics. *J Manuf Sci E-T ASME*, 124:32–40, 2002.

[72] D. Nayak, N. Bhatnagar, and P. Mahajan. Machining studies of UD-FRP composites part 2: finite element analysis. *Mach Sci Technol*, 9:503–528, 2005.

[73] L. Lasri, M. Nouari, and M. El Mansori. Modelling of chip separation in machining unidirectional FRP composites by stiffness degradation concept. *Compos Sci Technol*, 69:684–692, 2009.

[74] Z. Hashin and A. Rotem. A fatigue failure criterion for fiber reinforced materials. *J Compos Mater*, 7:448–464, 1973.

[75] L. Lasri, M. Nouari, and M. El Mansori. Wear resistance and induced cutting damage of aeronautical FRP components obtained by machining. *Wear*, 271:2542–2548, 2011.

[76] A. Mkaddem and M. El Mansori. Finite element analysis when machining UGF-reinforced PMCs plates: chip formation, crack propagation and induced-damage. *Mater Des*, 30:3295–3302, 2009.

[77] A. Mkaddem, I. Demirci, and M. El Mansori. A micro-macro combined approach using FEM for modelling of machining of FRP composites: cutting forces analysis. *Compos Sci Technol*, 68:3123–3127, 2008.

[78] X. Soldani, C. Santiuste, A. Mu noz Sánchez, and M.H. Miguélez. Influence of tool geometry and numerical parameters when modeling orthogonal cuting of LFRP composites. *Composites Part A*, 42:1205–1216, 2011.

[79] C. Santiuste, H. Miguélez, and X. Soldani. Out-of-plane failure mechanisms in LFRP composite cutting. *Compos Struct*, 93:2706–2713, 2011.

[80] S. Zhang. *An eulerian cutting model for unidirectional fiber-reinforced polymers*. PhD thesis, North Carolina State University, Mechanical Engineering, 2016.

[81] A. Abena, S.L. Soo, and K. Essa. A finite element simulation for orthogonal cutting of UD-CFRP incorporating a novel fibre-matrix interface model. *Procedia CIRP*, 31: 539–544, 2015.

[82] T. Hobbiebrunken, B. Fiedler, M. Hojo, S. Ochiai, and K. Schulte. Microscopic yielding of CF/epoxy composites and the effect on the formation of thermal residual stresses. *Compos Sci Technol*, 65:1626–1635, 2005.

[83] J.L. Jordan, J.R. Foley, and C.R. Siviour. Mechanical properties of Epon 826/DEA epoxy. *Mech Time-Depend Mater*, 12:249–272, 2008.

[84] J.D. Littell, C.R. Ruggeri, R.K. Goldberg, G.D. Roberts, W.A. Arnold, and W.K. Binienda. Measurement of epoxy resin tension, compression, shear stress-strain curves over a wide range of strain rrate using small test specimens. *J Aerosp Eng*, 21:162–173, 2008.

[85] W. Chen and B. Zhou. Constitutive behavior of epoxy 828/T-403 at various strain rates. *Mech Time-Depend Mater*, 2:103–111, 1998.

[86] F. Dunne and N. Petrinic. *Introduction to computational plasticity.* Oxford University Press Inc, 2005.

[87] H. Rodney. *The mathematical theory of plasticity.* Oxford University Press, 1998.

[88] W.F. Hosford. *Fundamentals of engineering plasticity.* Cambridge University Press, 2013.

[89] Y. ZhoY. Zhou. Wang and Y. XiaY. Xia. Jeelani. Tensile behavior of carbon fiber bundles at different strain rates. *Mater Lett*, 64:246–248, 2010.

[90] Y. Zhou, Y. Wang, S. Jeelani, and Y Xia. Experiment study on tensile behaviour

of carbon fibre and carbon fibre reinforced aluminium at different strain rate. *Appl Compos Mater*, 14:17–31, 2007.

[91] K. Honjo. Fracture toughness of PAN-based carbon fibers estimated from strength-mirror size relation. *Carbon*, 41:979–984, 2003.

[92] N. Oya and D.J. Johnson. Longitudinal compressive behaviour and microstructure of PAN-based carbon fibres. *Carbon*, 39:635–645, 2001.

[93] M. Ueda, W. Saito, R. Imahori, D. Kanazawa, and Tae-Kun Jeong. Longitudinal direct compression test of a single carbon fiber in a scanning electron microscope. *Composites Part A*, 67:96–101, 2014.

[94] V.A. Phadnis, F. Makhdum, A. Roy, and V.V. Silberschmidt. Drilling in carbon/epoxy composites: experimental investigations and finite element implementation. *Composites Part A*, 47:41–51, 2013.

[95] N. Feito, J. López-Puente, C. Santiuste, and M.H. Miguélez. Numerical prediction of delamination in CFRP drilling. *Compos Struct*, 108:677–683, 2014.

[96] J. Zhang and X. Zhang. Simulating low-velocity impact induced delamination in composites by a quasi-static load model with surface-based cohesive contact. *Compos Struct*, 125:51–57, 2015.

[97] J. Zhang and X. Zhang. An efficient approach for predicting low-velocity impact force and damage in composite laminates. *Compos Struct*, 130:85–94, 2015.

[98] P. P Camanho and C.S. Davila. Mixed-mode dechoesion finite elements for the simulation of delamination in composite materials. Technical Report NASA/TM-2002-211737, National Aeronautics and Space Administration (NASA), 2002.

[99] M. May. Numerical evaluation of cohesive zone models for modeling impact induced delamination in composite materials. *Compos Struct*, 133:16–21, 2015.

[100] S. Salih, K. Davey, and Z. Zou. Rate-dependent elastic and elasto-plastic cohesive zone models for dynamic crack propagation. *Int J Solids Struct*, 90:95–115, 2016.

[101] A. Mubashar and I. A. Ashcroft. Comparison of cohesive zone elements and smoothed particle hydrodynamics for failure prediction of single lap adhesive joints. *J Adhes*, 2015.

[102] G. Chennakesavelu. Orthogonal machining of uni-directional carbon fiber reinforced polymer composites. Master's thesis, Golden Valley Institute of Technology, 2006.

[103] X. Weixing, L. C Zhang, and Y. Wu. Elliptic vibration-assisted cutting of fibre-reinforced polymer composites: Understanding the material removal mechanisms. *Compos Sci Technol*, 92:103–111, 2014.

[104] M.J. Pitkethly and J.B. Doble. Characterizing the fibre/matrix interface of carbon fibre-reinforced composites using a single fibre pull-out test. *Composites*, 21(5):389–395, 1990.

[105] P.F.M. Meurs, B.A.G. Schrauwen, P.J.G. Schreurs, and T. Peijs. Determination of the

interfacial normal strength using single fibre model composites. *Composites Part A*, 29A:1027–1034, 1998.

[106] URL `https://en.wikipedia.org/wiki/Tungsten_carbide`.

[107] M.V. Ramesh, K.N. Seetharamu, N. Ganesan, and M.S. Sivakumar. Analysis of FRP using FEM. *Int J Mach Tool Manu*, 38(1531-1549), 1998.

[108] P.A. Cundall and O.D.L. Strack. A discrete numerical model for granular assemblies. *Géotechnique*, 29(1):47–65, 1979.

[109] ABAQUS User 's Manual, version 6.13.

[110] R.A. Gingold and J.J. Monaghan. Smoothed particle hydrodynimics: threory and application to non spherical stars. *Mon Not R Astron*, pages 375–389, 1977.

[111] A. Zahedi, S. Li, A. Roy, V. Babitsky, and V.V. Silberschmidt. Application of Smooth-Particle Hydrodynamics in metal machining. *J Phys: Conf Ser*, 382:12–17, 2012.

[112] F. Spreng and P. Eberhard. Machining process simulations with smoothed particle hydrodynamics. *Procedia CIRP*, 31:94–99, 2015.

[113] M. Madaj and M. Píška. On the SPH Orthogonal cutting simulation of A2024-T351 alloy. *Procedia CIRP*, 8:152–157, 2013.

[114] M. Zetterberg. A critical overview of machining simulations in ABAQUS. Master's thesis, KTH Royal Institute Of Technology, 2014.

[115] J. Limido, C. Espinosa, M. Salaün, C. Mabru, and R. Chieragatti. High speed machining modelling: SPH method capabilities. *4th SPHERIC*, 2009.

[116] J. Limido, C. Espinosa, M. Salaün, and J.L. Lacome. SPH mothod applied to high speed cuttign modelling. *Int J Mech Sci*, 49:898–908, 2007.

[117] URL *http* : *//nptel.ac.in/courses*/101104010/*lecture*12/12_5.*htm*.

[118] L. Iannucci and J. Ankersen. An energy based damage model for thin laminated composites. *Compos Sci Technol*, 66:934–951, 2006.

[119] Hexcel. HexPly® M21 Epoxy Matrix (180 °C/356 °F curing matrix) Product Data. Technical report.

[120] I N C . T O R A Y C A R B O N F I B E R S A M E R I C A. T800s data sheet.

[121] A.K. Parida, B.C. Routara, and R.K. Bhuyan. Surface roughness model and parametric optimization in machining of GFRP composite: Taguchi and Response surface methodology approach. *Materials Today: Proceedings*, 2:3065–3074, 2015.

[122] C.C. Tsao and Y.C. Chiu. Evaluation of drilling parameters on thrust force in drilling carbon fiber reinforced plastic (CFRP) composite laminates using compound core-special drills. *Int J Mach Tool Manu*, 51:740–744, 2011.

[123] K. Essa and P. Hartley. Optimization of conventional spinning process parameters by means of numerical simulation and statistical analysis. *Proc IMechE Part B: J Engineering Manufacture*, 224:1691–1705, 2010.

[124] G.R. Johnson and R.A. Stryk. Conversion of 3D distorted elements into mechless particles during dynamic deformation. *Int J Impact Eng*, 28(9):947–966, 2003.

[125] G.R. Johnson, S.R. Beissel, and C.A. Gerlach. A 3D combined particle-element method for intensive impulsive loading computations involving devere distortions. *Int. J Impact Eng*, 84:171–180, 2015.

[126] G.R. Johnson, S.R. Beissel, and C.A. Gerlach. A combined particle-element method for high-velocity impact computations. In *Procedia Eng*, volume 58, pages 269–278, 2013.

[127] G.R. Johnson, S.R. Beissel, and C.A. Gerlach. Another approach to a hybrid particle-finite element algorithm for high-velocity impact. *Int J Impact Eng*, 38(5):397–405, 2011.

[128] L.M. Bresciani, A. Manes, T.A. Romano, P. Iavarone, and M. Ciglio. Numerical modeling to reproduce fragmentation of a tungsten heavy alloy projectile impimpact a ceramic tile: adaptive solid mesh technique and the cohesive law. *Int J Impact Eng*, 87:3–13, 2016.

[129] Nan Xiao, Xiao-Ping Zhou, and Qiu-Ming Gong. The modelling of rock breakage process by TBM rolling cutters using 3D FEM-SPH coupled method. *Tunn Undergr Sp Tech*, 61:90–103, 2017.

[130] A. Gilat, R.K. Goldberg, and G.D. Roberts. Strain rate sensitivity of epoxy resin

in tensile and shear loading. Technical report, National Aeronautics and Space Administration (NASA), 2005.